The University of Nottingham

School of Mechanical, Materials, and Manufacturing Engineering

FINITE ELEMENT MODELLING OF THE STATIC AND DYNAMIC IMPACT BEHAVIOUR OF THERMOPLASTIC COMPOSITE SANDWICH STRUCTURES

by

Kevin Anthony Brown

MEng (Hons)

Thesis submitted to the University of Nottingham for the degree of Doctor of Philosophy

November 2007

Contents

Abstract

The overall objective of this study was to develop and validate a predictive modelling methodology for simulating the static and dynamic impact failure response of thermoplastic composite sandwich structures. The work has primarily focused on sandwich constructions with commingled woven fabric glass/polypropylene composite skins and a crushable polypropylene foam core.

The static and high strain rate mechanical properties of the thermoplastic composite skin material have been experimentally characterised. This investigation showed that the tensile and compressive modulus and strength increased with strain rate while the shear modulus and strength decreased as strain rate increased. A modelling methodology was developed for predicting damage in the thermoplastic composite using the advanced MAT 162 material model that is implemented in the LS-DYNA explicit finite element code. An inverse modelling technique for calibrating and validating the MAT 162 damage parameters was developed. The material model was validated for predictive simulation of the static and crash response of a large scale complex shaped demonstrator thermoplastic composite automotive component.

The static and dynamic mechanical properties of the thermoplastic foam core have been experimentally investigated and presented. This was followed by an experimental investigation and finite element modelling of the failure modes of the thermoplastic composite sandwich under static and dynamic localised indentation and bending loads. A fracture criteria was implemented in the model to simulate core shear fracture.

The main contributions to knowledge from this doctoral study are: the static and dynamic characterisation of the mechanical properties and failure modes of the thermoplastic composite and the crushable thermoplastic foam material; development of a validated modelling methodology for predicting damage in thermoplastic composites; and development of a finite element modelling procedure for simulating the static and dynamic impact failure behaviour of thermoplastic composite sandwich structures.

Acknowledgements

The author would like to thank the supervisors of this work, Dr Richard Brooks and Dr Nicholas Warrior, for their guidance and support throughout this project.

This study was financially supported by the EPSRC and the NIMRC and this support is gratefully acknowledged. I would also like to acknowledge the support of the industrial partners on this project: Security Composites, Dow Automotive, Arup, MIRA, TNO, Saint Gobain Vetrotex and Ellis Developments.

Thanks to the School of Mechanical, Materials and Manufacturing Engineering for the use of the school facilities and the support of the technical staff including Roger Smith, Paul Johns, Dave Smith and Geoffrey Tomlinson. Thanks also to the library, IT and Purchase Office staff members.

Thanks to all the members of the Polymer Composites Research Group, particularly the members of the Pedestrian Safety Group, Dr Martin Dunmore, Dr Palanivel Kulandaivel and Paul Williamson for their invaluable advice and assistance.

Thanks to Paul Boateng, Mohamed Jiffri and Paul Williamson for proof reading my thesis.

Special thanks to The Hon. Lord Bill Morris of Hansworth OJ for assisting me in gaining the opportunity to study in the UK.

Finally, special thanks to my family and friends who have supported and encouraged me throughout this work.

Dedicated to Grammy,
without your love and support
I would not be where I am now.

Abbreviations and Notations

Abbreviations

3PBD	Three-Point Bending
ASTM	American Society of Testing and Materials
BSI	British Standards Institute
CAD	Computer Aided Design
CDM	Continuum Damage Mechanics
CF	Carbon Fibre
CG-BPF	Composites Group of the British Plastics Federation
CRACTAC	Crashworthy Automotive Components Using Thermoplastic Composites
CRAG	Composites Research Advisory Group
CSM	Chopped Strand Mat
DCB	Double Cantilever Beam
ENF	End Notch Flexure
EPP	Expanded Polypropylene
FE	Finite Element
FMVSS	Federal Motor Vehicle Safety Standards
GF	Glass Fibre
GFRP	Glass Fibre Reinforced Plastic
GMT	Glass Mat Thermoplastic
IIHS	Insurance Institute for Highway Safety
ISO	International Organisation for Standards
LFT	Long Fibre Thermoplastic
MMB	Mixed Mode Beam Test
mPA-6	Modified Polyamide-6
PA6	Polyamide-6
PAI	Polyamide
PEEK	Polyether-ether Ketone
PEI	Polyetherimide
PMI	Polymethacrylimide
PP	Polypropylene
PPS	Polyphenylene Sulphide
PS	Polystyrene
PSUL	Polysulfone
PUR	Polyurethane
PVC	Polyvinylchloride
RTM	Resin Transfer Moulding
SAN	styreneacrylonitrile
SHPB	Split Hopkinson Pressure Bar

UD	Unidirectional
VCCT	Virtual Crack Closure Technique
wt	Weight Fraction

Notations

Composite Model Parameters

x	In-plane warp direction for woven fabric composite
y	In-pane weft direction for woven fabric composite
z	Out-of-plane direction
ρ	Density
E_x	Longitudinal Young's modulus
E_y	Transverse Young's modulus
E_z	Through thickness Young's modulus
υ	Poisson's ratio
G_{xy}	Shear modulus, x-y plane
G_{yz}	Shear modulus, y-z plane
G_{zx}	Shear modulus, z-x plane
S_{xT}	Longitudinal tensile strength
S_{xC}	Longitudinal compressive strength
S_{yT}	Transverse tensile strength
S_{yC}	Transverse compressive strength
S_{zT}	Through-thickness tensile strength
S_{Fz}	Crush strength
S_{FS}	Fibre shear strength
S_{xy}	Shear strength, x-y plane
S_{yz}	Shear strength, y-z plane
S_{zx}	Shear strength, z-x plane
ε_x	Longitudinal strain
ε_y	Transverse strain
ε_z	Through-thickness strain
ε_{xy}	Shear strain, x-y plane
ε_{yz}	Shear strain, y-z plane
ε_{zx}	Shear strain, z-x plane
ϖ_i	Damage variable
φ	Columb friction angle
EEXPN	Tensile volume strain limit
ECRSH	Compressive volume strain limit
ELIMIT	Fibre tensile axial strain limit
S	Delamination scale factor

m1	Fibre damage parameter (longitudinal)
m2	Fibre damage parameter (transverse)
m3	Fibre crush and punch shear damage parameter
m4	Matrix damage parameter
r_j	Damage threshold
C1	Strain rate parameter for strength properties
C2	Strain rate parameter for elastic modulii in the x-direction
C3	Strain rate parameter for shear modulii
C4	Strain rate parameters for elastic modulii in the z-direction
S_{RT}	Rate adjusted strength
S_0	Quasi-static strength
E_{RT}	Rate adjusted modulii
E_0	Quasi-static modulus
$\dot{\varepsilon}_0$	Quasi-static reference strain rate
$\dot{\bar{\varepsilon}}$	Effective strain rates

Foam Model Parameters

F_{ij}	Coefficient of the Tsai-Wu yield surface
σ_x	Longitudinal stress
σ_y	Transverse stress
σ_z	Through-thickness stress
σ_{xy}	Shear stress, x-y plane
σ_{yz}	Shear stress, y-z plane
σ_{zx}	Shear stress, z-x plane
ε_v	Volumetric strain
V_0	Initial volume
V	Current volume
σ_{yc}	Compressive yield stress
σ_{yt}	Tensile yield stress
σ_y	Symmetric yield stress

Chapter 1

Introduction

1.1 Background

Today automotive manufacturers are faced with several complex challenges. In a highly competitive market, customers are demanding more for their money. Motorists desire cars that offer high performance, comfort, refinement, safety as well as increased vehicle customisation. The automotive industry is also faced with Governments who are consistently introducing legislation that demand improvements in fuel efficiency, reduced emissions, increased recycling and greater safety for both occupants and pedestrians. The situation facing the auto industry is best summarised by quoting an article in the Polymotive magazine [1] *"Far-reaching efforts to achieve components that are rigid, strong, safe and at the same time, as light as possible are needed in order to survive in automotive manufacturing"*.

In response to the above factors, there has been a significant increase in the application of composites in the automotive industry. Composites are being selected for their high stiffness, high strength to weight ratio and energy absorbing properties. Composites offer significant weight savings as high as 35% compared to steel [2]. Reduced weight results in opportunities to improve fuel economy, which subsequently helps to reduce emissions. In particular, carbon fibre reinforced thermoset composites are being used in the high performance, low volume car market. However, their application remains limited because of high material and production costs; in addition to long manufacturing cycle times. In contrast, thermoplastic composites are experiencing dramatic growth due to the increasing application of glass mat thermoplastic (GMT) and long-fibre thermoplastic (LFT) composite components in the mass production automotive sector. In particular, LFT is one of the fastest growing sectors of the polymer industry with automotive applications accounting for over 95% of the worldwide demand [3]. According to car makers Volkswagen and DaimlerChrysler, the application of glass reinforced thermoplastics in automobiles will grow at an annual rate of 10% (cited in [3]). The

attractive benefits provided by thermoplastic composites over metallic and thermoset composites include [2, 4, 5]:

- Increased fracture toughness and impact tolerance.
- Rapid manufacturing with low cycle times that allow for medium to high volume production
- Reduced manufacturing costs with significant tooling cost savings
- Increased opportunity for part integration as numerous components can be combined into one single module which provides savings in tooling and assembly
- Higher chemical stability and unlimited shelf life of raw material
- No volatile organic compounds (VOCs) which results in a cleaner working environment with reduced issues around material handling.
- High recyclability potential which is very significant in light of the new European End-of-Life Vehicle (EELV) directive that specifies that at least 95% of the vehicle weight must be reused or recovered for new cars made after January 2015 [6].

The application of thermoplastic composites was initially restricted to semi-structural components such as front-end panels, spare wheel wells, underbody closures and door panels [4]. However, more structural applications are emerging, for example the rear axle support lid on the Volvo V70 XC AWD which supports the rear differential and is bolted directly to the vehicle axle [2, 4] as well as the thermoplastic composite bumper beam for the BMW M3 that enhances energy absorption while providing weight savings of 60% [2]. Another recent example is the development of an all thermoplastic composite front-end crash structure by Lotus Engineering in collaboration with Jacob Composites GmbH [6]. However, despite the increased application of thermoplastic composites, research into the dynamic impact and crash performance of these materials still remains limited [7].

Composite sandwich constructions are also being given increased consideration for application in vehicle front-end structures. The high energy absorbing capability of sandwich structures makes them an attractive passive solution for meeting crashworthiness countermeasure requirements [8]. Sandwich structures typically consist of two thin, stiff, high strength skins that are separated by a thick, low density, low strength

core [5, 9]. In a sandwich, the skins carry both in-plane and bending loads while the primary purpose of the core is to provide spacing between the skins and carry the transverse shear loads to which the sandwich maybe subjected. Sandwich constructions offer several advantages over monolithic composite laminates such as high stiffness to weight ratio, high bending strength to weight ratio, high energy absorption potential and good thermal and acoustic insulation. Furthermore, sandwich constructions with fibre reinforced thermoplastic skins along with a core made from the same thermoplastic material offers significant advantages. Thermoplastic composite sandwiches offer the potential for rapid, low cost mass production as the single thermoplastic polymer used in the skin and core allows for combined forming and joining in a one-step process [10]. Additionally, the all thermoplastic feature of the sandwich permits the production of shaped structures from flat plates by thermoforming techniques. Despite, these salient features, very little has been reported in the open literature on these structures [10, 11].

Today, finite element simulations are used extensively in vehicle design and crashworthiness assessment by virtually every car manufacturer. These tools have allowed car makers to reduce vehicle design cycles and avoid the high costs associated with experimental testing. Crashworthiness simulations of metallic structures are now well established; however, advanced finite element models for fibre reinforced composites are just emerging. In particular, the study of impact damage progression and failure in composite structures has become one of the most researched areas over the last two decades. However, in contrast to monolithic composite structures, composite sandwich structures have received limited attention. This is despite the fact that research into the theoretical analysis of sandwich structures began in the 1940s [9, 12]. Today, the emphasis is now moving more towards finite element techniques rather than analytical methods because of the difficulty in obtaining more exact solutions and deriving and solving the differential equations for sandwich constructions [13, 14]. Nonetheless, finite element modelling of sandwich structures poses several challenges. The level of structural and material complexity of the composite sandwich is greater than that of metallic and monolithic composite structures due to the inhomogeneous and anisotropic nature of the sandwich construction; in addition to the more complex failure mechanisms of the composite skins and core material. Advanced finite

element composite and foam constitutive material models that can simulate damage progression and fracture are emerging; however the development of a predictive modelling methodology for composite sandwich structure is still in its infancy.

1.2 Objectives and Scope of this Work

The overall objective of this thesis is to develop a methodology for predictive modelling of impact damage in thermoplastic composite sandwich structures. Specifically, the focus of this study will be on sandwich structures with Twintex commingled woven fabric glass/polypropylene skins and crushable anisotropic polypropylene foam cores. The main aims are to:

- Develop an appropriate finite element modelling methodology for the quasi-static and dynamic impact loading of thermoplastic composite sandwich structures which accurately predicts the damage and deformation behaviour of these structures.
- Identify appropriate material models for modelling damage onset and growth in the thermoplastic composite material and fracture in the foam core.
- Characterise the static and dynamic mechanical properties of the thermoplastic composite and foam materials so as to enable the accurate calibration and validation of the finite element models.
- Determine the failure modes of thermoplastic composite sandwich structures under localised static and dynamic impact indentation and bending loads.
- Determine limitations of the finite element method when modelling thermoplastic composite sandwich structures and recommend improvements.

1.3 Thesis Layout

This thesis is divided into six chapters. Following this introduction, the thesis is composed as follows:

Chapter 2 presents a comprehensive literature review of the state of the art in finite element modelling of the impact behaviour of thermoplastic composite sandwich structures. The literature review is divided into four main sections: characterisation of the mechanical properties of composite materials; FE modelling of damage in composite materials; cellular solids and FE modelling of composite sandwich structures.

Chapter 3 presents an extensive experimental program for investigating the mechanical properties of the thermoplastic composite material under static and high strain rate loading. These tests included tensile, compression, shear and three-point bending tests.

Chapter 4 is devoted to the development of a calibration and validation methodology for an advanced material model within the LS-DYNA explicit finite element code that is used for predictive modelling of the thermoplastic composite. The validation of the calibrated finite element model for simulating the static and crash response of a demonstrator thermoplastic composite automotive component is presented.

Chapter 5 presents the experimental characterisation of the static and dynamic mechanical properties of the foam core. This is followed by the description of an experimental investigation and finite element modelling of thermoplastic composite sandwich structures under static and dynamic indentation and bending loads.

Chapter 6 presents the conclusions of this thesis and summarises the areas in which this study has contributed to knowledge. Future research themes are also outlined.

Chapter 2

Literature Review

2.1 Introduction

This chapter presents a comprehensive review of the current state of knowledge concerning all the themes in this research. An overview on composite sandwich structures is presented. Methods for characterising the static and dynamic mechanical properties of monolithic composite laminates are examined. The development of models for predicting the onset and growth of damage in composite laminates are reviewed. The mechanical behaviour of foam core materials is reviewed along with constitutive foam material models. Finally, a review of finite element models for predicting the impact response of composite sandwich structures is presented.

No attempt is made here to reference all significant publications. Instead, selected references are cited to illustrate specific points related to this study. The discussion that follows is generally descriptive. For more details the reader is referred to the cited references.

2.2 Composite Sandwich Structures

Sandwich structures generally consist of a low density thick, low strength core that is bonded between two thin, high strength faces [5, 15]. The skins primarily resist in-plane and through-thickness bending loads. They create an efficient stress couple that resist the external bending moments [5]. The main role of the core is to resist shear loads and stabilise the face against buckling or wrinkling. Sandwich constructions offer several attractive advantages such as high-stiffness to weight ratio and high flexural strength to weight ratio, higher resistance to buckling, high fatigue strength, and good acoustical and thermal insulation. In addition, sandwich constructions offer a higher energy absorbing capability in comparison with other monolithic structures [5].

Both the face and core tend to be made from either metallic or non-metallic materials. Metallic face materials include steel, stainless steel and aluminium alloys. The most common non-metallic face materials are fibre reinforced polymer composites. This is due in part to their excellent mechanical properties. In addition, it is easier to manufacture sandwich composites than metallic face sandwich constructions [5]. Balsa wood was the first core material to be used and was generally applied in the marine industry. In the mid-1900s honeycomb cores were introduced. They offer the highest shear stiffness and strength to weight ratios in comparison to other core materials. However, their application remains primarily limited to the aerospace industry due to their high cost [5]. In contrast, polymeric foams are relatively inexpensive and are gaining more widespread application in the rail, aerospace and automotive industry. In addition, the manufacturing of foam cored sandwiches is much easier than honeycomb cored constructions. The most common polymeric foams include polyurethane (PUR), polystyrene (PS), polyvinylchloride (PVC) and Polymethacrylimide (PMI). Recently, we have seen the emergence of a new generation of thermoplastic foam cores where mechanical properties are tailored by orienting the cell structure much like a honeycomb. An example is the highly oriented polypropylene foam supplied by Dow Chemical Company under the trade name Strandfoam which is the focus of this research.

2.2.1 Thermoplastic Composite Sandwich Structures

The development of sandwich constructions with fibre reinforced thermoplastic skins combined with cores made from the same thermoplastic material presents major advantages, especially in contrast to thermoset based structures [10]. The use of the same thermoplastic polymer throughout the sandwich results in strong skin-core interface bonding and eliminates the need to apply an adhesive. Furthermore, the fully thermoplastic feature facilitates recycling and the production of shaped parts from flat panels by thermoforming techniques [16]. One of the major advantages of the thermoplastic composite sandwich construction is the potential for rapid, low cost high volume manufacturing. The single polymer in the skins and core allows for rapid production of flat and shaped parts by combining forming and joining in a one-step process [10, 17].

2.2.2 Application of Thermoplastic Composite Sandwich Structures

Zenkert [5] presents several examples of the application of sandwich structures in the automotive, rail and marine industry. In addition, sandwich constructions are being used in aerospace and civil engineering applications including wind turbine blades. These applications are dominated by thermoset based composite sandwiches.

There is growing application of thermoplastic composite sandwich constructions in automotive applications such as those shown Figure 2-1 which include the Microcar floor, Nissan trunk floor, rear parcel shelves and BMW M3 rear back seat [18]. These are mainly secondary semi-structural applications. However, recently, Brooks and Pharaoh [19] reported on a more structural crashworthiness application of a thermoplastic composite sandwich construction. They presented work on a thermoplastic composite bumper beam that was developed during the CRACTAC (Crashworthy Automotive Structures Using Thermoplastic Composites) program (see Figure 2-2). Bumper beams made from various combinations of skin and core materials were investigated. Skins were made from either GMT only, GMT/Plytron or GMT/Twintex laminates, while the core materials included either expanded polypropylene (EPP), polypropylene (PP) Strandfoam or polypropylene (PP) honeycomb cores. The beams were tested under static bending loads as well as dynamically in accordance to the IIHS 8 kmph rear pole test. The results show that all the beams with the various material configurations passed the stipulated peak load criteria although there was significant variation between the various skin-core material combinations. It was shown that beams with aligned continuous glass fibre/PP composite (Plytron and Twintex) skins exhibited reduced peak loads and intrusion in contrast to beams with only GMT skins. Additionally, beams with Strandfoam cores allowed more intrusion whilst minimising peak loads in comparison to beams with honeycomb cores that exhibited less intrusion but exhibited a higher peak load.

Microcar Floor

Sandwich construction: Twintex skins with PP honeycomb core

(a)

Nissan Trunk Floor

Sandwich construction: Twintex skins with PP honeycomb core

(b)

Sandwiform™ Rear Parcel Shelf

Sandwich construction: Twintex skins with PP honeycomb core

(c)

BMW M3 Back Seat

Sandwich construction: Twintex skins with foam core

(d)

Figure 2-1. Examples of automotive applications for thermoplastic composite sandwich constructions with glass reinforced thermoplastic composite skins and thermoplastic honeycomb or foam cores [18].

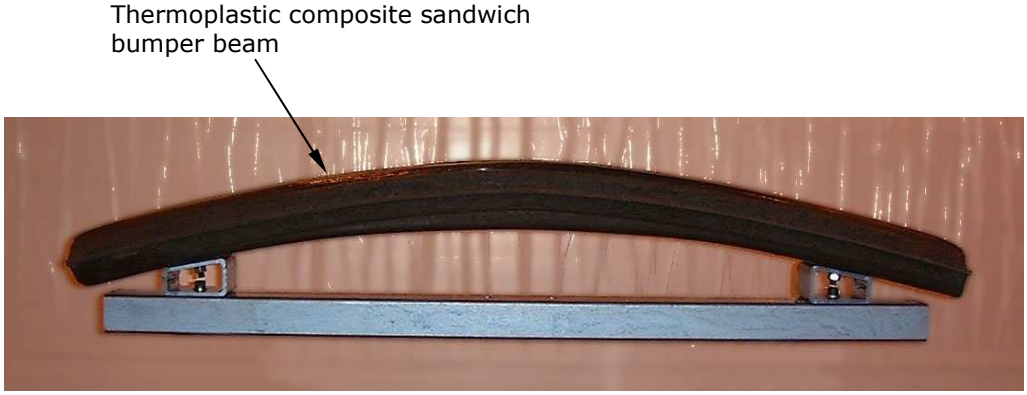

Figure 2-2. CRACTAC thermoplastic composite sandwich bumper beam [19].

2.3 Polymeric Composite Materials

This section presents a brief introduction to composite materials with specific focus on thermoplastic composites.

Composites consist of two or more materials that have been combined to produce a distinct material that has enhanced properties [20]. Typically composites consist of high strength fibre reinforcements that are supported by a polymeric matrix (binder) material. The most popular fibre reinforcements are: glass (E-glass, S-glass and S2-glass), carbon, and aramid fibres. Recently, there has also been an increased interest in natural fibres such as Hemp [21]. The two main categories of polymer matrix materials are thermoplastics and thermosets. The most common thermoset matrices are: polyester, vinylester, epoxies, phenolics and polyurethane. Thermoplastic matrices include nylon, polypropylene (PP), polyamide-imide (PAI), polyether-ether ketone (PEEK), polysulfone (PSUL), polyphenylene sulfide (PPS), and polyether-imide (PEI).

2.3.1 Thermoplastic vs Thermoset

Thermoset polymer matrices are generally low viscosity liquids that solidify through chemical cross-linking of a low weight monomer and prepolymer into a high-weight polymer network [5]. Once these cross-links are formed after the curing (polymerisation reaction), the thermoset polymer cannot be melted and reshaped by the application of heat and pressure. Thermoset composites provide the following advantages: good wet-out between the fibres and the matrix, and less creep and stress relaxation

than thermoplastic polymers. However, they have limited shelf life, long manufacturing times, low strain to failure and in some cases, low impact strengths [22].

Thermoplastics offer several advantages over thermoset polymer composites including high impact damage tolerance and fracture resistance due to their more ductile nature and larger strain-to-failure characteristics. In addition, thermoplastic composites provide other advantages including:

- Shorter manufacturing cycles (as short as 2 minutes or less)
- Lower processing cost
- Unlimited shelf life
- Ease of handling
- Post thermoforming capability and forming in multiple steps
- High recyclability during both manufacturing (recycling scrap) and end of life

Despite these advantages, impregnating continuous aligned fibres with a thermoplastic matrix is difficult due primarily to their high melting temperatures and viscosity [22, 23]. There are several impregnation processes that have been devised for the processing of thermoplastics. These include melt impregnation, solvent impregnation, powder impregnation, co-weaving, and commingling [23, 24]. Wakeman and Rudd [23] provide an excellent review of these impregnation techniques.

Thermoplastic composites are generally processed using thermoforming techniques which include: roll forming, match die stamping, vacuum forming, stretch forming and diaphragm forming. A detailed description of the various manufacturing techniques is beyond the scope of this thesis. However more details are available in references [23-26]

2.3.2 Commingled Woven Fabric Thermoplastic Composites

This section provides a brief review of commingled woven fabric thermoplastic composites which are the focus of this study.

Commingling is a well established textile process for developing an intimate combination of the two or more yarns [23]. In this system the yarns

consist of the reinforcing fibres and a fibrous form of the matrix. This results in a very short flow length between the fibres and matrix which leads to good consolidation and impregnation that occurs at lower pressures than those required for conventional impregnations.

Saint Gobain Vetrotex have patented a commingling process for the manufacturing of a commingled woven fabric glass/polypropylene composite which was introduced in 1997 under the trade name, Twintex [23, 25, 27]. The glass content is 60% by weight and the weave structure is either balanced twill or plain fabric. Twintex presents many attractive features including:

- High energy absorption due to continuous aligned fibres and ductile polypropylene (PP)
- Enhanced mechanical properties due to high glass content and aligned continuous fibres
- Better dimensional stability and resistance to moisture absorption than standard thermosets due to PP matrix
- Rapid manufacturing due to fast consolidation
- Good drapability
- Recyclability

In addition, due to its enhanced mechanical properties, Twintex is often used as a local reinforcement in GMT and LFT hybrid structures [16].

2.3.3 Application of Thermoplastic Composites in the Automotive Industry

There has been a strong growth in the use of thermoplastic composites in automotive applications. However, their use is still somewhat restricted to secondary and semi-structural components [22]. GMT, LFT and Twintex thermoplastic composites are now being used for front door modules, spare wheel wells, hatchback door modules and bumper beams (see Figure 2-3).

(a)

(b)

(c)

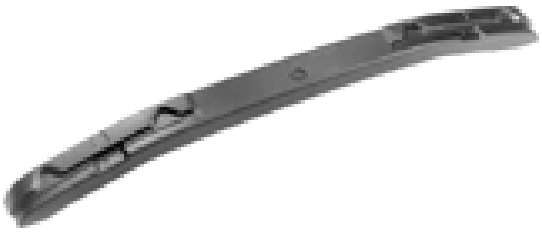

(d)

Figure 2-3. Current application of thermoplastic composites in (a) front door module (b) rear door module (c) spare wheel well (d) bumper beam.

Recently, there has been a growing interest in applying thermoplastic composites to primary structural crash components in passenger vehicles. A demonstrator thermoplastic composite side impact beam made from Twintex was developed during the CRACTAC (Crashworthy Automotive Structures Using Thermoplastics Composites) project which was part of the Link Foresight Vehicle Program [7, 28, 29] (see Figure 2-4). During testing, the thermoplastic composite beam was shown to exhibit a comparable performance to the steel side impact beams under large deformation loading. Additionally, a finite element model of the thermoplastic beam was developed using the PAM-CRASH explicit finite

element code with simulation results showing good agreement with test observations.

Recently, Lotus Engineering and Jacob Composites developed a glass reinforced thermoplastic front end crash structure as part of their joint project called ECOLITE (Efficient Composites – Lightweight and Thermoformed) [6]. The main objective of the ECOLITE program is to develop a passenger car with a composites body and chassis for medium volume production. The glass/polyamide 6 thermoplastic composite crash structure is shown in Figure 2-5. Crash tests have shown that the thermoplastic structure out performs both thermoset and metallic crash solutions.

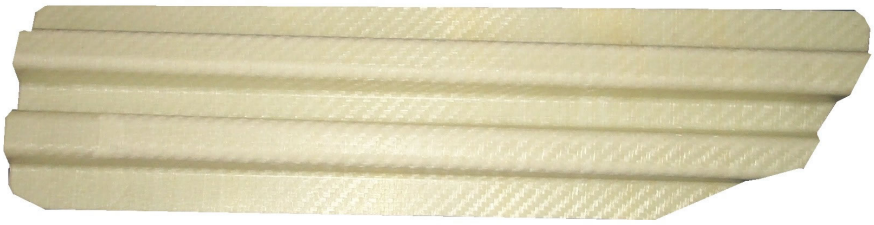

Figure 2-4. CRACTAC thermoplastic composite demonstrator side impact beam manufactured from Twintex material [7].

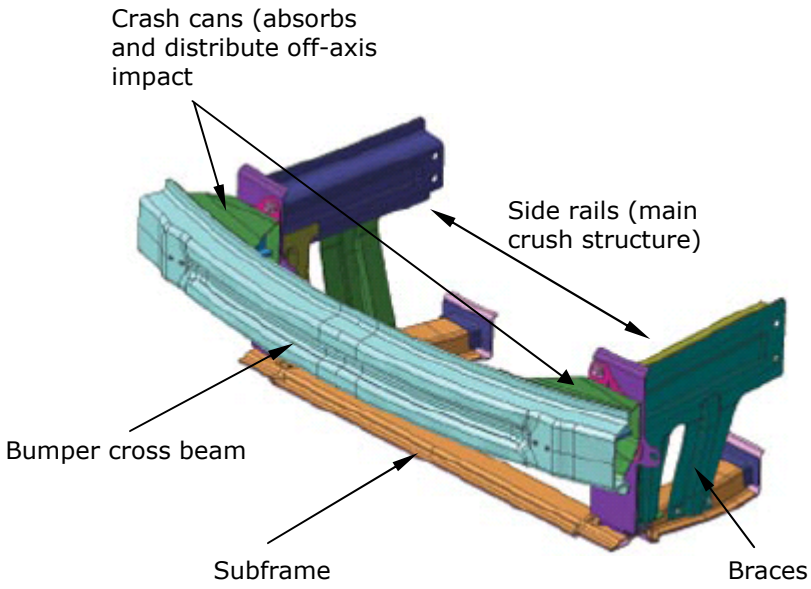

Figure 2-5. ECOLITE glass-reinforced thermoplastic composite front-end crash structure [6].

2.4 Characterisation of Composite Mechanical Properties

This section gives a review of the state-of-the-art on experimental methods that are used to characterise the quasi-static and high strain rate material properties of composite materials and discusses the effect of strain rate on such materials.

Generally, composite materials are orthotropic and have complex failure modes. Therefore, a larger number of strength and elastic properties must be determined for complete characterisation. Quasi-static mechanical properties are generally of primary interest. Quasi-static strain rates are in the range 10^{-4} – 10^{-3} s^{-1}. The stress-strain response of the material under quasi-static loading is considered to be an intrinsic property of the material and is only valid for the strain rate at which the test was conducted [30, 31]. Under dynamic loading, the stress-strain properties of the material may change. These changes typically initiate at a range of strain rates from 10^{-1} to 10^{2} s^{-1}. This strain rate range is generally referred to as the intermediate or medium strain rate regime. At the medium strain rate region inertia forces and mechanical resonance begin to become important considerations. However, wave propagation effects are often neglected and uniform stresses and strains are assumed in the test specimen. Strain rates of 10^{3} s^{-1} or higher are considered to be within the range for high strain rate response. At high strain rates, inertia, wave propagation and thermodynamic effects become important considerations [30]. This leads to difficulties and uncertainty in the interpretation of results. In addition, there are no direct methods for obtaining dynamic stresses and strains; instead, wave propagation theory has to be used to obtain such information [30]. Figure 2-6 shows a schematic that summarises the static and dynamic strain rate regimes.

2.4.1 Quasi-Static Experimental Methods

Comprehensive reviews of various test methods that are used for characterising quasi-static mechanical properties of composite materials have been presented by Adams [32] and Zenkert [5]. The development of quasi-static test methods for composite materials began in the late 1950s [32, 33]. Composite laminate test standards began to emerge in 1986

with the adoption of the Composites Research Advisory Group (CRAG) recommendations by the Composites Group of the British Plastics Federation (CG-BPF) [34]. These tests methods were aimed at aerospace applications but were considered appropriate for non-aerospace material characterisation. Today, several standardised approaches to experimental quasi-static analysis of composites have been published by the American Society of Testing and Materials (ASTM), the International Organisation for Standardisation (ISO) and the British Standards Institute (BSI). There are a multiplicity of test methods for characterising composite materials under quasi-static tension, compression, shear and flexural (bending) loading conditions. loading

The material of interest in this study is 60% wt commingled woven fabric balanced Twintex for which only limited data on its mechanical properties has been reported in the open literature. The suppliers of Twintex, Saint-Gobain Vetrotex provide a small range of static mechanical properties that were obtained from test methods based on ISO standards [35]. These include tensile stiffness and strength (ISO 527) and flexural modulus and strength (ISO 728). The impact resistance properties have also been reported using the Charpy impact unnotched (ISO 178) and the Izod impact notched (ISO 180) tests. A more detailed presentation of the static mechanical properties of Twintex was reported by the University of Wyoming [36]. All the tests conducted by the University of Wyoming were done according to ASTM standards. Wilson [7] also presented the static mechanical properties of Twintex based on ISO standards.

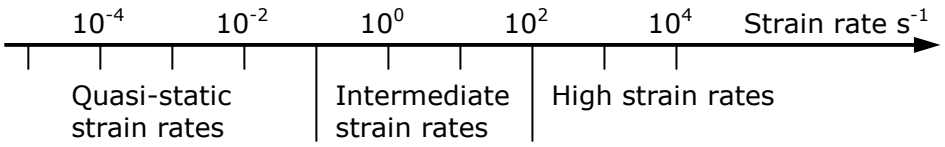

Figure 2-6. Quasi-static and dynamic strain rate regimes [30].

2.4.2 High Strain Rate Experimental Methods

Comprehensive reviews of experimental methods applicable to the high strain rate behaviour of composites have been presented by Sierakowski [31] and Hamouda and Hashmi [37]. There are few standard tests methods for dynamic characterisation of composite materials and generally specialised testing equipment have to be employed. The selection of an experimental method for high strain rate analysis depends on the strain rate range and the loading mode with each technique having its advantages and limitations. These techniques have been summarised in Table 2-1. The most widely used dynamic testing methods and results obtained by researchers for various types of composite systems are discussed in the following section.

Table 2-1. Summary of experimental techniques for quasi-static and high strain rate testing [31, 37, 38].

Strain rate	Tests	Testing method
<0.1	Tension	Electromechanical testing machine
0.1 – 100		Servo-hydraulic machine
0.1 - 500		Drop tower
100 – 500		Explosive
100 – 10^4		Split Hopkinson pressure bar in tension
10^4		Expanding ring
>10^5		Flyer plate
< 0.1	Compression	Electromechanical testing machine
0.1 – 100		Servo-hydraulic machine and charpy
0.1 - 500		Drop tower and cam plastometer
200 – 10^4		Split Hopkinson pressure bar in compression
10^4 - 10^5		Air gun
< 0.1	Shear	Electromechanical testing machine
0.1 - 100		Servo-hydraulic machine and charpy
0.1 – 500		Drop tower
10 – 10^3		Torsional impact
100 – 10^4		Split Hopkinson pressure bar in torsion
10^3 – 10^4		Double-notch shear and punch
10^4 – 10^7		Pressure-shear plate impact

2.4.2.1 Servo-hydraulic tests

Servo-hydraulic test machines are limited to strain rates within the quasi-static and intermediate strain rate regimes because of the inertial effects of the load cell and grips and wave propagation effects in the test specimens [31]. Today, servo-hydraulic machines have servo-valves with electronic feedback that can accurately control loading rate, displacement rate and strain rate [32]. These machines give good results up to strain rates of 100 s^{-1} [39]. A limited number of high strain rate tests on composites have been conducted on these machines.

Todo et al [40] conducted tensile testing of plain weave carbon/polyamide-6 (CF/PA6), carbon/modified polyamide-6 (CF/mPA6), glass/polyamide-6 (GF/PA6) and glass/modified polyamide-6 (GF/mPA6) composites in a servo-hydraulic machine at strain rates ranging from 10^{-2} to 40 s^{-1}. They observed that typically, the tensile strength and failure strain increased with an increase in strain rate with the exception of GF/mPA6 whose mechanical properties remained constant at strain rates above 10^{-2} s^{-1}. A viscoelastic damper was used to reduce inertial effects.

Thiruppukuzhi and Sun [41] used a closed loop servo-hydraulic machine to test unidirectional S2-glass/8553-40 and woven 7781/F155 E-glass fabric under tensile loading at strain rates from 10^{-4} to 1 s^{-1}. Both material systems showed marginal rate sensitivity.

2.4.2.2 Drop weight tests

Drop weight tests are typically conducted in falling weight drop towers at high strain rates up to 10^{2} s^{-1}. The drop tower assembly generally consist of a free falling, weighted striker that is raised to a predefined height and then released, imparting a load on the test specimen. For this test, the maximum strain rate is limited by the maximum speed of the striker which is directly related to the height of the tower. The maximum striker speed is typically 10 ms^{-1} [42]. Higher velocities and consequently higher strain rates can be achieved by installing rubber bungee cord systems into the drop tower which can increase the velocity and strain rate to over 30 ms^{-1} and 10^{3} s^{-1}, respectively [39]. The drop weight test offers several advantages including, simple setup, low cost, accommodates different specimen geometries and easy variation of strain rate [43]. However, the

sudden impact in this test causes spurious vibrations, transient stress waves and the inability to achieve constant strain rates at very large strains [30].

Lifshitz [44] used an instrumented drop tower to study the dynamic tensile strength of angle ply glass/epoxy laminates. The results for all tests showed that strength increased with an increase in strain rate, while failure strain and initial modulus remained unchanged.

Barre et al [38] used a new specimen design in a drop weight tests to characterise the dynamic tensile behaviour of glass fibre-reinforced phenolic and polyester matrix composites at strain rates between 10^{-1} and 10^{1} s^{-1}. The specimens were manufactured using resin transfer moulding (RTM) and pultrusion processes. For all material systems tested, the elastic modulus increased with increasing strain rate. The tensile strength increased with increasing strain rate with the exception of the pultruded E-glass/polyester continuous mat roving specimens which showed a slight decrease.

Groves et al [39] conducted dynamic compression testing on IM6/974 [0/90] carbon/epoxy tapered cube specimens in a modified drop tower at strain rates from 10^{1} to 10^{3} s^{-1}. The drop tower had an acoustically damped base system that eliminated shock wave reflections. In addition a compression alignment fixture was used to minimise end effects in the specimens. A significant increase in the compression strength was observed for strain rates above 10^{1} s^{-1}. Groves et al [39] also designed special fixtures for high strain rate tension and shear tests at strain rates up to 100 s^{-1}. The tensile fixture uses small flared solid or tubular specimens. However, the small size of the specimens makes them difficult to fabricate.

Montiel and Williams [45] designed a novel compression fixture (see Figure 2-7) for dynamic testing of AS4 graphite/PEEK $[0_2/90]_{8s}$ composites in a drop tower at strain rates up to 8 s^{-1}. At high strain rates the strength and failure strain increased by 42% and 25% over the static values, respectively. There was a modest 7% increase in the initial modulus at high strain rates.

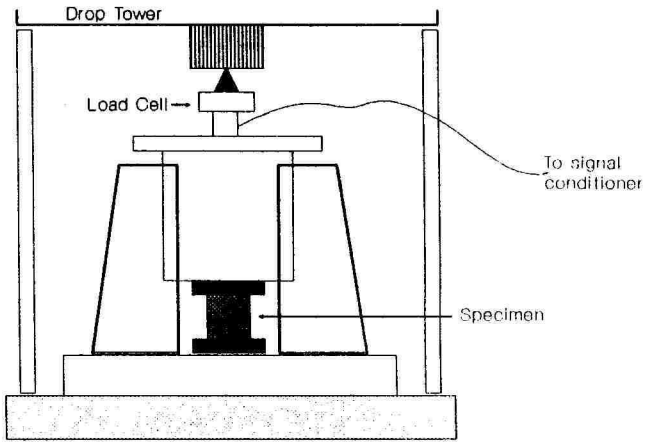

Figure 2-7. Schematic of dynamic compression fixture [45].

Hsiao and Daniel [43] used a drop tower apparatus to investigate rate effects on the compressive and shear behaviour of carbon/epoxy composites at strain rates between 10 to 500 s^{-1}.

2.4.2.3 The split Hopkinson pressure bar (SHPB)

The split Hopkinson pressure bar shown in Figure 2-8 and Figure 2-9 was first introduced by Kolsky in 1949 [46]. It is one of the most widely used test configurations for high strain rate testing at strain rates between 10^2 and 10^3 s^{-1}. The technique was initially used for dynamic compression tests; however, it has been modified for tension, shear and torsion loading. A schematic of a typical SHPB apparatus is shown in Figure 2-8. In this approach a small cylindrical specimen is sandwiched between two long steel bars. A compression pulse is generated in the incident bar by a striker bar which is propelled by a gas gun apparatus or torsion bar spring. This compression wave propagates down the incident bar at constant amplitude with a finite duration that is directly proportional to the length of the striker bar. When the compressive wave reaches the specimen, a portion of the wave is reflected back down the incident bar as a tensile wave and the remaining portion transmits through the specimen towards the transmitter bar. When the wave passes through the specimen, the material deforms because of the impedance mismatch at the specimen interface. The continuous strain-time histories of the three pulses, incident, reflected and transmitted, are recorded with strain gauges mounted on the pressure bars. One-dimensional wave theory is then used to obtain the stress, strain and strain rate in the specimen. The general theory for a classic split Hopkinson pressure bar test is well documented.

See for example Nicholas [30] and Hauser [47]. The equations for the SHPB assume that dynamic equilibrium is achieved in the specimen whereby the forces at both the front and back faces of the specimen are equal. Furthermore, the specimen is assumed to undergo homogeneous deformation.

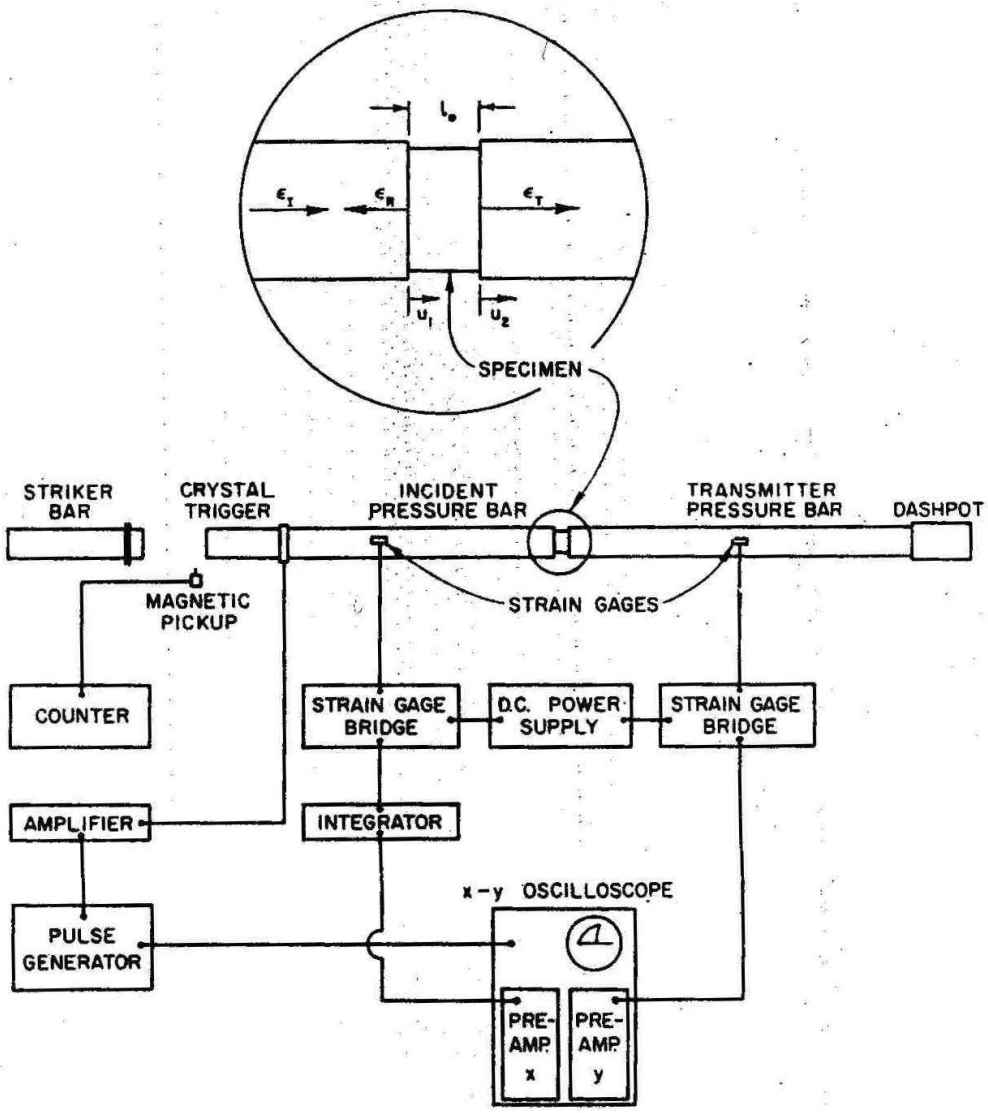

Figure 2-8. Schematic of split Hopkinson pressure bar apparatus [48].

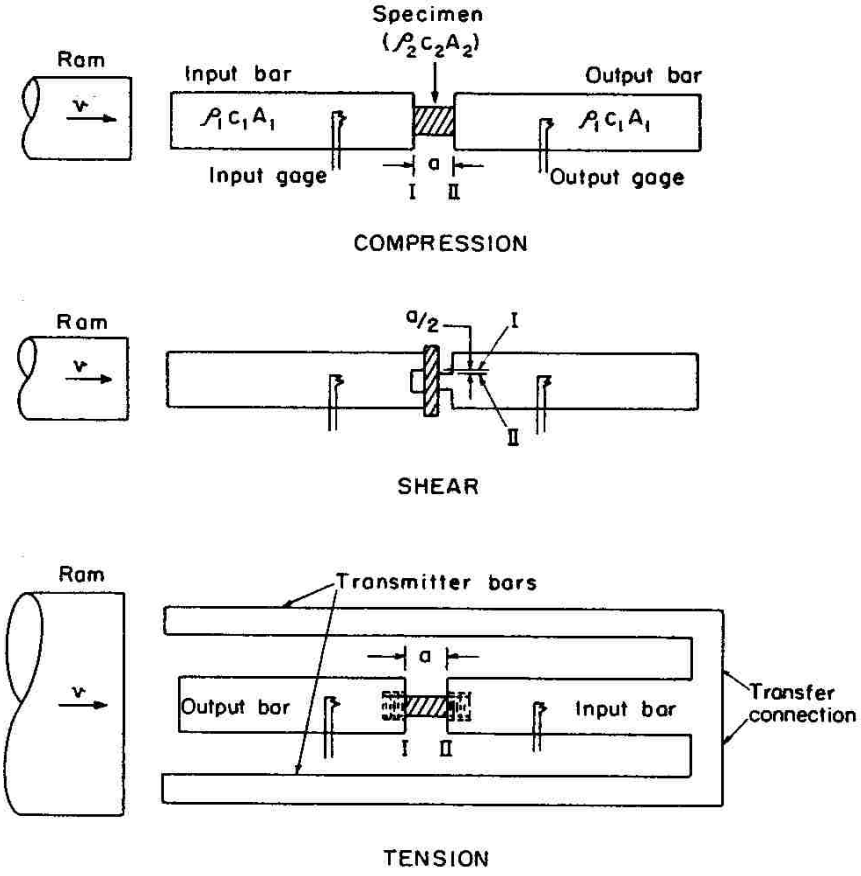

Figure 2-9. Schematic of typical compression, shear and tension split-Hopkinson pressure bar test setups [47].

Lindholm [48] summarised the advantages of the SHPB apparatus as follows: extremely simple mechanical system consisting of well aligned elastic bars and an accelerating device; the recording system only requires strain gauge circuits; dynamic calibration of the entire system may be obtained directly if the striker velocity is known. However, Hauser [47] disagrees with the suggestion that the SHPB method is a *"simple routine test."* He argued that the operation of the SHPB apparatus and the interpretation of the results require a thorough understanding of the mechanical and electrical systems. Furthermore, an understanding of wave propagation theory is required. Some inherent limitations of the SHPB have been discussed by Hamouda and Hashmi [37], Hauser [47], Mulliken [49] and Nicholas [30]. There is still no standard design for the SHPB apparatus and many issues related to the application of this unique test method are still in contention. The accuracy of the split Hopkinson bar is limited to where the fundamental assumptions of this technique are satisfied.

The SHPB method assumes that dynamic equilibrium is achieved during the test. For this assumption to be valid a large number of stress wave reverberations have to occur in the specimen. However, at high strain rates, the amplitude of the stress waves increase and the number of reverberating stress waves decreases, eventually invalidating the basic assumptions of a uniform stress state in the specimen. In addition, at high strain rates the neglect of radial inertia and end friction all become invalid. Consequently, there are limitations to the strain rates that can be achieved with the SHPB apparatus.

The assumption of dynamic equilibrium and a constant strain rate do not occur during the first few micro seconds of the test [30]. Therefore data obtained at very low strain rates and in the elastic region of the stress-strain results are not reliable.

A major challenge for the SHPB test is the specimen dimensions which have to be small so as to minimise radial inertia and wave propagation effects within the specimen. The need for small specimens may conflict with the general requirement for a specimen that is large relative to the scale of the reinforcement. Therefore, the SHPB technique is potentially limited to testing unidirectional or fine weave composite specimens with very small unit cells. In addition, care has be taken in designing the load transfer method between the specimen and pressure bars so as to avoid the introduction of significant impedance mismatch which could introduce stress wave reflections and invalidate the SHPB analysis. In addition, the anisotropic nature of composite materials can complicate the design of the load transfer interface [37].

For the SHPB setup, the uniaxial alignment of the striker bar and the pressure bars has to be near-perfect so as to validate the assumption of one dimensionality [49]. Any misalignment or strong reaction forces from the bearings may result in an alteration of the stress pulse and high frequency noise.

An example of the split Hopkinson bar being used for high strain rate analysis of thermoplastic composite materials is presented by Weeks and Sun [50]. They characterised the strain rate dependence of AS4/PEEK

(APC-2) thermoplastic composite using a split Hopkinson pressure bar. Balanced angle ply laminates with fibre orientations of $[90]_{64}$, $[\pm30]_{16s}$, $[\pm45]_{16s}$, and $[\pm60]_{2s}$ were tested at strain rates ranging from 100 to 1000 s^{-1}. The material was found to exhibit significant strain rate sensitivity.

2.4.2.4 Explosive testing

A specially designed impact loading machine propelled by explosives (see Figure 2-10) was used by Armenàkas and Sciammarella [51] to perform dynamic tests on S-glass (316)/epoxy in the fibre direction at strain rates up to 500 s^{-1}. The results show a 50% increase in the longitudinal modulus over the static value while there is a decrease in the longitudinal strength at high strain rates. In addition, greater fibre breakage occurs at high strain rates.

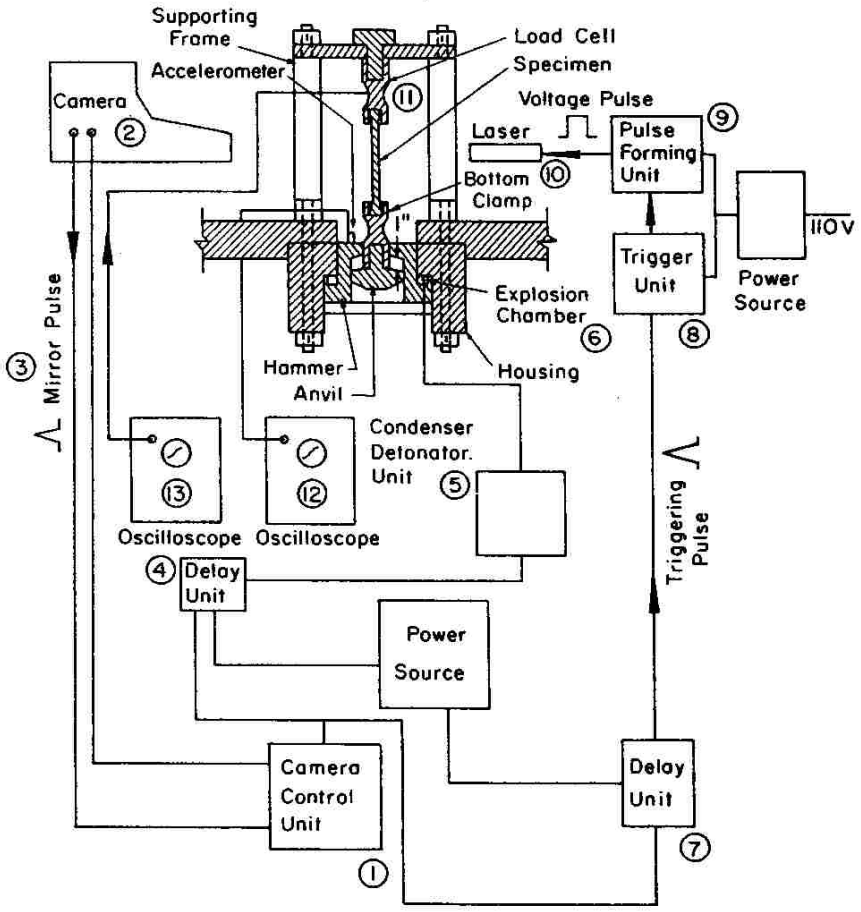

Figure 2-10. Schematic diagram of the high speed tensile machine [51].

2.4.2.5 Expanding ring

The expanding ring can be used for medium and high strain rate characterisation of composite material properties. Very high strain rates of 10^4 s^{-1} or greater can be obtained by this technique.

Daniel et al [52] performed dynamic tensile tests at strain rates ranging from 100 to 500 s^{-1} using composite ring specimens loaded by an internal pulse applied explosively through a liquid in a specially designed fixture shown in Figure 2-11. The tests were conducted on graphite/epoxy ring specimens with fibre orientations of 0°, 90° and 10° with respect to the circumferential direction. The results showed that the dynamic modulus for the 0° specimens were approximately 20% higher than the static value, while the dynamic strength and dynamic failure strain showed little or no change from the static values. For the 90° specimens, the modulus and strength increases two and four times the static values, respectively, while the failure strain showed little or no change. The in-plane shear strength and modulus from the 10° specimens are 30% higher than the static values, while the shear strain is less than the static result.

Further dynamic testing of carbon/epoxy and hybrid carbon/glass/epoxy material systems with the expanding ring test fixture was reported by Chamis and Smith [53]. They concluded that at strain rates of about 150 s^{-1}, the transverse dynamic modulus was three to four times greater than the static values; the transverse tensile strength increased three to five times the static values; the transverse compressive strength was about one and one-half to two times the static value. There was a small effect on the in-plane shear modulus and strength and a negligible effect on Poisson's ratio and the strain failure.

Commenting on the expanding ring test, Daniel et al [52] claims that the problem of wave propagation effects is somewhat eliminated by the short transit time for the wave across the thickness of the thin specimen [52]. In addition, problems associated with end effects and gripping of the specimen are reduced [54]. However, this test technique has several limitations. The maximum strain rate that can be attained is limited by wave propagation effects occurring when radial wave reflections through the thickness of the ring become significant which invalidates the assumption of a uniform circumferential stress state [30, 31]. In addition,

the accuracy of the calculated stress is reduced especially because of the process of double differentiating the measured displacement data [30]. Harding and Welsh [54] have noted that the strain rate is continuously decreasing during the test and a complex stress state is developed in the specimen that includes membrane stresses, radial stresses and shear stresses. Also, the practical difficulty of manufacturing the specimen and performing the tests limits its use [54].

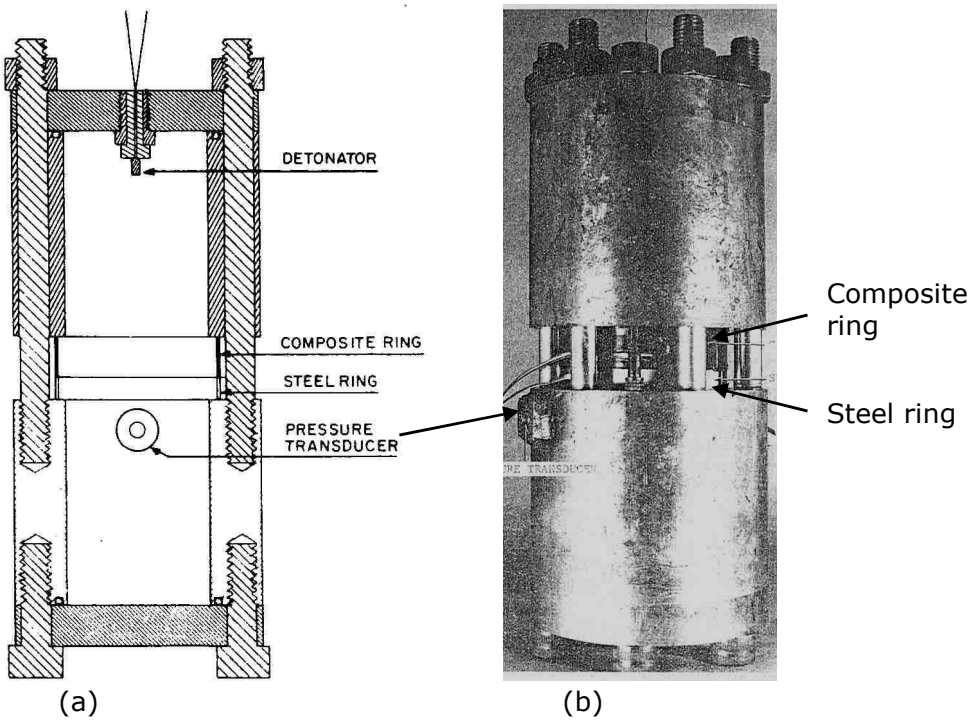

Figure 2-11. Expanding ring test for high strain rate loading of composite ring specimens [52] (a) Schematic diagram of test fixture (b) photograph of test assembly.

2.5 Core Materials: Cellular Solids

Sandwich cores are generally made from cellular solids. Cellular solids generally consist of an interconnected network of solid struts or plates which form the edges and faces of cells [55]. The simplest example of a cellular structure is the honeycomb which is a two-dimensional array of hexagonal polygons that are combined to fill a plane area. More popular, three-dimensional cellular solids are foams that have polyhedra cells. Foam cells can be classified as either open or closed cells. Open celled foams simply have cells that are connected by open faces while closed cell foams have solid faces that separate adjacent cells. There are also foams that have partially open and closed cells.

Honeycombs are generally manufactured from aluminium, impregnated glass or aramid fibre mats [5]. Recently we have also seen the emergence of thermoplastic polypropylene honeycombs [24]. Honeycomb properties tend to vary along each plane (anisotropic) and they have very high stiffness and shear properties. However, the main disadvantages of honeycombs are their high cost and difficult handling during sandwich manufacturing.

Almost any solid can be foamed including polymers, metals, ceramics and glasses. Polymeric cellular foams are the most common (e.g. PVC, PUR and PMI). They do not offer the same high stiffness and strength to weight advantages as honeycombs but they have other attract features. Polymeric foams are typically less expensive. In addition, there solid macroscopic nature makes sandwich manufacturing easier [5]. Additionally, their low strengths and large compressive strain range make foams an attractive solution for energy absorbing applications [55].

2.5.1 Mechanical Characterisation of Polymeric Foams

Foams possess very unique mechanical properties in comparison to solid materials. The application of polymeric foams as energy absorbers requires an understanding of their mechanical behaviour and the various characterisation test methods available.

2.5.1.1 Compressive properties

The analysis of foam mechanical properties has been dominated by assessment of their compressive response [55]. Indeed, in the open literature the most commonly reported mechanical property is the static and dynamic compressive response of foams. Typically the compressive stress-strain response for a polymeric foam exhibits an initial response that is linear elastic followed by a long near constant stress plateau over a large strain range, after which densification occurs as the stress rises steeply. The linear elasticity is attributed to cell wall bending for open cells and cell wall stretching for closed cells [55]. The plateau is associated with the collapse of the cells through a combination of cell wall buckling and plastic collapse. Finally, densification is due the cell walls beginning to touch as the foam compacts, causing a rapid rise in stress. Gibson [55] has shown that increasing the relative density of the foam increases the Young's modulus and plateau stress and reduces the strain at which densification occurs.

The static and dynamic compressive properties of polymeric foams have been extensively reported. Static uniaxial compressive properties are generally obtained using ASTM C365 [5, 56-58]. Dynamic uniaxial compressive properties have been obtained using servo hydraulic test machines [59, 60], drop towers [60, 61] and Split-Hopkinson bars [62, 63]. For example, Tagarielli et al [63, 64] investigated the strain rate sensitivity of H100 and H250 Divinycell PVC foams over a strain rate range of 10^{-4} to 4000 s^{-1}. A servo hydraulic test machine was used for strain rates between 0.01–250 s^{-1}, while higher strain rate tests (500 s^{-1} to 4000 s^{-1}) were performed using a split-Hopkinson bar apparatus. They observed that the plateau stress increased with increasing strain rate.

Zhang et al [59] used a pneumatically driven ICI impact machine for high strain rate compression tests. These tests were conducted on PP, PS and PU foams up to a strain rate of 88 s^{-1}. In all cases, the plateau stress increased with increasing strain rate.

Static biaxial compression tests were conducted by Stender et al [61] for PU and EPP foams using a specially designed fixture. Biaxial compression tests were also performed by Rizzi et al [65] for an epoxy syntactic foam.

Hydrostatic compression tests have been reported by Zhang et al [59] for PP and PU foams. For this test the foam specimens were wrapped in latex rubber and immersed into a specially designed hydrostatic compression chamber filled with water. A hydrostatic compression test method was also described by Bilkhu et al [66]

2.5.1.2 Tensile properties

Gibson [55] provides a general description of the tensile response of foams. Initially there is a linear elastic response caused by cell wall bending, as well as stretching if the cells are closed. The cell walls rotate at larger strains towards the tensile loading axis, giving a yield point followed by an increase in the stress-strain response before ultimate fracture. Polymeric foams tend to be plastic in compression but brittle in tension. According to Gibson [55] this is because of the stress-concentrating effect of a crack, which can cause cell wall damage and fracture during tensile loading, but which is less damaging in compression.

ASTM test standards D638, D1623 and D1261 have been used to obtain static uniaxial tensile properties [56, 59]. The dynamic tensile behaviour of polymeric foams has received very limited attention. Loup et al [67] reported the dynamic tensile properties for a PVC foam for strain rates up to 70 s^{-1}. These tests were conducted in a specially designed fixture that was installed in an instrumented drop tower. They observed that the tensile modulus and strength increased with increasing strain rate. However, the strain to failure decreased as strain rate increased.

2.5.1.3 Shear properties

For polymeric foams the typical static shear stress-strain response is initially linear elastic followed by non-linear yielding up to a maximum load point [59, 68].

Static shear properties have been reported using test methods based on ASTM C273 [5, 56, 69]. In this test method the foam specimen is shear loaded between two rigid plates. A similar approach is also applied in the *simple shear test* [59, 68]. Zhang et al [59] conducted static simple shear tests for PS and PU foams by bonding foam specimens between two L

shaped loading fixtures. Yoon et al [70] reported on a simple shear test that was conducted on thermoplastic foams. Rizzi [65] presented the application of a torsion test for obtaining the static shear properties of an epoxy syntactic foam. Daniel et al [71] used an Arcan test to characterise the static shear properties of a PVC closed cell foam.

Mills and Gilchrist [68] and Stender et al [61] used an oblique impact test fixture to obtain the dynamic shear compression properties of PP, PU and EPP polymeric foams.

The literature indicates that, in general, the mechanical properties (compression, shear, tensile) of PVC foams have been the most extensively investigated. However, other thermoplastic polymeric foams have received limited attention.

2.5.2 High Energy Absorbing Thermoplastic Foams

Typically foams absorb energy by elastic-plastic micro and macro compression of the cellular structure. In automotive applications, a limitation of existing foams is their ability to minimise occupant and pedestrian rebound effects [72]. Recently we have seen the emergence of an anisotropic high energy absorbing polypropylene foam. This foam is been developed by Dow Chemical Company under the trade name Strandfoam and is proving to be an attractive solution in structural energy absorbing countermeasure applications in automobiles [72-74]. Strandfoam is the focus of this doctoral research and a brief review of the state-of-the-art for this material is provided below.

2.5.2.1 Material and manufacture

Strandfoam consists of polypropylene and blowing agent. The foam is manufactured by extruding the molten polymer along with the blowing agent through a pinhole die configuration [72, 73, 75]. The material exits the die as individual foam strands that expand and fuse together with adjacent strands to create a unique honeycomb structure (see Figure 2-12). After cooling, the strands form rectangular planks that can be cut and shaped to desired dimensions. A more detailed description of the

manufacturing process for PP Strandfoam planks is presented by Park and Garcia [76].

2.5.2.2 Mechanical properties

The honeycomb structure and orientation of the foam strands results in an anisotropic product that has enhanced compressive properties in the extrusion direction. A typical compressive stress-strain curve for the Strandfoam in the extrusion direction is shown in Figure 2-13, (titled "Olefinic Foam" in legend) [73]. The initial response is a very steep linear elastic behaviour that has been attributed to microbuckling of the cells between the strand walls. This is followed by a ductile, perfectly plastic response resulting from macro-buckling, shear and inter-strand debonding. Most of the energy absorbed by the foam is dissipated in this region. Finally, the buckled and debonded strands are crushed into a densified medium [75]. Figure 2-13 presents a comparison of the compressive properties of the polypropylene Strandfoam (extrusion direction), recoverable polyurethane and expanded PP (EPP) bead foam with the same density of 64 kgm^{-3} where Strandfoam clearly outperforms all the other foams [73]. Strandfoam exhibits a significantly high energy absorption efficiency of 80% - 90% in comparison to other currently available foams which have energy efficiencies between 35% – 55% [74].

The high strain rate compression properties for Strandfoam (density = 40 kgm^{-3}) have been presented by Vogel and Burr [75] and Hirth et al [77]. Vogel and Burr [75] conducted dynamic compression tests on Strandfoam in the extrusion direction for strain rates ranging from 0.01 to 2 s^{-1}. They observed that the yield (plateau) stress increased with strain rate. In addition the transition region between the near constant stress region and densification occurred over a longer strain range as strain rate increased.

Hirth et al [77] reported the dynamic compression behaviour of Strandfoam at a strain rate of 100 s^{-1}. The strand offset angle in the foam specimens was varied during the tests (0° - extrusion direction, 10°, 35°, 45°, 60°, and 90°). It was shown that that the stiffness and yield stress reduced with an increase in strand offset angle between 0° and 90°.

Vogel and Burr [75] reported that under compression loading the Strandfoam initial stiffness and yield stress increase with increasing specimen thickness. Furthermore, they also reported that Strandfoam exhibited some level of sensitivity to impactor shape under indentation loading.

2.5.2.3 Applications

Strandfoam is being evaluated extensively throughout the automotive industry in the following energy absorbing countermeasure applications [8, 19, 73, 74]:

- Pillar trim reinforcements for occupant head impact
- Headliner reinforcement for meeting the FMVSS 201U head impact regulation. Strandfoam has been shown to out perform other foams in meeting the safety performance requirements for occupant head impact [73-75].
- Door reinforcement for FMVSS 214 side impact regulations
- Knee bolster reinforcement for FMVSS 208 knee impact regulation
- Front and rear end system countermeasures for chassis protection
- Foot padding for occupant ankle protection
- Front-end system countermeasures for pedestrian lower leg impact protection. Kulandaivel et al [8, 17] reported on the evaluation of a thermoplastic composite sandwich construction with Twintex skins and Strandfoam core for potential pedestrian protection applications in small passenger vehicles.
- Bumper systems for vehicle crashworthiness. Brooks and Pharaoh [19] reported on the development of a thermoplastic composite sandwich bumper beam with a Strandfoam core.

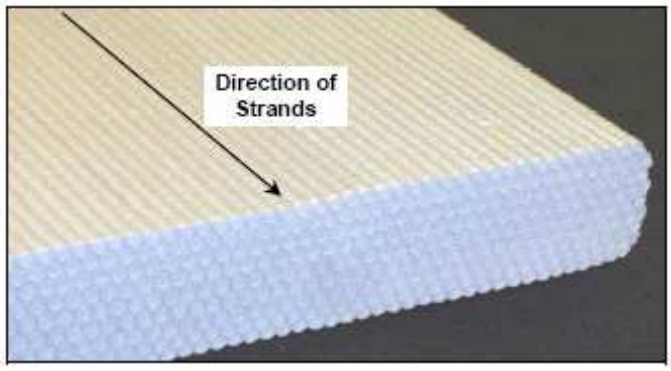

(a)

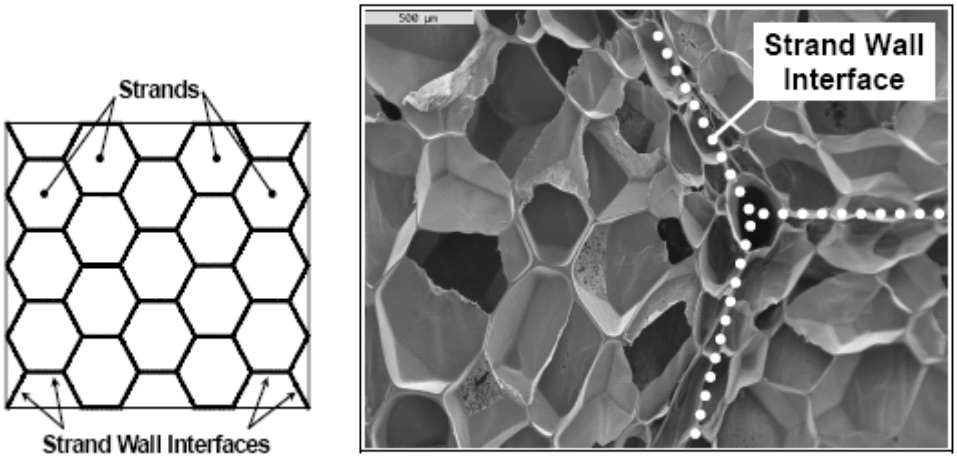

(b)

Figure 2-12. Showing (a) polypropylene Strandfoam plank and (b) honeycomb cellular strand structure of Strandfoam [75].

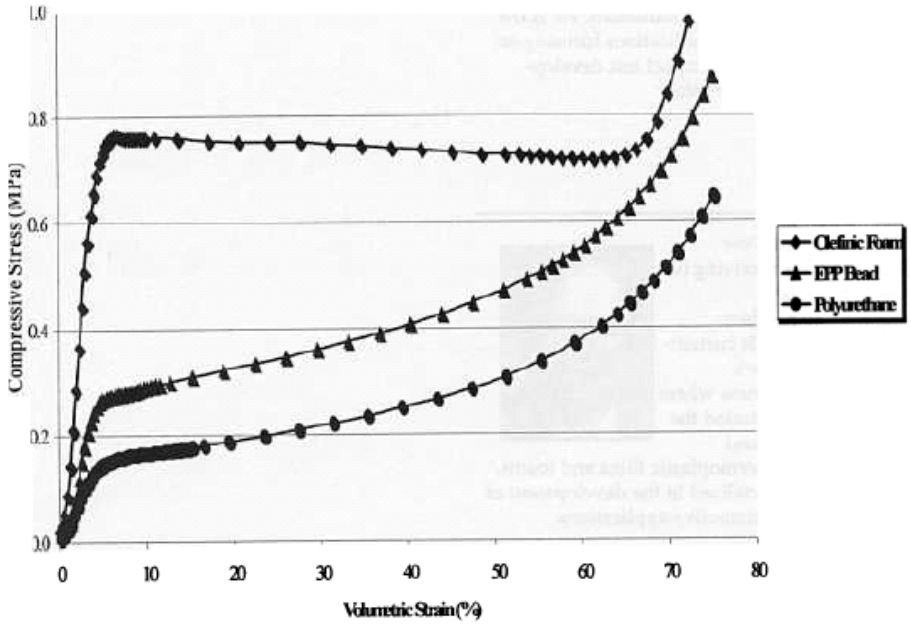

Figure 2-13. Comparison of the compressive stress-strain response for Strandfoam (Olefinic Foam), EPP Bead and PU [73].

2.6 Finite Element Analysis

This thesis is primarily focused on the application of finite element techniques for predictive modelling of impact damage in thermoplastic composites. This section presents a brief background to the finite element analysis technique.

Finite element analysis has become one of the dominant modelling tools used by academics and engineers. This in part, has been facilitated by ever increasing computing power for desktop, workstation and mainframe computers. According to Reddy [78]:

"The finite element method is the most powerful numerical technique ever devised for solving solid and structural mechanics problems in geometrically complicated regions. The finite element analysis of a problem is so systematic that it can be divided into a set of logical steps that can be implemented on a digital computer and can be used to solve a wide range of problems by merely changing the data input defining the domain, its physical properties and initial and boundary conditions."

In the finite element (FE) method, a structure with complex boundaries and properties can be discretised into a series of small *finite elements*. Within each element reasonable approximations can be made on the variation of parameters such as displacement, strain and stress using differential governing equations. For a global problem, provided that the boundary conditions are satisfied, a unique solution can be obtained by solving for the element variables. FE is well suited for implementation on computers because the solution process is ordered and repetitive, which can be programmed for automatic execution.

The two main solution techniques for finite element analysis are the *implicit* and *explicit* methods [79, 80].

2.6.1 Implicit Method

In the implicit solution, global equilibrium is first achieved by iteration, followed by the evaluation of local element variables. If equilibrium is not achieved, this method becomes computationally expensive, as the matrix coefficients have to be recalculated with a different time step. The implicit method is *"unconditionally stable"*, allowing the use of a large time step increment. The implicit FE method is more suited for problems that tend to be highly linear, static or quasi-static (see Figure 2-14). Commercially available implicit FE analysis softwares include: ABAQUS™, ANSYS™, NASTRAN™ and LUCAS™.

2.6.2 Explicit Method

The explicit method allows for an element by element solution so in contrast to the implicit method there is no requirement for a global matrix as the nodal velocities and displacements can be calculated directly using the central difference integration scheme. However, the time step is limited in magnitude for numerical stability. Subsequently, this method is considered to be *"conditionally"* stable because if the time step is too large, significant numerical errors will develop. In the explicit method there is no requirement for equilibrium; subsequently, this method is well suited for highly dynamic analysis, e.g. high velocity impact (see Figure 2-14).

The early development of commercial explicit finite element codes was initially for military applications such as weapons development. Since the mid-1980s, the automotive industry, in particular, vehicle crashworthiness analysis, has had a significant impact on the growth and development of commercial explicit FE codes[81]. Today, FE analysis allows for the detailed analysis of all the main vehicle components such as vehicle structure (metallic and composite), airbags and human dummies [82]. In addition, explicit finite element codes are now used extensively in the aerospace, nuclear and rail industry to simulate, for example, bird strike [83], transport flask safety [84] and train crashworthiness [85], respectively. The most popular commercial explicit FE analysis softwares include: PAM-CRASH™ [86], LS-DYNA™ [87] and RADIOSS™ [88].

For more detail, the book, "An Explicit Finite Element Primer" authored by Jacobs and Goulding [79] provides an excellent overview on the explicit FE

method. Furthermore, the proceedings of the International and European LS-DYNA Users' Conferences provides excellent examples of the application of explicit FE codes in science and engineering [89].

A more detailed theoretical discourse on FE is provided by Becker [90], Spyrakos et al [91], Zienkiewicz [92], Cheung [93], Liu [94], and Reddy [95]. Noor provides an expansive bibliography [96] on the subject. For an introduction to FE analysis theory for composite materials, the reader should refer to Matthews et al [97] and Ochoa and Reddy [78].

Finite element (FE) analysis was initially developed for metallic, isotropic materials. However, different element formulations are required for composite materials so as to adequately represent their anisotropic or orthotropic stiffness and strength, as well as their laminated construction [97]. Today, most FE software packages include material models that have been developed specifically for composite materials. Some of these FE composite material modelling techniques will be discussed in the following Section.

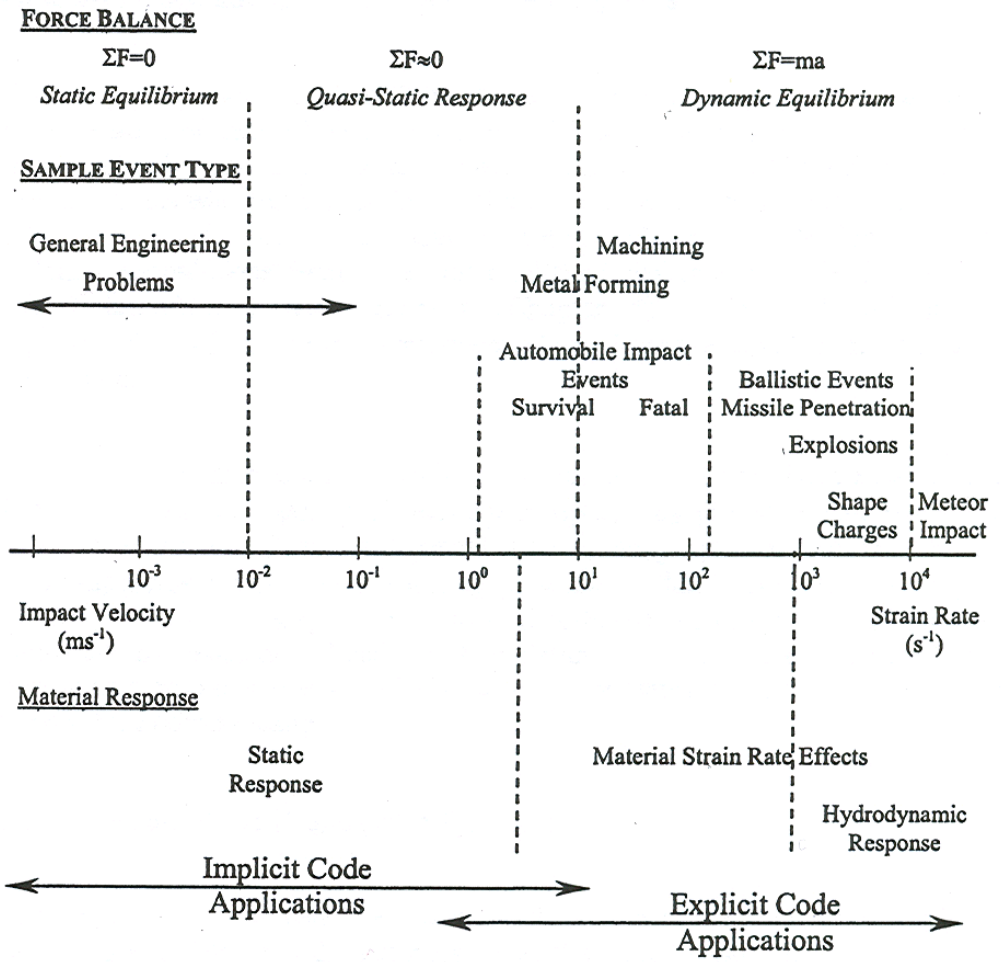

Figure 2-14. Problems more suited for both implicit and explicit methods [79].

2.7 Meso and Macro-Scale Modelling of Damage in Composites

This research is concerned with numerical modelling of damage progression and failure in thermoplastic composites. This section presents a review of the state of the art for damage modelling techniques.

There are two primary approaches to modelling the impact damage response of composite materials, namely micromechanical or macromechanical.

The micro mechanical approach represents damage growth at the level of the constituents of the ply, i.e. the fibre and matrix. This detailed model can be used to predict the onset and growth of micro cracks and fibre pull-out (for example [98]). These models are potentially more accurate but

they also tend to be more complex, computationally expensive and inefficient when attempting to model large scale structures.

Macromechanical approaches, which will be focus of this study, generally represent the damage onset and progression in the individual constituents by smearing the response over a representative volume of elements. These models are more computationally efficient, especially for simulating damage in large scale structures. The main macromechanical approaches for modelling damage progression in composites are:

- plasticity or yield surface approach,
- stress (or strain) based failure criteria approach,
- fracture mechanics approach,
- continuum damage mechanics (CDM) approach.

2.7.1 Elastic-Plastic Models

A number of combined elastic-plastic and progressive failure approaches to modelling damage in composite materials have been developed and implemented into finite element codes (see e.g. [99-106]).

Vaziri et al [107] developed a constitutive model that combined the orthotropic plasticity formulation in the pre-failure regime with brittle or ductile damage modes in the post-failure regime. A novel feature of this model was the incorporation of yielding and failure in a unified manner. This model was implemented into a purpose built implicit finite element code and validated for in-plane loading. Good agreement between predicted and experimental results was observed.

Cooper and Warrior [100, 106] developed an elastic–plastic model for simulating the crush response of fibre reinforced thermoset composites. The model consisted of three sections: an elastic formulation, a failure criterion and a post-failure regime. The elastic model is essentially linear elastic orthotropic with a plane stress assumption applied. The Tsai-Hill failure criterion is used for the yield surface. Post-failure behaviour is modelled with a piecewise linear plastic yielding. The material model was implemented into finite element code ABAQUS/Explicit using the VUMAT user routine. Here, a single layer of shell elements was used to represent

the entire laminate. The simulation results were fitted to the experimental values so as to obtain good correlation.

2.7.2 Failure Criteria Approach

Reddy [78] states that:

*"Once the mechanical properties of a ply are known, the initial failure of the ply, known as the **first–ply failure**, within a laminated structure can be predicted by applying an appropriate failure criterion."*

Several failure criteria have been proposed for the prediction of the onset of damage and its progression. Failure criteria can be classified into two groups [78, 108-110]: *independent* or *interactive*. Independent criteria separate the various failure modes and provide a failure criterion for each (e.g. maximum stress criteria). The criteria for each mode are then superimposed to form a complete failure criterion for the laminate. In contrast interactive criteria attempt to encompass all failure modes into a single expression (e.g. Hashin criteria). Details of the most common failure criteria that have been implemented into finite element codes are available in [78, 109]. Most failure criteria based models assume an elastic-brittle failure with stiffness and stress values reduced to zero almost instantaneously.

Chang and Chang [111] developed a stress related failure criteria model that was implemented in LS-DYNA as MAT 22. The model uses a series of failure criteria based on maximum failure stress to predict fibre fracture, matrix cracking and matrix compression failure. Failure is considered to be instantaneous and the elastic modulii are reduced to zero in the failed elements over a specified number of time steps. Hallett and Symons [112] attempted to validate the Chang and Chang model for composites by simulating tension, shear and impact tests on beams and plates. The results were mixed and several limitations of the Chang and Chang model were highlighted including its inability to accurately model shear stresses and delamination. Hou et al [113, 114] modified the Chang and Chang model by including an improved stress based delamination criterion that considered both interlaminar shear and through-thickness compression stresses. This resulted in good correlation between predicted delamination

and experimental results for composite plates subjected to impact loading. Other applications of the Chang and Chang model for impact on composites include [115] and [116].

Other stress based failure models based on enhancements to the Chang and Chang approach have been implemented in LS-DYNA as MAT 54 and MAT 55 [117, 118]. Mamalis et al [119] used MAT 55 to simulate the static and dynamic crush response of square carbon fibre composite tubes. Hörmann and Wacker [120] simulated the crash response of a thermoplastic composite modular crash box using MAT 55.

2.7.3 Fracture Mechanics

Fracture mechanics based approaches are generally used to model delamination. Delamination is a major failure mode in laminated composites and has received considerable attention. Generally there are three modes of delamination fracture: opening (Mode I), shearing (Mode II), and tearing (Mode III). The various modes are shown in Figure 2-15. Experimental work is well documented (see e.g. [121-127]) and there is also considerable literature on the computational modelling of delamination in composite laminates (see e.g. [114, 125, 127-139]). Fracture mechanics in conjunction with the virtual crack closure technique (VCCT) have traditionally been the principal approach applied to delamination analysis. Alternative methods to fracture mechanics include damage mechanics, and interface and cohesive models

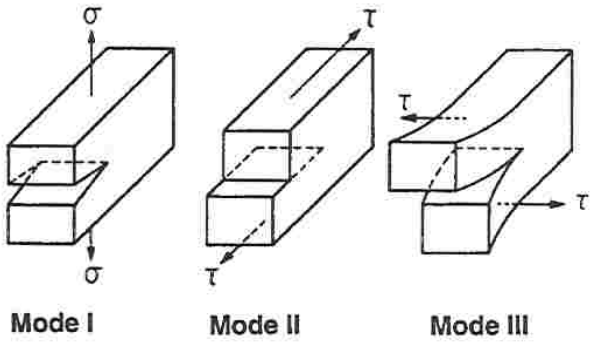

Figure 2-15. Delamination fracture modes [140].

For fracture mechanics applied to delamination, a predefined interlaminar crack has to be introduced. This initial crack generally has a characteristic

length that usually coincides with the length of the element at the crack tip [140]. This is usually based on a non-physical formulation. The strain energy release rate is generally calculated using the virtual crack closure technique (VCCT). The advantage of the VCCT is that, provided a suitable characteristic length is selected, the total strain energy release rate, G, can be calculated in a single FE analysis by using the nodal force at the crack front and the displacement behind the crack front [140]. Crack propagation is simulated by advancing the crack front when the local energy release rate, G, rises to the critical value.

A disadvantage in using fracture mechanics in the analysis of delamination is the need to identify a suitable and consistent characteristic length. Several examples of the application of fracture mechanics to FE analysis of delamination in composite laminates are presented in [140]

Other techniques for modelling delamination include interface or cohesive layer based models. These models are based on a thin (generally zero thickness) interface or cohesive layer between the delaminating surfaces, having either a linear or non-linear normal and shear stress-strain response [140]. It has been shown that discrete cohesive elements are suited for low velocity impact damage FE analysis [140, 141].

Wisheart and Richardson [137] developed an interface element for modelling delamination in composite laminates. For two-dimensional problems, the interface element is modelled as a quadratic line element, while for three dimensional problems, a plane element is used. Both elements consist of a set of double nodes which follow separate material models for the three modes of fracture. These elements have a zero thickness with variables being the forces and relative displacements between node pairs. The material model for the interface element is shown in Figure 2-16. During loading, once the critical strength value has been exceeded the node pair softens until complete separation. The two and three-dimensional models were implemented into the commercial finite element code LUSAS to simulate pure Mode I, Mode II and Mixed Mode delamination. Good correlation between the simulation and experimental results were reported. However, this may have been due in part to the authors' selecting appropriate material parameters in order to achieve the desired nodal behaviour.

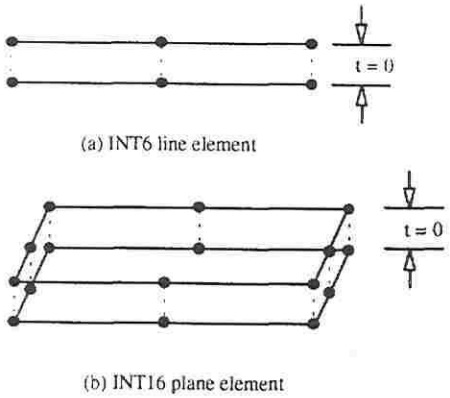

Figure 2-16. One and two-dimensional interface elements [137].

Various interface and cohesive finite elements have been formulated that also include damage mechanics in the constitutive equations (see e.g. [141-144]).

2.7.4 Continuum Damage Mechanics

In recent times, continuum damage mechanics has become a very popular approach for modelling damage in composite laminates. Several damage mechanics models have been developed and implemented into finite element programs.

Kachanov [145] and Rabotnov (cited in [146, 147]) are noted as the pioneers of damage mechanics. The classical damage theory presented by Kachanov and Rabotnov conjectured that the damage state can be represented by a damage variable or internal state variable which characterises damage evolution. When applied to composites, the internal state variable tends to be defined as a vector variable so as to characterise both the magnitude and direction of the damage entities. The damage mechanics approach described by Kachanov and Rabotnov was initially applied to composites by Frantziskonis [148-150] and Talreja [146, 151, 152]. Both Frantziskonis and Talreja introduced a tensor form of the damage variable. Each term in the tensor represented the effects of one or more damage modes such as fibre breakage, matrix cracking and fibre-matrix debonding in a particular direction. This formed the platform for composite damage mechanics as presented by many authors.

Allen et al [153-155] developed a generic continuum mechanics model where damage is characterised by internal state variables representing locally averaged measures of specific damage such as matrix cracking. They applied the model to the prediction of stiffness loss in several graphite/epoxy crossply laminates due to matrix cracks. A comparison between experimental results and the model showed good correlation. However, this model is limited to crossply laminates with symmetric damage states. Furthermore, the actual use of this model is complicated by the requirement for numerous experimentally determined quantities.

Later on, Allen and coworkers [156, 157] developed a multi-scale, micro-meso-local-global methodology in order to model all damage modes including matrix cracking, and delamination at multiple sites in laminated continuous fibre composite plates. Interface degradation is first modelled analytically on the microscale, and the results are homogenized to produce a cohesive zone model that is capable of predicting interface fracture. Matrix cracking in the plies is modelled analytically on the meso-scale, and this result is homogenized to produce a ply level damage dependent constitutive equation. The evolution of delamination is considered on the local scale, and this effect is modelled using a three-dimensional finite element algorithm. Results of this analysis are homogenized to produce damage dependent laminate equations. Finally, the global response of a damaged plate is modelled. The evolution of all three modes of damage is predicted by interfacing all four scales into a single multi-scale algorithm that is computationally tenable for use on a desktop computer. Results obtained suggest that this model may be capable of accurately predicting complex damage patterns such as those observed near open holes in laminated plates.

Ladevèze and co-workers [158-165] developed a meso-scale damage model that was based on continuum damage mechanics. This model was able to simulate matrix cracking and fibre-matrix debonding in a single elementary ply of a unidirectional fibre reinforced composite, assuming a plane-stress state [158] (see Figure 2-17). The damage model was later refined to include an interlaminar interface [142, 162-164] and delamination predictions for laminates [142, 143, 166]. The interface is a two-dimensional surface entity which transfers displacements and forces between two adjacent plies [162]. Ladevèze introduced three damage

indicators, d, d' and d_F which are constant through the thickness of the ply [86, 163]. These variables quantify the damage due to fibre-matrix debonding in shear, matrix microcracking in the transverse direction and fibre breakage [86, 162]. The model also takes into account the difference between tension and compression failure in the fibre direction [86, 158].

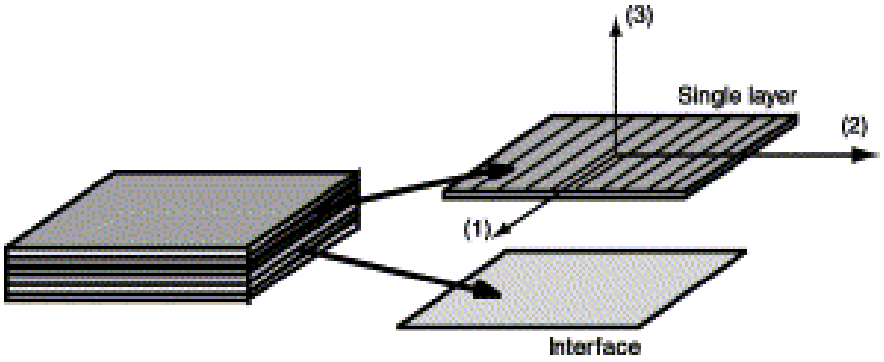

Figure 2-17. Ladeveze laminate mesomodel: single layer and interface [159, 165].

Later on, Ladevèze and Lubineau [162, 163, 165] compared and coupled his model with a micro-mechanical model. They have noted that the mesomodel can now be interpreted as the homogenized result of micromodels involving common microdamaging mechanisms such as: transverse microcracking; delamination at the tips of transverse microcracks; fibre-matrix debonding. These mechanisms are homogenized on the mesoscale[1], which leads to an improved version of earlier damage model, involving only a small number of material constants [165]. This model is valid for arbitrary values of thickness unlike its predecessor. Furthermore, the mesodamage model is nearly independent of stacking sequence. The model can be used for both static and dynamic loading with the latter introduced by using delay effects [167]. Comparisons with experimental results have provided satisfactory results. However, the mesomodel is computationally expensive. Furthermore, the calibration procedure is intensive and non-standard. A modified version of the Ladevèze et al model was implemented in the explicit finite element code PAM-CRASH [86].

[1] The mesoscale is the intermediate between the scale of the structure and that of the degradation micromechanisms. It is characterised by the thickness of the plies.

Another mesoscale model was proposed by Barbero et al [168]. They presented a continuum damage mechanics model (CDM) coupled with Classical Thermodynamics Theory which combines both damage evolution and plastic deformation. A mesoscale approach is used where constitutive equations refer to a single lamina while a modified Classical Laminate Theory (CLT) is used to capture the global damage and plastic deformation of the laminate. Several state variables are used to account for the evolution of damage and inelastic behaviour. Barbero and coworkers have noted that this model has fewer state variables in comparison to other mesoscale damage models. Good comparisons were obtained between experimental data and model predictions

Pickett et al [80, 169] developed a novel damage model for both unidirectional continuous fibre reinforced composites and random short fibre reinforced composites. This model has been implemented in the commercial explicit finite element code, PAM-CRASH™ [86]. For unidirectional composite material, they implemented the *bi-phase* model which is a heterogeneous material model that separates the fibre and matrix phases with independent constitutive laws for each. During loading, the stresses are calculated separately for each phase and damage propagates independently, based on the failure criteria selected. For random short fibre composites a *degenerate* bi-phase model is employed where the material is considered quasi-homogeneous and essentially isotropic in-plane. The model includes an idealised bilinear damaging and modulus function in addition to a strain softening phase. The total damage is the sum of the damage resulting from the hydrostatic state of strain and the deviatoric shear state of strain. However, Pickett and coworkers have noted that this may not be accurate as there may be some independence between these two damage modes. The damage model can be calibrated from laboratory coupon tests [81, 86]. Initial simulations involving a tensile loaded notched plate and an impact loaded disc showed close agreement with experimental results.

Some of the first wide-scale applications of the bi-phase damage model developed by Pickett et al [80, 169] and implemented in PAM-CRASH are outlined in [81, 170, 171]. The most noteworthy being the joint study carried out by ESI and Tonen Corporation in which the crash response of a

prototype composite car was assessed. Details are available in [81, 170, 171].

Later on, McCarthy et al [172] outlined the use of the bi-phase model that was implemented in the PAM-CRASH finite element code to simulate the crash response of a composite helicopter subfloor (see Figure 2-18). The pre-test simulations, calibrated using coupon specimens were able to provide a reasonably representation of the overall crash response. However, the degenerate bi-phase material model proved to be inadequate for modelling composite fabrics and presented very poor results for off-axis behaviour. Shear was severely underestimated when compared to experimental results. The predicted energy absorption was approximately 15% less than the experimental value. This was attributed to delamination not being accounted for in the bi-phase model. Considerable post simulation adjustments were required to provide a close match to experimental results.

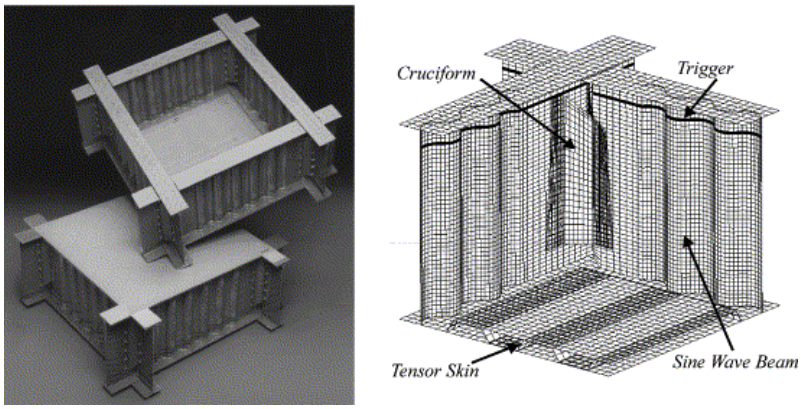

Figure 2-18. FE model of composite helicopter subfloor [172].

Recently the CRACTAC (Crashworthy Automotive Structures Using Thermoplastics Composites) project used the degenerate bi-phase material model in PAM-CRASH to analysis and design a thermoplastic composite side intrusion beam [7, 173, 174]. Figure 2-19 shows the simulated damage results for the side intrusion beam under large deformation bending load [7]. The simulation and experimental results showed good correlation. However, like McCarthy et al [172], poor simulation results for shear were also observed.

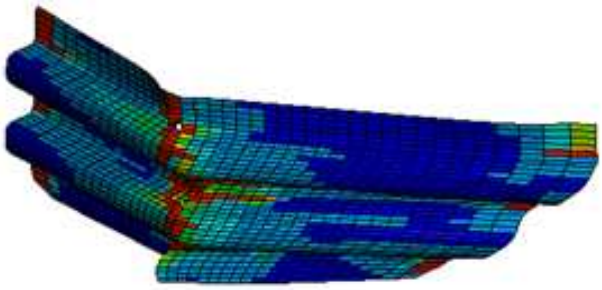

Figure 2-19. FE model of a thermoplastic composite side impact beam showing predicted damage with PAM-CRASH Bi-phase model [7].

For the CRACTAC project the PAM-CRASH bi-phase model was also used to model a thermoplastic composite sandwich bumper [173]. Good comparisons were observed between experimental and simulation results. Other examples of the application of PAM-CRASH bi-phase model include [135, 175-177]

Johnson et al [178-181] presented a generalised version of the Ladevèze et al [158, 159] damage model for a fabric reinforced composite ply. In this model the fabric reinforced composite ply is modelled as a homogenous orthotropic elastic or elastic-plastic damaging material whose properties are degraded on loading by microcracking prior to ultimate failure. Internal state variables are used as degradation parameters which are governed by damage evolution equations. The model considers elastic damage along the principal fibre directions, along with elastic-plastic damage in in-plane shear. The authors used the simulation of a low velocity impact test on a composite plate to validate the model. The simulation results revealed close correlation with the experimental impact test observations [178]. A novel feature of the fabric model is its ability to distinguish between different failure modes. The progression of fibre and shear damage parameters, the plastic shear strains, total shear strains and the fibre strains can be followed during post-processing; in addition to the extent of delamination [181].

Recently, modified versions of the generalised Ladevèze model have been developed and used to successfully model damage in biaxial non-crimp fabric composites [182, 183], braided reinforced composites [184] and carbon woven fabric composites [185].

Matzenmiller et al [186] presented a continuum damage mechanics (CDM) lamina model with three damage parameters which are related to damage in the principal in-plane and shear directions. The damage evolution was based on a Weibull distribution of strengths of fibre bundles. Internal state variables were used to describe the propagation of the damage and subsequent degradation of material stiffness.

Williams et al [187] implemented the Matzenmiller et al [186] damage model in the LS-DYNA3D finite element code [87] as a user defined material model for laminated shell elements. The performance of the model relative to that of the Chang and Chang model [111] that was already implemented in LS-DYNA3D was assed by comparing simulation results with a series of impact test results. They concluded that the damage model developed by Matzenmiller et al [186] provides significant improvements in the prediction of damage growth and force-time history when compared to the Chang and Chang composite model. However the parameters used in the Matzenmiller et al [186] model are often non-physical and difficult to characterise.

Iannucci [188] presented two damage mechanics based failure models that were implemented in the DYNA3D explicit finite element code. The first formulation was concerned with in-plane failure in a woven fabric composite, with six damage variables introduced to model fibre and matrix damage. In the second formulation, three damage variables are introduced to model damage in the interface between the plies. Simulations were compared to bird strike impact tests and double cantilever delamination tests with relatively good correlation.

Later on, Iannucci et al [189] developed a progressive damage model that was implemented in DYNA3D. The approach uses a novel damage mechanics formulation to predict in-plane damage in a woven fabric composite defined by matrix cracks and fibre fracture in the warp and weft directions. The model uses a stress based energy dissipation approach and an advanced post failure strain softening methodology. Strain rate effects were modelled using a damage lag formulation within the constitutive model. Simulation results indicate that the damage model can predict with reasonable accuracy the damage modes observed in both the laboratory and full-scale experiments.

Very recently, Iannucci [190] presented a damage mechanics model that was implement into the DYNA3D code. The formulation is concerned with in-plane failure in woven fabric carbon composites. Three damage variables per ply were introduced to model fibre and fibre/matrix damage. The model also uses an unconventional thermodynamic maximum energy dissipation approach. Reasonable correlation was observed between simulation and experimental results for low energy impact tests.

Iannucci and Willows [191, 192] described an energy based damage mechanics model for woven carbon composites under high strain rate loading. This damage mechanics approach introduces five damage variables for in plane damage per ply layer. The damage variables are associated with warp and weft fibre damage in both tensile and compressive failure modes, with an additional damage variable to determine the deterioration of the fibre–matrix interface. The damage variables are directly related to the stiffness degradation within the composite lamina and ultimately within the laminate. The evolution of damage in each mode is controlled via a series of damage-strain equations, thus allowing the total energy dissipated for each damage mode to be set as a material parameter, which is mesh size independent. This model has been implemented into DYNA3D for plane stress (shell) elements. Validation examples were presented. The simulation results show very good agreement with the experimental data. The authors also presented an interface modelling technique for explicit FE codes. The formulation is again based on damage mechanics and uses only two constants for each delamination mode; firstly, a stress threshold for damage to commence, and secondly, a critical energy release rate for the particular delamination mode. The model has also been implemented into the LLNL DYNA3D Finite Element (FE) code and the LS-DYNA3D commercial FE code. The interface element modelling technique is applied to a series of common fracture toughness based delamination problems, typically the Double Cantilever Beam (DCB) test, and validated for the dynamic case via a simple analytical plate impact simulation. Finally, Iannucci and Willows [191] presented the results of simulations using the proposed damage mechanics based models on a series of experimental CRAG plate impact tests.

Williams et al [193] developed a continuum damage mechanics based model for composite materials, COmposite DAMage (CODAM) which was implemented in LS-DYNA as a user material subroutine. The model is a physically-based macromechanical material model that represents the constitutive behaviour of polymer composite laminates through both the elastic and post-initial failure regimes. This model can simulate matrix cracking, fibre breakage, and delamination. The model represents the non-linear and softening stress-strain response at the damage state through a stiffness reduction scheme. However, unlike most other damage mechanics models, in the CODAM model, the strain state is defined by an effective strain function. The damage growth law in this model is a general piece-wise linear relationship between the damage potential and the damage parameter and between the modulus reduction. Reasonable correlation was observed between predicted and experimental results for an impact test with respect to force-time histories and damage modes and size.

McGregor et al [194] further modified the CODAM model and used it to simulate damage propagation in braided composite tubes. The damage propagation, failure morphology and energy absorption predictions correlated well with the experimental results.

Xiao [195] evaluated the application of the CODAM model for simulating impact damage in random glass mat and continuous glass fibre mat reinforce polypropylene composites. The author presented a methodology for calibrating the CODAM damage parameters through correlations of simulations with standard coupon tests (tension, compression and shear). The model was validated using a simulation of a driven dart test which yielded good correlation.

Yen [196] implemented in LS-DYNA an elastic-damage model (MAT 162) by generalising the layer failure model (MAT 161). MAT 162 may be used to simulate the onset and progression of damage in unidirectional and orthotropic fabric composites. This model adopts the damage mechanics approach, Matzenmiller et al [186, 187], that uses a set of damage history variables to relate the onset and growth of damage to stiffness losses in the material. This model is implemented for single integration point solid elements. MAT 162 can be used to effectively simulate fibre dominated

failures, matrix damage, and includes a stress-based delamination failure criterion. It is able to simulate delamination without having to model the physical inter-laminar interface. Strain rate effects on material properties are also accounted for by logarithmic based functions within the model.

Researchers have attempted to validate the LS-DYNA MAT 161 continuum damage mechanics model for simulating the damage response of composite plates under high velocity loading. Yen [196] successfully used this model to simulate high velocity ballistic impact damage in S2-glass/epoxy composite panels. Chan et al [197] used both tests and the LS-DYNA MAT 161 model to study the high velocity impact behaviour of carbon/epoxy laminates of various stacking sequences. Deka et al [198] applied MAT 161 to the modelling of ballistic impact damage in E-glass/polypropylene composite plates.

Recently, Xiao et al [199] studied the damage characteristics of S2-glass/epoxy thick composite plates under static punch shear loading. Static punch shear tests were modelled using the LS-DYNA MAT 162 material model. The authors presented a methodology for systematically calibrating the MAT 162 damage parameters for shear punch modelling. There was reasonable agreement between the experimental and simulation results for the load-displacement curves and damage modes and size.

Tasdemirci and Hall [200] used the LS-DYNA MAT 162 material model to simulate S2-glass/epoxy composites under high strain rate compressive loading using the split Hopkinson pressure bar test. There was very good agreement between the predicted and experimental results for stress-time histories, progressive deformation and damage.

Kwon et al [201] outlined a novel multilevel, micro/macro analysis for laminated woven-fabric composites. Their model can predict the stiffness, strength and progressive failure by using the material properties of the fibre and matrix materials, their volume fractions and the orientation of the weave and lamination. The fundamental failures described are fibre failure, matrix failure and fibre/matrix interface failure. The analysis is divided into three modules: fibre-strand, strand-fabric and lamination. A finite element analysis program using the Mindlin-Reissner theory was implemented. Both experimental results and theory showed good correlation.

Continuum damage mechanics (CDM) was used by Jiang et al [202] to develop an incremental damage constitutive law which was implemented into a 3-D finite element programme for a composite plate subjected to transverse impact. The damage variable is assumed to be represented by a 2^{nd} order tensor which reflects local damage. For the laminate plate each ply was modelled as an orthotropic elastic continuum. The damage distribution in the laminate is then predicted by stress analysis without consideration of the damage. The model also predicted the distribution of delamination along the laminate interfaces which correlated well with experimental results.

Li et al [203, 204] have developed a FE model based on a 9-node Mindlin plate element for simulating damage in laminated plates. The model has integrated various damage criteria and includes an updating strategy for plate stiffness as damage progresses. Computational efficiency has been enhanced by employing adaptive techniques. The model reasonably predicted various damage entities including delamination, matrix cracking and fibre breakage.

Yazdchi et al [205] developed a generic CDM model for brittle dynamic damage progression in an anisotropic brittle material. Two damage evolution models are presented. Damage is defined as a state variable within a second order tensor. A measured Weibull strength distribution is used to statistically describe flaw distribution which affects the damage accumulation rate. The model was implemented in a Lagrangian dynamic finite element program. Although this model was not specifically developed for composites, Williams et al [187] suggest that it could be used for such materials.

Other notable generic damage models that could be applied to composites include work by Simo et al [206, 207].

2.7.5 Macro-Scale Modelling of Foams

This section will review material constitutive models that are suitable for modelling foams with specific focus on low density crushable polymeric foams.

2.7.5.1 Analytical methods

An exhaustive list of analytical models for the prediction of almost any mechanical property of cellular solids (mainly foams and honeycombs) was derived and compared with experimental results by Gibson and Ashby [55]. They considered various aspects of both closed and open celled materials, based on unit cells and micro-mechanical considerations. The theoretical background of most of these models is based on the assumption that the properties of the solid form of the foam material and the cell structure (e.g. cell wall thickness and geometry) are known. Although the analytical results compare well with experimental data, Gibson and Ashby's work has been criticised by Zenkert [5]. Zenkert argues that the analysis generally requires inaccessible microscopic data such as the ratio of open and closed cells, cell wall thickness and geometry. Furthermore such micro analysis is very academic and in reality, engineers are more concerned with macro–mechanical properties.

Phenomenological models have been proposed for the modelling of the stress-strain behaviour of foams [208]. These models divide the total stress into the contributions from the gas enclosure and cell walls. It is assumed that for foams subjected to compression, the gas is compressed and the cell walls deform and buckle. The analysis is more suited to small deflections and becomes difficult for large deflections. Furthermore, knowledge of the cell geometry is required and results from these models have been less than satisfactory. A simple phenomenological model for polyethylene foam is shown in Figure 2-20.

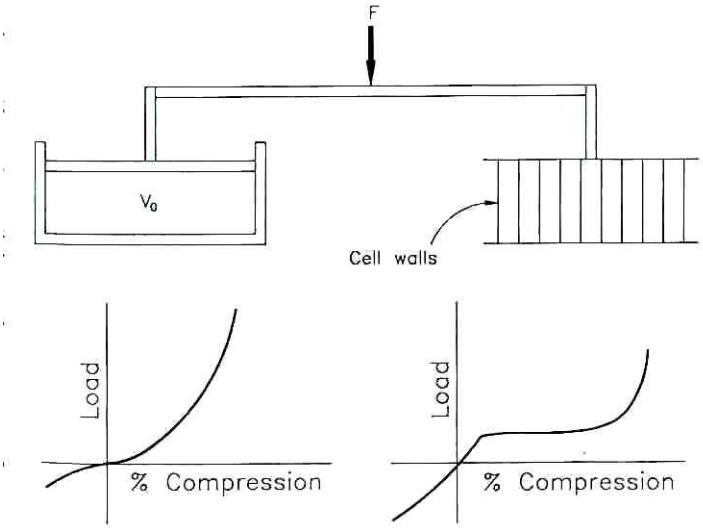

Figure 2-20. Phenomenological model for polyethylene foam [208].

2.7.5.2 Finite element modelling of polymeric foams

This section provides a brief review of foam constitutive models that are available in the LS-DYNA finite element code that maybe applicable for modelling low density crushable anisotropic Strandfoam.

Only three orthotropic, crushable foam laws in LS-DYNA are considered suitable for modelling Strandfoam. These material models are MAT 26 (*MAT_HONEYCOMB), MAT 126 (*MAT_MODIFIED_HONEYCOMB) and MAT 142 (MAT_TRANSVERSELY_ANISOTROPIC_CRUSHABLE_FOAM)

MAT 26 is a non-linear elasto-plastic material model with uncoupled normal and shear stress formulations. The corresponding yield surface is a rectangular box in principal stress space. MAT 26 tends to over estimate the off-axis strength of orthotropic foams and honeycomb materials [77]. The accurate prediction of the foam off-axis strength is important for foams such as Strandfoam where the strands tend to rotate under large deformation bending loads. MAT 126 is a modified version of MAT 26 that attempts to overcome this problem by offering the user the option of three different yield surfaces. The first is similar to the one in the MAT 26 model. The second yield surface is transversely isotropic and considers the effects of off-axis loading. Here the uniaxial limit stress is defined as a function of the off-axis angle. A drawback of this approach is that the material often collapses in shear mode due to low shear resistance. Therefore, for the

third yield surface, the user can prescribe the shear and hydrostatic resistance in the material independent of the uniaxial behaviour.

MAT 142 was recently developed by Hirth et al [77] to overcome the systematic overestimation of off-axis strength by MAT 26. MAT 142 is a transversely anisotropic elastic-plastic foam model with a modified Tsai-Wu yield surface that hardens or softens as a function of volumetric strain. The yield surface is symmetric and its evolution is directional. MAT 142 was validated for use with Strandfoam by comparing simulations with a series of off-axis compression tests. The predicted results from the MAT 142 model showed good agreement with the experimental results. The model was further validated by successfully simulating the FMVSS 201 head impact test on a block of Strandfoam.

2.8 Modelling Composite Sandwich Structures

This section presents a review on composite sandwich modelling state of the art.

2.8.1 Classical Laminate Plate Theory

In the 1970s, Classical Laminate Plate Theory (CLPT) was developed for laminated composite material structures [15]. CLPT is the simplest form of equivalent single layer (ESL) laminate theory. CLPT is an extension of the Kirchhoff-Love hypothesis (see Figure 2-21) which states that [78, 209]:

"*Straight lines normal to the midplane before deformation remain straight, inextensible and normal to the midsurface after deformation*."

Therefore, transverse shear (through-thickness) and transverse normal effects are neglected. CLPT is adequate for the analysis of thin plates.

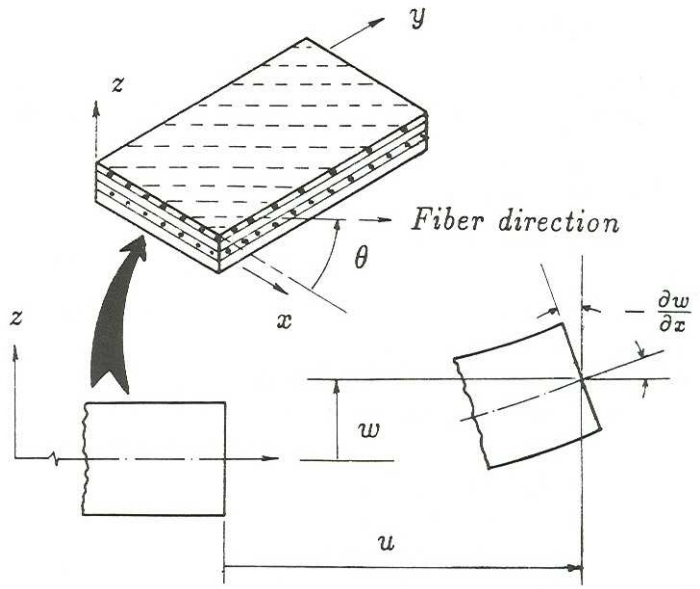

Figure 2-21. The Kirchoff-Love hypothesis for thin laminates [78].

However, the analysis of sandwich structures involves incorporating a number of non-classical effects, among which include:

- the transverse shear flexibility (especially for thick plates),
- the need for fulfilling the continuity requirement of transverse shear stresses at the layer interfaces (particularly when large variations in transverse shear modulii from layer to layer are experienced),
- interfacial fracture between the constituents of sandwich structures.

Consequently, most authors have concluded that CLPT is inappropriate for the analysis of sandwich structures [78, 209, 210].

2.8.2 First-Order Shear Deformation Theories

First-order shear deformation theory (FSDT) based on the Mindlin-Reisser theory assumes a constant transverse shear strain with respect to the thickness coordinate [209]. However, according to three-dimensional elasticity theory, through thickness shear strains show at least a quadratic variation. Therefore, shear correction factors have to be used to adjust the transverse shear stiffness [211, 212]. The validity of the FSDT is mainly dependent on the shear correction factors used [211]. The values of the shear correction factor depend on the lamination scheme, geometric boundary conditions and constitutive properties. Several methods have

been proposed for calculating shear correction factors which have been reviewed by Birman et al [213]. In general, these methods are based on comparing the gross response characteristics, as obtained from FSDT, with the corresponding characteristics of the three-dimensional continuum theory [211, 213].

FSDT yields good predictions of overall laminate behaviour (deflections, natural frequencies and buckling loads) and in-plane stresses provided the structure is relatively thin and material properties of adjacent constituents have insignificant differences. Conversely, FSDT does not account for warpage of the cross-section [214]. Finite elements based on FSDT have the advantage of only requiring C^0 – continuity of all primary variables; however, they can exhibit spurious transverse shear stiffness also known as *shear locking* [78, 209, 212, 215]. Reddy's defines shear locking as follows:

"Shear locking is due to the inability of the shear deformable elements to accurately model the curvature within an element under a state of zero transverse shearing strain"

Shear locking can be alleviated by several methods including: reduced integration [216], mixed formulations [217], hybrid formulations [218-224], and assumed strain techniques [212, 225]

Of the large number of new displacement-based finite elements for FSDT in the literature, only a few have been fairly successful [209, 216]. Reddy [209], states that there is still room for improvement with respect to accuracy, ease of implementation, and computational efficiency. In order to reduce the inaccuracies of FSDT, higher-order shear deformation theories (HSDT) have been proposed.

2.8.3 Higher-Order Shear Deformation Theories

Higher order shear deformation plate theories (HSDT) give displacements that are expanded using higher order polynomials (e.g. quadratic) with respect to the thickness coordinate [209, 212]. HSDT allow for the non-linear warping of the cross-section by using extra degrees-of-freedom [210]. Furthermore, non-linear variation of transverse shear stress is

accommodated which eliminates the need for shear correction factors. HSDT provides a minor increase in accuracy; however, computational effort is greatly increased as well. Finite element models based on HSDT have the disadvantage of requiring C^1 – continuity of the transverse displacement component. Yang [216] has shown that it is very difficult to derive generalised finite elements based on C^1 continuity. Examples of HSDT include [226-229]

2.8.4 Finite Element Implementation

2.8.4.1 Two-dimensional models

Two dimensional (2D) finite element sandwich models are derived from assumptions regarding the variation of displacements and/or stresses through the thickness [78, 211]. Several classifications are available for 2D plate and shell models. The two main categories include [211]:

- Global approximation models
- Discrete-layer models

Global approximation models

Global approximation models are also known as *equivalent single layer* (ESL) models by some authors [78, 209]. Here, the heterogeneous layers of the sandwich structure are treated as a statically equivalent single layer with global through-thickness approximations for the displacements and/or strains in the thickness direction [211]. Global models provide inherent simplicity and low computational cost along with a sufficiently accurate description of the global response of relatively thick plates. Finite element models based on FSDT, of the ESL models, provide the best comprise with respect to accuracy, computational cost and compatibility with other displacement based finite element models [209]. However, global models have several disadvantages that limit their usage. They are incapable of describing the discontinuity of transverse shear strain that occur at interfaces between two adjacent layers or regions of concentrated loading [209, 212]. Furthermore, interfacial debonding cannot be modelled; and accuracy depreciates as thickness increases [209]. These shortcomings are somewhat surmounted by discrete layer models.

Discrete-layer models

Discrete-layer models or layerwise models [78, 209] are based on a unique displacement field for each layer and impose interlaminar continuity (IC) of displacements and sometimes transverse stresses as well [214, 230]. A major disadvantage of discrete layer models is that they tend to be very computationally expensive because as the number of layers increase, the number of unknowns increases proportionally.

Zig-zag (ZZ) theory was introduced by Di Sciva [231, 232] where the in-plane displacements in a multilayered plate are assumed to be piecewise linear and continuous through the thickness. This theory has been shown to be very accurate and provides a more realistic description of the mechanical behaviour of sandwich structures by introducing layer-wise transverse shear effects into the displacement field. Many researchers have now made considerable improvements to Di Sciva's ZZ theory (see for example [214, 230, 233-239]. However, Reddy [209] states that these models cannot accurately determine interlaminar stress near discontinuities such as holes and delamination fronts.

Major emphasis has been given to displacement-based models in the sections above; however, a brief overview of alternative methods is presented below.

2.8.4.2 Hybrid finite elements

Hybrid stress elements have been developed which are based on an independently assumed displacement and stress field in conjunction with an assumed intra element and statically equilibrating stress field [209]. This approach was introduced by Pian and Tong [222, 223, 240] and has been applied to multilayered and sandwich plates by various authors, e.g. Spilker [219], Spilker et al [220-222] and more recently, Manet et al [218, 241, 242]. A review of the use of hybrid stress based elements for the FE analysis of sandwich plates has also been presented by Ha [210]. In general, hybrid-stress elements tend to be accurate and do not exhibit spurious displacement modes. However, the element stiffness matrices tend to be non-symmetrical [218] and the formulation involved is complex. Furthermore, they are computationally expensive and do not combine well

with other displacement-based elements found in many commercial FE codes [209].

2.8.4.3 Reissner mixed variational theorem (RMVT)

The Reissner mixed variational theorem (RMVT) is based on both displacement formulations and mixed principles that makes this theorem particularly suitable for multilayered structures [243]. The application of RMVT to conventional finite elements was introduced by Rao and Meyer-Piening [244] who used the Toledano and Murakami theory [245]. Recently in a series of papers, Carrera [233, 234, 243, 246-251] has shown that RMVT can yield a quasi-three-dimensional description of both the in-plane and out-of-plane stress-strain response of multilayered structures such as sandwiches. Here, both the interlaminar continuous transverse stresses and normal transverse stress fields are determined a priori with good accuracy. An exhaustive review on RMVT has been presented by Carrera [243]. RMVT is noted to have the same disadvantages as hybrid models especially due to their complex formulation.

Other computational models that may be used for the analysis of sandwich structures include multiple models and hierarchical models described by Reddy [209], predictor-corrector methods presented by Noor and Burton [211, 252] and a unit cell approach developed by Meraghni et al [253].

2.8.5 Macro-Scale Finite Element Modelling of Composite Sandwich Structures

This section reviews the state of the art in macro-scale finite element modelling of sandwich structures with polymeric cores and composite skins with specific focus on sandwich models that were developed using commercially available finite element codes.

Lee and Shyu [254] studied the static and low velocity impact behaviour of sandwich beams made from GFRP skins and PVC Divinycell foam core. The ABAQUS finite element software and a user-defined subroutine UMAT are used to simulate the failure behaviour of the sandwich beams. A maximum principal stress failure criterion along with a stiffness degradation method

was used to predict the onset of yielding and cracks in the foam core. For the skin material model a stiffness reduction approach was used to simulate fibre damage. Delamination and matrix cracking were not accounted for by the skin material model. In all case there was good general agreement between the predicted and experimental results. However, the predicted static force-displacement curve did show a slight premature load drop at the yield point which was not observed in the test results. The authors attributed this discrepancy to the method that was used to simulate the fibre damage by degradation of the stiffness after the failed element is detected. The model was able to correctly predict core shear and yielding in the core.

Quaresimin and Michelazzo [255] simulated the impact response of open and closed (boxed) section sandwich beams with woven carbon/epoxy faces, aluminium honeycomb or PU foam cores. The beams were subjected to quasi-static three and four point bending loads. The analysis was conducted using the ANSYS commercial finite element code. Several modelling strategies are adopted which included modelling the composite faces with various types of shell or solid elements while the cores were modelled with solid elements. The finite element results were compared with both experimental and analytical solutions. There was reasonable agreement in some cases; however, significant discrepancies were also observed. It was concluded that the out-of-plane elastic properties of both the skin and core contributed significantly to the estimation of the stiffness and strain field in the FE and analytical solutions. In addition, the results were also influenced by the modelling strategy and choice of elements.

Borsellino et al [57] modelled the behaviour of sandwich beams under static flatwise and edgewise compression and three-point bending test using the ANSYS FE software. The sandwich specimens consisted of a combined PVC and polystyrene foam core with different woven fibre skins (glass, carbon or Kevlar). There was good agreement between the simulation and experimental results for the flatwise and edgewise compression tests. However, the model was only able to simulate the initial elastic behaviour of the non-linear elastic-plastic load-displacement response for the three-point bend test.

Corigliano et al [58] simulated the response of sandwich beams subjected to quasi-static three and four-point bending. The sandwich beam specimens were manufactured with glass fibre skins and epoxy syntactic foam core. A simplified modelling procedure was used for simulating failure in the core, skin and skin-core interface. This model was based on local stiffness release at the element Gauss point level through the assumption of an elastic perfectly brittle failure in the sandwich constituent materials. A Rankine criterion was used for simulating failure in the core and skins, while a maximum shear stress criterion was adopted for the skin-core debonding. The material model was implemented through a user subroutine in the commercial ABAQUS finite element code. There was good qualitative and quantitative agreement between the simulation and test results.

Sharma et al [256] investigated the low velocity impact response of sandwich panels made of PU core and glass/polyester or glass/epoxy faces. A finite element model of the sandwich panel was developed using the ANSYS code. The faces were modelled with an orthotropic shell element material while the core was modelled with an elasto-plastic solid element material model. The experimentally observed skin-core delamination was not modelled as a perfect bond was assumed between the skin and foam core. The predicted maximum transverse shear strain was concentrated at the centre of the panels which corresponded with the experimental observation for core shear failure in this area.

Aktay et al [257] studied the behaviour of sandwich panels under high velocity (60 ms^{-1}) impact loading. The sandwich panels were made from woven fabric carbon/epoxy skins and polyetherimide (PEI) and Nomex honeycomb cores. A finite element model was developed using the PAM-CRASH explicit finite code. The skins were modelled with the PAM-CRASH elastic-damage degenerate bi-phase material model. The core is modelled with the PAM-CRASH Material Model 2. In this model the foam material elastic behaviour is described by the shear modulus and the initial tangent modulus while the volumetric (bulk) and deviatoric (shear) plasticity are coupled by a pressure dependent von Mises yield surface. Predicted deformation and force-time history curves show good agreement with the experimental observations.

Lindholm [258] studied the static and low velocity impact behaviour of sandwich beams with glass fibre composite skins and PVC foam core. The static test was simulated with the commercial FE ABAQUS code using an axisymmetric model along with the *CRUSHABLE FOAM and *CRUSHABLE FOAM HARDENING foam material model that are implemented in ABAQUS. The FE results correlated well with both the experimental and analytical (Olsson's model [259]) results.

Skawinski et al [10] studied the static bending behaviour of thermoplastic sandwich constructions that consisted of glass/PP faces and expanded polypropylene (EPP) bead foam core. A sheet of PP and glass surface veils were also stacked on top of the composite skins for improved surface quality. The sandwich was modelled with the ABAQUS finite element code through a one-quarter shell element based model. The predicted deflections showed reasonable agreement with the experimental results. The panel deflection was over estimated by 2 to 28% for various panel thicknesses and foam densities.

Koissin et al [260] studied the static and low velocity impact performance of sandwich beams and panels. The sandwich specimens were made from GFRP skins and Rohacell WF51 PMI foam core. The ABAQUS finite element code was used to model the static indentation behaviour of the sandwich panel. The face sheets were modelled as linear-elastic material while the foam core was represented by the ABAQUS *CRUSHABLE_FOAM material model with no hardening employed. The FE results showed good agreement with both experimental and analytical results

Rizov et al [261] studied the static indentation behaviour of sandwich panels with E-glass/vinylester skins and PMI Rohacell WF51 foam core. An axisymmetrical finite model of the sandwich model was developed using the ABAQUS finite element code. The core was modelled with the *CRUSHABLE FOAM and *CRUSHABLE FOAM HARDENING material models in the ABAQUS code. The skins were modelled as linear elastic quasi-isotropic material with no consideration given to damage onset and progression. The predicted initial elastic response shows good agreement with the experimental load-indentation curve. However, at large deflections the simulation overestimated the experimental stiffness. This was attributed to the fact that the FE model did not account for damage

initiation and progression in the face sheets; whereas experimental observations revealed significant damage in the composite face sheets. Furthermore, following unloading, the recovery of the residual dent was underestimated because the model does not account for creep mode deformation.

Later on, Rizov [262] again used the same modelling approach described above in Rizov et al [261] to model the static indentation response of sandwich beams with E-glass/vinylester skins and PVC foam core. In this study a one-half plane strain model of the sandwich beam was developed using ABAQUS. The same material models were implemented for the skin and core as presented in Rizov et al [261]. In general, there was good agreement between the predicted and experimental force-displacement results. However, at large deflections the indentation load was slightly overestimated. This was associated with the assumption of no damage in the FE face sheet material model. In addition, the simulation underestimated the residual creep recovery as creep was not account for in the model.

Lim et al [263] studied the failure modes of sandwich beams under static and impact bending loads. The sandwich beams were composed of E-glass/epoxy skins and PVC foam core. A finite element model of the sandwich beam under impact loading was developed using the finite element software ABAQUS explicit. A quarter of the sandwich beam was modelled with both the faces and core represented by solid elements. The foam was idealised as elastic-perfectly plastic. For the estimation of the failure modes, the strain data of the face and core were obtained from the FE results and then the maximum strain failure criteria was applied. The strain components related to failure were the compressive strain of the face and shear strain of the core. It was assumed that first ply failure occurred in the skins when the strain of the centroid point of the element reached the failure strain of the skin material. The test results showed that the sandwich beam failed primarily through core shear fracture, skin-core delamination and face damage. From the test and FE results it was concluded that the impact energy capability was strongly related with the failure mode. It was recommended that for enhanced energy absorption, sandwich beams should be designed to fail in the skins.

Berger et al [264] investigated the impact damage modes of sandwich panels using impact tests and the LS-DYNA finite element code. The sandwich panels consisted of skins made from glass fibre reinforcements of woven fabric and CSM in a polyester matrix. A wide range of core materials at various densities were evaluated including balsa wood, linear PVC, crosslink PVC and linear SAN foams. The primary failure modes observed were core shear, skin core debonding and skin compression failure. A finite element model of the impact test for the sandwich panel with the PVC core was developed using LS-DYNA. The skins and core were modelled with shell and solid elements, respectively. The LS-DYNA *MAT_LAMINATED_COMPOSITE_FABRIC material model was used to model the skin materials while the PVC foam was modelled with the LS-DYNA *MAT_HONEYCOMB material model. There was generally good correlation between the predicted and experimental force-displacement response. However the peak force is underestimated. They concluded that more accurate mechanical input data is required for improved simulation results.

Later on, a more detailed version of the FE model presented by Berger et al [264] has been reported by Fritzsche et al [265] and Morgenthaler et al [266]. In there work the FE sandwich was modified by modelling the core with the LS-DYNA *MAT_MODIFIED_ HONEYCOMB material model which is the more advanced version of *MAT_HONEYCOMB. In addition, core shear fracture was modelled by element erosion which was governed by tensile and shear strain criteria. Skin-core debonding was also modelled using the LS-DYNA TIED_SURFACE_SURFACE contact algorithm. In all cases there was good general agreement between the acceleration-time and force-time plots (see Figure 2-22). However, there is a difference in the time scale as the simulation is slower than the experiment. It was assumed that this discrepancy was caused by the influence of air in the foam core which is not taken into account in the material model. The predicted core shear fracture was in good agreement with the test observations as depicted in Figure 2-22.

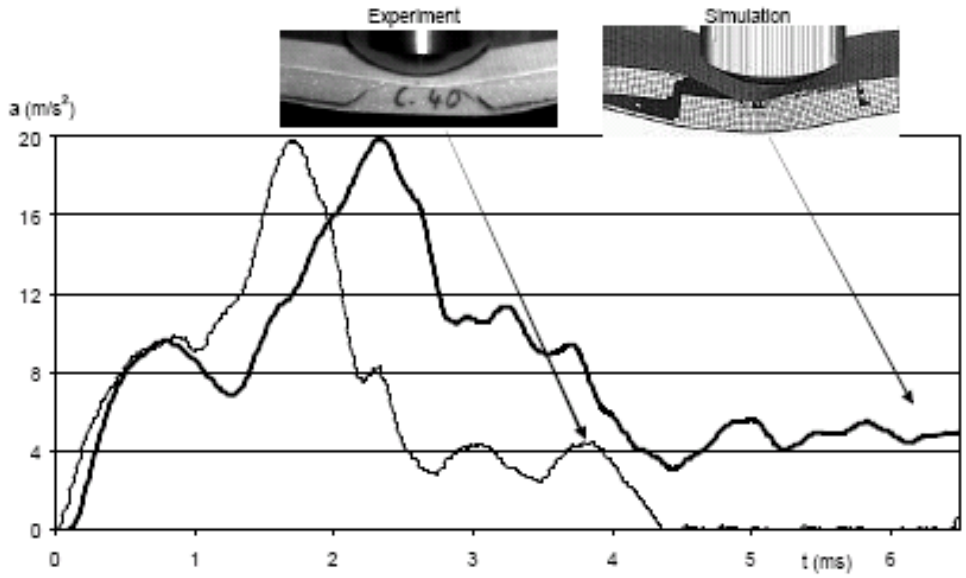

Figure 2-22. Comparison of the predicted and experimental acceleration-time histories and failure modes [266].

Mines and Alias [13] studied the static bending behaviour of sandwich beams made from glass/epoxy skins and either PVC Divinycell H100 (density = 100 kgm^{-3}) or H200 (density = 200 kgm^{-3}) foam cores. A two dimensional, plane strain model was developed using the ABAQUS finite element code. The failure in the skins was modelled with a stiffness reduction approach where the in-plane stiffness was degraded with respect to in-plane strain while the core was modelled with the ABAQUS *FOAM model. For the sandwich beam with the H100 core, the primary failure mode was large scale core crush followed by top skin compression failure near the indenter. The H200 core fails by skin failure with negligible core crush. The tensile hydrostatic yield pressure (Pt) input parameter for the *FOAM model was difficult to experimentally measure. Subsequently, values for Pt were varied in the sandwich beam FE analysis until the simulation results showed good agreement with the experimental results. It was shown that skin failure was highly sensitive to the value of Pt. The authors concluded that the skin failure model required further refinement.

Later on, the same finite element model for the sandwich beam with the PVC Divinycell H200 core (described above, Mines and Alias [13]) was used by Mines [14] to perform a dynamic impact analysis using the ABAQUS code. Again core is modelled with ABAQUS *FOAM material model while the skin is modelled using a strain based stiffness degradation approach. In this model strain rate effects have been accounted for with the ABAQUS *RATE_DEPENDENT command. There was reasonably good agreement

between the simulation and experimental results. However the initial peak load was underestimated. It was concluded that improvements were required in the model with respect to strain effects and numerical instabilities. Following on from this, the same sandwich model was analysed using the LS-DYNA explicit finite element code under the same boundary conditions. However, in the LS-DYNA model the skin was modelled with shell elements and the foam core was represented by solid elements. The failure in the skin was modelled with the LS-DYNA MAT 54 material model which is based on the Hashin critical stress approach. The foam core was modelled with the LS-DYNA MAT 83 foam model which is an elastic viscoplastic model and accounts for strain rate effects. The simulation results were reported to be similar to the ABAQUS model.

Mines [14] also studied the static and dynamic impact behaviour of sandwich beams with clamped ends. The skin material was carbon/epoxy unidirectional laminates and PMI Rohacell 51WF core. The static simulation was developed using LS-DYNA. The skin was modelled using the elastic-plastic LS-DYNA MAT 24 material model. Damage in the skins was not accounted for in this model. The core was modelled with the LS-DYNA MAT 83 model. In addition foam facture was modelled by including a maximum principal tensile strain criterion coupled with element erosion. In the case of the static analysis, there was reasonably good agreement between the simulation and experimental force-deflection results. The predicted shear cracks through the core near the indenter as well as the core separation from the bottom skin corresponded with experimental observations. However, skin failure was under-predicted. For the dynamic model, there were significant discrepancies between the predicted and experimental force-displacement results. The predicted failure modes were similar to the static case with shear cracks near the indenter. It was found that the impact analysis was sensitive to the inertia of the clamps and the friction conditions. Mines concluded that the out-of-plane stresses needed to be taken into account in the skin material model. In addition, a more elementary approach to composite damage modelling was required. He further noted that the multiple failure modes of the foam core were difficult to model using continuum theory. Furthermore, the element erosion approach for simulating core shear fracture could result in a mesh sensitive solution. For dynamic analysis, large strain gradients and foam core failure growth are difficult to model and can result in numerical instabilities.

Therefore, both the skin and foam core material models need further refinement.

Lolive and Berthelot [56, 267] studied the static indentation and bending behaviour of sandwich beams with glass/epoxy skins and PVC core. The authors developed a finite element procedure that incrementally evaluates the strain field in the sandwich structure. At each step, the principal strains are calculated in every element, allowing the separation of the tensile or compressive state from the shear state. Then the stress-strain relations are evaluated from these strain states considering the incrementally linearised stress-strain curves derived from the tensile, compressive and shear tests which were carried out on the constituents of the sandwich construction. This modelling approach was applied to the analysis of sandwich beams subjected to static indentation and three-point bending loads. In the case of the indentation analysis, the FE results showed that the non-linear behaviour of the sandwich beam was induced by the non-linear behaviour of the foam core followed by fracture progression in the skins. For the bending investigation, the FE model slightly over-predicts the fracture loads. However, the general shape of the predicted load-displacement curves were in good agreement with the experimental results.

Very recently, Russo and Zuccarello [268] used the ANSYS code to simulate the quasi-static three and four point bending response of sandwich beams. The sandwiches were manufactured from glass/polyester skins and PVC foam or polyester mat cores. A plane strain, non-linear model was developed using isoparameteric plane elements to represent the skin and core material. In all cases, good correlation between simulation and experimental results was reported with respect to failure modes and corresponding strengths.

2.9 Conclusions

This chapter has presented an extensive review of the state of the art in modelling the behaviour of composite sandwich structures. It has been shown that there is a growing interest in increasing the application of thermoplastic composite sandwich structures in the automotive industry. Sandwich constructions offer several advantages such as high stiffness to

weight ratio and high energy absorption capabilities. In particular, thermoplastic composite sandwich structures allow for rapid one-step manufacturing and offer significant recycling potential.

Experimental characterisation of composite materials has been discussed. This review has shown that the characterisation of the static mechanical properties of composite materials has developed significantly since the late 1900s with many new test methods emerging in the mid 1980s. While the state-of-the-art of static mechanical tests methods for composites appear to be stabilising, high strain rate mechanical tests are still emerging and there are still few universally accepted standard techniques available for characterising the high strain rate mechanical properties of composites. This makes comparative analysis of high strain rate test results from various test houses and research institutions near impossible. In terms of composite materials, the focus has primarily been on glass and carbon reinforced thermoset composite materials with thermoplastic composites receiving very limited attention. For the characterisation of thermoplastic composites, a number of important research issues still remain outstanding. Among these are the characterisation of the complex failure modes which also tend to change with increasing strain rate, and quantification of micro-damage on composite response and failure. In addition, further consideration needs to be given to temperature effects, moisture effects and processing variables.

Finite element techniques for simulating damage in composite materials were investigated. It was shown that several continuum damage mechanics models have been developed that are able to simulate composite macroscopic damage modes such as matrix cracking, fibre fracture, and delamination. However, these models have mainly been validated for thermoset composites with the predictive modelling of impact damage in thermoplastic composites remaining largely underinvestigated.

A reasonable state-of-the-art has been achieved concerning the macro-scale finite element modelling of foams; however, some problems still remain. In particular, the simulation of high energy absorbing anisotropic crushable thermoplastic PP foams such as Strandfoam remains largely underinvestigated. In addition, modelling the failure modes such as core shear fracture and tensile brittle failure has received limited attention.

Strain rate effects may be attributed to air in the cells of the foam. However, this micro-structural effect is currently not included in any of the existing FE foam models. In addition, current foam models are limited in their ability to simulate the diverse response of foam components due to the global and local density variations and skin formations in foam materials. Furthermore, simulation of the influence of climate conditions such as temperature and humidity on the foam material behaviour has been largely ignored in the open literature.

Finite element modelling of sandwich structures has been reviewed. It was shown that sandwich constructions with thermoset composite skins and polymeric foam cores (especially PVC or PMI foam cores) have received significant attention. However, thermoplastic sandwich constructions have been underinvestigated. It was shown that most FE sandwich models are able to model the static loading performance of sandwich beams with reasonable accuracy. However, further work is still required with respect to obtaining an accurate representation of the dynamic impact response of sandwich structures. Several attempts have been made at simulating core shear fracture and skin-core debonding. However, further research is required in this area.

Chapter 3

Experimental Characterisation of the Mechanical Properties of a Thermoplastic Composite Material at Quasi- Static and High Strain Rates

3.1 Introduction

The literature review in the previous chapter concluded that the experimental characterisation of the quasi-static mechanical behaviour of composites is established and several standard test procedures have been developed. However, few attempts have been made to study the dynamic mechanical behaviour of composites and there are few standard dynamic experimental techniques. Furthermore, most studies have involved thermoset composites with little attention given to thermoplastic composite materials.

This chapter focuses on the experimental characterisation of the mechanical properties of a commingled woven fabric glass fibre reinforced polypropylene thermoplastic composite under both quasi-static and high strain rate loading. The material, manufacturing process, experimental procedures and results are presented in detail. In particular, the development and application of novel test methods for high strain rate testing of the thermoplastic composite is outlined. In addition, the effect of strain rate on the mechanical properties and the corresponding macro and micro scale failure modes are discussed. The results from this work are used in later chapters to calibrate and validate an advanced composite material model within the LS-DYNA explicit finite element software.

3.2 Experimental Methods

3.2.1 Material

The material system used in this study is Twintex, which is a commingled E-glass/polypropylene woven fabric composite, balanced 1:1 twill weave with a 60 % fibre weight fraction (T PP 60 745 AF) that is supplied by Saint Gobain Vetrotex (see Figure 3-1 (a)-(b) and Figure 3-2).

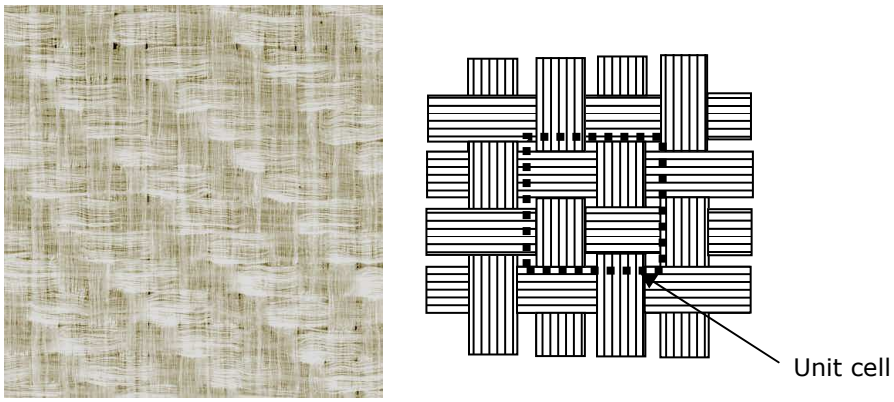

Figure 3-1. (a) Twintex commingled E-glass/polypropylene woven fabric (b) schematic of woven structure.

3.2.1.1 Material coordinate system

A xyz Cartesian coordinate system was used to define the principal material coordinate system as depicted in Figure 3-2. For the in-plane orthogonal directions, the x-axis is aligned with the warp fibres, while the y-axis is aligned to the weft fibres. The z-axis is aligned perpendicular to the plane of the material (the through-thickness direction). It was assumed that the in-plane material properties were equal because of the balanced, symmetric nature of the Twintex woven fabric. Therefore, all in-plane tension and compression tests were conducted in only the x-direction which is aligned with the warp fibres.

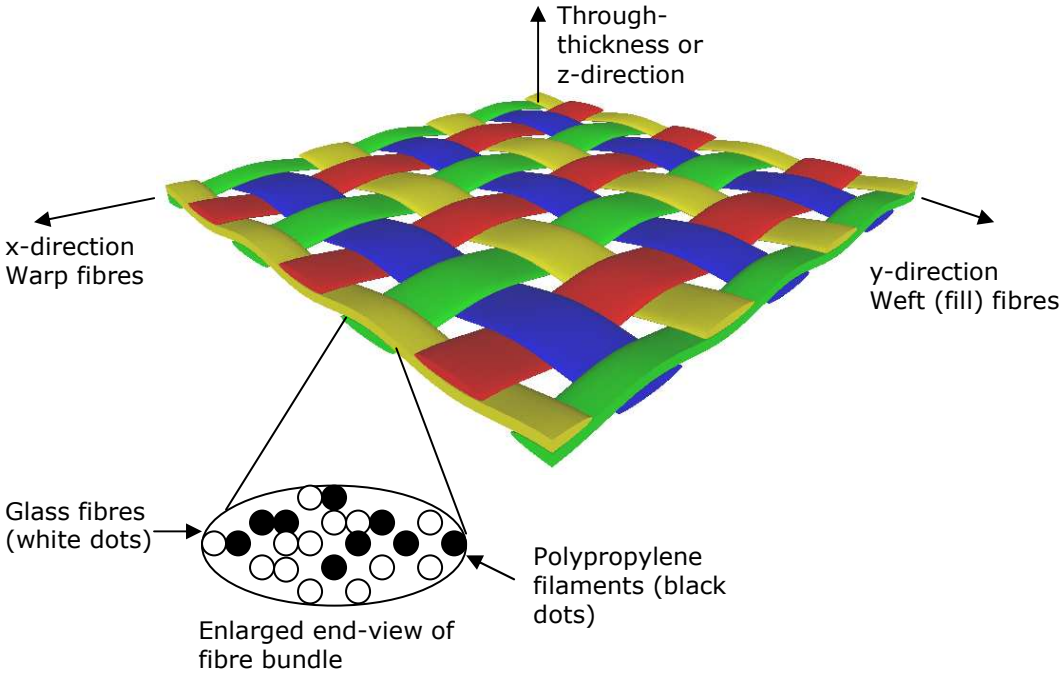

Figure 3-2. Graphical representation of Twintex commingled woven fabric and the material coordinate system.

3.2.2 Manufacturing Process

A non-isothermal compression moulding process was used to manufacture all specimens in this study. The optimal processing parameters were taken from Wakeman et al [25]. The manufacturing procedure involved preheating stacks of preconsolidated sheets of Twintex in a 4.5 kW infrared oven at a temperature of 200 °C. Thermocouples were used to monitor the temperature in the middle of the stack. The stack was then rapidly transferred to a heated tool (80 °C) which is installed in an up stroking hydraulic press. The tool is closed and a pressure of 16 bar is applied for 60 s. Finally, the tool is opened and the plaque is ejected. Test specimens are cut from the plaque using a bandsaw and a Bridgeport horizontal milling machine. A schematic of the non-isothermal compression moulding process is shown in Figure 3-3.

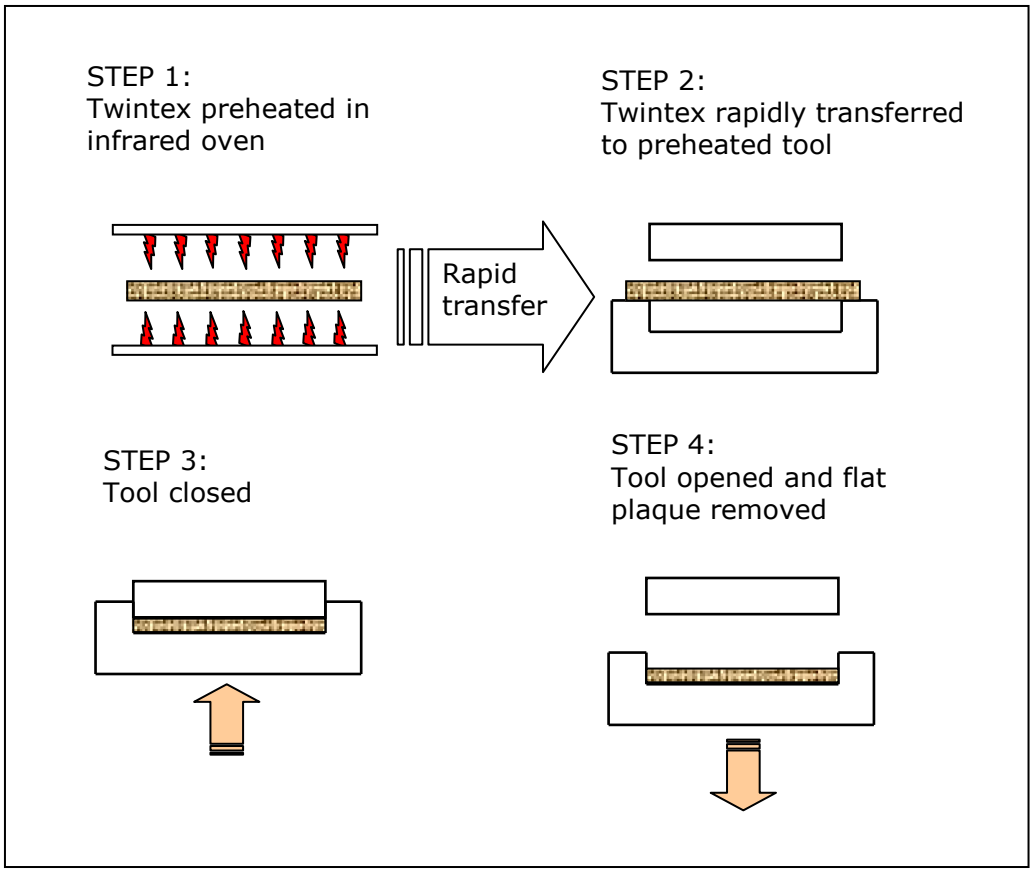

Figure 3-3. Schematic diagram of non-isothermal compression moulding process.

3.2.2.1 Tool design

The moulding tool was designed to manufacture flat plaque laminates of dimensions 260 x 120 mm with thickness ranging from 1 mm to 10 mm. The tool consisted of two halves. The top half is a simple flat plate while the bottom half which is shown in Figure 3-4 has a sprung blankholder which maintains tension in the fibres during mould closure and a sprung shear edge to minimise matrix flow outside the tool [7, 19].

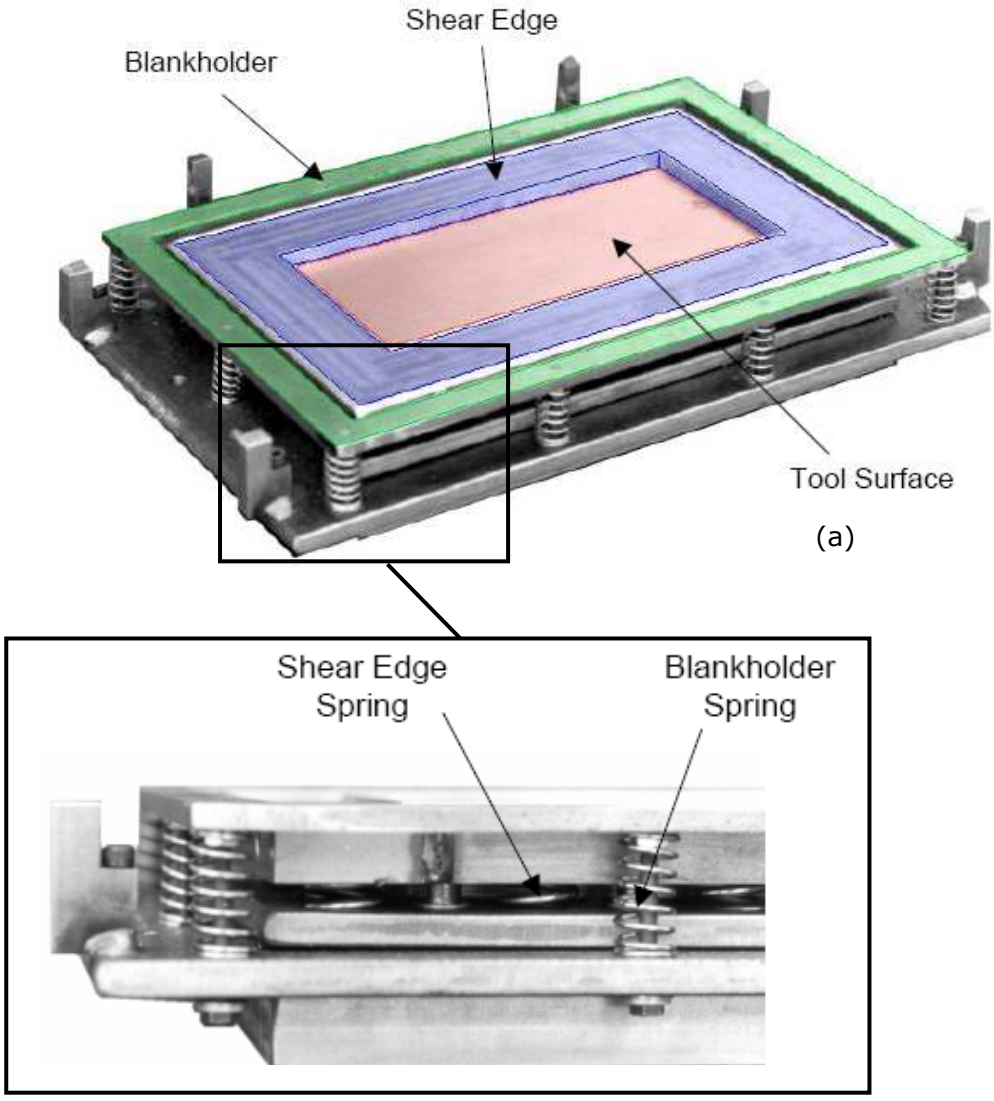

Figure 3-4. Tool design (a) top half (b) enlarged side view of tool.

3.2.3 In-Plane Tensile Tests

3.2.3.1 Test machines and fixtures

Quasi-static tensile tests were conducted according to ASTM standard D3039 [269]. The tests were conducted on an Instron electro-mechanical universal test machine at a crosshead speed of 5 mm min^{-1} (see Figure 3-5). The Instron machine was fitted with rotationally self-aligning wedge grips to minimise bending stresses in the specimen. Previous tests have shown that surface damage from the machine grips can result in undesired failure in or near the grips [7]. In order to solve this problem, folded strips of medium grade (120 grit) emery cloth were used as friction tabs. These tabs were placed between the specimen faces and the grip jaws (grit-side against specimen) and provided a non-slip grip and eliminated jaw serration damage to the surfaces of the specimen. The specimen strain response was determined by a 50 mm gauge length extensometer that was placed symmetrically about the mid-span, mid-width location of the specimen gauge area. The extensometer had a maximum strain capability of 10%.

Dynamic tensile tests were conducted in a Rosand instrumented falling weight drop tower using a specially designed fixture. The drop tower as depicted in Figure 3-6 uses a free falling, weighted crosshead with a striker, guided by two long steel rods, to impart an impact load. A near constant strain rate is required during a dynamic test. This was achieved by using very high masses on the drop tower crosshead and striker. A crosshead mass of 100 kg was used in the dynamic tensile tests. The tests were conducted at speeds of 3, 5 and 7 ms^{-1} which corresponded to strain rates of 36, 50, 70 s^{-1}, respectively. The strain rate during the test was derived from the gradient of the strain-time history results.

The test fixture shown in Figure 3-7 was used for dynamic tensile testing. The dynamic tensile test fixture was originally developed at the University of Nottingham for high strain rate testing of thermoset composites in a falling weight drop tower [42]. The fixture is installed in the drop tower as shown in Figure 3-8. In this fixture, the specimen is clamped at each end between steel grips. The top grip is directly bolted through the load cell to a fixed carriage. A moving carriage is supported by the lower grip and is

guided by two steel rods through two linear bearings on one side and two nylons dowels on the other side. The drop tower striker imparts a load on the moving carriage which loads the specimen in tension through the lower grip as it travels downward.

In the original design, the specimen was clamped and bonded to steel grips that had smooth jaws [42]. However, in this current study, the Twintex polypropylene matrix has a very low activation energy surface, which made it difficult to find a suitable adhesive that would bond the specimens to the steel grips. Preliminary dynamic tests were conducted with the specimens clamped tightly in the grips with no adhesive applied but as expected the specimens slipped out of the grips during the tests. Another modification that was tried involved the application of Permabond™ surface primer on the surface of the specimen so as to improve the effectiveness of a cyanoacrylate adhesive that was applied between the specimen and the grips. However, when the test was conducted with the application of the surface primer and cyanoacrylate adhesive, the specimens slipped out of the grips before the specimens failed. The final modification involved roughening the jaws of the grips, reducing the specimen thickness from 4 mm to 2.5 mm and applying a very high clamping torque. These modifications worked well with the specimen failing in the gauge area without slipping.

Load was measured with a Kistler 9051A piezoelectric load cell. Strain data was recorded with Kyowa 120 Ohms strain gauges (KFG-20-120-C1), having a 20 mm gauge length. The gauges were bonded centrally on the specimen using cyanoacrylate adhesive. The strain gauge length was selected to be equal to or greater than the 10 mm square characteristic repeating unit cell of the Twintex weave (see Figure 3-1 (b)). This ensured an accurate measurement of the average strain magnitude in the specimen. Strain gauges were connected to a quarter bridge circuit. Both load cell data and strain gauge readings were recorded at a sample rate of 40 kHz on to a personal computer using an InstruNet™ data logger.

3.2.3.2 Specimens

The tensile specimen dimensions are shown in Figure 3-9 (a)-(b). The quasi-static specimens were straight sided with a nominal thickness of 4

mm by 25 mm wide and a length of 250 mm, which included a 150 mm gauge section (Figure 3-9 (a)). The high strain rate specimens were also straight sided with a nominal thickness of 2.5 mm by 25 mm wide and a length of 180 mm, which included a 100 mm gauge section (Figure 3-9 (b)). All specimens had a [0/90] stacking sequence with 8 plies for quasi-static specimens and 5 plies for the dynamic specimens.

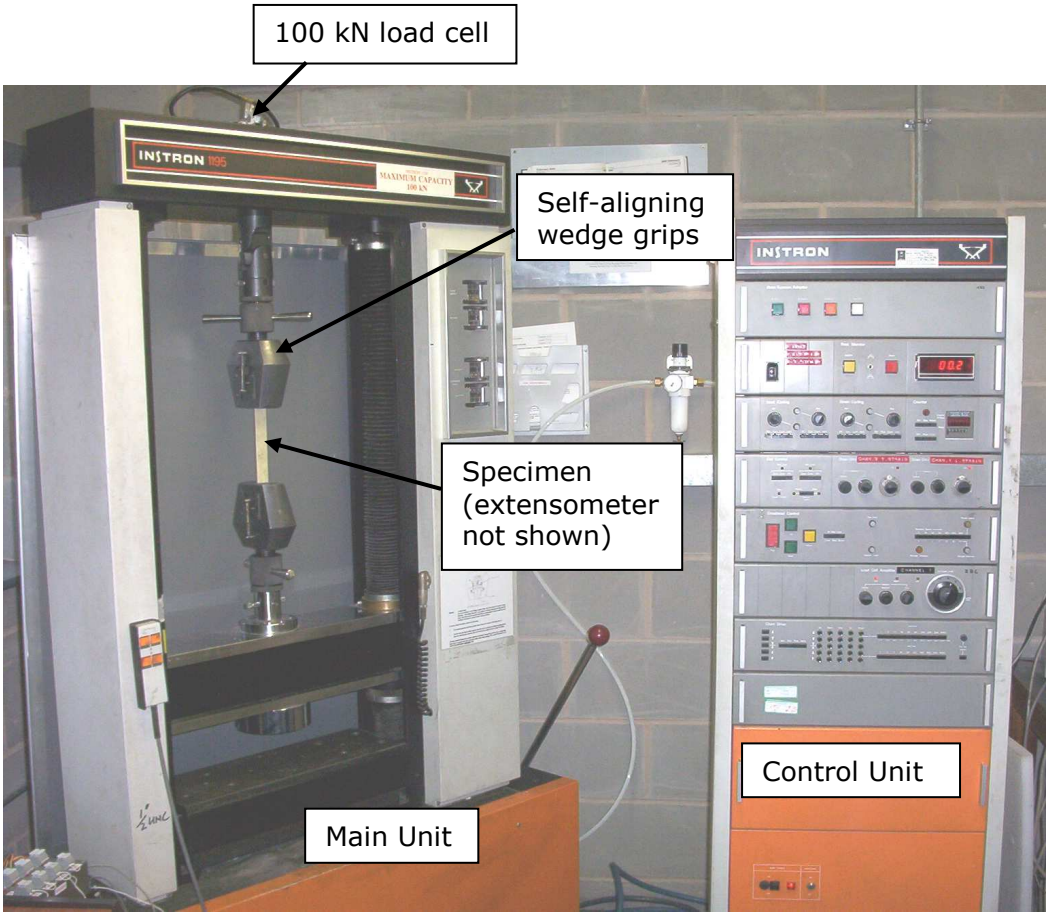

Figure 3-5. Picture of HK100 Instron universal testing machine with a 100 kN load cell.

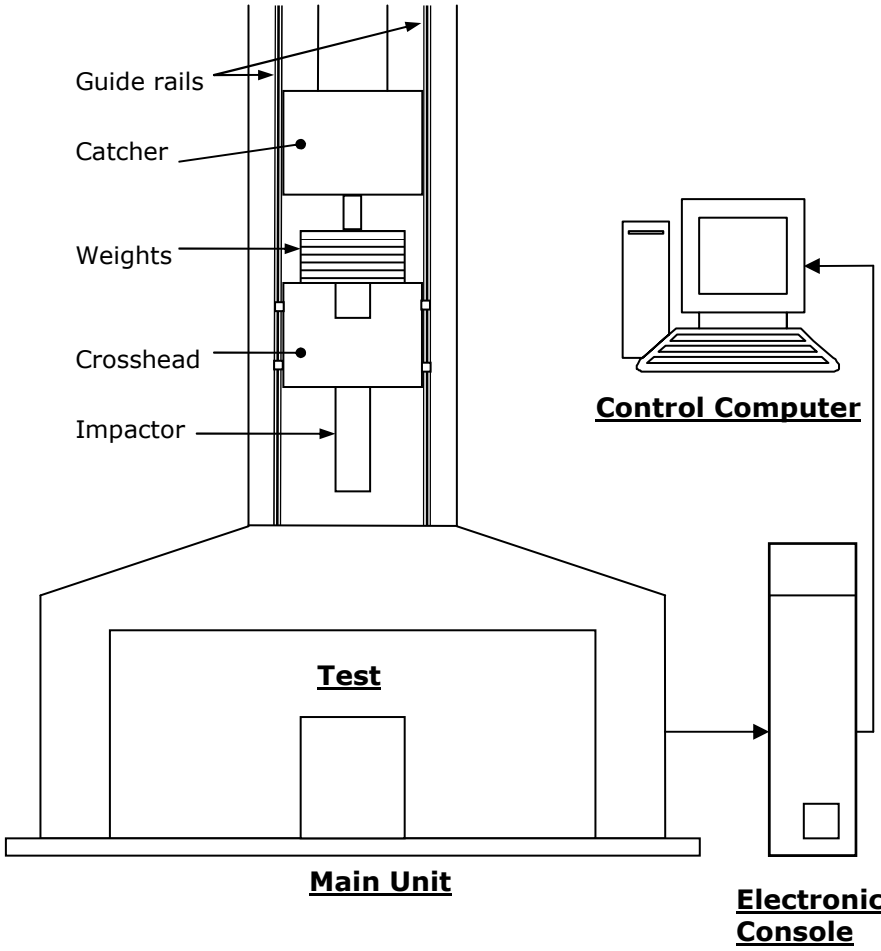

Figure 3-6. Schematic of Rosand instrumented falling weight drop tower.

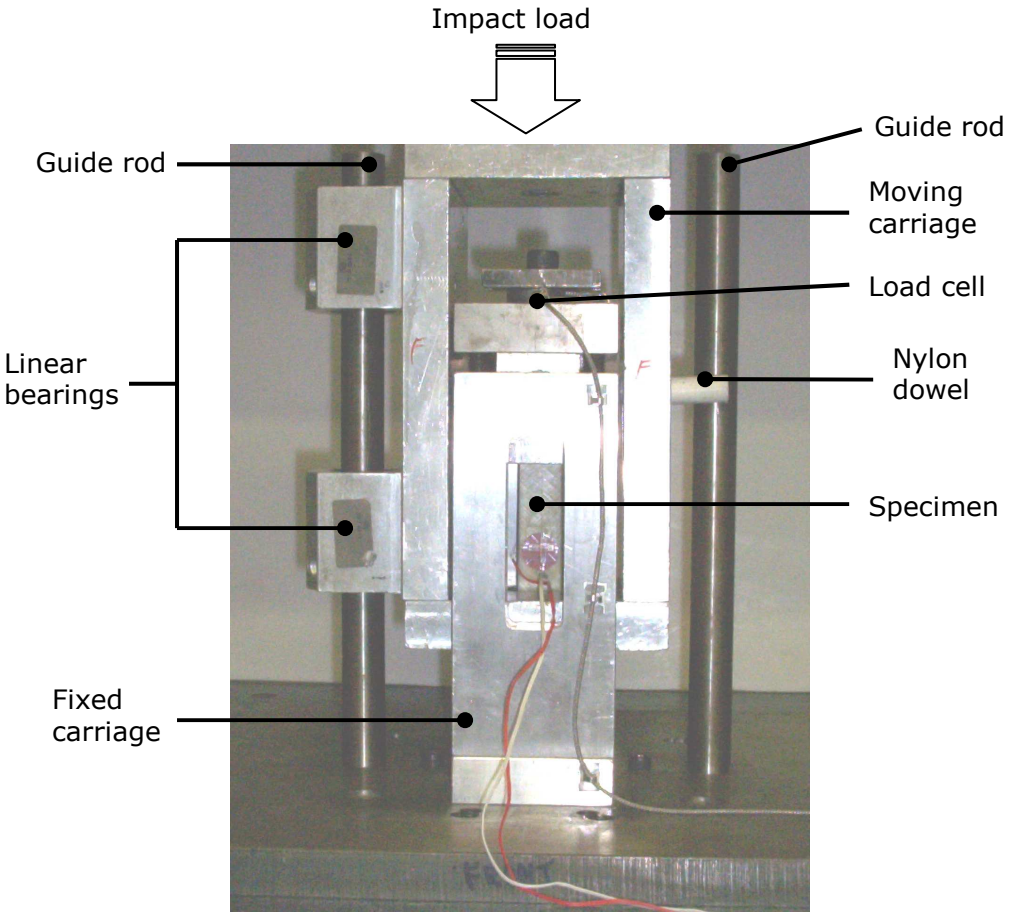

Figure 3-7. Dynamic tensile test fixture.

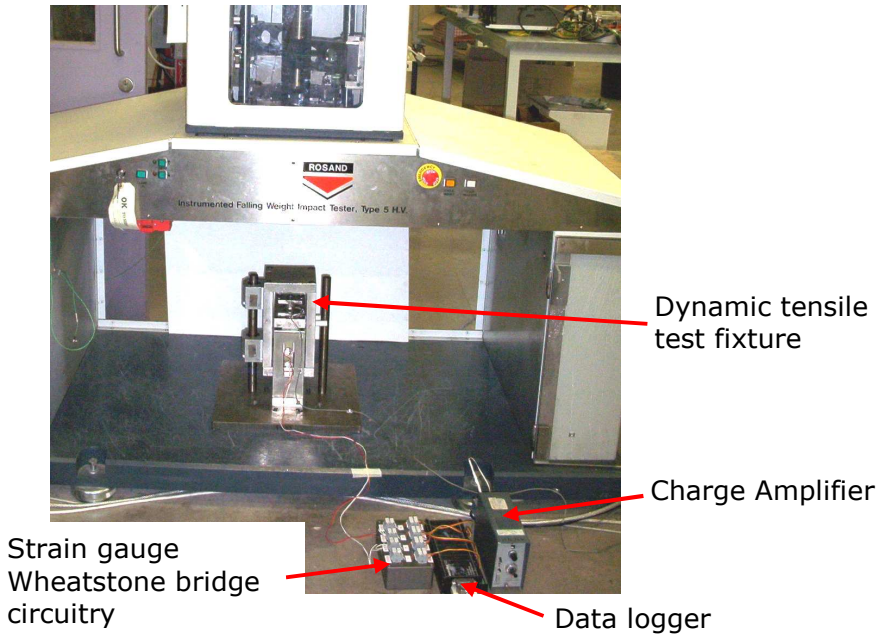

Figure 3-8. Showing dynamic tensile test fixture in Rosand instrumented falling weight drop tower.

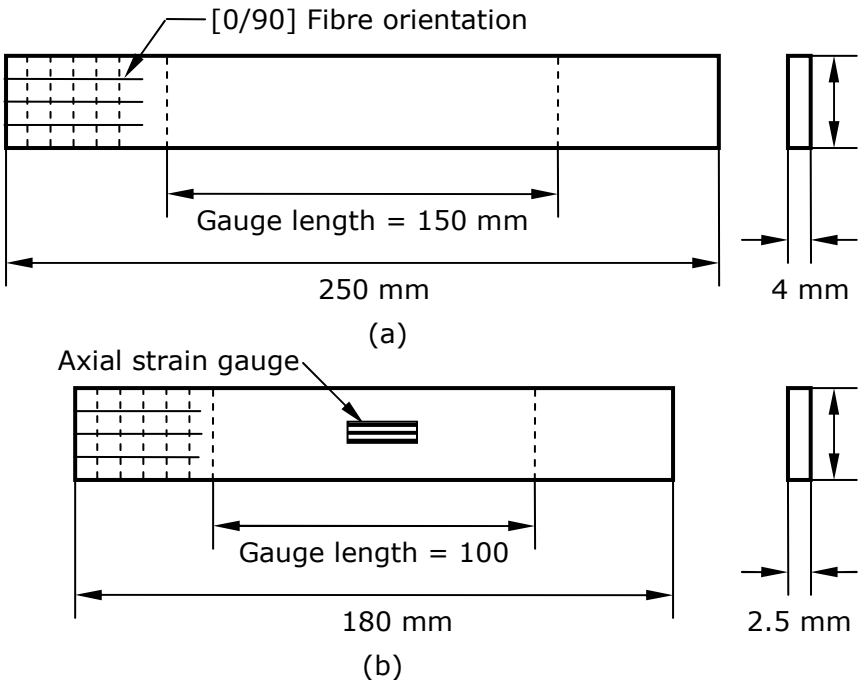

Figure 3-9. In-plane tensile test specimen dimensions (a) quasi-static specimen (b) dynamic specimen.

3.2.4 In-Plane Shear Tests

3.2.4.1 Test machines and fixtures

The quasi-static in-plane shear test was based on a tensile test of a ±45° laminate as described by ASTM standard D3518 [270]. The same test equipment and fixtures as described above for the quasi-static and dynamic in-plane tensile tests were used for the in-plane shear tests.

Strain data was recorded with bi-axial 0-90° T-rosette Kyowa 120 Ohms strain gauges (KFG-10-120-D16), having a 10 mm gauge length (Figure 3-10 (a)-(b)). The gauges were bonded centrally on the specimen in the material principal in-plane directions using cyanoacrylate adhesive.

3.2.4.2 Specimens

The specimen dimensions are similar to the quasi-static and dynamic tensile tests as shown in Figure 3-10 (a)-(b). The specimens had a [±45] layup with a nominal thickness of 3.5 mm (8 plies).

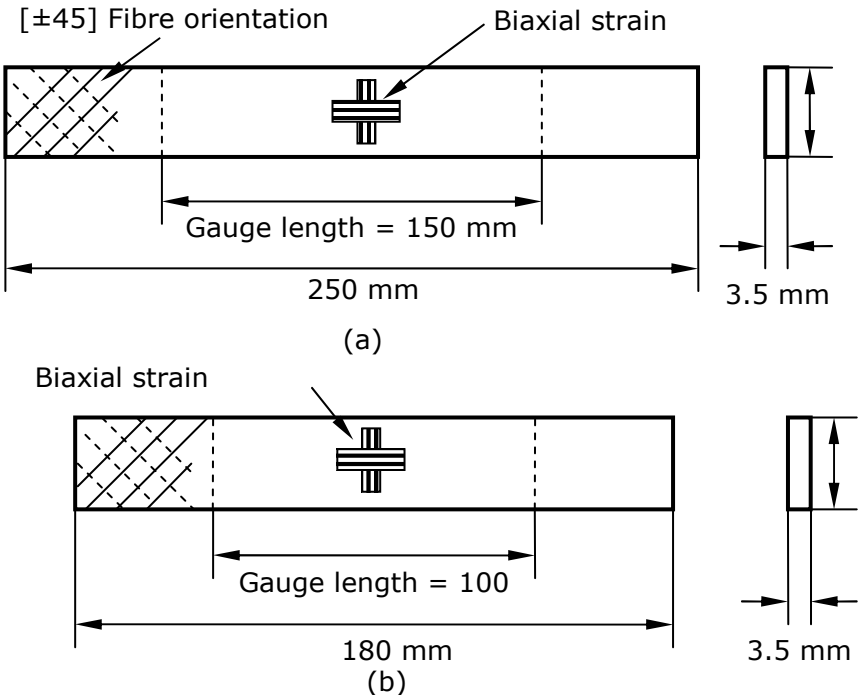

Figure 3-10. In-plane shear test specimen dimensions (a) quasi-static (b) dynamic.

3.2.5 In-Plane CompressionTests

3.2.5.1 Test machines and fixtures

A compression fixture shown in Figure 3-11 (a)-(b), was used for the quasi-static and dynamic compression tests. The fixture is based a design by Montiel and Williams [45] that was later modified by Fernie [42]. The fixture consists of a T-shaped impactor that is guided by two closely toleranced vertical channels in a steel supporting block. The specimen is clamped between two steel end-caps and placed directly under the impactor. Montiel and Williams recorded the dynamic compression load in the specimen by placing a load cell above the T-shaped impactor; however, Fernie, found that placing the load cell directly below the specimen resulted in more accurate load measurements and reduced noise in the test data. This modification to the compression fixture was retained in this current investigation. Preliminary tests during this study showed that at high impact speeds, plastic deformation was observed in the horizontal section of the original T-shaped impactor. Subsequently, the original thickness of the horizontal section was increased from 15 mm to 50 mm.

For quasi-static testing, the compression fixture was installed in an Instron test machine. High strain rate compression tests were conducted in the drop tower using a crosshead mass of 40 kg at speeds of 3, 5 and 7 ms^{-1} which corresponded to strain rates of 56, 78, 126 s^{-1}, respectively.

In all cases, compression strain data was recorded with Kyowa 120 Ohms strain gauges (KFG-10-120-C1), having a 10 mm gauge length. The gauges were bonded centrally on the specimen using cyanoacrylate adhesive.

3.2.5.2 Specimens

All specimens had a stacking sequence of [0/90] with a nominal thickness of 4 mm. The specimen length is 40 mm, which includes a 30 mm unsupported gauge section and a 5 mm grip length on either end (see Figure 3-12). Close tolerances were specified for flatness and perpendicularity on the specimen ends so as to minimise out-of-plane loading and ensure uniform load introduction.

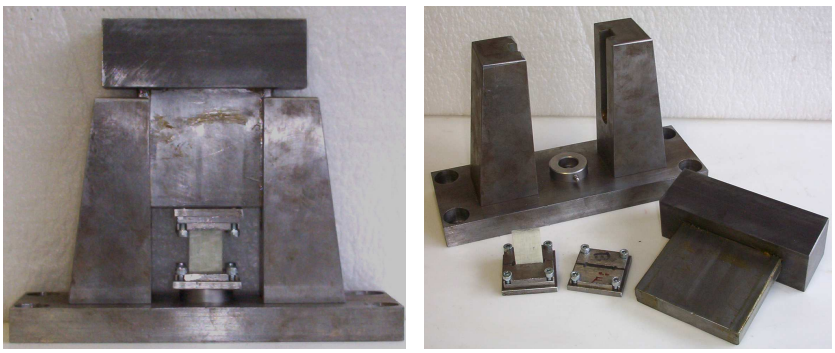

(a)

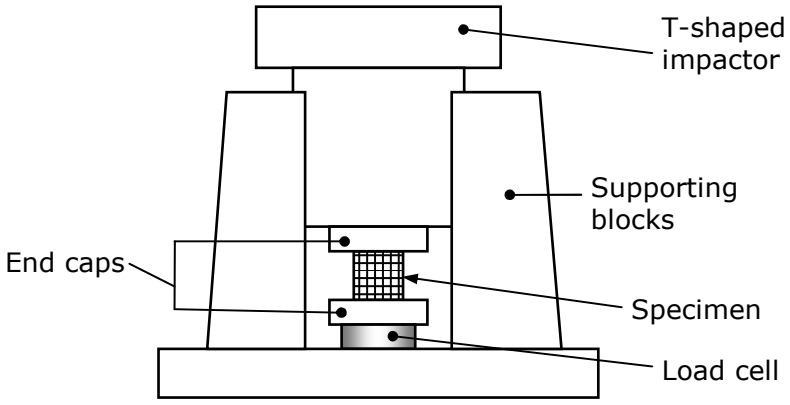

(b)

Figure 3-11. In-plane compression fixture used for quasi-static and dynamic high strain rate tests (a) photograph of fixture (b) schematic of fixture.

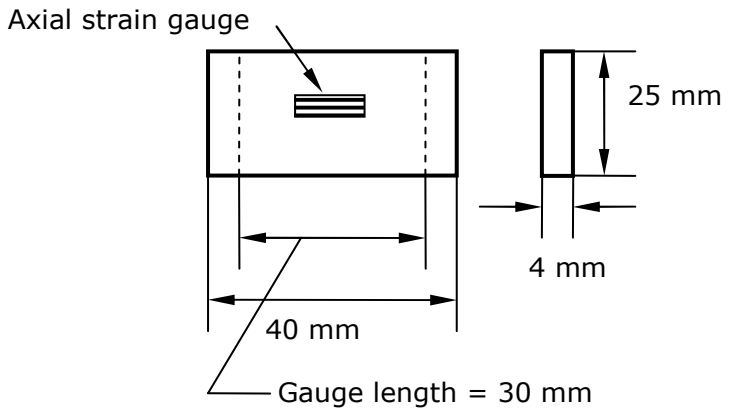

Figure 3-12. In-plane compression test specimen dimensions.

3.2.6 Through-Thickness Shear Tests

The main two test methods that are used for obtaining the through-thickness shear properties of polymers and composites are the punch shear test [271, 272] and the Iosipescu method [175]. A shear punch test method was developed here because of the potential simplicity and reliability of this technique over the Iosipescu shear method.

3.2.6.1 Test machines and fixtures

A new novel shear punch fixture was designed to determine the through-thickness shear strength of Twintex. The new fixture is shown in Figure 3-13 (a)-(b). The specimen is clamped between a cover plate and a hardened steel punch die with a 15.05 mm hole in the centre. The punch fixture assembly is mounted into an Instron machine and a flat ended hardened steel punch of 15 mm diameter is driven through the unsupported specimen at a constant displacement rate of 5 mm min^{-1} to produce shear.

The through-thickness shear strength was calculated using

$$\tau = \frac{P}{\pi dt} \qquad \textbf{(3-1)}$$

where P is the peak load, d is the diameter of punch hole and t is the specimen thickness.

3.2.6.2 Specimens

The through-thickness shear test specimen dimensions are shown in Figure 3-14. Specimens are 50 mm square with a 3 mm thickness and had a [0/90] stacking sequence (4 plies).

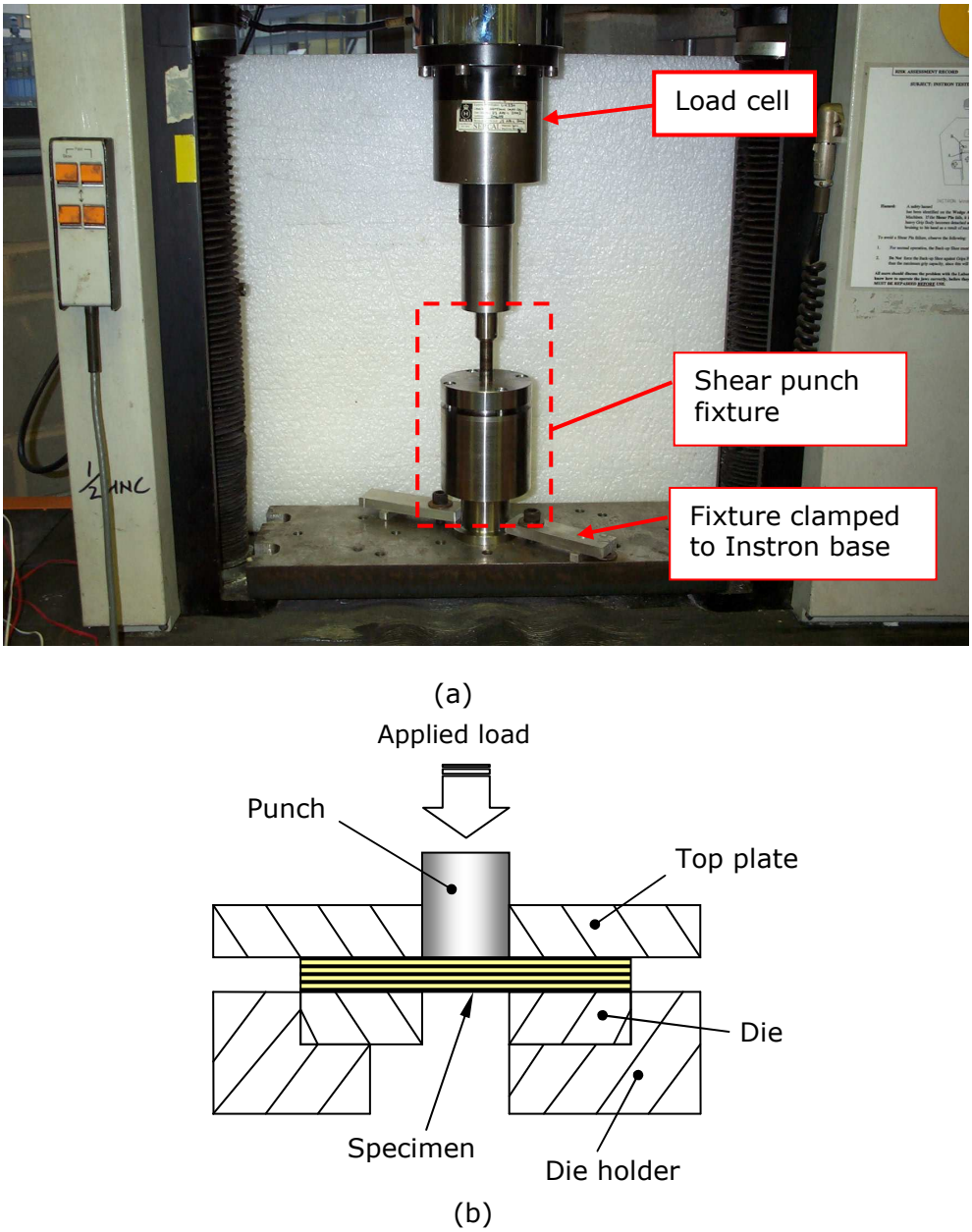

Figure 3-13. Shear punch fixture (a) picture of fixture assembly in Instron (b) schematic of shear punch fixture.

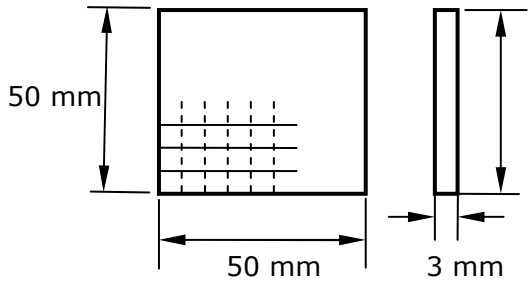

Figure 3-14. Through-thickness shear test specimen dimensions.

3.2.7 Flexural Tests

3.2.7.1 Test machines and fixtures

The flexural tests were based on a three-point loading setup as shown in Figure 3-16. The quasi-static flexural tests were conducted according to British Standard 14125 [273] and were carried out on a Tinius Olsen electro-mechanical test machine at a crosshead speed of 5 mm min^{-1}. Displacement as a function of the applied load was recorded during the entire test until the applied load dropped substantially, as a result of damage in the specimens.

The dynamic tests were conducted in the drop tower at speeds of 3, 5 and 7 ms^{-1}. The quasi-static and dynamic test setups are shown in Figure 3-15 (a) and (b), respectively. In all cases, a 10 mm diameter cylindrical rod is used to apply a load to the centre of the specimen that is simply supported over a span of 80 mm.

3.2.7.2 Specimens

All specimens had a stacking sequence of [0/90] with a nominal thickness of 4 mm and width of 25 mm. The specimen length is 120 mm, which includes a support span of 80 mm (see Figure 3-16).

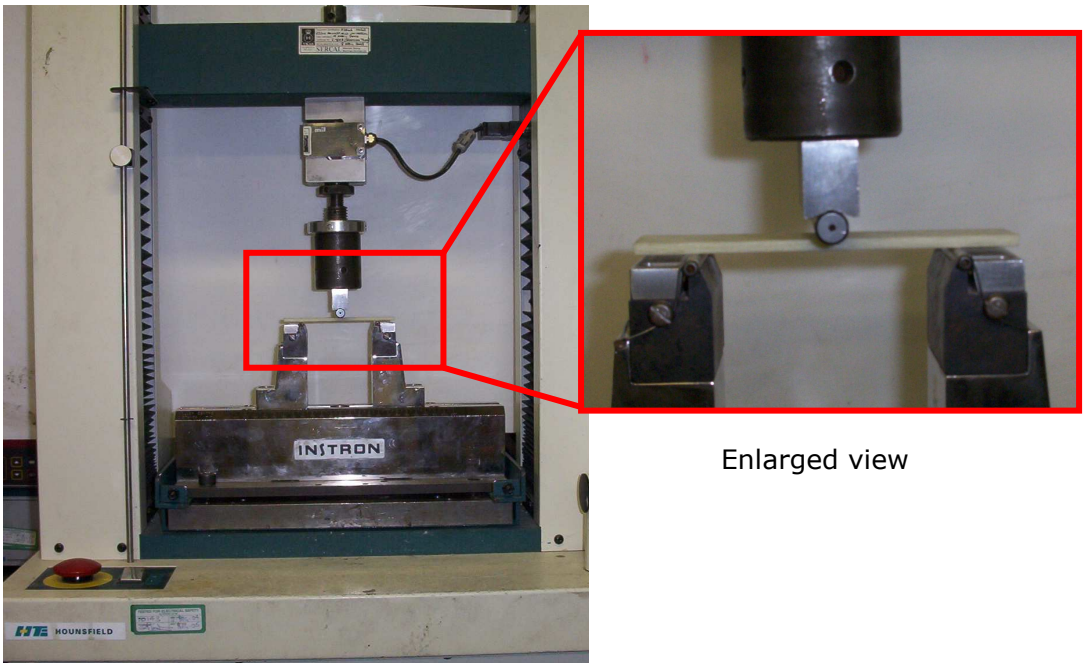

Enlarged view

(a)

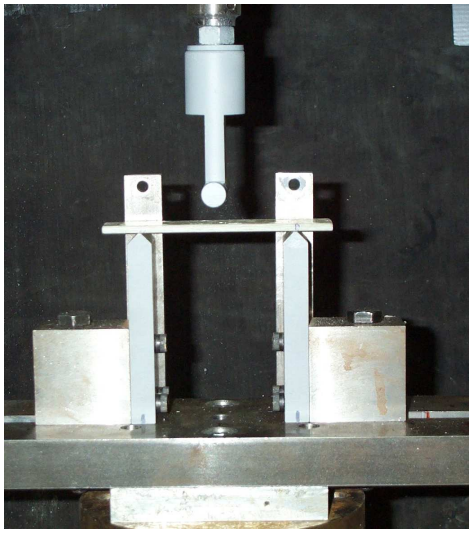

(b)

Figure 3-15. Three-point bending test (a) picture of quasi-static test setup in electro-mechanical test machine (b) picture of dynamic test setup in drop tower.

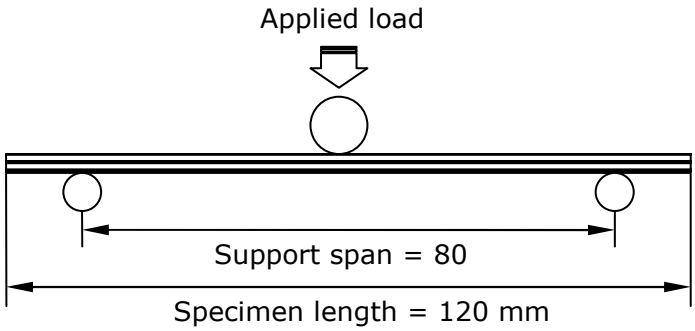

Figure 3-16. Schematic of flexural test.

3.2.8 Microscopic Analysis

Optical microscopy and scanning electron microscopy (SEM) were used to investigate local failure mechanisms in the fractured composite specimens. Typically, microscopic analysis was conducted on fractured specimens that were loaded at quasi-static strain rates and at the highest dynamic strain rate.

For optical microscopic analysis, sample sections were cut from the failure region of the fractured specimens. The samples were cast in polyester resin and polished in six stages ranging from 200 to 4000 grit abrasive wheel and 0.1 μm alumina particles. These prepared samples were then examined using a Zeiss Axiolab optical microscope.

For SEM microscopic analysis, sample sections from the specimen fracture zone were bonded to a sample holder and gold plated. The samples were then examined in a SEM microscope.

3.3 Results

This section presents the results of the experimental procedures described above. A minimum of three repeats per test was undertaken with the results in most cases exhibiting high levels of reproducibility. Therefore only the typical, average stress-strain histories are presented along with an assessment of strain rate effects and failure modes.

3.3.1 Data Analysis

This section describes the data reduction techniques that were employed so as to make the raw data more comprehensible.

3.3.1.1 Stress-strain data

For dynamic tensile, compression and shear loading, the typical dynamic stress-strain curve as depicted in Figure 3-17, exhibited an initial nonlinear toe region (AB) followed by elastic deformation (BC), yielding, plastic deformation and failure. The toe region (AB) does not represent a property of the material. It is an artefact caused by takeup of slack and alignment or seating of the specimen in the test fixtures. Subsequently, the dynamic elastic modulus was measured between the BC region of the curve (see Figure 3-17). Point F is then taken as the corrected zero strain point from which all strains are measured resulting in the corrected plot as shown in Figure 3-17.

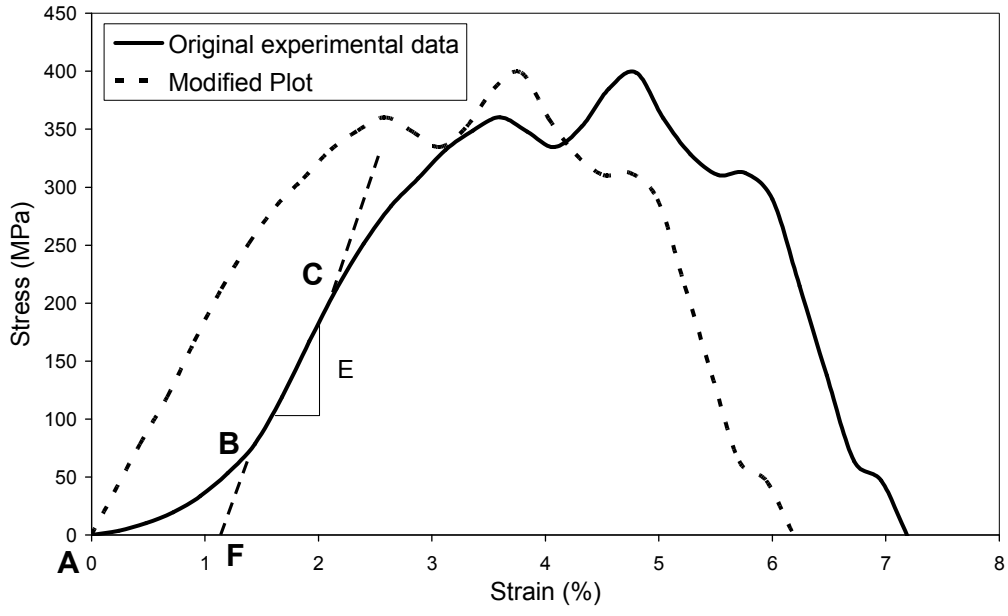

Figure 3-17. Comparison of original experimental stress-strain data and the modified curve with corrected zero strain point.

In some cases during dynamic compression loading the strain gauges failed at or just before the peak load. Therefore, the strain over the final stages of the test had to be extrapolated. This is illustrated in Figure 3-18 which shows the stress-strain curve obtained from the measured strain and the amended stress-stain curve obtained from extrapolated strain data.

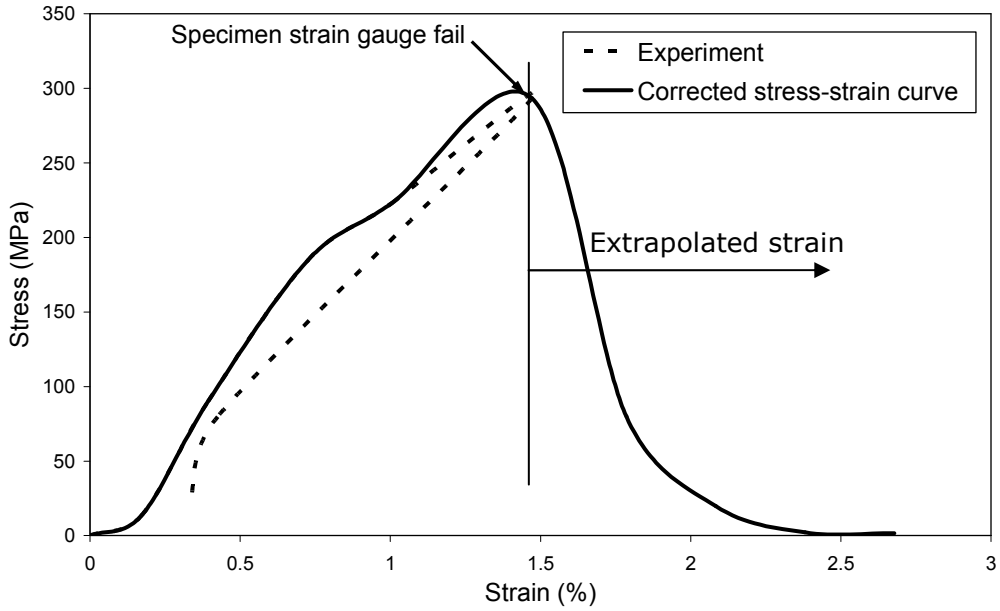

Figure 3-18. Comparison of typical dynamic compression stress-strain curve obtained from the measured strain with strain gauge failure occurring near peak load and the amended stress-stain curve with the extrapolated strain data.

3.3.1.2 Strain rate data

The effect of strain rate on the material modulus and strength under tensile, shear and compression loading, are assessed using a semi-logarithmic function defined by:

$$E_{RT} = E_0\left(1 + C_{RT}\ln\frac{\dot{\bar{\varepsilon}}}{\dot{\varepsilon}_0}\right) \quad \textbf{(3-2)}$$

$$S_{RT} = S_0\left(1 + C_{RT}\ln\frac{\dot{\bar{\varepsilon}}}{\dot{\varepsilon}_0}\right) \quad \textbf{(3-3)}$$

where S_{RT} are rate adjusted strengths, S_0 is the quasi-static strength, E_{RT} are rate adjusted modulii, E_0 is quasi-static modulii, $\dot{\bar{\varepsilon}}_0 = 1$ are reference strain rates and $\dot{\bar{\varepsilon}}$ are effective strain rates and C_{RT} are the strain rate constants.

The strain rate constants C_{RT} will be required as input data for a composite material model which is described in the next chapter.

3.3.1.3 Filtering noisy dynamic data

For the dynamic flexural tests, the high strain rate force-displacement results tended to exhibit high frequency oscillations due to vibration waves. Subsequently, all the dynamic force–displacement curves were filtered with a Butterworth filter at 600 Hz to increase data interpretation and readability. Figure 3-19 shows a comparison of the filtered and unfiltered force-displacement curves.

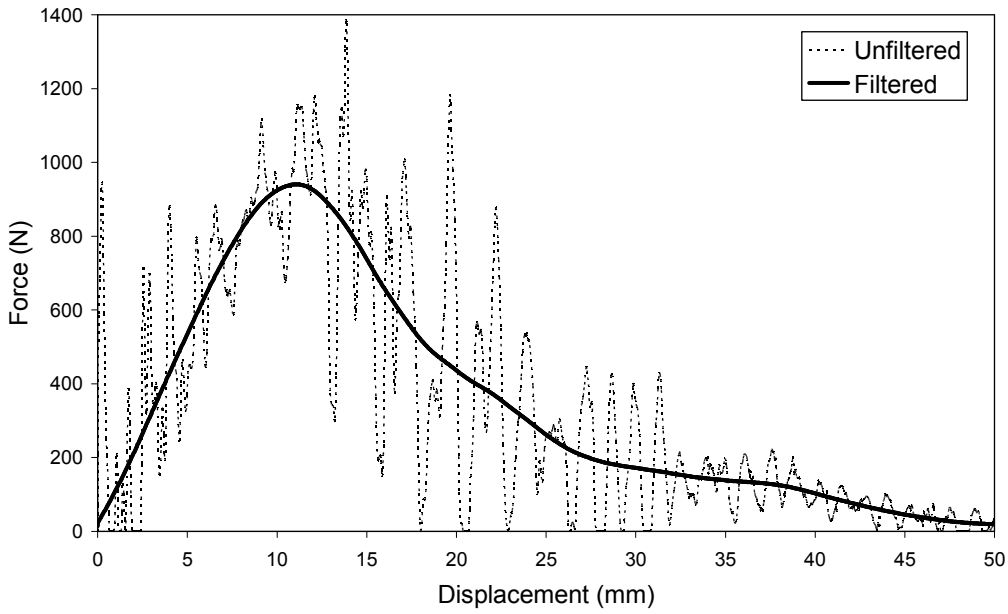

Figure 3-19. Typical filtered and unfiltered dynamic flexural force-displacement curves.

3.3.2 In-Plane Tensile Tests

3.3.2.1 Stress-strain response

Figure 3-20 shows the typical in-plane tensile stress-strain response for Twintex at different strain rates. Under quasi-static loading the stress-strain response is approximately linear elastic up to the maximum stress point followed by abrupt failure at a strain of 2.18%. At a strain rate of 36 s^{-1}, the initial stress-strain response leading up to the peak stress is relatively similar to the quasi-static results. However, in contrast, the post peak stress response is very ductile and almost perfectly plastic with a final failure strain that is 4 times higher than at the quasi-static rate. Final failure strain is defined here as the strain at which the material exhibits complete cross-sectional failure. In addition, it should be noted that at 36 s^{-1}, small oscillations developed in the stress-strain plot between 175 MPa and the peak load (267 MPa) which did not result in any significant deviation in the curve but indicates the initiation of damage in the matrix.

At higher strain rates, between 50 and 70 s^{-1}, the material stress-strain response is non-linear with premature yielding followed by strain hardening and then maximum peak stress and strain softening. In addition, the final failure strain is 3 times larger than the quasi-static result.

3.3.2.2 Strain rate effect

The tensile modulus and strength properties at different strain rates are presented in Table 3-1. Figure 3-21 and Figure 3-22 illustrate the effect of strain rate on the tensile modulus and strength, respectively. The results suggest that the tensile modulus and strength are relatively insensitive to increases in strain rate up to 36 s^{-1}. However, at higher strain rates the tensile modulus and strength significantly increased. At the highest strain rate (70 s^{-1}), the increase in the tensile modulus was 11% above the quasi-static value, while that of the tensile strength exhibited a significant 46% increase.

3.3.2.3 Damage mechanisms

Macroscopic analysis

Photographs of the post test tensile specimens for quasi-static and high strain rates are shown in Figure 3-23 (a) – (d). Under quasi-static loading damage occurred around a localised through-thickness shear fracture plane with an angle of about 45° to the axis of loading. The quasi-static macroscopic damage mechanisms generally included matrix cracking, localised warp fibre fracture, weft fibre pull-out, and delamination along the middle plies.

At high strain rates, there is extensive macroscopic damage along the entire specimen gauge area. The dominant failure modes again include matrix cracking, warp fibre fracture, weft fibre pull-out, and delamination along all ply interfaces.

Microscopic analysis

Optical micrographs of the damage region in the fractured tensile specimens at quasi-static strain rates are shown in Figure 3-24 (a)–(c). Matrix cracking was observed in the weft fibre bundles as depicted in Figure 3-24 (b). These cracks propagate in an opening mode normal to the in-plane axis due to normal stresses acting in the direction of the applied load. Some of these cracks propagate towards the tow interfaces resulting in interfacial debonding and interply delamination as shown in Figure 3-24 (c). Similar damage mechanisms were observed in the fracture region of the post test specimens at the highest strain rate of 70 s^{-1} as shown Figure 3-25 (a)–(b). Figure 3-25 (a) shows delamination occurring along all plies while matrix fracture in the weft fibre bundles is depicted in Figure 3-25 (b).

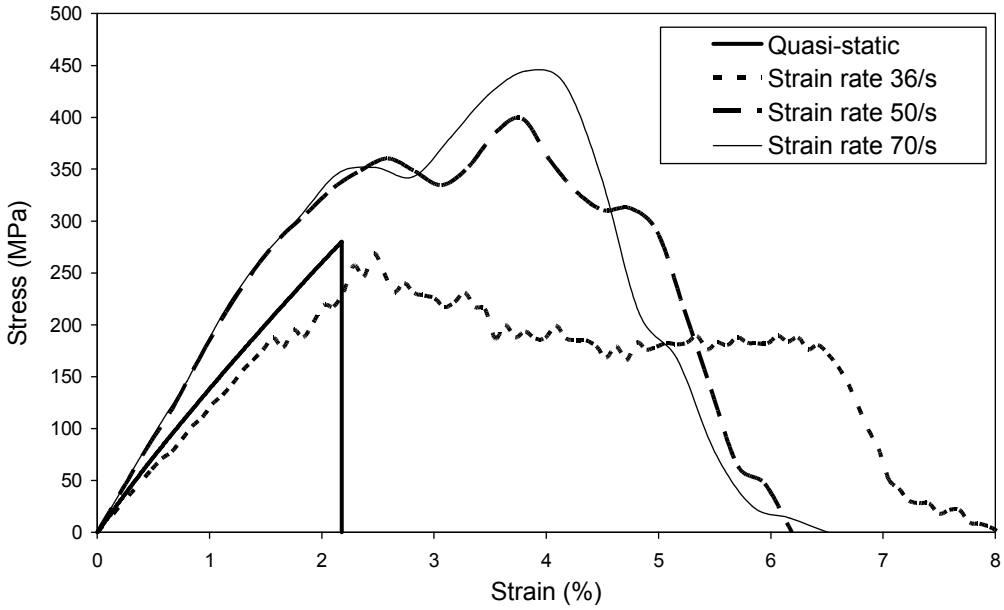

Figure 3-20. Typical in-plane tensile stress-strain curves for Twintex at quasi-static and high strain rates.

Table 3-1. In-plane tensile modulus and strength for Twintex at quasi-static and high strain rates.

Strain Rate (s^{-1})	Tensile Modulus (GPa)	Tensile Strength (MPa)
Quasi-static	14.46	269.03
36	13.19	266.75
50	17.51	382.40
70	16.08	391.88

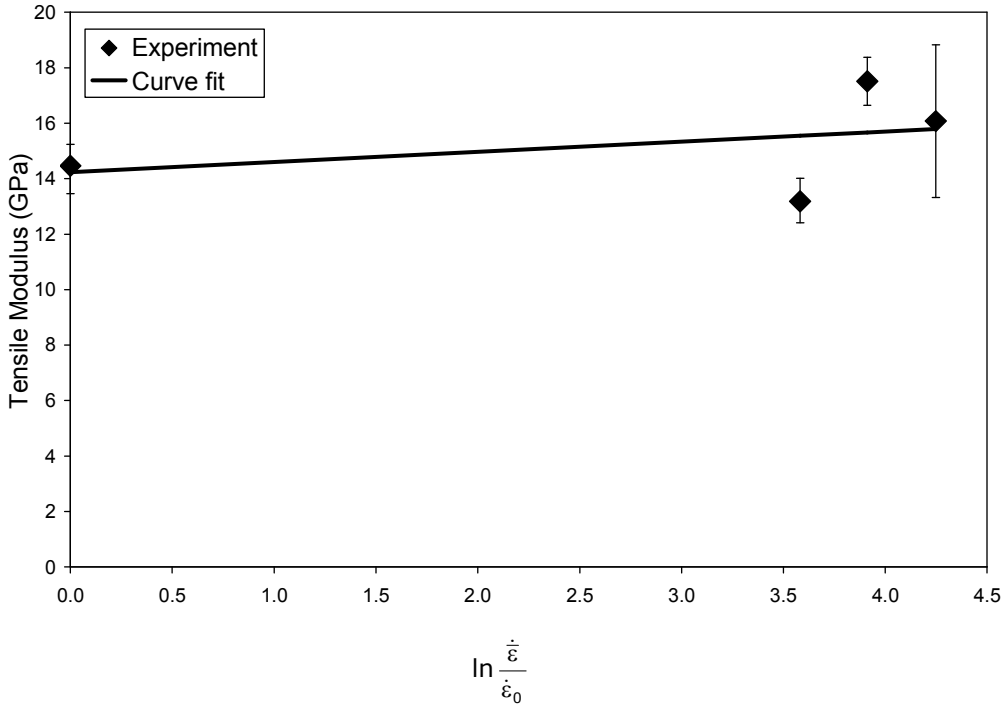

Figure 3-21. The strain rate effect on the in-plane tensile modulus of Twintex.

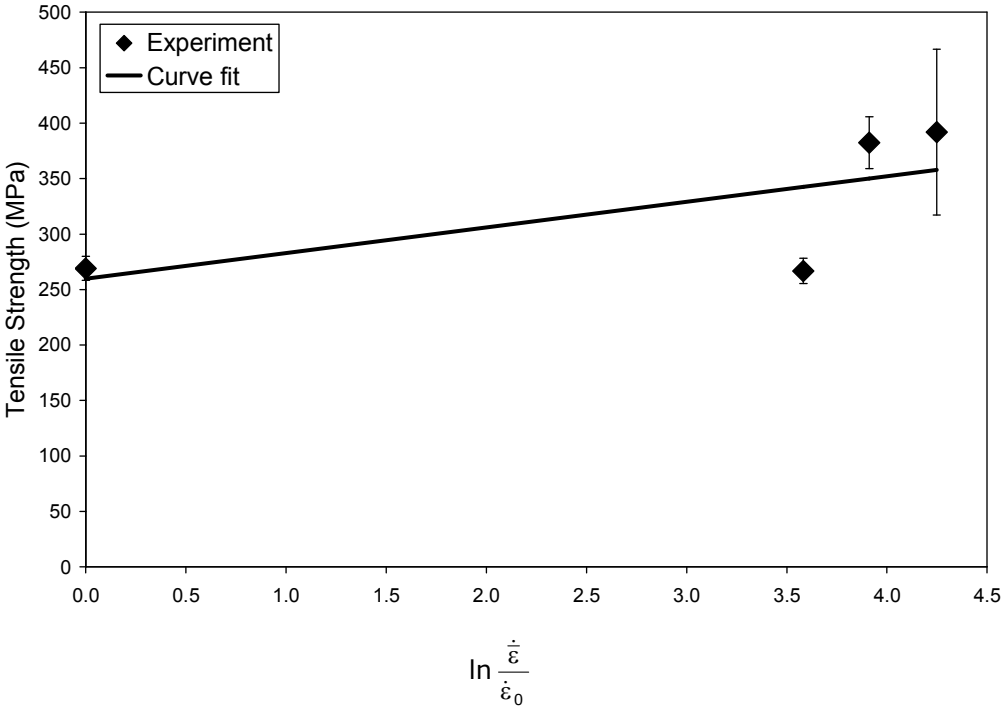

Figure 3-22. The strain rate effect on the in-plane tensile strength of Twintex.

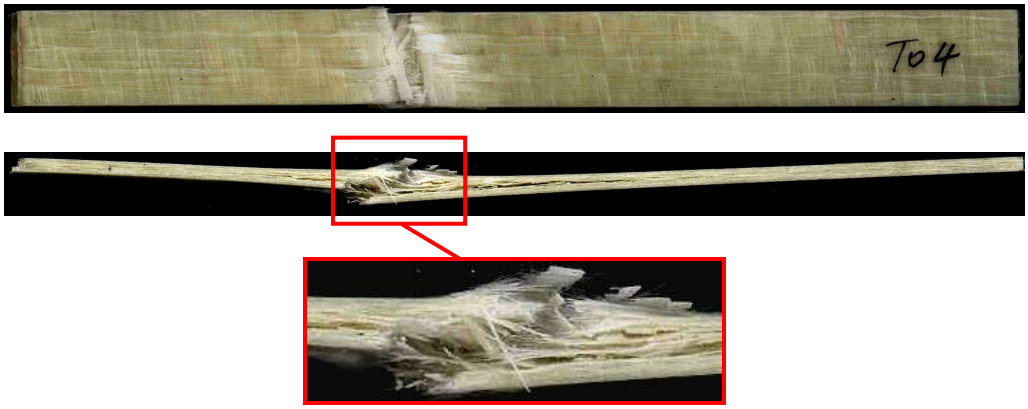

(a)

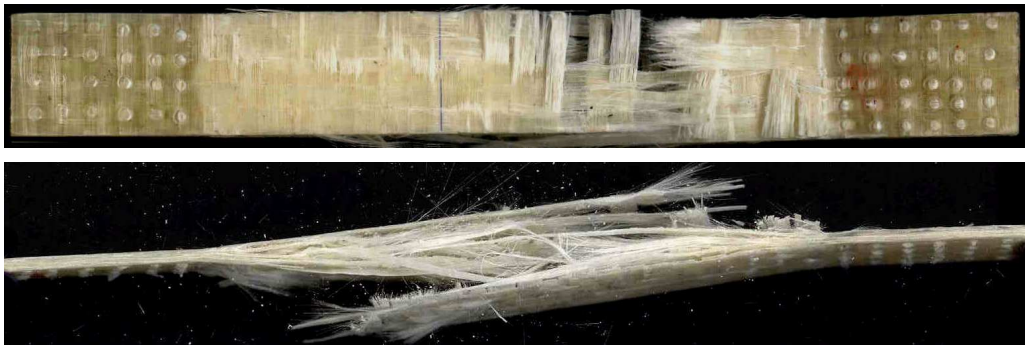

(b)

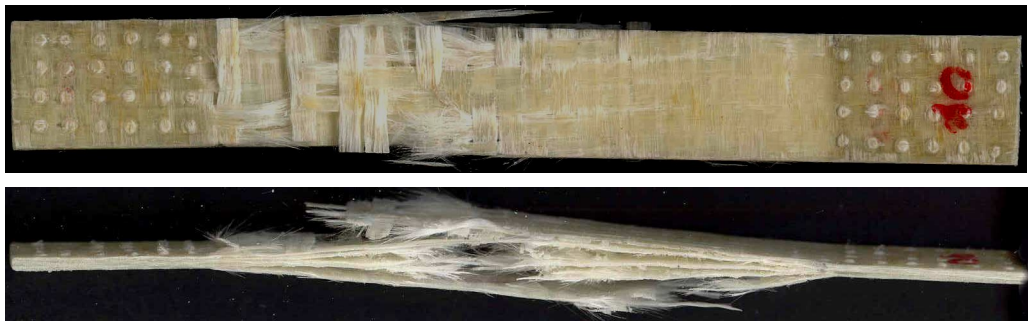

(c)

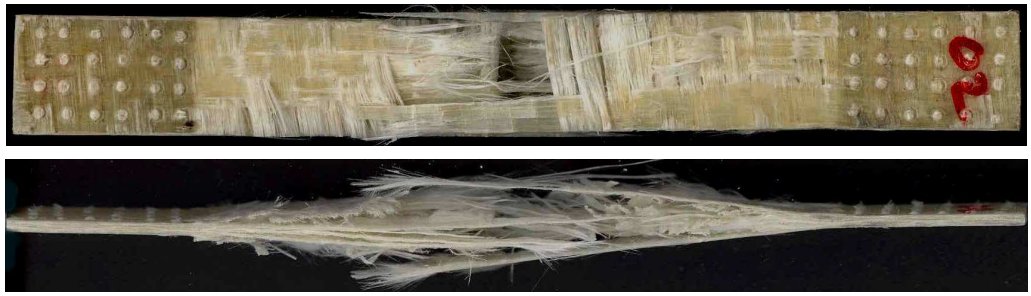

(d)

Figure 3-23. Photograph of the damage regions in in-plane tensile test specimens (a) quasi-static (b) 35 s^{-1} (c) 50 s^{-1} (d) 70 s^{-1}.

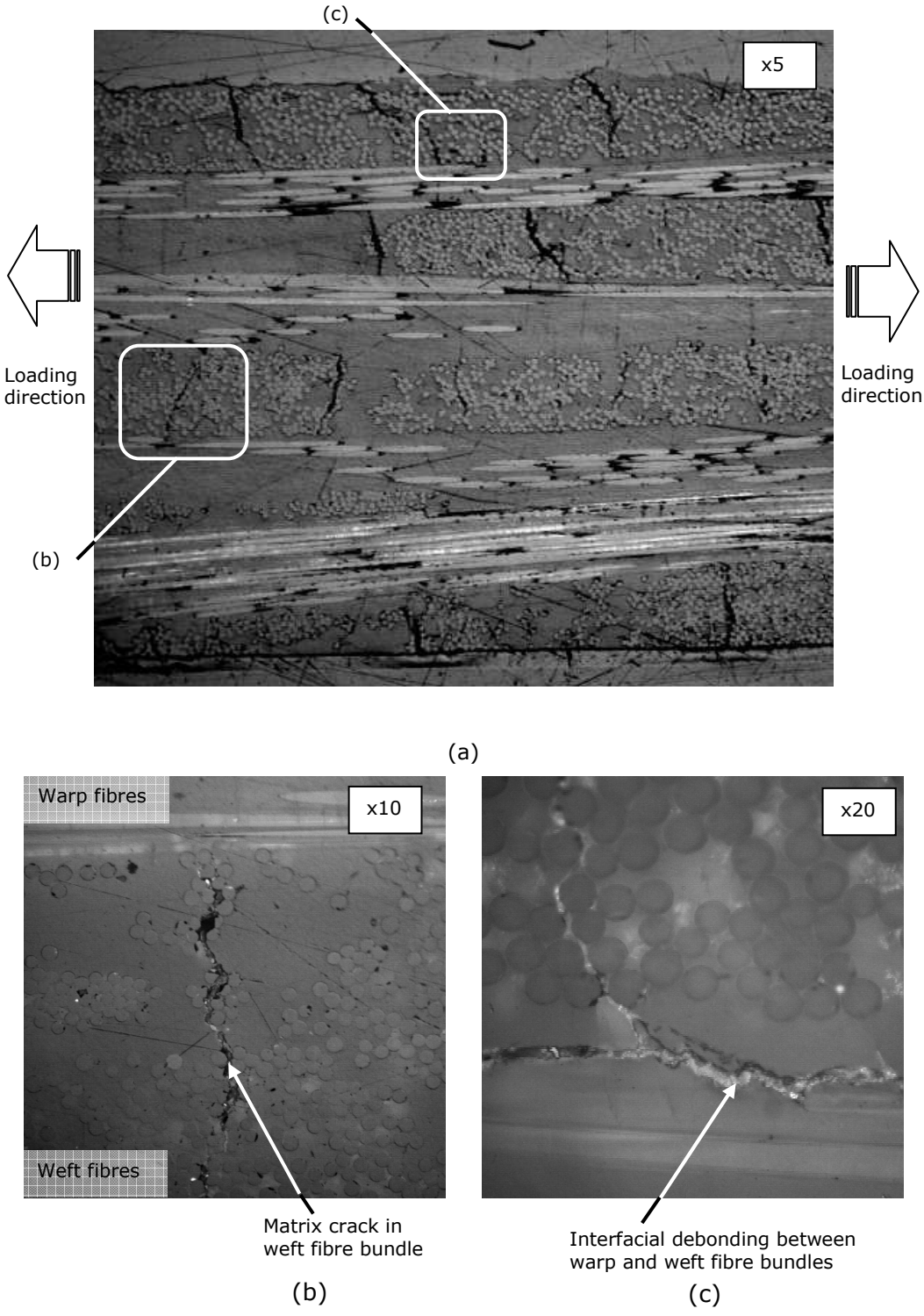

Figure 3-24. Optical micrograph of the quasi-static in-plane tensile specimen fracture zone (a) micrograph of fracture zone (x5) (b) detailed view showing matrix crack in weft bundle (x10) (c) detailed view showing interfacial debonding between warp and weft fibre bundles (x20).

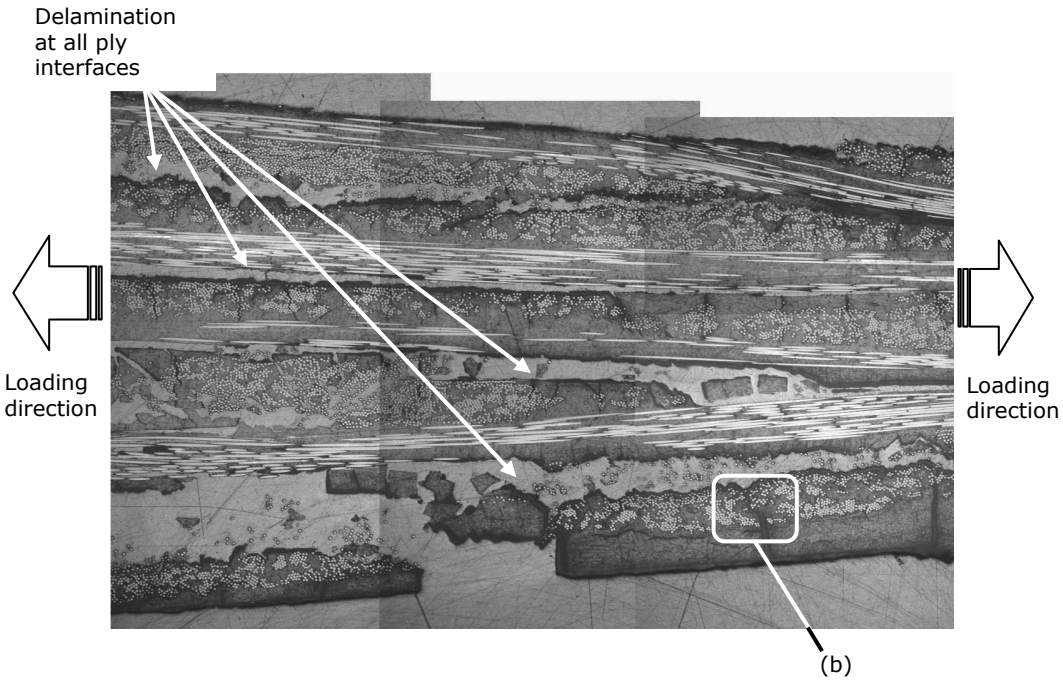

(a)

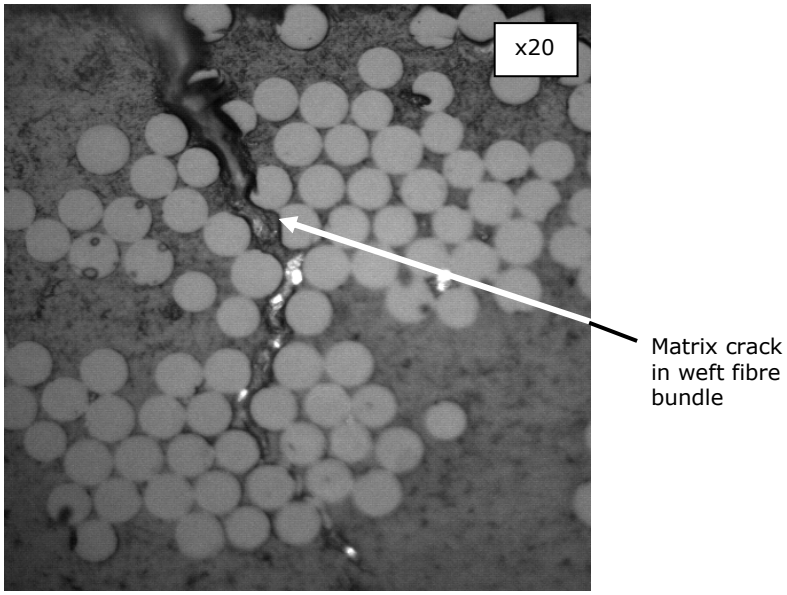

(b)

Figure 3-25. Optical micrograph of dynamic in-plane tensile specimen fracture zone at highest strain rate of 70 s^{-1} (a) micrograph of fracture zone (b) detailed view showing transply matrix crack in weft fibre bundle (x20).

3.3.3 In-Plane Shear Tests

3.3.3.1 Stress-strain response

Typical shear stress-strain plots for quasi-static and high strain rate loading ranges are shown in Figure 3-26. Under quasi-static loading the material exhibits a non-linear hardening stress-strain response over a large strain range followed by abrupt failure at a shear strain of 13.8%. At high strain rates, the response is initially elastic followed by yielding, steep strain hardening to peak stress and strain softening.

3.3.3.2 Strain rate effects

The in-plane shear modulus and strength properties at different strain rates are presented in Table 3-2. The effect of strain rate on the in-plane shear modulus is depicted in Figure 3-27. The average shear modulus dramatically decreased by 82% between the quasi-static and 33 s^{-1} strain rates. Following this significant decrease, the modulus appears to have reached a threshold and exhibits very little sensitivity to increasing strain rate between 33 and 91 s^{-1}.

Figure 3-28 shows the effect of strain rate on the in-plane shear strength. It should be noted that in this study, the quasi-static shear strength was taken at the 5% shear strain point as recommended by the ASTM standard [270] while at high strain rates the shear strength was taken at the peak stress point. The average shear strength decreased by 47% between quasi-static and 33 s^{-1} strain rates. However, at higher strain rates above 33 s^{-1}, the shear strength exhibited a marginal average decrease of 8% below the quasi-static values. Overall, the results suggest that the shear strength decreases as strain rates increases. However, it should be noted that there is significant data scatter and for shear strength, the quasi-static values lie within the scatter band of the values obtained at the highest strain rates.

3.3.3.3 Damage mechanisms

Macroscopic analysis

Photographs of the post test in-plane shear specimens for quasi-static and high strain rates are shown in Figure 3-29. For both the quasi-static and high strain rate specimens, the major macroscopic failure modes were matrix cracking, fibre pull-out, fibre bundle pull-out and delamination. Under quasi-static loading, fibre reorientation (scissoring) in the direction of the applied load was observed.

Microscopic analysis

Optical micrographs of the damage region in a quasi-static in-plane shear specimen are shown in Figure 3-30 (a)–(b). Transply matrix cracks were observed along with delamination. Figure 3-31 (a)–(b) shows the micrographs for a fractured in-plane shear specimen at the highest strain rate of 91 s^{-1}. The failure mechanisms are similar to the quasi-static observations.

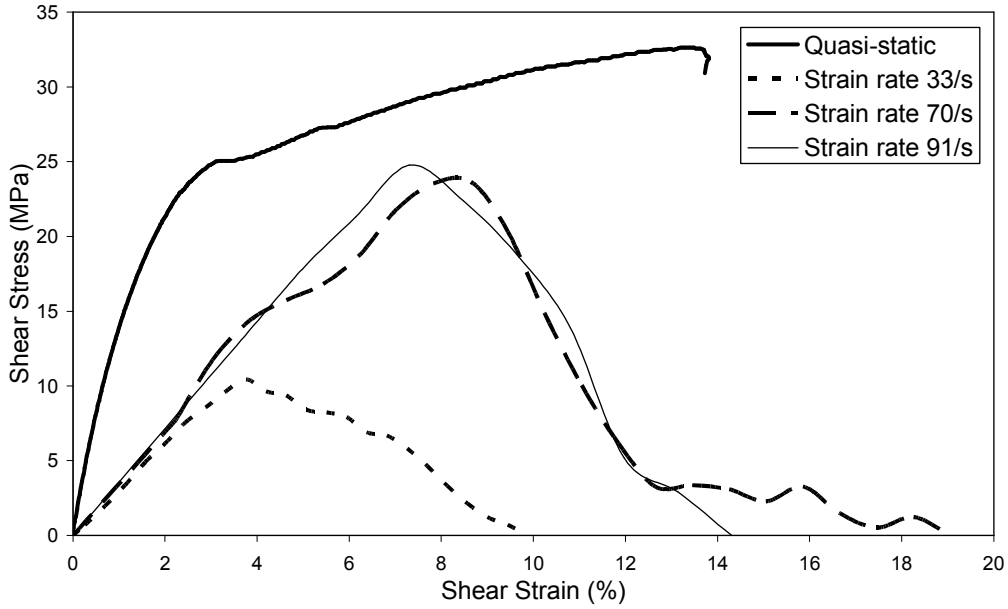

Figure 3-26. Typical in-plane shear stress-strain curves for Twintex at quasi-static and high strain rates.

Table 3-2. In-plane shear modulus and strength for Twintex at quasi-static and high strain rates.

Strain Rate (s^{-1})	In-plane Shear Modulus (GPa)	In-plane Shear Strength (MPa)
Quasi-static	1.79	26.79
33	0.33	14.10
70	0.47	25.12
91	0.22	24.17

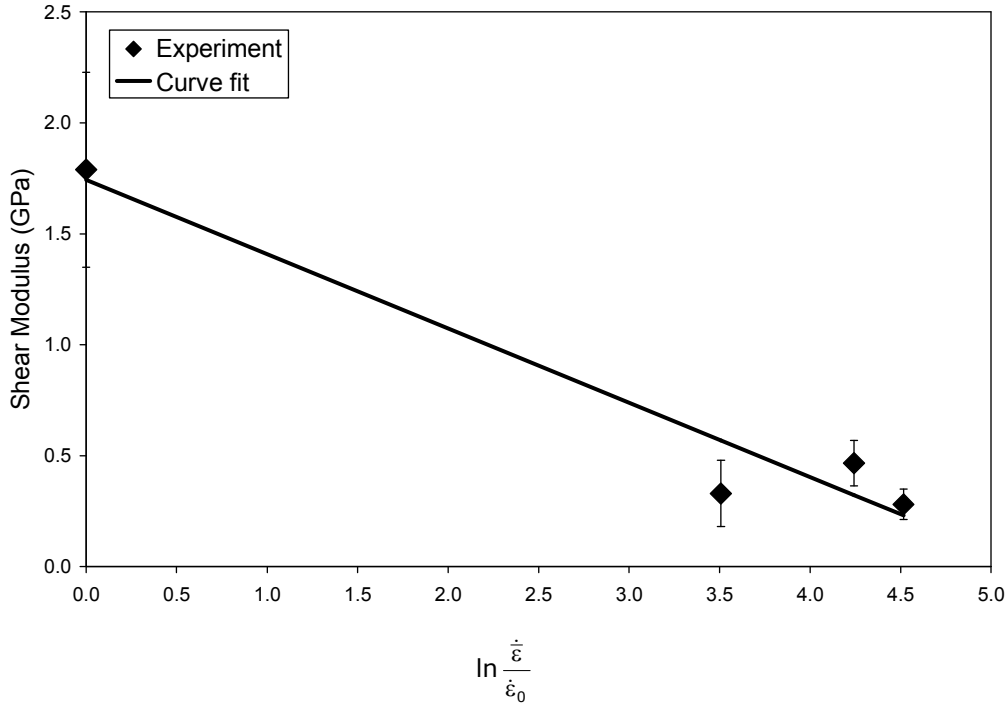

Figure 3-27. The strain rate effect on the in-plane shear modulus of Twintex.

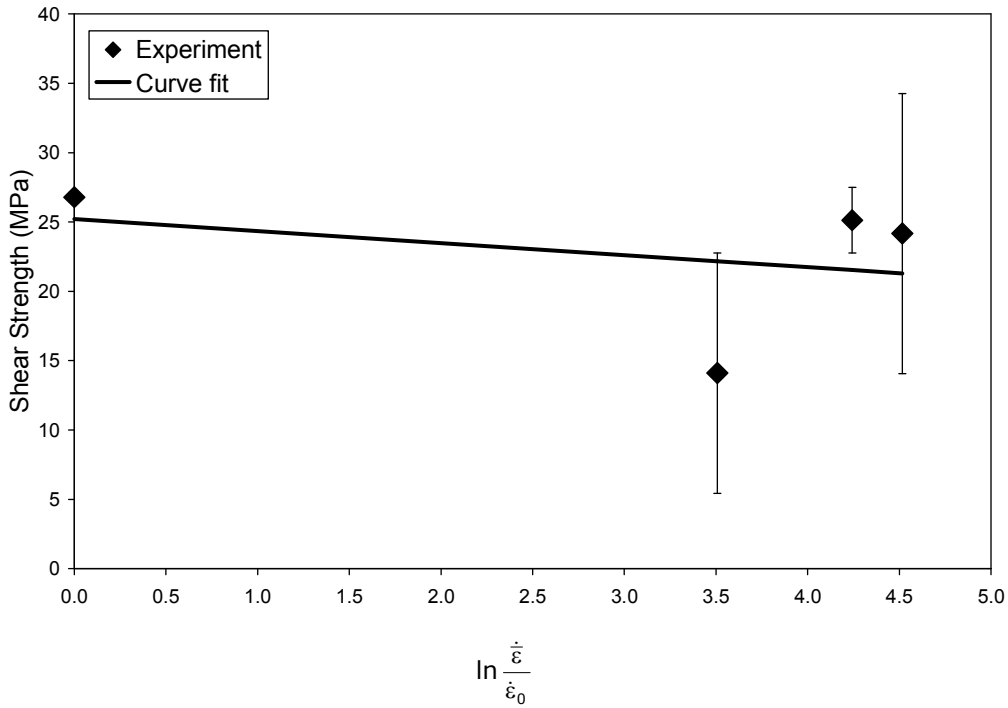

Figure 3-28. The strain rate effect on the in-plane shear strength of Twintex.

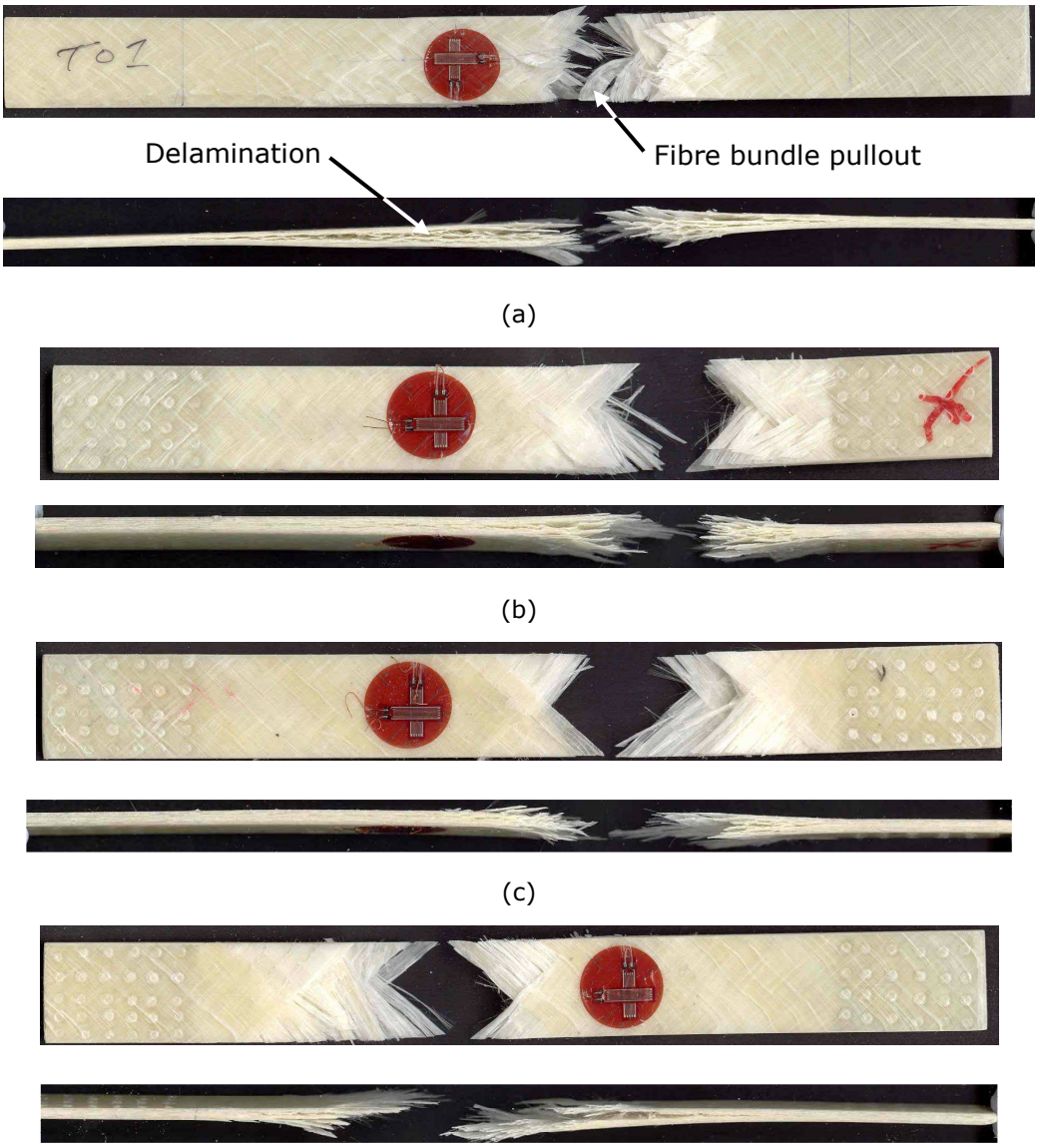

Figure 3-29. Photograph of the damage regions in in-plane shear test specimens (a) quasi-static (b) 33 s^{-1} (c) 70 s^{-1} (d) 91 s^{-1}.

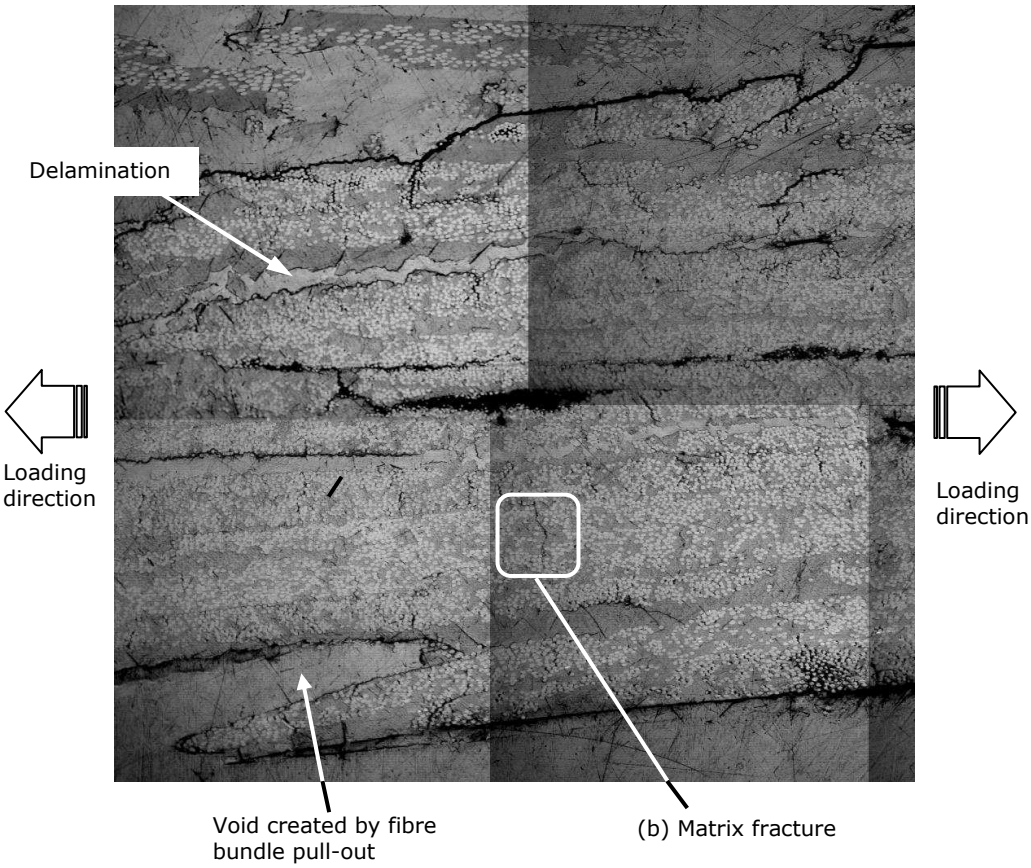

(a)

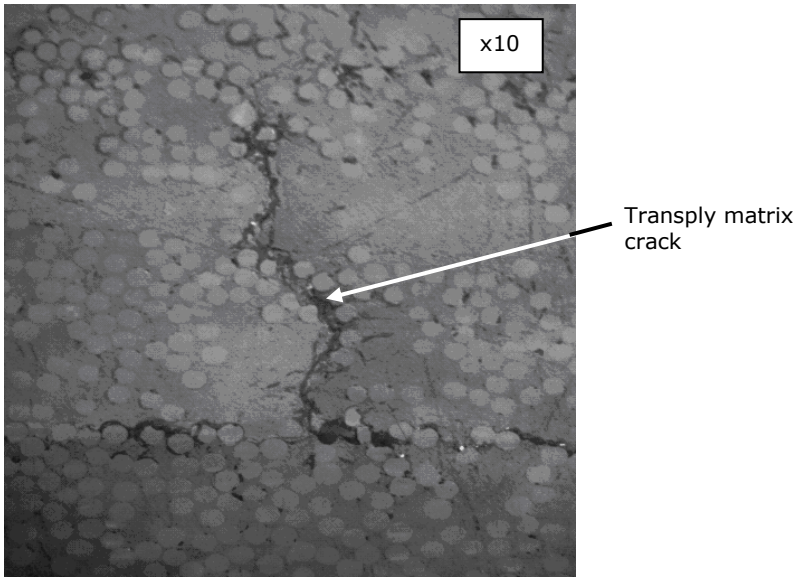

(b)

Figure 3-30. Optical micrograph of quasi-static in-plane shear specimen fracture zone (a) micrograph of fracture zone (b) detailed view showing transply matrix crack (x10).

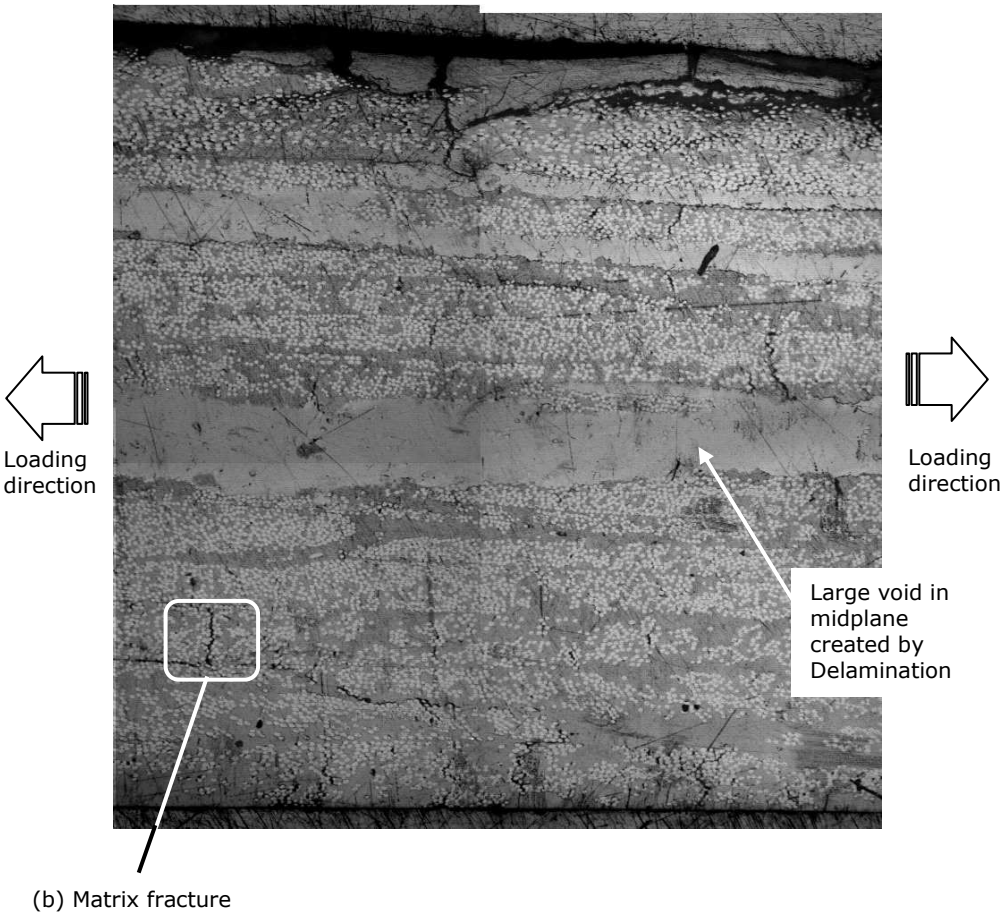

(a)

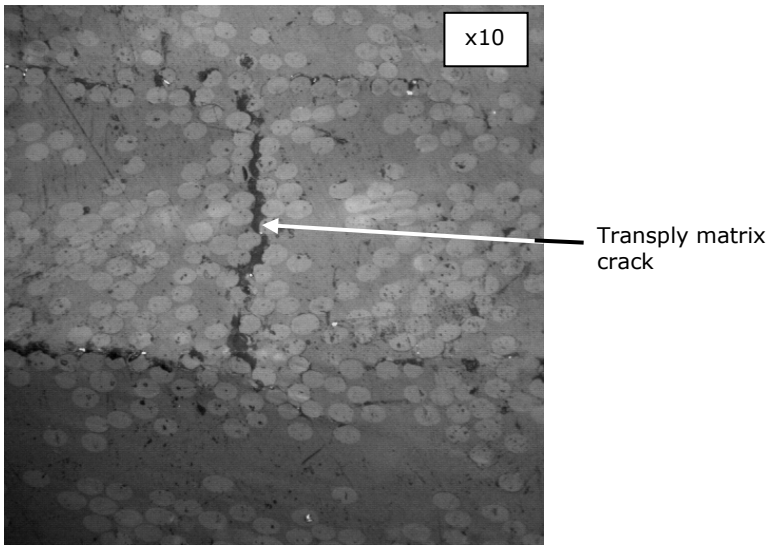

(b)

Figure 3-31. Optical micrograph of in-plane shear specimen fracture zone at highest strain rate of 91 s^{-1} (a) micrograph of fracture zone (b) detailed view showing transply matrix crack (x10).

3.3.4 In-Plane Compression Tests

3.3.4.1 Stress-strain response

Figure 3-32 shows the typical stress-strain response for Twintex at different strain rates. Under quasi-static loading, the material response is approximately linear elastic up to the maximum stress point followed by abrupt failure. The high strain rate stress-strain response was characterised by an initial elastic region, then yielding followed by a steep hardening up to the peak stress and post-failure softening.

3.3.4.2 Strain rate effects

The in-plane compression modulus and strength properties at different strain rates are presented in Table 3-3. The effect of strain rate on the compression modulus is shown in Figure 3-33. The average compression modulus increased by a dramatic 128% between quasi-static and 56 s^{-1} strain rates and remained relatively constant as strain rate increased with all the high strain rate values lying within the dynamic experimental scatter band.

Figure 3-34 shows the effect of strain rate on the compression strength. The average compression strength increased by a significant 78% between quasi-static and 56 s^{-1} strain rates. At the highest strain rate (126 s^{-1}) the compressive strength increased by 86% over the quasi-static value.

3.3.4.3 Damage mechanisms

Macroscopic analysis

Photographs of the failure regions of the compression specimens for quasi-static and high strain rates are shown in Figure 3-35. The failure mode of the specimens under both quasi-static and high strain rates are relatively similar; although greater damage occurred at high strain rates. Failure was primarily by localised through-thickness shear. In addition, at high strain rates delamination (splitting) was also observed in the outer plies. The orientation of the shear failure bands range from 36° to 55° for all specimens inspected, with the average angle being 48°.

Microscopic analysis

Optical micrographs of the damage region in the fractured compression specimens at quasi-static strain rates are shown in Figure 3-36 (a)–(c). Figure 3-36 (a) shows fibre micro buckling which leads to fibre kinking followed by failure of the fibres and matrix through the thickness of the specimen along a distinct shear band fracture plane. A detailed view of through thickness shear failure in the fibres and matrix is shown in Figure 3-36 (b). Figure 3-36 (c) shows a high magnification SEM fractograph of shear failure in the fibres.

Similar damage mechanisms were observed in the fracture region of the post test compression specimens at the highest strain rate of 126 s^{-1}, as shown in Figure 3-37. Figure 3-37 shows extensive delamination occurring in the outer plies which is due in part to continued displacement of the impactor after specimen failure.

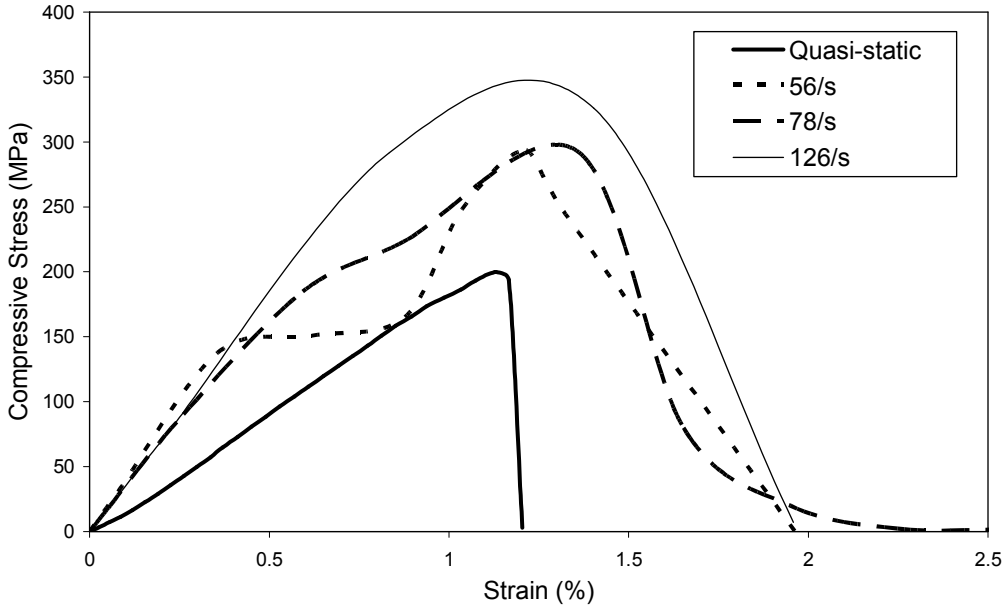

Figure 3-32. Typical in-plane compression stress-strain curves for Twintex at quasi-static and high strain rates.

Table 3-3. In-plane compression modulus and strength for Twintex at quasi-static and high strain rates.

Strain Rate (s^{-1})	Compression Modulus (GPa)	Compression Strength (MPa)
Quasi-static	14.55	178.14
56	33.30	317.27
78	36.09	316.29
126	28.35	333.08

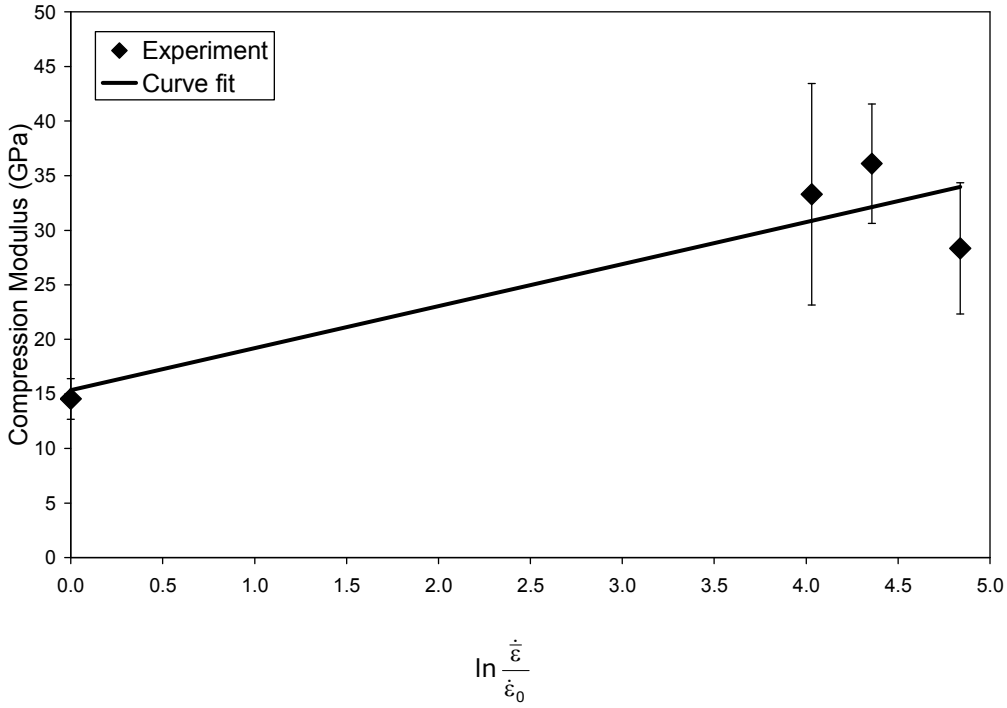

Figure 3-33. The strain rate effect on the in-plane compression modulus of Twintex.

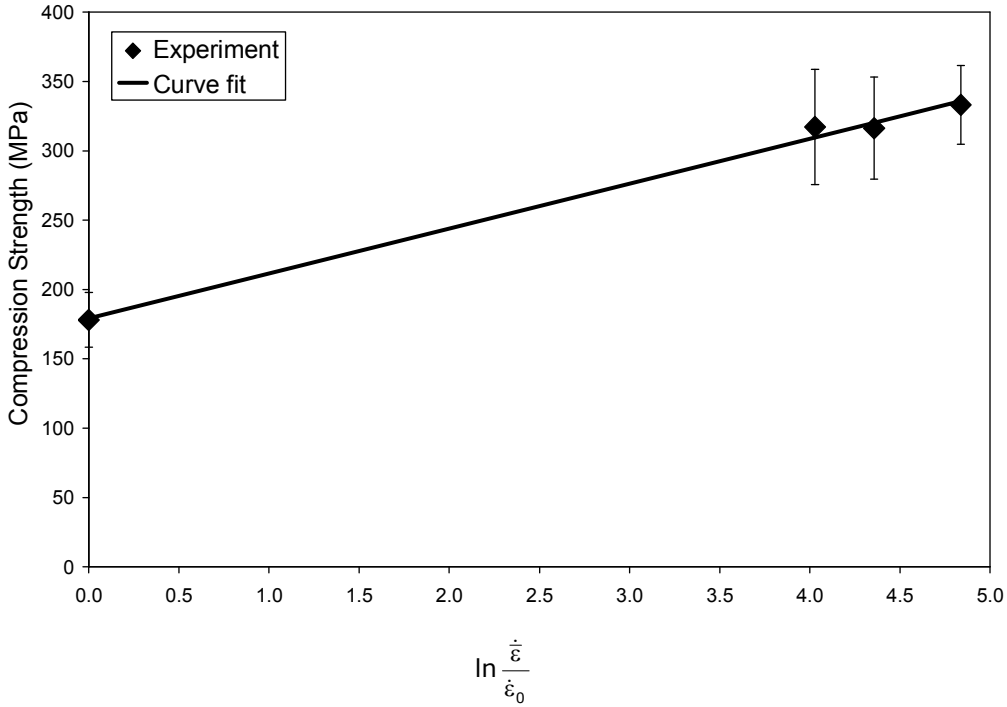

Figure 3-34. The strain rate effect on the in-plane compression strength of Twintex.

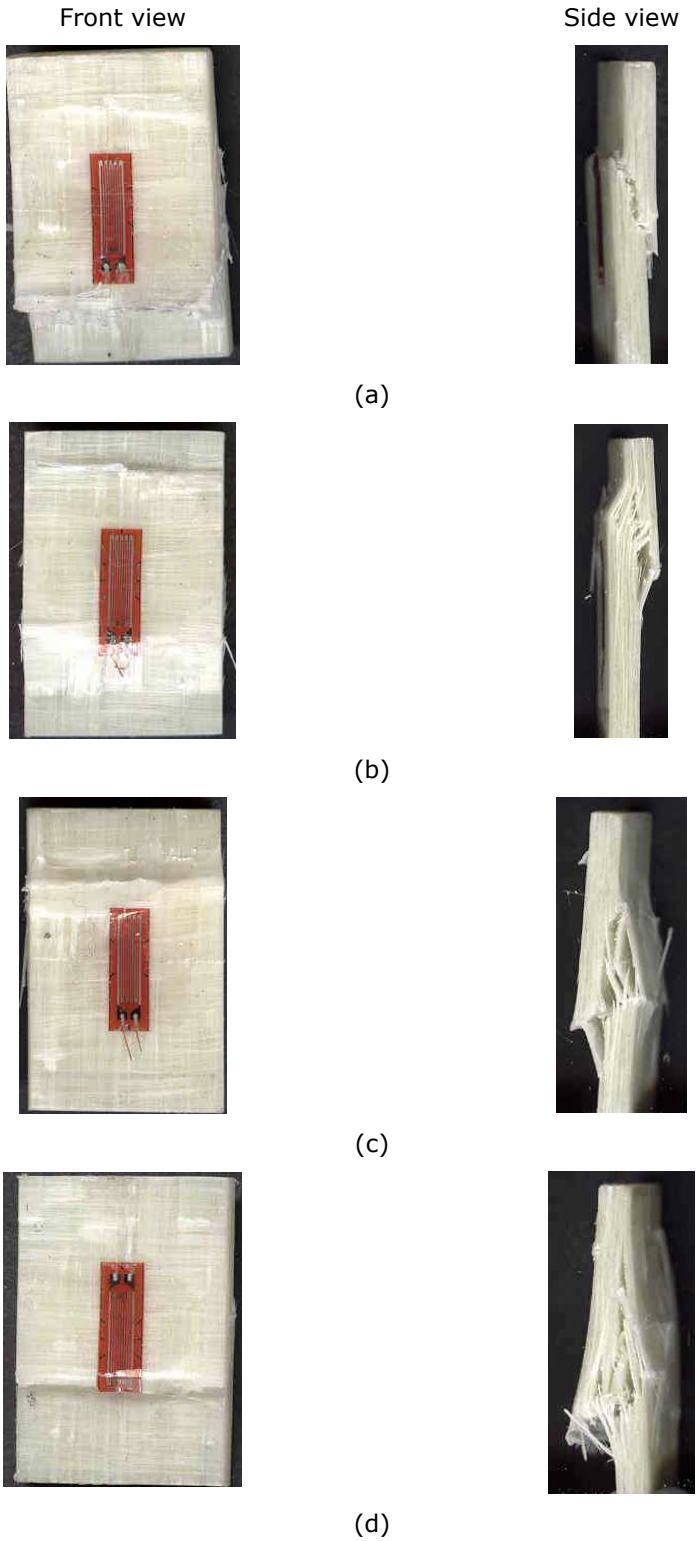

Figure 3-35. Photograph of the damage regions for in-plane compression test specimens (a) quasi-static (b) 56 s^{-1} (c) 78 s^{-1} (d) 126 s^{-1}.

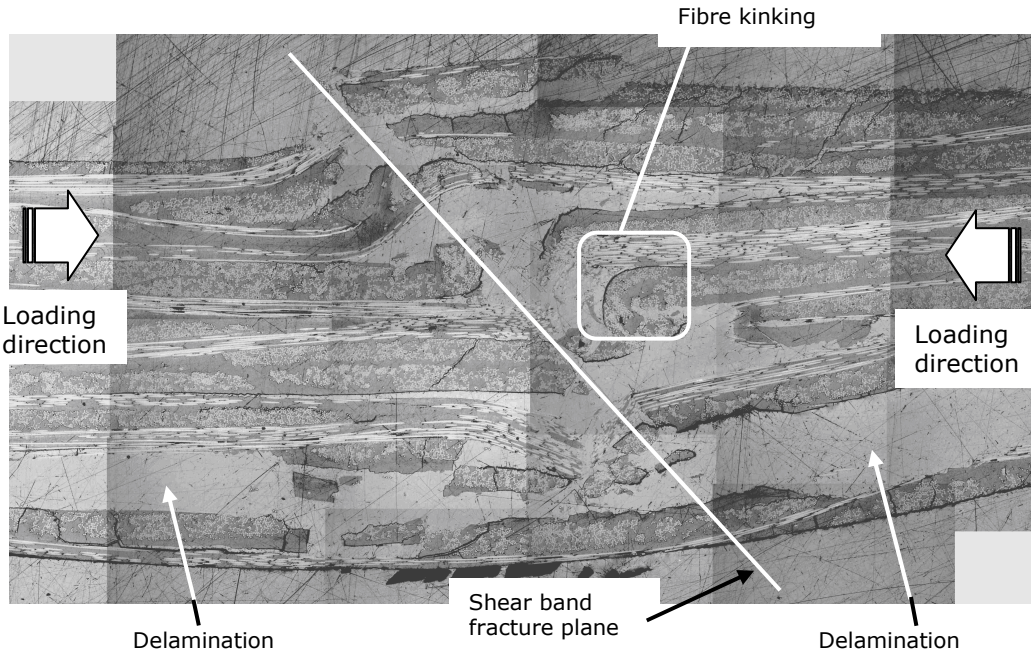

(a)

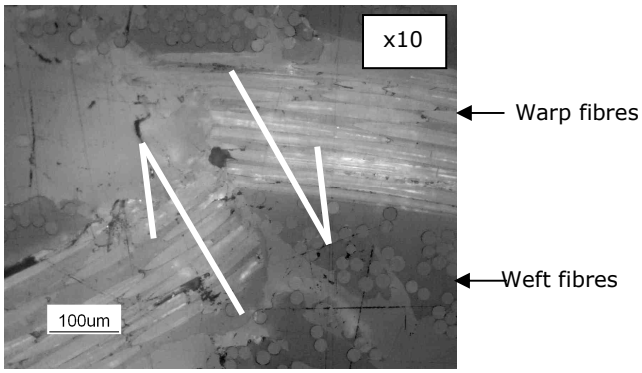

(b)

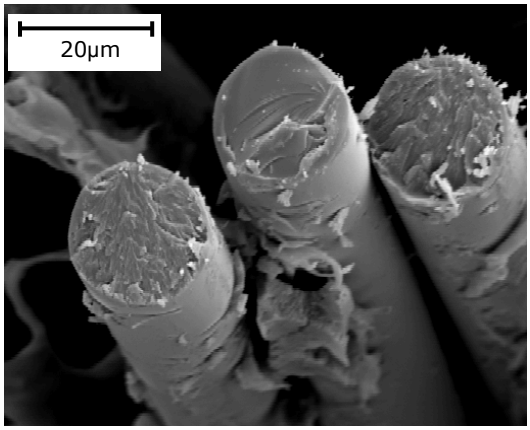

(c)

Figure 3-36. Optical micrograph of in-plane compression specimen fracture zone at quasi-static strain rate (a) micrograph of fracture zone (b) detailed view showing through-thickness shear failure in fibres and matrix (x10) (c) SEM image of fibre shear failure.

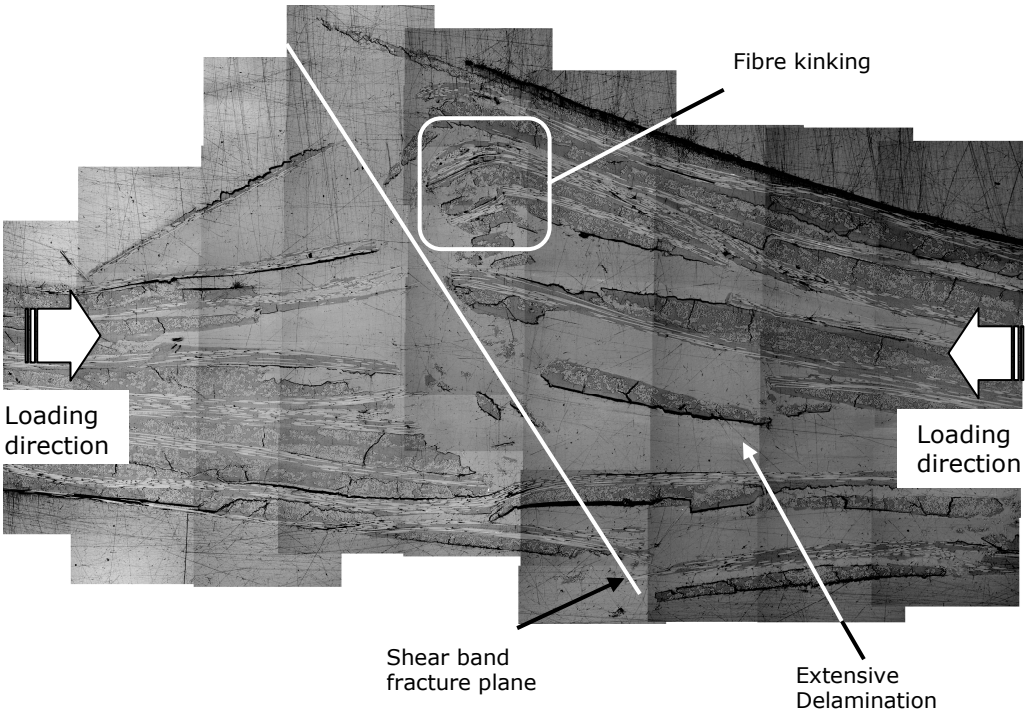

Figure 3-37. Optical micrograph of in-plane compression specimen fracture zone at the highest strain rate of 126 s^{-1}.

3.3.5 Through-Thickness Shear Tests

3.3.5.1 Stress-strain response

Six repeats of the test were carried out so as to evaluate the repeatability and consistency of the test method. The through-thickness shear stress-strain curves are shown in Figure 3-38. The shear stress-strain plot shows an initial elastic response with a nonlinear deviation prior to the peak load followed by a gradual softening. The average through-thickness shear strength was calculated to be 111 MPa.

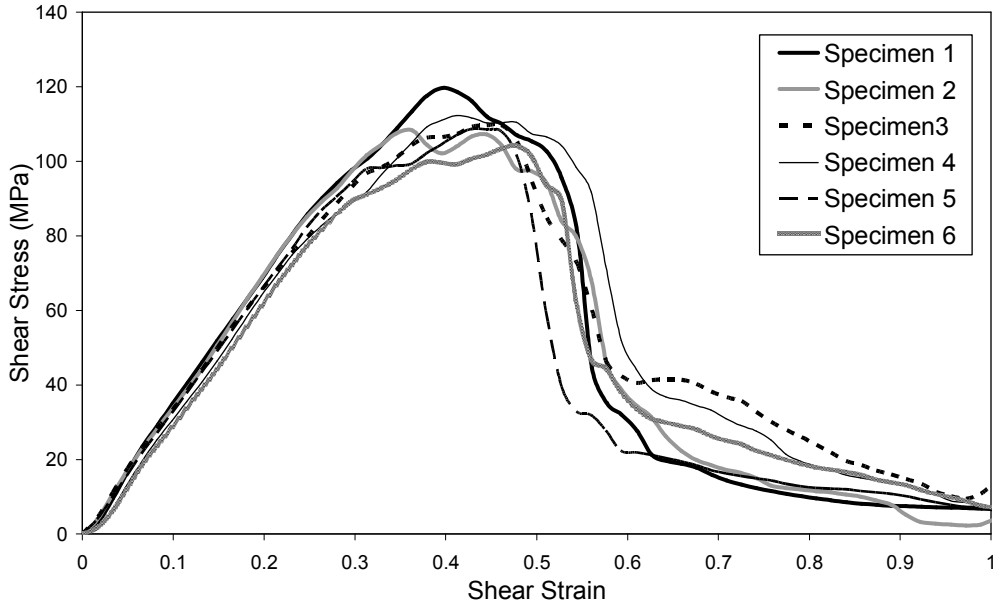

Figure 3-38. Through-thickness shear stress-strain curves for Twintex under quasi-static loading.

3.3.5.2 Damage mechanisms

Macroscopic analysis

The post test specimen shows a cleanly punched hole with a cylindrically shaped plug, and only minimal damage around the sheared faces as shown in Figure 3-39 (a).

Microscopic analysis

An optical micrograph of the fracture zone is depicted in Figure 3-39 (b). The damage zone is confined to a very narrow area close to the fracture surface. A relatively clean shear edge is observed in the top plies; however, the shear edge becomes jagged in the bottom plies. A few matrix cracks are observed in the weft fibre bundles of the top plies.

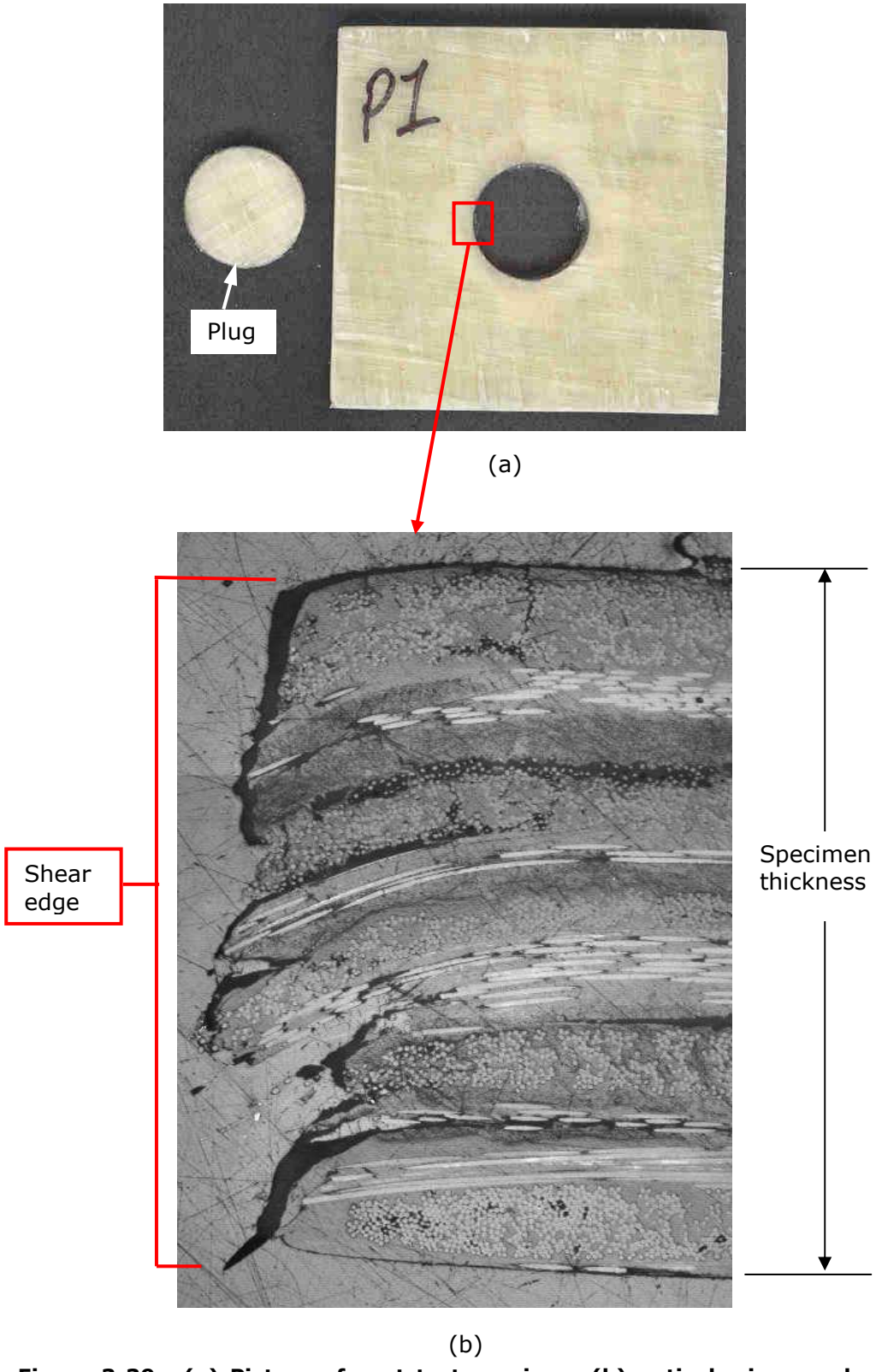

Figure 3-39. (a) Picture of post test specimen (b) optical micrograph of the fracture zone.

3.3.6 Flexural Tests

3.3.6.1 Force-displacement response

Figure 3-41 (b) shows the force-displacement curves for Twintex at quasi-static and dynamic test speeds. The dynamic plots are filtered as described in Section 3.3.1.3. In all cases, the curves are almost linear elastic up to the peak load, followed by gradual softening. For the quasi-static test, after the peak load there is a brief ductile softening, followed by an abrupt load drop which corresponds with tensile fibre failure in the bottom plies.

3.3.6.2 Strain rate effects

The flexural modulus and strength were calculated from the force and displacement data using the bending equations presented in BS 14125 [273]. Table 3-4 lists the flexural modulus and strength as a function of impact speed. The flexural modulus remains relatively constant and appears to be insensitive to increasing strain rate. The flexural strength at 3 ms^{-1} was 10% higher than for the quasi-static loading case. Further increase in the impact speed had a negligible effect as the flexural strength remained almost constant for dynamic impact speeds that were applied in this study.

3.3.6.3 Damage mechanisms

Macroscopic analysis

Photographs of the failure regions of the flexural specimens for quasi-static and dynamic loading are shown in Figure 3-40. Compression fibre fracture is observed in the top plies while tensile fibre fracture occurs in the bottom plies. All the damage occurs directly under the impactor. Limited delamination is also observed in the dynamic specimens.

Figure 3-41 (a) shows photographs of progressive deformation of the quasi-static flexural test specimen. High speed camera footage of the progressive deformation of the dynamic flexural test specimen at 7 ms^{-1} is shown in Figure 3-41 (c).

Microscopic analysis

Optical micrographs of the fracture zone for the quasi-static flexural specimen are shown in Figure 3-42 (a)–(c). Figure 3-42 (a) shows that fibre micro buckling leading to kinking and compression fibre failure in the top plies. Figure 3-42 (b) indicates that fibre compression failure also occurs in the plies near the mid plane. Matrix cracks occur in the weft fibre bundles in the bottom plies as depicted in Figure 3-42 (c).

Figure 3-43 (a) – (c) shows an optical micrograph of the fracture zone of a flexural specimen at the highest impact speed which shows similar failure modes to the quasi-static specimen. However, more extensive delamination is observed in the high impact speed specimen. Figure 3-43 (b) shows a detailed view of matrix cracks in the bottom plies. A detailed view of tensile fracture of the warp fibres in the bottom plies is shown in Figure 3-43 (c).

Table 3-4. Flexural modulus and strength for Twintex at quasi-static and dynamic impact speeds

Test Speed (ms^{-1})	Flexural Modulus (GPa)	Flexural Strength (MPa)
$8.33x10^{-5}$	8.93	256
3	8.10	284
5	7.43	284
7	7.36	282

(a)

(b)

(c)

(d)

Figure 3-40. Photograph of failure region in the centre of the flexural post-test specimens (a) quasi-static (b) 3 ms^{-1} (c) 5 ms^{-1} (d) 7 ms^{-1}.

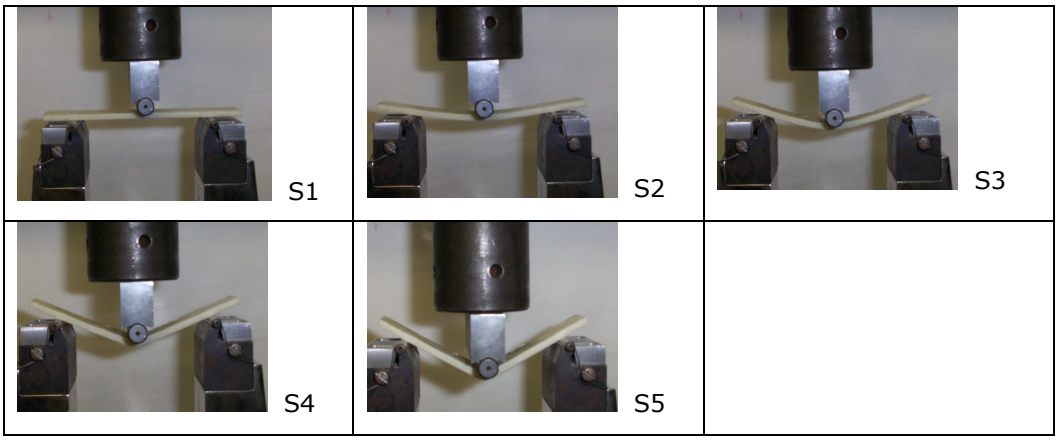

(a)

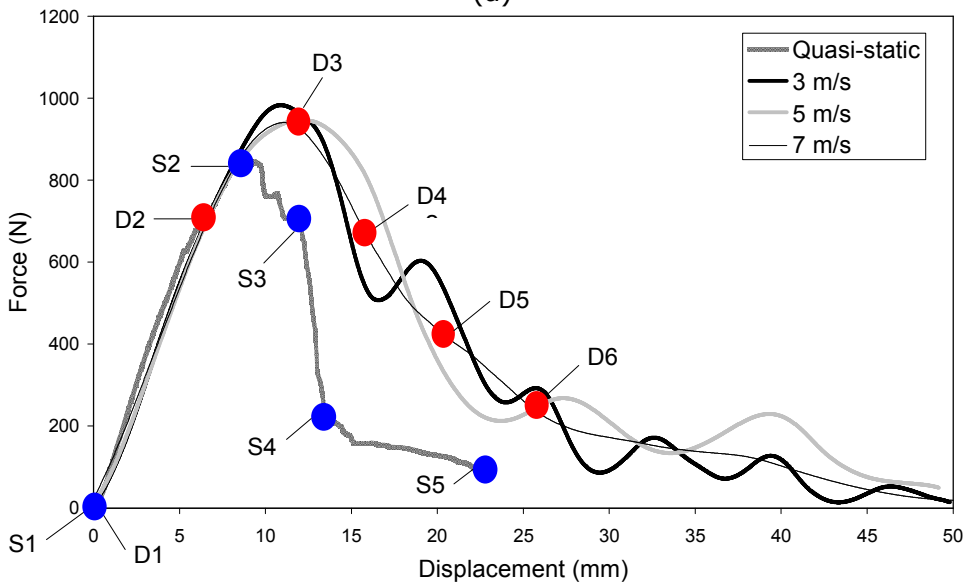

(b)

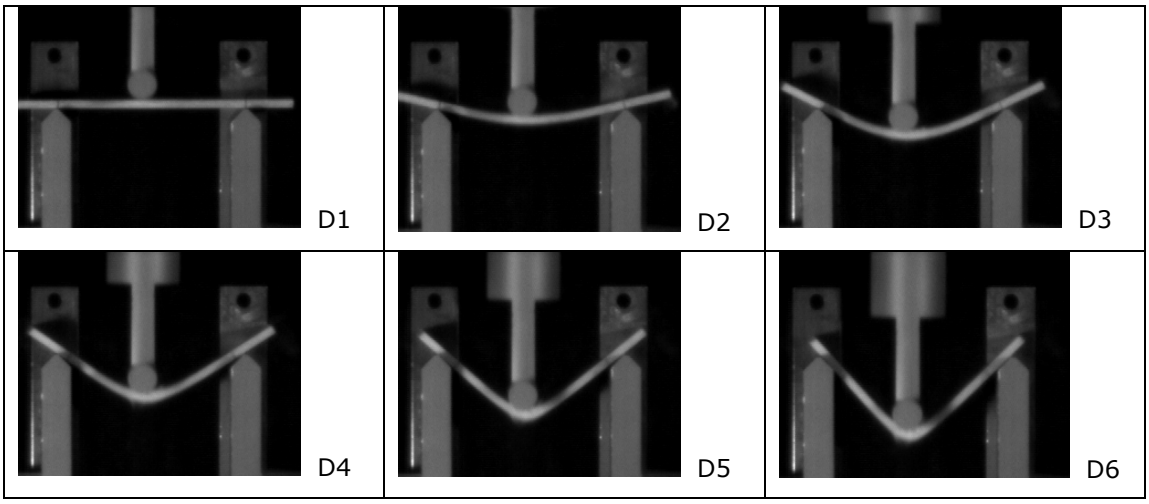

(c)

Figure 3-41. Flexural test results (a) Pictures of the deformation of the quasi-static bending test specimen (b) force – displacement curve for various impact speeds (c) high speed camera footage of the deformation of the dynamic bending test specimen at 7 ms^{-1} impact speed.

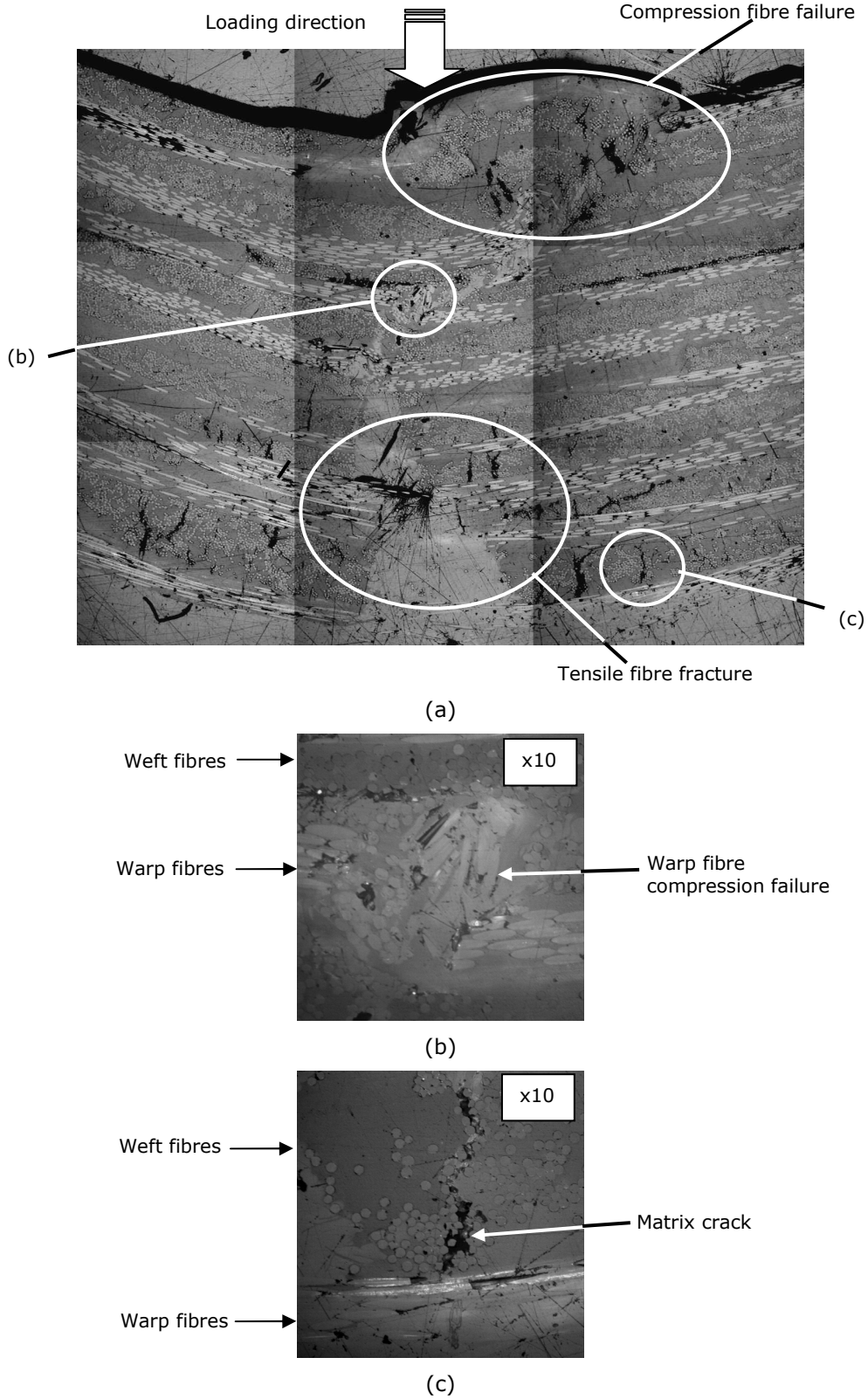

Figure 3-42. Optical micrograph of flexural specimen fracture zone at quasi-static impact speed (a) micrograph of fracture zone (b) detailed view showing fibre compression failure in the warp fibres (x10) (c) detailed view showing matrix crack in weft fibres (x10).

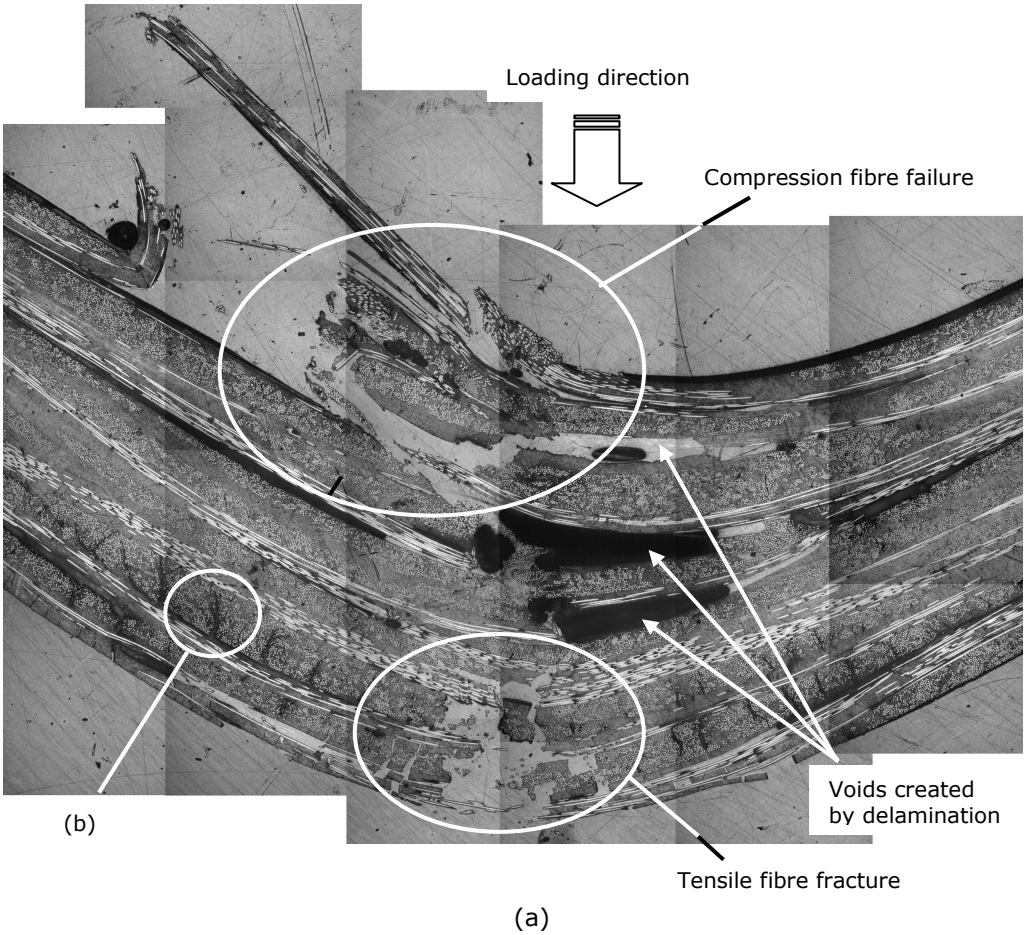

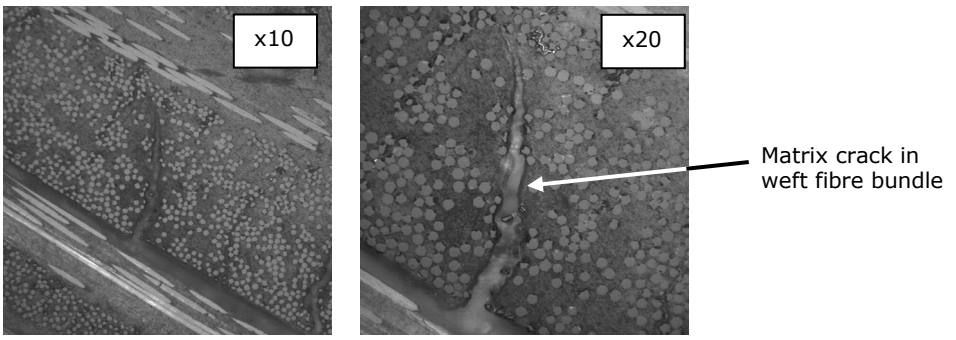

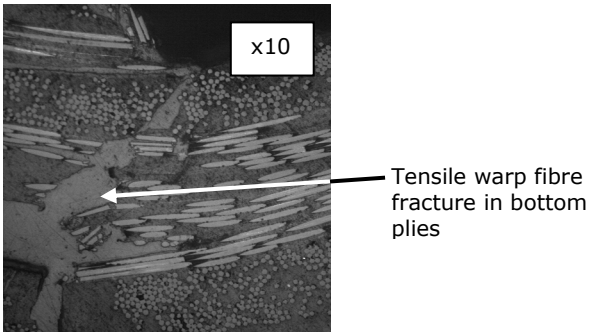

Figure 3-43. Optical micrograph of flexural specimen fracture zone at 7 ms^{-1} impact speed (a) micrograph of fracture zone (b) detailed view showing matrix crack in weft fibres (x10 and x20) (c) detailed view showing warp fibre fracture (x10).

3.4 Discussion

This section presents a detailed discussion of the experimental techniques and results that were described above. No other directly comparable test data on the dynamic behaviour of commingled glass/polypropylene woven fabric thermoplastic composites is available in the public domain. Therefore, a direct comparison between the experimental tests in this study and the literature is impossible. However, reference will be made to the literature where it is considered to be appropriate.

3.4.1 Experimental Techniques

3.4.1.1 Drop tower

The use of the falling weight drop tower along with special fixtures has been demonstrated to be a successful technique for determining the dynamic mechanical response of a commingled woven fabric glass fibre reinforced thermoplastic composite at strain rates ranging between 33 to 126 s^{-1}. Strain rates up to 100 s^{-1} can be achieved in a drop tower setup but it is difficult to increase the maximum strain rate limit because the speed is directly related to the drop height [38]. Furthermore, this technique is limited by inertial and wave propagation effects which could result in vibration waves being superimposed on the test results [38]. Groves et al [39] attempted to solve this problem by installing an acoustically damped base system between the load cell and the concrete drop tower. They also used aluminium absorbers to minimise the intensity of reflected stress waves. However, the difficulty with this solution is that the absorber significantly reduced the effective strain rate in the specimen [39]. In this present study, placing the load cell in the test fixtures, in close proximity to the specimen [42] has been proven to reduce the effects of spurious noise and stress wave reflections on the test data.

3.4.1.2 Shear punch test

A novel shear punch test method has been proven to be a simple, and reliable test method for obtaining the through-thickness shear strength and failure data for Twintex. One of the main advantages of the shear punch test is the ease of specimen manufacture. The shear punch specimen is only required to have two flat parallel faces. The quality of the specimen edges does not influence the test results. In contrast, the Iosipescu shear test requires a more complex specimen with good quality edges and

accurately machined V notches on each side. Furthermore, although the Iosipescu specimen is essentially in a state of pure shear, shear stress concentrations may develop at the root of the notches [33]. It has been noted that the specimen also bends [175] and tensile stresses are induced in the notched region [274]

In the shear punch test, the specimen is in a pure state of shear because of the restraints on the specimen and the tight tolerances between the die and the punch prevent the specimen from bending with could induce tensile and compression stresses.

The through thickness shear strength of the thermoplastic composite was found to be 4 times the in-plane shear strength under quasi-static loading. This suggests that through thickness shear failure is fibre dominated in contrast to the in-plane shear behaviour which tends to be matrix driven. However, it should be noted that stress-concentrations at the die edge may have influenced the shear strength. Furthermore, the shear strength may be dependent on the specimen thickness, especially since the shear strength is calculated by dividing the load by the area of the sheared edge [275]. This needs further investigation. Frictional forces, especially on the side of the punch as it is forced through the specimen may have been superimposed on the test results. However, these effects are considered to be minimal.

Although the punch test was only conducted at quasi-static loading rates in this present research, the fixture could also be adopted to work in a falling weigh drop tower for dynamic testing in future work.

3.4.2 Strain Rate Effects on Mechanical Properties

3.4.2.1 Tensile properties

The tensile modulus and strength of Twintex exhibited very little rate sensitivity up a strain rate of 33 s^{-1}. At higher strain rates, the tensile modulus and strength increase substantially above the quasi-static values. The increase in the tensile modulus and strength may be attributed to matrix viscoelastic effects, the rate sensitivity of the composite

constituents, i.e. the fibre and matrix, the strength of the fibre matrix interface and the woven geometry of the material.

In the literature, the rate sensitivity of a composite laminate modulus is generally explained by the viscoelastic effect of the matrix material [39, 276]. Groves et al [39] who studied the dynamic properties of carbon/epoxy has noted that under high strain rate loading the matrix viscoelasticity results in restricted molecular mobility and shear flow which increases the strength and modulus of the composite laminate. In this present investigation, the mechanical properties of the viscoelastic polymeric matrix, polypropylene, are known to be strongly rate dependant [277]. Therefore, it is postulated that the rate sensitivity of the laminate tensile stiffness may be partly attributed to matrix viscoelasticity. Matrix viscoelastic effects may have also contributed to the non-linear strain hardening stress-strain response that was observed at high strain rates. Other factors that may have caused strain hardening include the woven fabric structure and the interfacial interactions between the fibres and matrix [276].

The tensile strength of the Twintex laminate is primarily governed by the fibre strength. It has also been noted that glass fibres are rate dependent [116]. It then follows that the observed increase in tensile failure strength of Twintex may be attributed to the increasing strength of the glass fibres with increasing strain rate.

Under quasi-static loading, specimen failure is primarily by a localised through-thickness shear band failure of the fibres and matrix. At high strain rates, failure extends across the entire gauge length with delamination occurring at each ply interface. The propagation of damage along the specimen gauge length appears to correspond with the observed ductile non-linear post yield stress-strain response that occurs over a large strain range and this is most evident at 33 s^{-1} where the material behaviour is almost elastic-perfectly plastic. This suggests that matrix yielding was dominant during dynamic tensile loading. Although the damage sequence is not clear from the macroscopic and microscopic results, it is postulated that at high strain rates, delamination that occurs at each ply interface is caused by compression shock waves (stress reversal) that follows fibre fracture.

3.4.2.2 Shear properties

Overall trends show a decrease in in-plane shear strength with increasing strain rate. There is a very dramatic decrease in the in-plane shear modulus of Twintex at high strain rates which was unexpected and this is not easily explained. Other investigators have reported somewhat similar observations for rate effects on the in-plane shear modulus of composite materials.

Barre et al [38] observed that the shear modulus for a woven E-glass/phenolic composite obtained by 15° off-axis test decreased with increasing strain rate while the shear modulus obtained from a ±45° off-axis test remained relatively unchanged. They noted that these observations may have been due to the nature of the stress-strain field in the specimens but did not provide an explanation to support there conclusions. The effect of strain rate on the in-plane shear strength was not determined by Barre et al [38].

Papadakis et al [278], investigated strain rate effects on the shear properties of a unidirectional glass/polypropylene thermoplastic composite, using ±45° tensile test method with a dog bone specimen. They reported a 38% decrease in the in-plane shear strain modulus; however a 10% increase in the in-plane shear strength at the highest strain rates applied was observed. Papadakis et al [278] did not provide an explanation for the reported strain rate effects on the in-plane shear properties.

In this present research, the shear failure appears to remain constant over the range of strain rates examined. During tensile loading, the specimens undergo a mixed mode of failure. Firstly, trans-ply through-thickness cracks develop primarily in the surface and middle plies. Then inter-ply failure occurs in the form of delamination as the fibres rotate in the direction of the applied load. Finally, the fibres and fibre bundles pull-out along the ±45° direction of the fibre layup, resulting in a V-shaped in-plane failure surface. These observations are in very close agreement with the shear failure modes presented by Papadakis et al [278]. This suggests that in-plane shear failure modes are the same for both unidirectional and

woven fabric thermoplastic composites for both quasi-static and dynamic loading cases.

The in-plane shear also showed a non-linear behaviour that can be attributed to the softening of the matrix as transply cracks accumulate. The strain hardening that was observed at large shear strains may be due to fibre realignment.

Kellas et al [279] provides one of the most detailed discussions on the failure mechanisms in ±45° angle ply laminates. They studied two material systems; graphite/epoxy and graphite/PEEK thermoplastic matrix laminates with ±45° layups under quasi-static tensile loading conditions. They also observed that transply through-thickness cracks developed primarily in the surface and middle plies. Kellas et al [279] postulates that the transply cracks are caused by in-plane normal stress with the cracks propagating in an opening mode which they have defined as Mode I failure. These in-plane normal stresses develop perpendicular to the fibre orientation and are at a maximum value in the surface and middle plies. Furthermore, the reorientation of the fibres induces interlaminar stresses at the ply interfaces which results in delamination.

Clearly, the in-plane shear behaviour of Twintex is dominated by the matrix and interfacial properties. The fibre-matrix interface has been shown to have a direct effect on the macroscopic mechanical properties of Twintex commingled glass/polypropylene composites [280]. It is postulated here that perhaps the fibre-matrix interfacial stiffness decreases with increasing strain rate. This results in a more ductile response and a subsequent decrease in the apparent in-plane shear modulus at high strain rates. Further investigation in future work is required to definitively elucidate the effect of strain rate on the shear modulus and strength.

3.4.2.3 Compression properties

The compression modulus and strength increase with increasing strain rate. The increase in the compression modulus maybe attributed to viscoelastic effects and the time dependent nature of damage accumulation [281].

The failure modes for the compression specimens remained relatively the same under quasi-static and dynamic loading. In all cases, the dominant failure modes were fibre micro buckling leading to fibre kinking followed by a localised through-thickness shear fracture in the fibres and matrix along a distinct shear band. Delamination also occurred primarily in the outer plies. Micro buckling in the fibres may be attributed to local premature failure of the surrounding matrix [39]. Delamination is perhaps initiated by through-thickness tensile stress in the laminate which results in Mode II fracture [39]. The local shear band failure observed in this current research agrees with results reported by Harding [282] for woven carbon epoxy composite specimens under dynamic compression loading. He has postulated that woven fabric composites are predisposed to fail by a through-thickness shear band that initiates at a shear fracture across an axially aligned fibre tow.

3.4.2.4 Flexural properties

The flexural modulus showed little or no change with increasing impact speed which was unexpected, especially since the in-plane tensile, shear and compression modulus have been shown to be rate sensitive. The flexural strength at an impact speed of 3 ms^{-1} increased by 10% over the quasi-static value and appeared to reach a threshold, remaining relatively unchanged with increasing impact velocities. The observations at dynamic loads show relative agreement with results presented by Okoli and Adul-Latif [116]. They conducted dynamic three-point bending tests on cross-ply plain weave glass/epoxy material. The tests were carried out at impact speeds of 2 and 4 ms^{-1}. They observed that there was relatively no change in the peak load and stiffness of the laminates over the impact velocity range applied in their study.

Under bending loads, a complex stress field develops in the specimen which results in mixed mode failure. There is a maximum tensile stress at the lower surface, maximum compression stress at the upper surface and maximum interlaminar shear stress at the midplane [33]. Throughout the beam, is a combined stress state of normal and shear stresses [33]. Subsequently failure can be in tension, compression and shear or a combination of these. From this study, it is postulated that the damage sequence initiates with through-thickness cracks in the weft fibre bundles

in the bottom plies. These cracks propagate in an opening mode as a result of tensile normal stresses. Compression stresses in the top plies then follow which cause fibre kinking, fibre crush and eventually compression fibre fracture. Finally, the beams fail when tensile fibre fracture occurs in the bottom plies. The damage described above is common to all specimens at both quasi-static and high strain rates. However, localised delamination which was not observed in quasi-static specimens is prevalent in the midplane at higher strain rates.

3.5 Conclusions

The main conclusions drawn from this study are:

- A drop tower along with novel special fixtures have been successfully developed for characterising the dynamic mechanical properties of a commingled woven fabric glass fibre reinforced thermoplastic composite. Tensile, shear, compression and flexural behaviour of the material was investigated for strain rates ranging between 0.0001 to 126 s^{-1}.

- A novel shear punch technique has been developed as a simple method for determining the quasi-static through-thickness shear properties of Twintex.

- The tensile and compression modulus and strength increased with increasing strain rate. However, in contrast, the shear modulus and strength decreased as strain rate increased. The flexural modulus appears rate insensitive; however, the flexural strength increased with increasing strain rate.

- The strain rate effects in the material appear to be influenced primarily by the matrix viscoelasticity, fibres and matrix interfacial properties and the composite woven reinforcement architecture.

- Further detailed study is required to explain the relationship between damage modes and the strain rate sensitivity of the mechanical properties.

Chapter 4

Modelling the Quasi-Static and Dynamic Impact Response of Thermoplastic Composite Materials

4.1 Introduction

The subject of modelling impact damage progression in composite materials has received extensive attention and today, several composite constitutive models have been developed [80, 117, 181, 189, 193, 196]. Some of these models have been implemented into commercially available finite element (FE) analysis codes [117, 118, 181, 283] . However, most of these models have only been validated for thermoset composite materials, with the modelling of thermoplastic composites receiving very limited attention [7, 120].

This chapter deals with the numerical simulation and prediction of the static and dynamic impact response of components and structures made from thermoplastic composite materials. Specifically, the current study evaluates the application of the advanced MAT 162 material model for simulating impact damage progression in the Twintex E-glass/polypropylene commingled woven fabric thermoplastic composite material. This model has been recently implemented in the commercial LS-DYNA explicit finite element code [118]. MAT 162 has been used for the analysis of thermoset composites but has yet to be fully calibrated and validated for predicting impact damage in thermoplastic composites. The MAT 162 model is based on a continuum damage mechanics (CDM) constitutive model [186]. It is capable of simulating various damage modes including matrix damage, fibre fracture, fibre crush and delamination. The chapter presents a modelling methodology for calibrating and validating the material model and the damage parameters using an inverse modelling technique. The calibrated and validated model is then successfully applied to the crashworthiness predictive modelling of a large scale demonstrator thermoplastic composite structure.

4.2 Modelling Tools

The finite element modelling process typically consists of three primary steps: (1) pre-processing, (2) solver and (3) post-processing. The general finite element modelling steps are shown in Figure 4-1.

In this study, pre-processing involved using the Hypermesh™ software to create and mesh all geometric models. The LS-PREPOST™ software was used to create the input files which contained all the data required to define the model including element types, material properties and boundary conditions.

When the model is fully defined, it is sent to the solver. The solver essentially calculates the system of equations that describe the behaviour of the model as a whole. The solver used in this study is the commercial LS-DYNA explicit finite element software which is described in Section 4.2.1.

Finally, the post-processing step involved the use of the LS-PREPOST™ and HyperView™ softwares for qualitative and quantitative interpretation of the results obtained from the solver, e.g. displacement or stresses. These results are then validated against experimental tests or other analytical calculations.

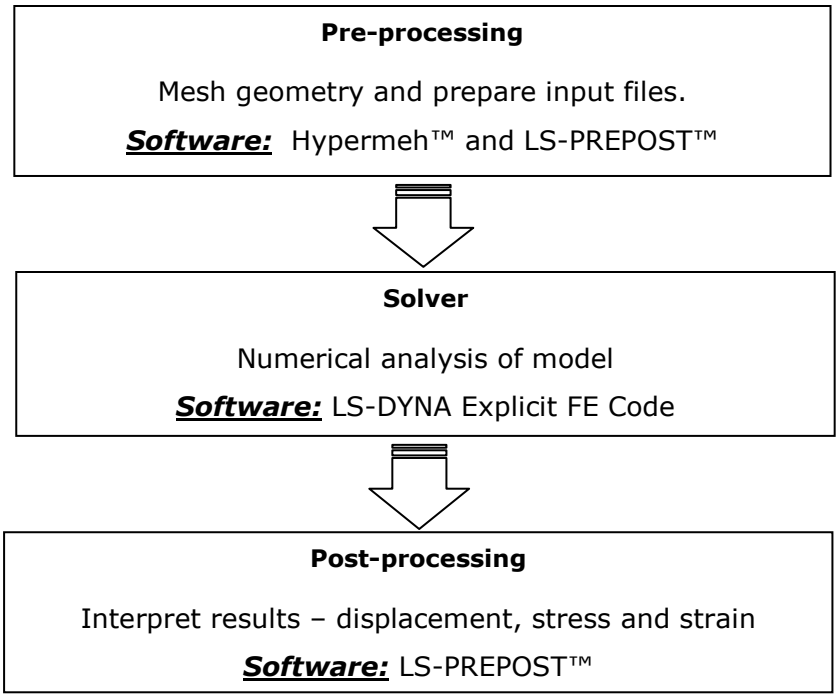

Figure 4-1. General finite element modelling steps.

4.2.1 Explicit Finite Element Solver

The solver used in this study is the commercial LS-DYNA explicit finite element code [87, 118], which for the purpose of the simulation of fibre-reinforced composites, contains several composite material models [87, 117, 118]. The LS-DYNA code was developed at the Lawrence Livermore National Laboratory. It is based on a Lagrangian formulation and an explicit time integration scheme with a central difference algorithm. The explicit method evaluates local variables directly without the need for global equilibrium calculations. As such, LS-DYNA is primarily suited for performing impact and large deformation non-linear dynamic analysis. LS-DYNA has a wide variety of analysis capabilities including a large number of material models, a variety of contact and interface modelling algorithms, a large library of element formulations including beams, plates, shells and solid elements and a robust algorithm for controlling the solution process.

The finite element process is very CPU intensive. All computations were done on a Viglen® personal computer with a Microsoft Windows XP® operating system, dual Intel Xeon processor (2.8 GHz), 2 GB RAM, a 120 GB primary hard disk and 250 GB secondary hard disk.

4.2.2 Quasi-Static Modelling

In the explicit method, the time step is usually very small (in the order of microseconds) to maintain numerical stability. For quasi-static events where the time of the overall event tends to be large (seconds or minutes), it becomes prohibitive to use the explicit technique as the computational times are very long. There are two main methods for reducing the solution times for quasi-static problems (1) mass scaling, and (2) time scaling [284].

Mass scaling refers to a method where non-physical mass is added to the model in order to achieve a larger explicit time step and subsequently reduce the solution time [284]. Whereas, time scaling involves increasing the loading rate which does not increase the time step but reduces the total number of time steps required to complete the solution [285]. To avoid introducing spurious high frequency noise in the solution, the increased loading must be applied smoothly using either a linear or sinusoidal ramp curve [82].

Both these methods have been applied in all the quasi-static models in this current research. Care was taken to ensure that dynamic effects were not introduced into the model by ensuring that the kinetic energy remained very small relative to the peak internal energy.

4.2.3 Hourglass Control

In this present research, all the finite element composite models will primarily use single integration point eight node solid elements. These under integrated solid elements are considered to be more robust than fully integrated solid elements in the case of large deformation [198]. In addition they also provide significant computational savings. However, single point solid elements are susceptible to zero energy modes called Hourglassing. Hourglassing is the development of non-physical deformation and zero strain energy modes that result in zero strain and no stress [87]. The two main methods that are used for preventing hourglass modes are viscous damping control and stiffness control formulations [82]. In the event of hourglass modes occurring, viscous control prevents further development of the hourglass mode while the stiffness control will return the element back to its original deformation state [82]. The latter was

applied in this study. Stiffness hourglass control can stiffen the behaviour of solid elements and care was taken to ensure that the hourglass energy remained very small relative to the peak internal energy.

4.3 Modelling Methodology

A major objective of this research was to develop a robust modelling methodology for predictive simulation of impact damage in commingled woven fabric thermoplastic composites. The proposed methodology that was developed consisted of three phases: (1) material model calibration, (2) material model validation and (3) structural validation. A schematic of the modelling methodology is shown in Figure 4-2.

4.3.1 Material Model Calibration Phase

The determination of model parameters is referred to as a calibration procedure in this study. The parameters for the model were determined by direct experimental measurement, estimation and/or inverse modelling techniques. An extensive experimental material characterisation program that covered a wide range of static and dynamic tests has been conducted to support the material model calibration process (see previous chapter).

4.3.2 Material Model Validation Phase

To validate the material model and the calibrated parameters, a series of benchmark impact coupon tests are simulated. The quasi-static and dynamic three-point bending tests described in the previous chapter and a series of low velocity falling weight impact tests described by Santulli et al [286] are used as a basis for validating the model. These coupon tests were selected because these modes of loading are considered to be representative of the complex nature of loading in structural composite components subjected to crash loads. The predicted force-displacement histories and damage modes are correlated with experimental results.

4.3.3 Structural Validation Phase

Finally, the calibrated and validated composite material model was applied to the predictive analysis of a large scale complex shaped automotive

demonstrator component. The component is a small passenger vehicle thermoplastic composite side-impact beam loaded under quasi-static and crash loading conditions. Successful predictive analysis of the component's response should provide a significant level of confidence in the proposed modelling methodology.

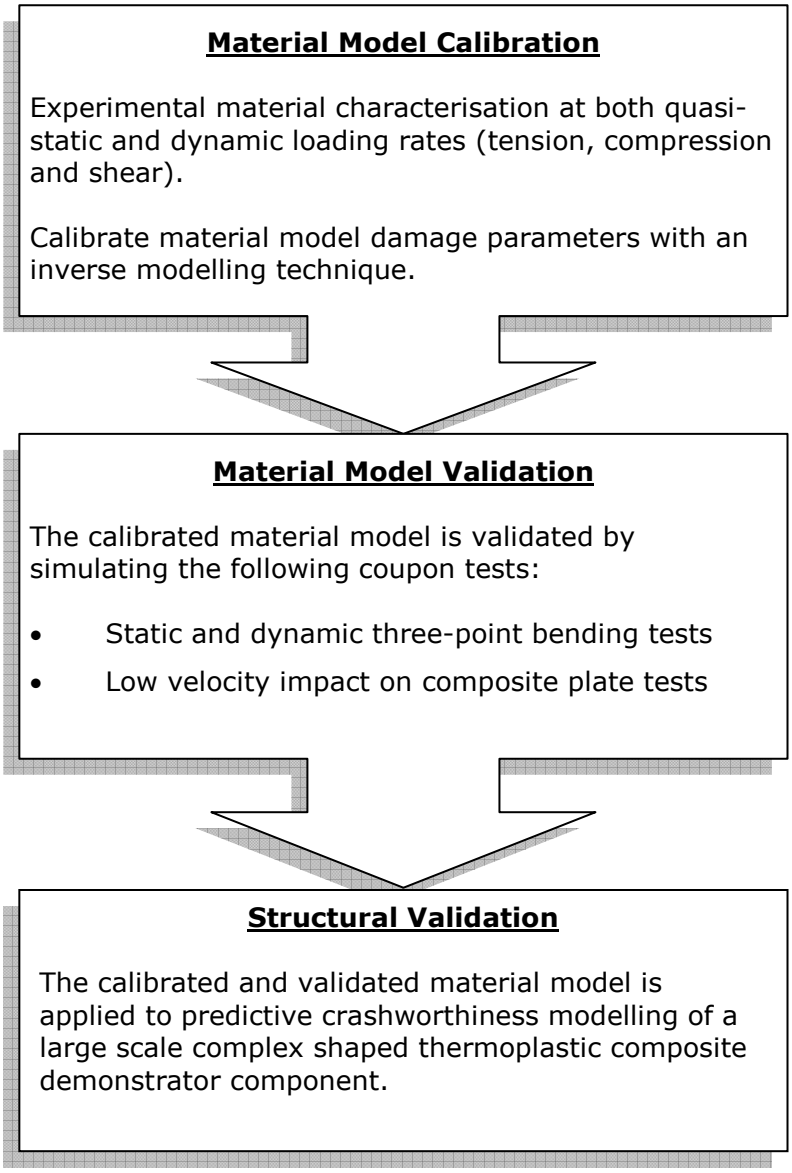

Figure 4-2. Modelling methodology.

4.4 Composite Material Model

The MAT 162 composite material model is used to model the Twintex commingled woven fabric thermoplastic composite material. This model was developed by the Materials Science Corporation (MSC) and was recently implemented into LS-DYNA for solid elements [118]. MAT 162 is an advanced composite model which is based on the continuum damage mechanics formulation of Matzenmiller et al [186], which characterises the post-elastic growth of damage and strain softening after failure. This model is able to simulate various complex composite failure modes such as matrix damage, fibre fracture (tensile and compressive), fibre crush and delamination under all loading conditions. Furthermore, the model has the advantage of predicting delamination without prior definition of an interlaminar crack surface or the need to implement an interface or cohesive model between plies. In addition, MAT 162 accounts for strain rate effects which are important for dynamic impact simulations.

A detailed description of MAT 162 is available in [118]; however, for completeness a brief description is provided below.

4.4.1 Failure Criteria

The failure criteria for various failure modes are described below.

4.4.1.1 Fibre tensile/shear damage modes

The Hashin failure criterion [287], in a generalised form, is used to characterise fibre damage with respect to strain components for a plain weave ply. The warp and weft fibre tensile and shear damage are given by the quadratic interaction between the related axial and through thickness shear strains

$$\left(\frac{E_x.\varepsilon_x}{S_{xT}}\right)^2 + \left(\frac{G_{xz}.\varepsilon_{xz}}{S_{xFS}}\right) - r_1^2 = 0 \qquad \textbf{(4-1)}$$

$$\left(\frac{E_y.\varepsilon_y}{S_{yT}}\right)^2 + \left(\frac{G_{yz}.\varepsilon_{yz}}{S_{yFS}}\right) - r_2^2 = 0 \qquad \textbf{(4-2)}$$

where for the fabric composite, x, y, and z denote the in-plane warp and in-plane weft and out-of-plane direction, respectively. E and G are the tensile and shear modulii, respectively. S_{xT} and S_{yT} are tensile strengths in the warp and weft directions, and S_{xFS} and S_{yFS} are fibre shear failure strengths in the warp and weft directions, ε_x and ε_y are the tensile strains in the x and y directions, ε_{xz} and ε_{yz} are shear strains in the x-z and y-z planes and r_1, r_2 are the damage thresholds.

4.4.1.2 Fibre compression damage modes

In-plane compressive fibre damage in the warp and weft direction is given by the maximum strain criterion

$$\left(\frac{E_x.\varepsilon_x}{S_{xC}}\right)^2 - r_3^2 = 0, \quad \varepsilon_x' = -\varepsilon_x - \langle\varepsilon_z\rangle\frac{E_z}{E_x} \qquad \textbf{(4-3)}$$

$$\left(\frac{E_y.\varepsilon_y}{S_{yC}}\right)^2 - r_4^2 = 0, \quad \varepsilon_y' = -\varepsilon_y - \langle\varepsilon_z\rangle\frac{E_z}{E_z} \qquad \textbf{(4-4)}$$

where S_{xC} and S_{yC} are the axial compressive strengths in the warp and weft directions, respectively, and r_3, r_4 are the associated damage thresholds.

4.4.1.3 Fibre crush damage mode

Fibre crush damage caused by high through thickness compressive pressure is given by

$$\left(\frac{E_z.\varepsilon_z}{S_{FC}}\right)^2 - r_5^2 = 0 \qquad \textbf{(4-5)}$$

where S_{FC} is the fibre crush strength, ε_z is the through thickness strain and r_5 is the associated damage threshold.

4.4.1.4 Matrix damage

Matrix damage can occur in a plain weave layer without the occurrence of fibre fracture. The in-plane matrix damage is given by

$$\left(\frac{G_{xy}.\varepsilon_{xy}}{S_{xy}}\right)^2 - r_6^2 = 0 \qquad \textbf{(4-6)}$$

where S_{xy} is the layer shear strength and r_6 is the damage threshold.

4.4.1.5 Delamination damage

Delamination damage is given by:

$$S^2\left\{\left(\frac{E_z.\varepsilon_z}{S_{CT}}\right)^2 + \left(\frac{G_{yz}.\varepsilon_{yz}}{S_{YZ0}}\right)^2 + \left(\frac{G_{zx}.\varepsilon_{zx}}{S_{ZX0} + S_{SR}}\right)^2\right\} - r_7^2 = 0 \qquad \textbf{(4-7)}$$

where S_{CT} is the through-thickness tensile strength, S_{YZ0} and $S_{ZX0,}$ are interlaminar shear strengths in the x-y and y-z planes, respectively. Scale factor, S, accounts for the stress concentration the axial compressive strengths in the warp and weft directions, respectively, and r_7 is the related damage threshold. The interlaminar shear strengths are considered to decrease under through thickness tensile stress and increase with through thickness compressive stress according to Mohr-Columb theory

$$S_{SR} = -\varepsilon_z.E_z \tan\phi \qquad \textbf{(4-8)}$$

where ϕ is the internal friction angle?

4.4.2 Damage Progression in MAT 162

A set of damage variables ϖ_i with i = 1,…,6 are introduced to relate the onset and progression of damage to stiffness losses in the material. The compliance matrix [C] is related to the damage variables as [186]:

$$[C] = \begin{bmatrix} \frac{1}{(1-\varpi_1)E_x} & \frac{-\nu_{yx}}{E_y} & \frac{-\nu_{zx}}{E_z} & 0 & 0 & 0 \\ \frac{-\nu_{xy}}{E_x} & \frac{1}{(1-\varpi_2)E_y} & \frac{-\nu_{zx}}{E_z} & 0 & 0 & 0 \\ \frac{-\nu_{xz}}{E_x} & \frac{-\nu_{yz}}{E_y} & \frac{1}{(1-\varpi_3)E_z} & 0 & 0 & 0 \\ 0 & 0 & 0 & \frac{1}{(1-\varpi_4)G_{xy}} & 0 & 0 \\ 0 & 0 & 0 & 0 & \frac{1}{(1-\varpi_5)G_{yz}} & 0 \\ 0 & 0 & 0 & 0 & 0 & \frac{1}{(1-\varpi_6)G_{zx}} \end{bmatrix} \quad \textbf{(4-9)}$$

The stiffness matrix S is obtained by inverting the compliance matrix, $[S] = [C]^{-1}$.

The growth rate of damage variables, ϖ_i, is governed by [186]

$$\varpi_i = \max\{q_{ij}\phi_j, j = 1,...,5\} \quad \textbf{(4-10)}$$

$$\phi_i = 1 - e^{\frac{1}{m}\left(1-r_j^m\right)}, \quad r_j \geq 1 \quad \textbf{(4-11)}$$

The vector-value function q_{ij} provides the coupling between the damage variables and the various damage modes and takes the form

$$[q] = \begin{bmatrix} 1 & 1 & 1 & 0 & 0 \\ 0 & 0 & 1 & 0 & 0 \\ 0 & 0 & 1 & 0 & 1 \\ 1 & 1 & 1 & 1 & 1 \\ 0 & 0 & 1 & 0 & 0 \\ 1 & 1 & 1 & 0 & 1 \end{bmatrix} \quad \textbf{(4-12)}$$

in order that

$$E_i = (1-\varpi_i)E_{i0}, \; G_i = (1-\varpi_i)G_{i0} \quad \textbf{(4-13)}$$

where r_j are the damage thresholds, ϖ_i are the damage variables and m are the post-elastic strain softening parameters. The damage variable ϖ_i varies from 0 (no damage) to 1 (complete failure) as r_j varies from 1 to infinity according to the distribution of Equation 4-13. There are four

damage parameters m that are used to model the post-elastic damage response of the material under various loading conditions. These are:

m1 – fibre damage in local x-direction
m2 – fibre damage in local y-direction
m3 – fibre crush and fibre shear punch damage
m4 – matrix and delamination damage

As a first step, the effect of the MAT 162 damage parameter, m was initially investigated using a single solid element model. The dimensions of the single solid element were representative of the Twintex composite material unit cell which was about 10 mm^2 (see Figure 4-3). The thickness of the element was equivalent to one ply (~ 0.5 mm). Figure 4-4 shows the tensile and compression stress-strain curves for different values of m.
It can be seen that under monotonic loading the model provides an initial elastic region up to the strength value which is followed by a post-elastic damage region. For large values of m, the predicted post-elastic response is brittle while as m decreases the material behaviour is more ductile. As m approaches 0 the predicted result represents a perfect elastic-plastic response. For values of m below 0, a hardening stress-strain response is predicted.

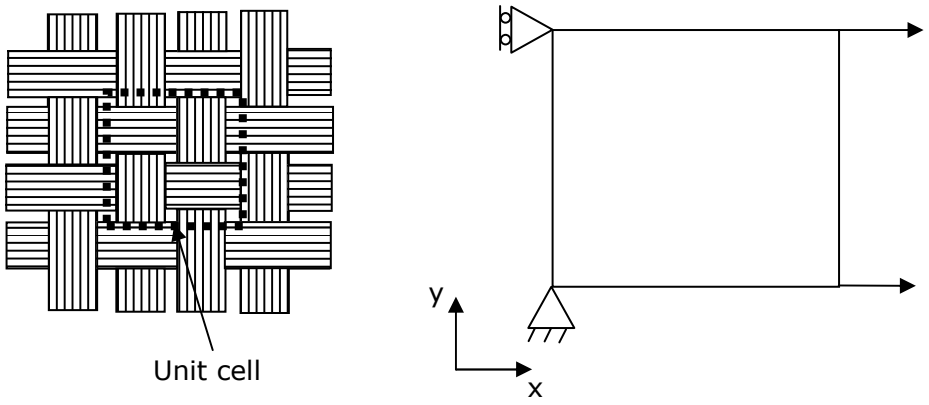

Figure 4-3 Schematic of unit cell for Twintex woven fabric thermoplastic composite material and single element model of unit cell.

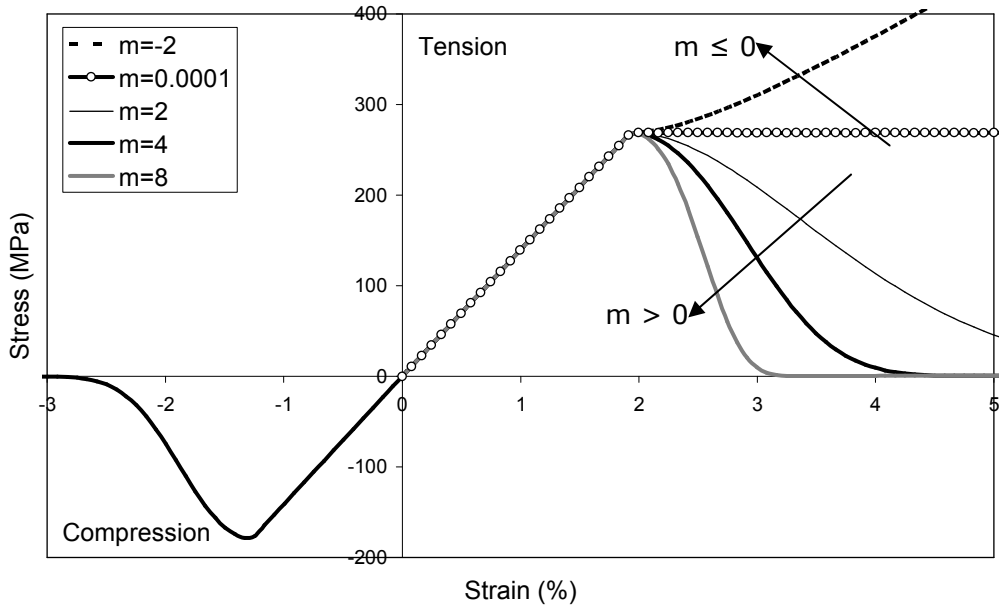

Figure 4-4. Effect of various damage parameters on the tensile and compression stress-strain relationship. Only the compression response for m = 4 is shown; however, the effect of varying the value of m on the compressive post-elastic behaviour is similar to the tensile case.

4.5 Material Model Calibration

This section presents a methodology for systematically calibrating the parameters in the MAT 162 model. There are 36 model parameters required for MAT 162 which include standard material properties such as density, elastic modulii and strength; in addition to strain rate and damage parameters.

4.5.1 Elastic Modulii and Strength Properties

The in-plane elastic modulii and strength properties were primarily obtained from the experimental characterisation test program using the recorded stress-strain results (see previous chapter). However, the through-thickness properties and the crush strength were either obtained from the open literature, material supplier's database or were estimated.

Through-thickness properties

The static through-thickness shear properties for Twintex were based on the experimental Iosipescu shear tests that were conducted at University of Wyoming [36]. Based on their work, values of G_{yz} = 1.66 GPa, G_{zx} = 1.76 GPa, S_{yz} = 12.14 MPa and S_{zx} = 13.66 MPa were adopted in the current study.

The Twintex through thickness elastic modulus was estimated using a rule of mixtures approach [7]. This resulted in an estimate of 5.3 MPa for the through-thickness modulus.

The through-thickness tensile strength S_{CT} was estimated to be 25 MPa which is about the same value as the tensile strength of the polypropylene matrix material [288].

Crush strength

The crush strength for the Twintex material was not available. The crush strength was estimated to be 300 MPa. This is approximately twice the in-plane compression strength which is a trend observed in other composites [289].

4.5.2 Strain Rate Effect

The MAT 162 model incorporates the effect of strain rate on the stress-strain response of a composite lamina by scaling the elastic modulii and strength values using the following functions:

For strength properties

$$S_{RT} = S_0\left(1 + C\ln\frac{\dot{\bar{\varepsilon}}}{\dot{\varepsilon}_0}\right) \qquad \textbf{(4-14)}$$

$$\{S_{RT}\} = \begin{Bmatrix} S_{xT} \\ S_{xC} \\ S_{yT} \\ S_{YC} \\ S_{FC} \\ S_{FS} \end{Bmatrix} \text{ and } \{\dot{\bar{\varepsilon}}\} = \begin{Bmatrix} |\dot{\varepsilon}_x| \\ |\dot{\varepsilon}_x| \\ |\dot{\varepsilon}_y| \\ |\dot{\varepsilon}_y| \\ |\dot{\varepsilon}_z| \\ \left(\dot{\varepsilon}_{zx}^2 + \dot{\varepsilon}_{yz}^2\right)^{1/2} \end{Bmatrix}$$

For elastic modulii properties

$$E_{RT} = E_0\left(1 + C\ln\frac{\dot{\bar{\varepsilon}}}{\dot{\varepsilon}_0}\right) \qquad \textbf{(4-15)}$$

$$\{E_{RT}\} = \begin{Bmatrix} E_x \\ E_y \\ E_z \\ G_{xy} \\ G_{yz} \\ G_{zx} \end{Bmatrix}, \{\dot{\bar{\varepsilon}}\} = \begin{Bmatrix} |\dot{\varepsilon}_x| \\ |\dot{\varepsilon}_y| \\ |\dot{\varepsilon}_z| \\ |\dot{\varepsilon}_{xy}| \\ |\dot{\varepsilon}_{yz}| \\ |\dot{\varepsilon}_{zx}| \end{Bmatrix} \text{ and } \{C\} = \begin{Bmatrix} C_2 \\ C_2 \\ C_4 \\ C_3 \\ C_3 \\ C_3 \end{Bmatrix}$$

where S_{RT} are rate adjusted strengths, S_0 is quasi-static strength, E_{RT} are rate adjusted modulii, E_0 is quasi-static modulii, $\dot{\bar{\varepsilon}}_0 = 1$ is the quasi-static reference strain rate, $\dot{\bar{\varepsilon}}$ are effective strain rates and C is the strain rate constants.

There are four strain rate parameters:

C_1 – strain rate constant for strength properties

C_2 – strain rate constant for elastic modulii in the x-direction

C_3 – strain rate constant for shear modulii

C_4 – strain rate constant for elastic modulii in the z-direction

Values for the four strain rate constants were derived from the dynamic test program described in the previous chapter. Table 4-1 shows the values for the strain rate constants obtained from the dynamic test results.

It should be noted that the strain rate constants C_3 and C_4 were not used in this study because strain rate data for the through thickness shear and through-thickness elastic modulii was not available. The static through thickness shear properties were used in both static and dynamic models.

Table 4-1. Input values for the MAT 162 strain rate constants for Twintex

Strain Rate Constants	Tensile	Compression	Shear
C_1	0.089	0.181	
C_2	0.026	0.251	
C_3	-	-	-
C_4	-	-	-

4.5.3 Delamination and Scale Factor S

Delamination is a major failure mechanism that occurs between composite plies [290]. It is caused by interlaminar stresses that result in the development of micro/macro matrix cracks that propagate parallel to the ply interfaces. MAT 162 is able to simulate delamination with the advantage of not requiring a physical interface or cohesive model between the plies. However, interface element layers need to be defined. For models in this study, interface element layers were defined by varying the material orientation angles at specified interface layers using the BETA function in the MAT 162 material input card in LS-DYNA (see Figure 4-5). Beta values for element layers adjacent to the ply interface were alternated between 0° and 90° as shown in Figure 4-5.

If the matrix failure criterion given by Equation (4-7) is satisfied within elements that are adjacent to the ply interface, the elements are identified for delamination failure with the failure plane being parallel to the layer planes. A delamination scale factor S is also used to account for stress concentrations. S can be used to calibrate the predicted delamination area with experimental results. Both the experimental falling weight low

velocity impact work of Santulli et al [286] and the experimental dynamic bending impact work described in the previous chapter show that the Twintex thermoplastic composite exhibits limited and very localised levels of delamination damage under impact. Therefore, in this current study, S = 1 is applied in all models.

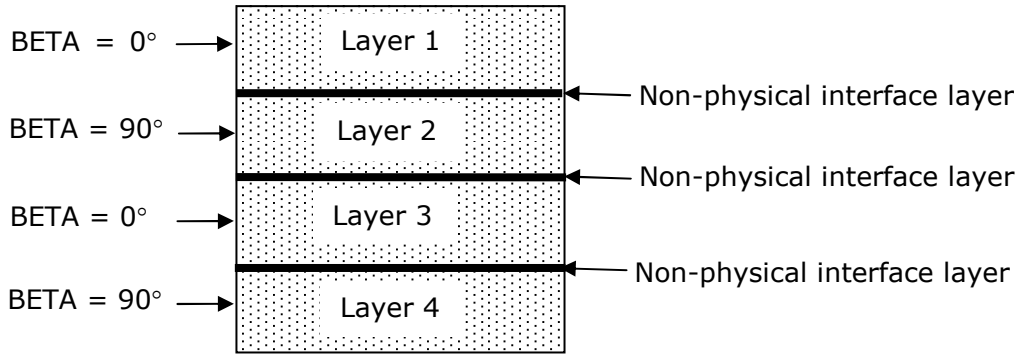

Figure 4-5. Definition of a non-physical delamination interface layer.

4.5.4 Element Erosion Parameters

Failed elements are deleted to avoid thinning of the elements and negative volumes due to excessive distortion which may lead to increased computational time and even numerical instabilities. MAT 162 incorporates three element erosion criteria for deleting failed elements [118]. Elements are deleted if any of the following are satisfied:

- Fibre tensile failure occurs in both in-plane directions (x and y) of the fabric ply and axial strain exceeds a specified value for E_LIMIT.
- Compressive relative volume strain in a failed element is less than ECRSH.
- Tensile relative volume strain in a failed element exceeds a specified value for EEXPN

It is important not to delete failed elements too early as this may result in a brittle response; however, keeping elements too long after failure may result in long solution times and numerical instabilities [291]. Furthermore, element erosion may cause vibrations in the model. These vibrations are undesirable because they sometimes cause stress spikes in

surrounding elements which may result in premature element deletion [291].

For simplicity, in all simulations, element erosion was based on the tensile relative volume strain criterion (EEXPN). EEXPN was set to values ranging between 2 and 4, ensuring that the elements were completely damaged prior to deletion.

4.5.5 Damage Parameter Calibration

An aim of this current research work is to use calibrated values for the damage parameters for predictive modelling of impact damage progression in coupon specimens and large scale structures without the need for additional adjustment to the damage parameters.

In this study, a calibration methodology based on an inverse modelling technique was developed for determining the MAT 162 damage parameters. In this methodology, the damage parameters were systematically obtained by correlating simulations with standard coupon tests (shear, tensile, compression). Firstly, initial damage parameter values are assigned and used in simulating a test. Model predictions are then compared with the corresponding test stress-strain results. The parameters are adjusted iteratively over several simulation runs until satisfactory correlation is obtained. During the calibration of a particular damage parameter, all other parameters are kept constant during the iterations.

The damage parameters are sequentially calibrated. Firstly, the damage parameter, m4 that treats matrix cracks is calibrated using the [±45] in-plane shear tests. Then, m1 and m2 the fibre fracture damage parameters are calibrated using the tensile and compression tests. Detailed finite element models of the quasi-static and dynamic shear, tensile and compression tests were developed.

For most of the analysis in this current study, fibre crush is not considered a primary failure mode. Therefore, the fibre crush and shear punch damage parameter m3 was not calibrated by the inverse modelling technique described above as this would have required the development of

a potentially complex finite element model of the shear punch test setup. Instead an estimated baseline value of m3 = 2 was used in all models. This is considered to be an acceptable value for fibre crush damage.

4.5.5.1 Quasi-static matrix damage parameters

The matrix damage parameter m4 is calibrated for quasi-static shear loading by correlating the experimental quasi-static in-plane shear stress-strain results with simulation results.

Finite element model

Figure 4-6 shows the finite element model for the quasi-static [±45] in-plane shear test. The specimen was modelled with single point integration quadratic 8 node solid elements. The model has the same dimensions as the actual test specimen. A uniform square mesh density was used so as to avoid localisation and maintain an unbiased damage progression development. The mesh had elements with in-plane dimensions of 2.5 mm x 2.5 mm. Each ply is represented individually by a layer of solid elements. The boundary conditions for the quasi-static model are shown in Figure 4-6. Nodes at one end of the specimen are fully constrained in all directions while a prescribed velocity in the x-direction is applied at the other end. The ±45° layup in the test specimens was modelled by using the BETA option in the MAT 162 material input card to rotate the material axes in each element by 45° about the normal direction vector.

Calibration

The experimental quasi-static shear stress-strain response exhibited considerable non-linear hardening. In order to capture the non-linear hardening behaviour, a novel calibration strategy has been adopted. In this strategy the non-linear stress-strain behaviour is approximated to a bilinear response, see Figure 4-7. In Figure 4-7, section A-B approximates the initial elastic response (no damage). Point B marks the end of the elastic response and the onset of non-linear hardening and matrix damage. The value for shear stress at point B is taken as the maximum shear strength (S_{xy} = 23 MPa) for input into Equation 4-6. Based on observations from the single element analysis described above we know that $m < 0$ results in a hardening post-elastic stress-strain response. Therefore, section B-C in Figure 4-7 is calibrated using iterative simulations with

different values of m4 < 0. A value of m4 = -0.15 provided the best correlation with experimental results as shown in Figure 4-8.

Figure 4-9 shows the good agreement between the predicted matrix damage and experimentally observed damage pattern. Matrix damage is predicted along the 45° fibre orientation in the same 'V' shape as in the actual fractured test specimen.

4.5.5.2 Quasi-static tensile fibre damage parameters

The fibre damage parameters m1 and m2 are calibrated for quasi-static tensile loading by correlating the experimental quasi-static in-plane tensile stress-strain results with simulation results.

Finite element model

The [090] in-plane tensile model has a similar mesh and boundary conditions to the [±45] in-plane shear model (see Figure 4-6) with the exception that the fibre orientation is now [090].

Calibration

It is assumed that m1 = m2 because of the balanced, symmetric nature of the Twintex woven fabric material in-plane properties. Test results show that the Twintex material exhibits an elastic-brittle response when subjected to quasi-static tensile loading. Following several iterative simulations, a value of m1 = m2 = 4.0 yielded good agreement between the simulation and experimental stress-strain results as shown in Figure 4-10.

Figure 4-11 compares the predicted and experimental fibre damage. Experimental damage occurs in a fairly localised region along the gauge length near the grips. The predicted tensile fibre damage is over estimated. The simulation shows that fibre damage initiates near the moving grip and propagates along the entire gauge length (see Figure 4-11 (a)). The initiation of damage near the grips may be due to stress concentrations.

4.5.5.3 Quasi-static compression fibre damage parameters

The fibre damage parameters m1 and m2 are calibrated for quasi-static compression loading by correlating the experimental quasi-static in-plane compression stress-strain results with simulation results.

Finite element

Figure 4-12 shows the finite element model for the quasi-static [090] in-plane compression test. The dimensions of the model are similar to the actual test specimen. Each ply is represented individually by a layer of solid elements. The mesh had elements with in-plane dimensions of 2.5 mm x 2.5 mm. The boundary conditions for the quasi-static model are shown in Figure 4-12. Nodes at one end of the specimen are fully constrained in all directions while a prescribed velocity in the negative x-direction is applied at the other end.

Calibration

Like the tensile results, the compression test results exhibited an elastic-brittle stress-strain response. Following several iterations, a value of m1 = m2 = 4.0 yielded good agreement between the simulation and experimental stress-strain results as shown in Figure 4-13.

Figure 4-14 compares the predicted and experimental compression fibre damage. Experimental damage occurs in a fairly localised region in the middle of the gauge section. The predicted compression fibre damage is over estimated. The simulation shows that fibre damage initiates in the middle of the specimen and propagates along the entire gauge length.

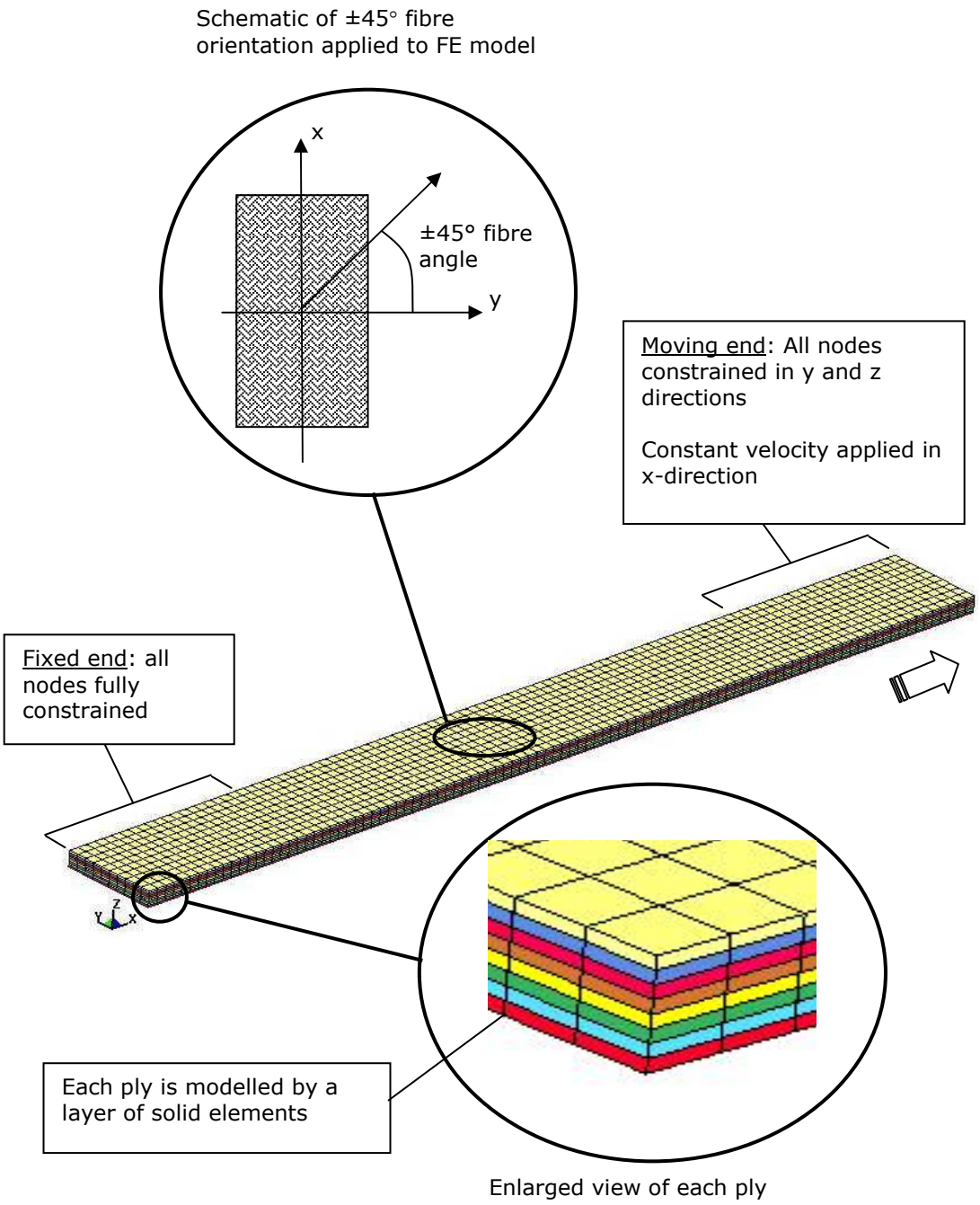

Figure 4-6. Quasi-static in-plane ±45° tensile shear finite element model and boundary conditions. The same model is used for the quasi-static in-plane tensile analysis with fibres oriented at [090].

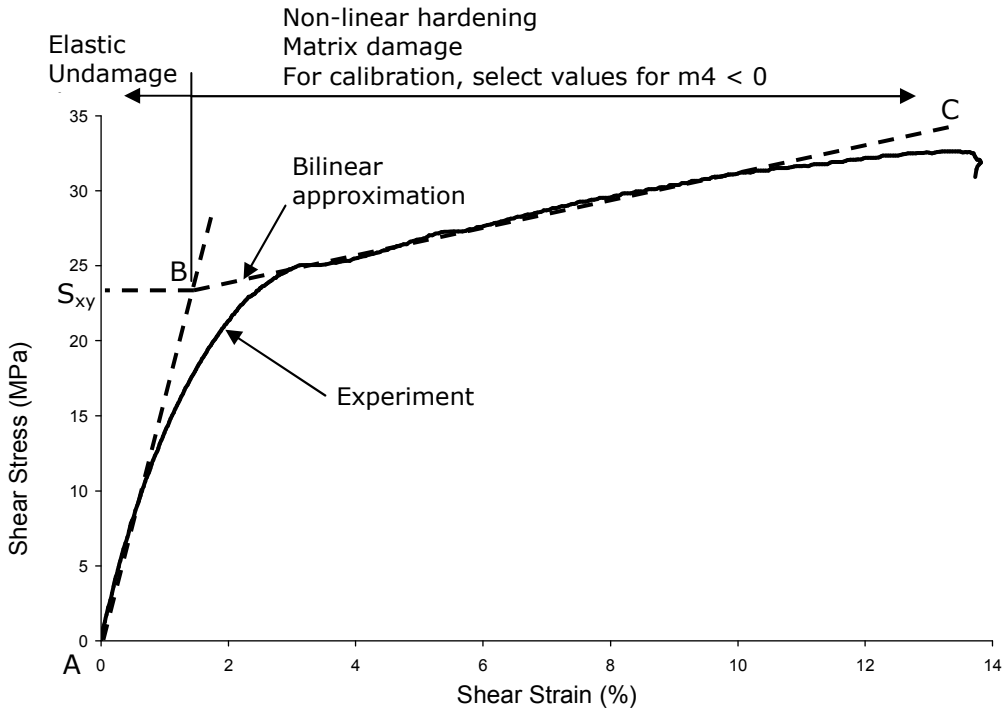

Figure 4-7. The non-linear quasi-static shear stress-strain behaviour is approximated to a bilinear response for the calibration of the matrix damage parameter m4.

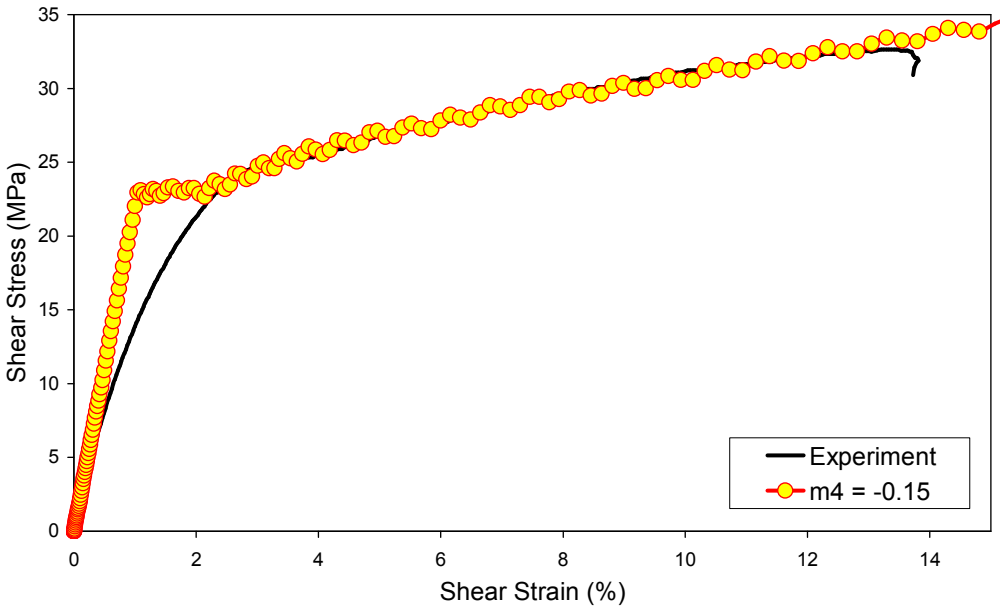

Figure 4-8. Calibration of damage parameter m4 by comparing the predicted and experimental stress-strain curves for the quasi-static [±45] in-plane shear test.

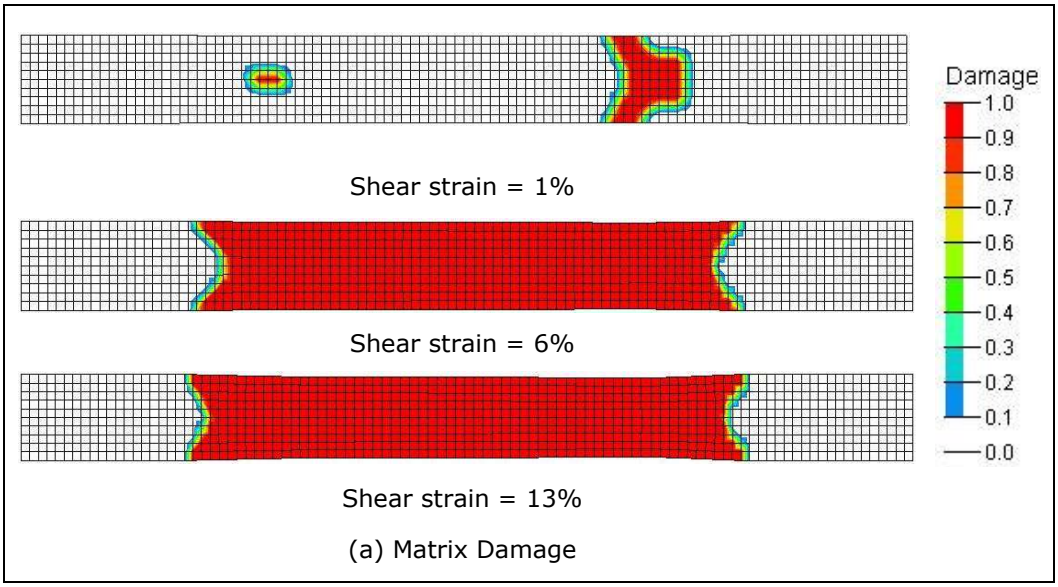

(a) Matrix Damage

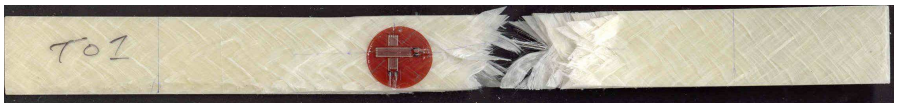

(b) Failed specimen

Figure 4-9. Comparison of experimental and simulation damage results for quasi-static [±45] in-plane shear test (a) predicted matrix damage (b) failed specimen.

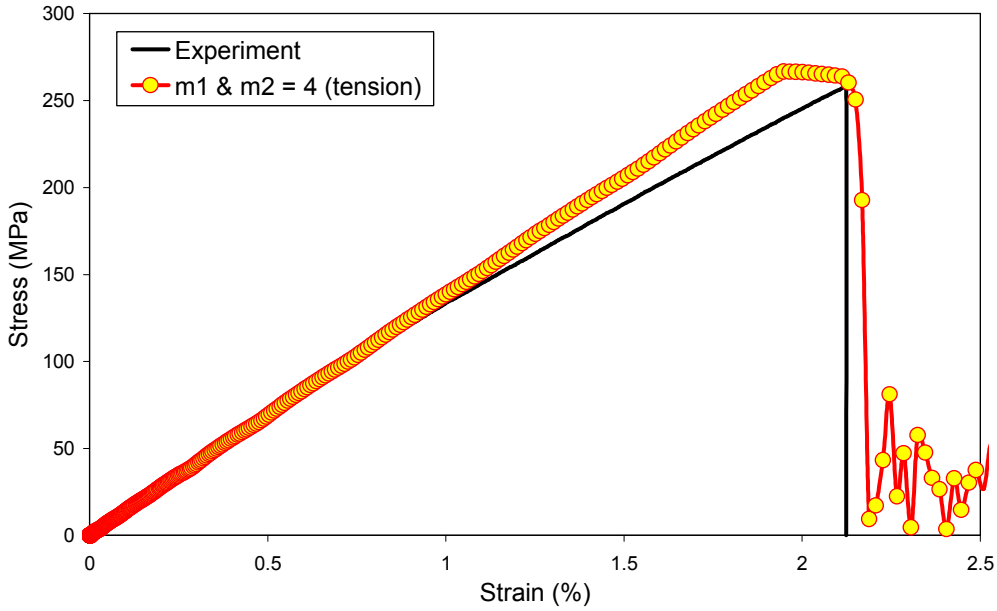

Figure 4-10. Calibration of damage parameters m1 and m2 by comparing the predicted and experimental stress-strain curves for the quasi-static [090] in-plane tensile test

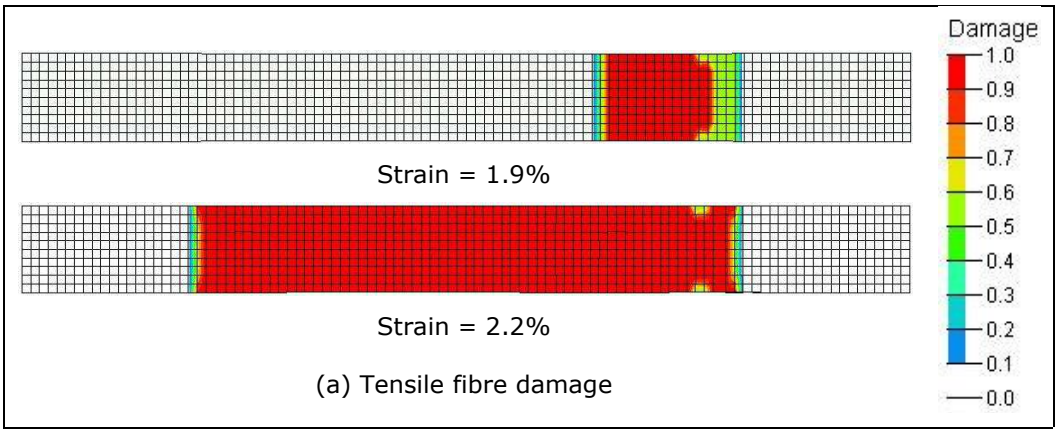

(a) Tensile fibre damage

(b) Failed specimen

Figure 4-11. Comparison of predicted damage and experimental results for the quasi-static [090] in-plane tensile test (a) predicted tensile fibre damage (b) failed specimen.

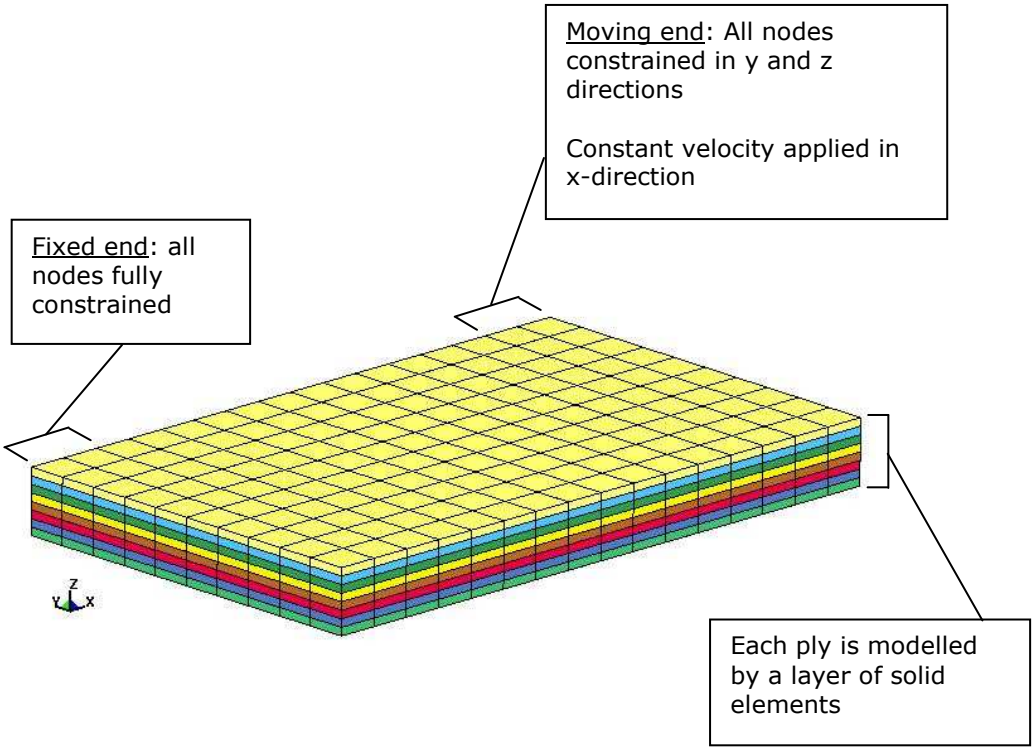

Figure 4-12. Quasi-static in-plane compression finite element model and boundary conditions.

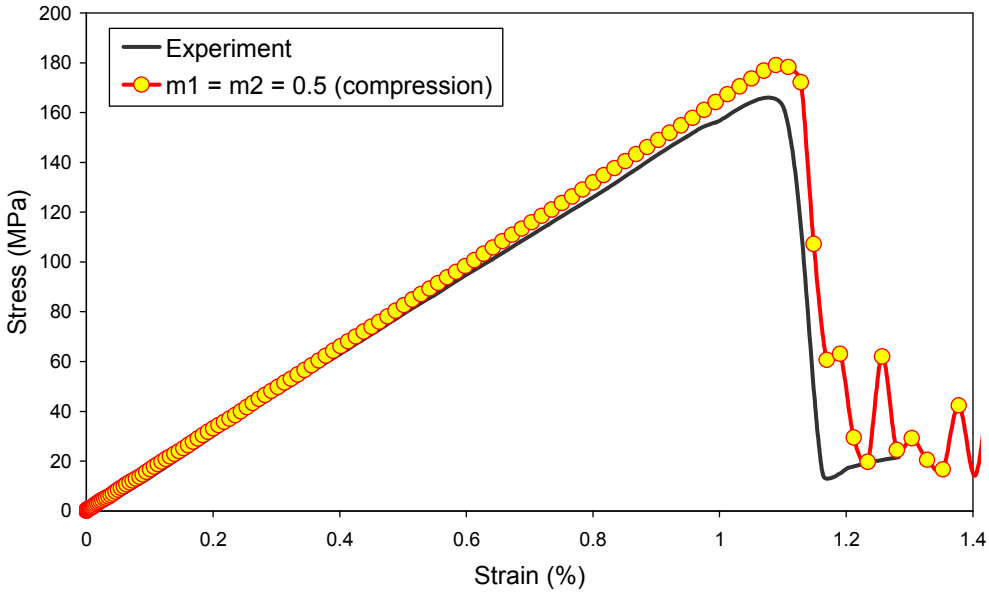

Figure 4-13. Calibration of damage parameter m4 by comparing the predicted and experimental stress-strain curves for the quasi-static [090] in-plane compression test.

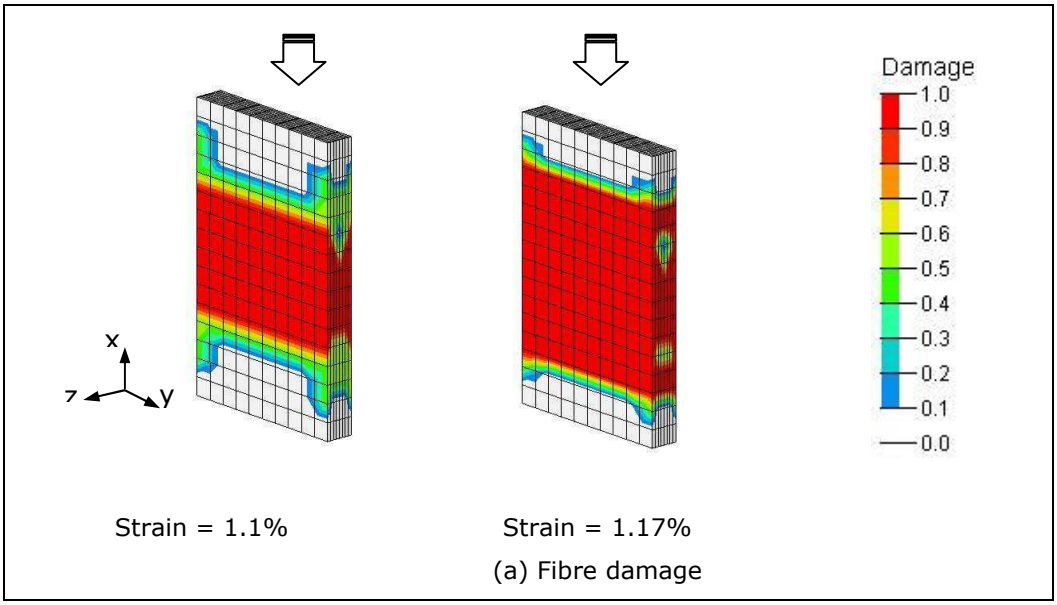

(a) Fibre damage

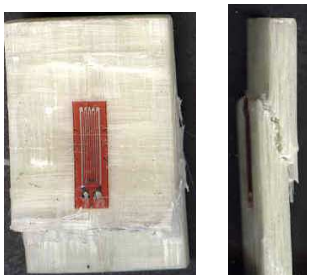

(b) Failed specimen

Figure 4-14. Comparison of experimental and predicted damage results for quasi-static [090] compression test (a) predicted compression fibre damage (b) failed specimen.

4.5.5.4 Dynamic matrix damage parameters

The matrix damage parameter m4 is calibrated for dynamic shear loading by correlating the experimental dynamic in-plane shear stress-strain results with simulation results.

Finite element model

Figure 4-15 shows the finite element model for the dynamic [±45] in-plane shear test. Attempts were made to model the boundary conditions in the test as closely as possible. Nodes at one end of the specimen are fully constrained in all directions while a rigid steel grip is attached to the other end. The rigid grip was given an initial velocity and an additional nodal lump mass (100 kg) such that the experimental impact mass, energy and strain rates were simulated. The rigid grip was given the same initial velocities as in the actual dynamic tests, i.e. 3, 5 and 7 ms^{-1} that corresponds to strain rates of 33, 70, and 91 s^{-1}, respectively.

Calibration

The dynamic shear stress-strain response exhibited non-linear hardening. Therefore, the same novel bilinear calibration strategy that was used in the quasi-static case is applied here as shown in Figure 4-16. The dynamic shear strength values that were obtained from transition point B for input into Equation 4-6 are listed in Table 4-2.

Following several iterations, Figure 4-17 (a) –(c) shows that m4 = -4 provides a good correlation between the simulation and the experimental stress-strain results for all the strain rates in this study.

Figure 4-18 shows the good agreement between the predicted matrix damage and experimentally observed damage pattern for the highest strain rate test (91 s^{-1}). Matrix damage is predicted along the 45° fibre orientation in the same V shape as in the actual fractured specimen.

Dynamic shear properties

The calibrated dynamic in-plane shear modulus and strength that are listed in Table 4-2 will be used in the dynamic validation and component analysis.

The proposed procedure for selecting the appropriate shear properties for various strain rates is as follows: Preliminary simulations of the dynamic model are run with the static shear properties. The strain rate is derived for an element in the failure region. Using Table 4-2 the dynamic shear properties that correspond with the strain rate in the model are selected for input. The simulations are then repeated with the selected dynamic shear properties.

Table 4-2. Calibrated in-plane shear properties for Twintex

Strain Rate (s^{-1})	G_{xy} (GPa)	S_{xy} (MPa)
Static	1.79	23
33	0.33	7.5
70	0.47	14
91	0.27	11

4.5.5.5 Dynamic tensile fibre damage parameters

The fibre damage parameters m1 and m2 are calibrated for dynamic tensile loading by correlating the experimental dynamic in-plane tensile stress-strain results with simulation results.

Finite element model

The finite element model for the dynamic [090] in-plane tensile test has a similar mesh and boundary conditions to the dynamic [±45] in-plane shear model (see Figure 4-15) with exception that the fibre orientation is now [090]. The rigid grip was given the same initial velocities as in the actual dynamic tests, i.e. 3, 5 and 7 ms^{-1} that corresponds to strain rates of 36, 50, and 70 s^{-1}, respectively.

Calibration

Experiments reveal that under tensile dynamic loading the material exhibits an elastic-plastic response over a large strain range. Following several iterations, Figure 4-19 (a) – (c) shows that m1 = m2 = 0.05 provides good agreement between the simulations and experimental stress-strain results for all strain rate levels applied in this study.

Figure 4-20 shows good agreement between the experimental and the predicted tensile fibre damage progression for the highest tensile strain rate test (70 s^{-1}).

4.5.5.6 Dynamic compression fibre damage parameters

The fibre damage parameters m1 and m2 are calibrated for dynamic compression loading by correlating the experimental dynamic in-plane compression stress-strain results with simulation results.

Finite element model

The mesh and boundary conditions for the dynamic [090] compression model is shown in Figure 4-21. Nodes at one end of the specimen are fully constrained in all directions while a rigid steel grip is attached to the other end. The rigid grip was given an initial velocity and an additional nodal lump mass (40 kg) such that the experimental impact mass, energy and strain rates were simulated. The rigid grip was given the same initial velocities as in the actual dynamic tests, i.e. 3, 5 and 7 ms^{-1} that corresponds to strain rates of 56, 78, and 126 s^{-1}, respectively.

Calibration

The experimental dynamic compression stress-strain response is highly non-linear. Following several iterative simulation runs, Figure 4-22 (a) – (c) shows that damage parameters m1 = m2 = 0.5 results in a good correlation between the simulation and experimental results for all strain rates applied in this study.

Figure 4-23 shows good agreement between experimental and the predicted compression fibre damage for the highest compression strain rate test (126 s^{-1})

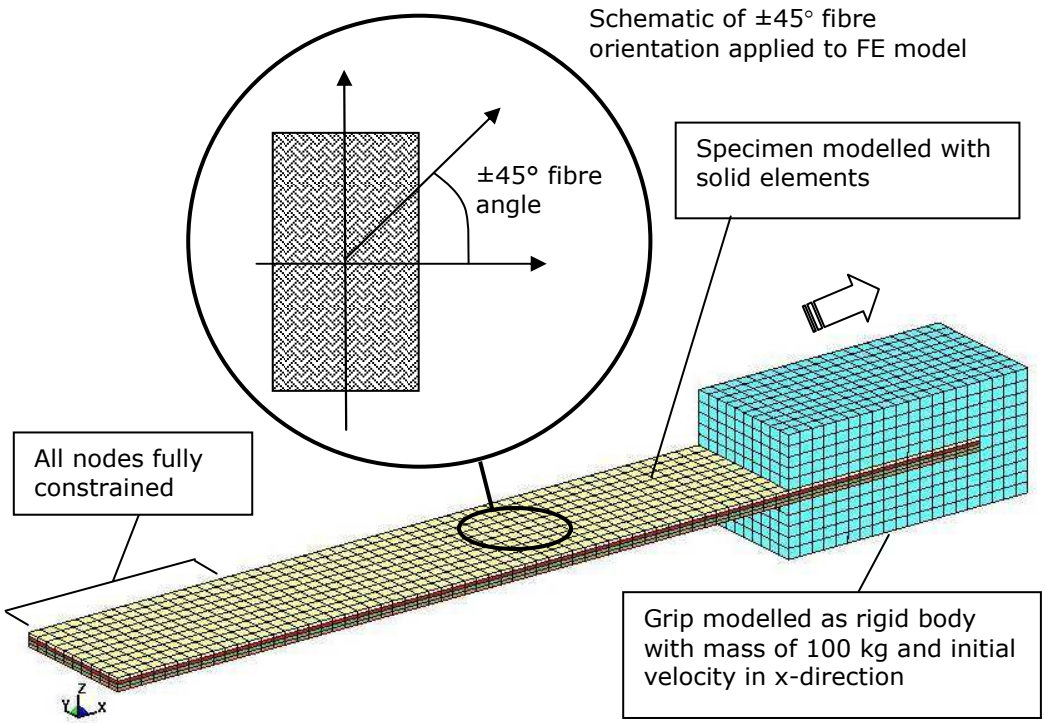

Figure 4-15. Dynamic in-plane ±45° tensile shear finite element model and boundary conditions. The same model is used for the dynamic in-plane tensile analysis with fibre oriented at [090].

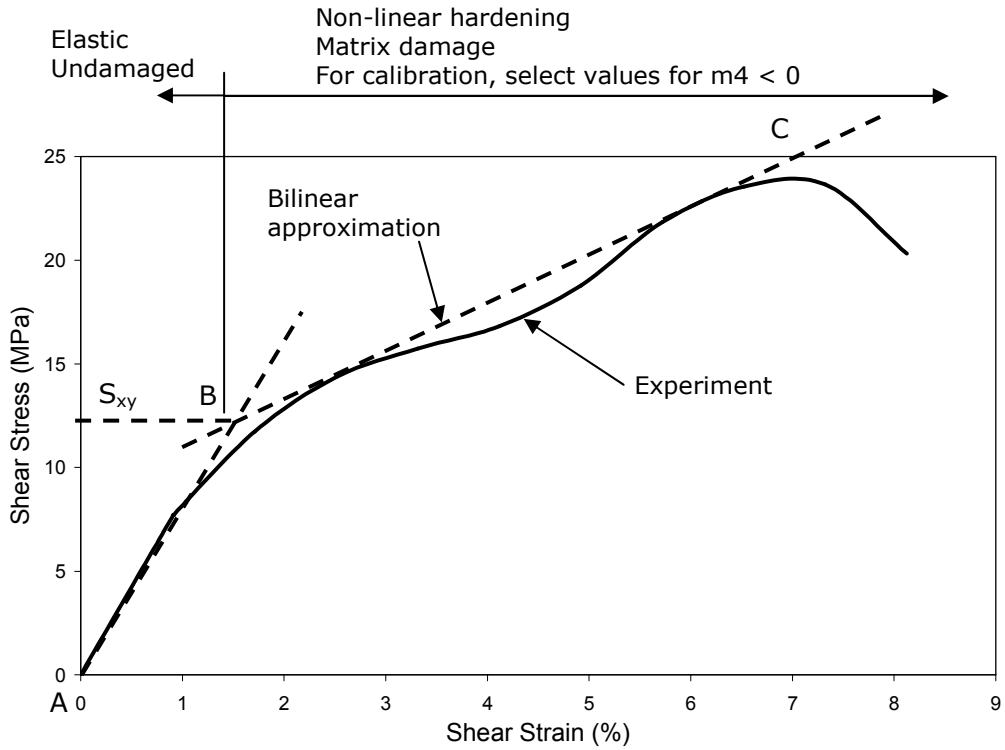

Figure 4-16. The non-linear dynamic shear stress-strain behaviour is approximated to a bilinear response for the calibration of matrix damage parameter m4.

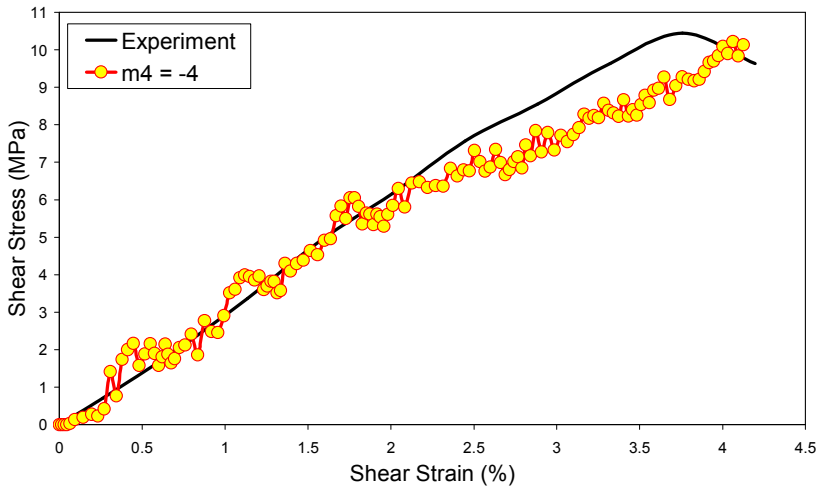

(a)

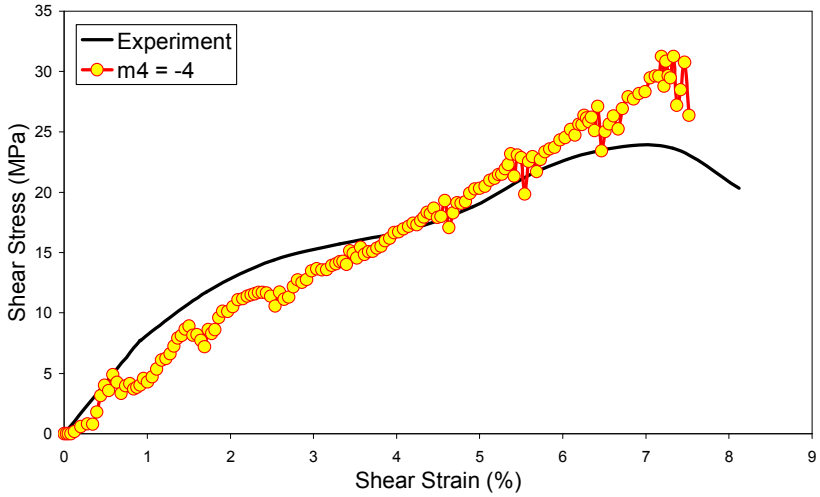

(b)

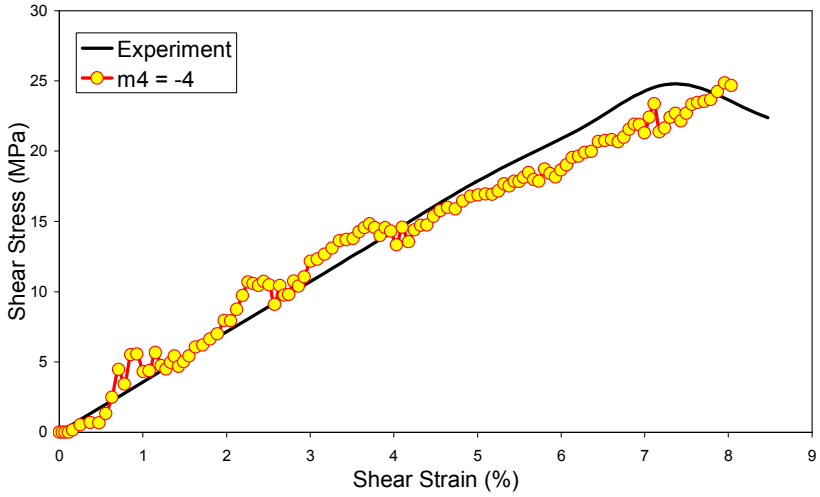

(c)

Figure 4-17. Calibration of damage parameter m4 by comparing the predicted and experimental stress-strain curves for the dynamic [±45] in-plane shear tests at various strain rates (a) 33 s^{-1} (b) 70 s^{-1} (c) 91 s^{-1}.

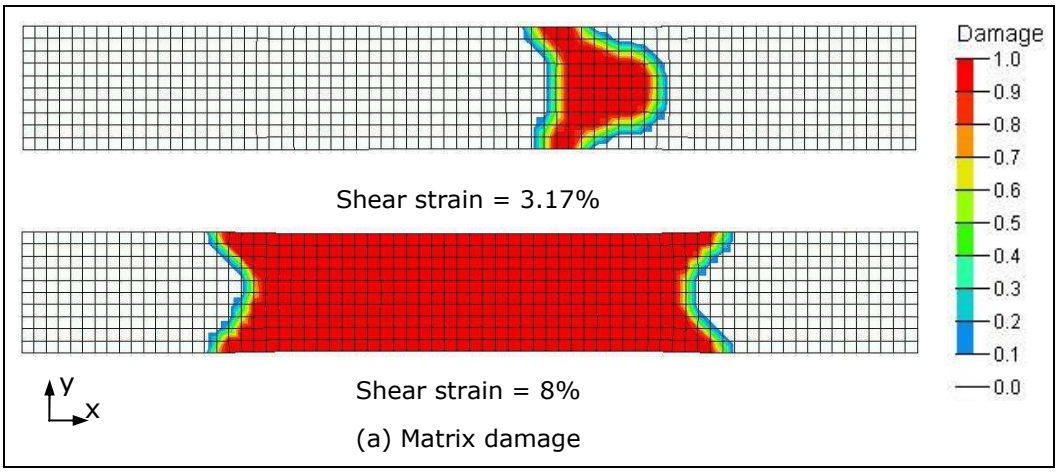

(a) Matrix damage

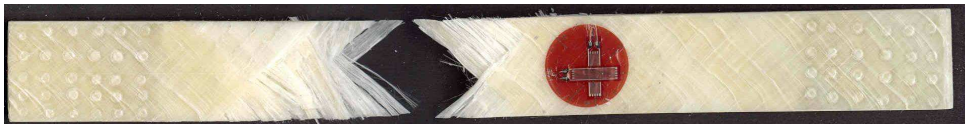

(b) Failed specimen

Figure 4-18. Comparison of predicted and experimental damage results for the dynamic [±45] in-plane shear tests at a strain rate of 91 s^{-1}. (a) predicted matrix damage progression (b) failed specimen.

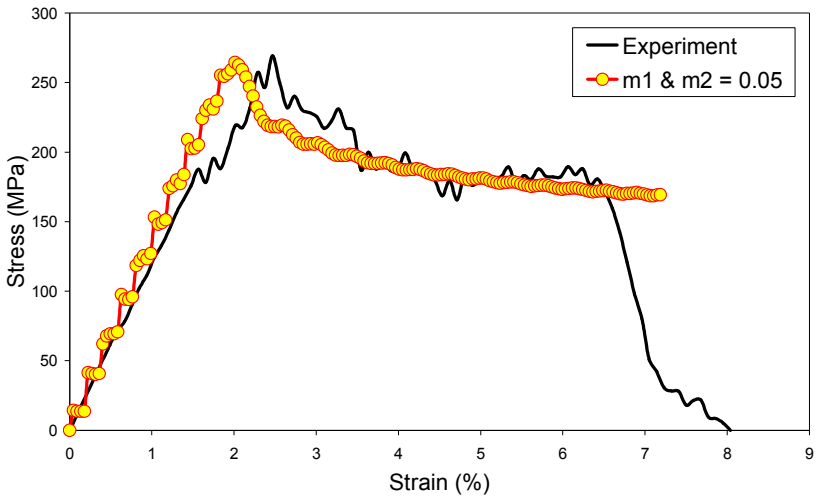

(a)

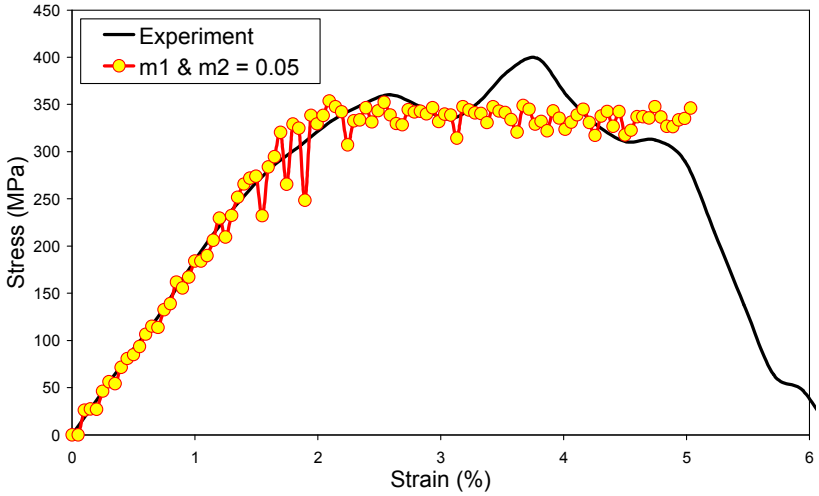

(b)

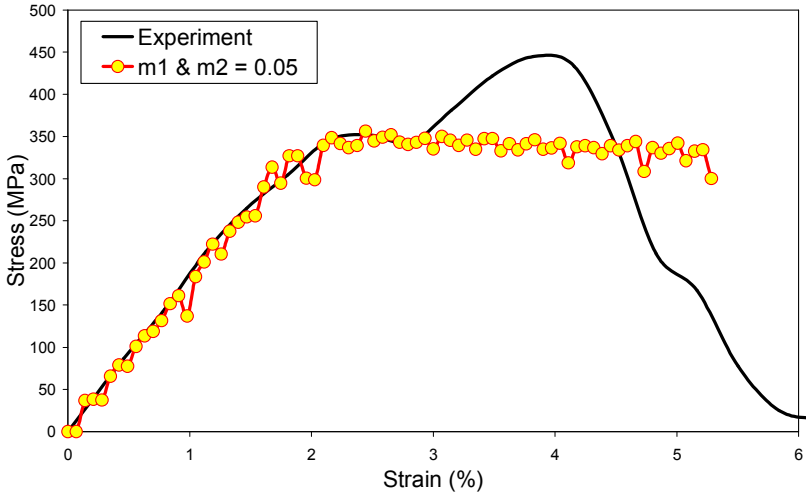

(c)

Figure 4-19. Calibration of damage parameters m1 and m2 by comparing the predicted and experimental stress-strain curves for the dynamic [090] in-plane tensile tests at various strain rates (a) 36 s^{-1} (b) 50 s^{-1} (c) 70 s^{-1}.

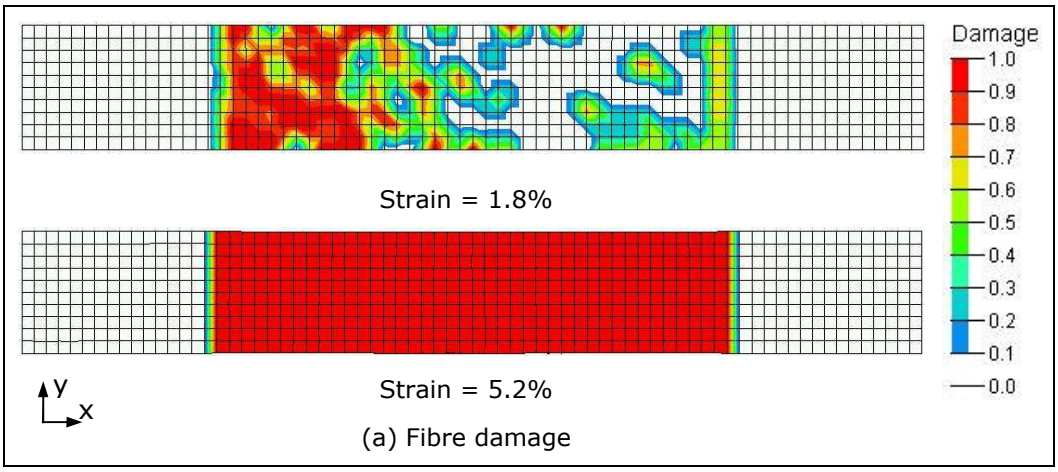

(a) Fibre damage

(b) Failed specimen

Figure 4-20. Comparison of predicted and experimental damage results for the dynamic [090] in-plane tensile tests at a strain rate of 70 s^{-1}. (a) predicted fibre damage progression (b) failed specimen.

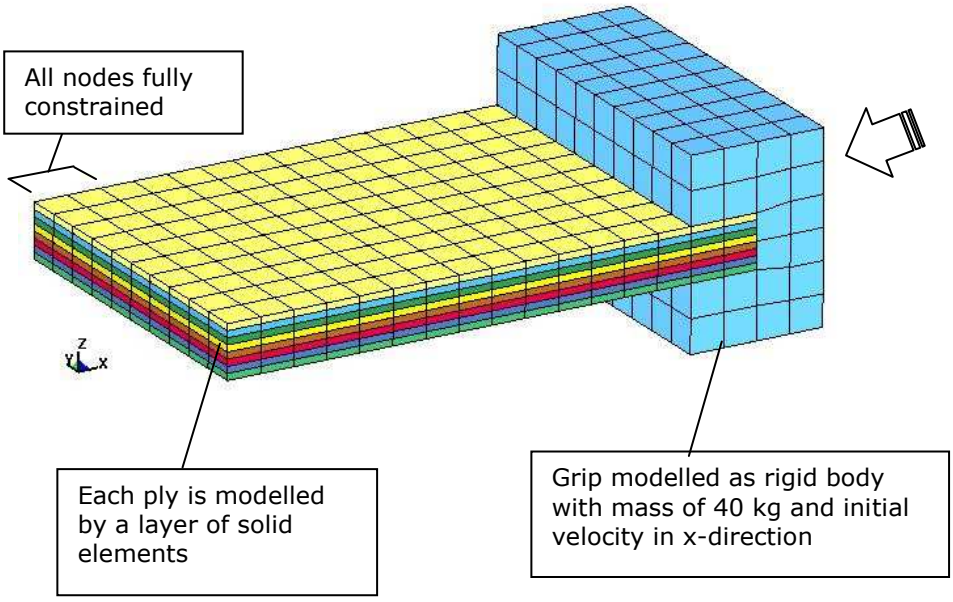

Figure 4-21. Dynamic in-plane compression finite element model and boundary conditions.

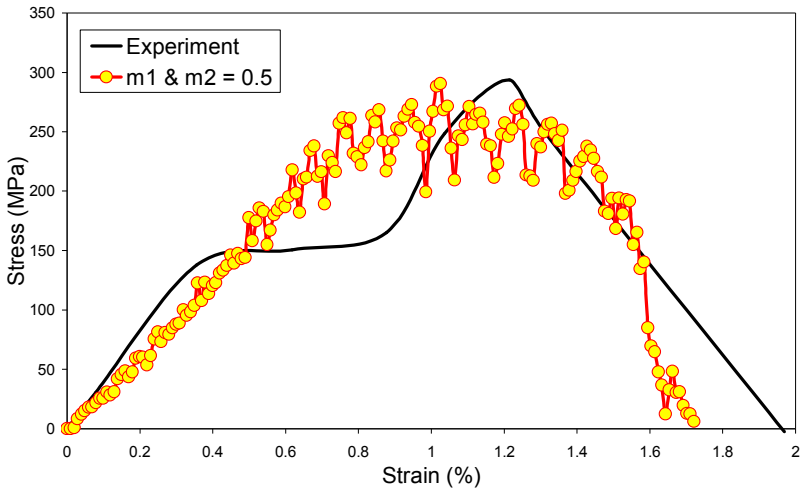

(a)

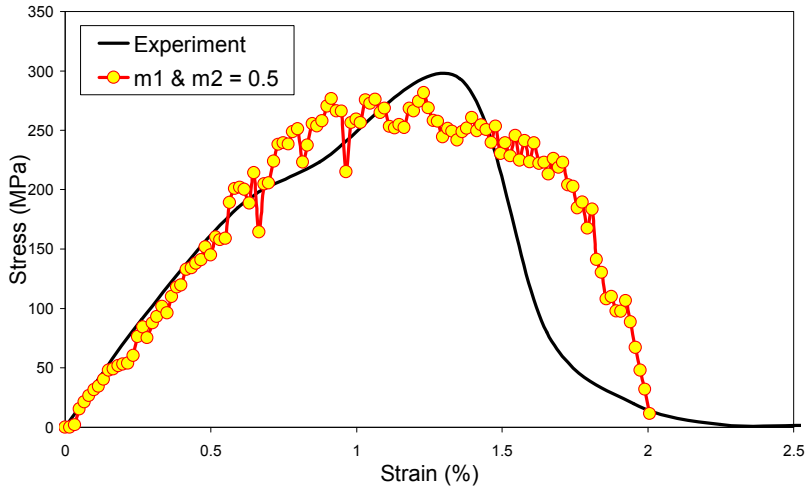

(b)

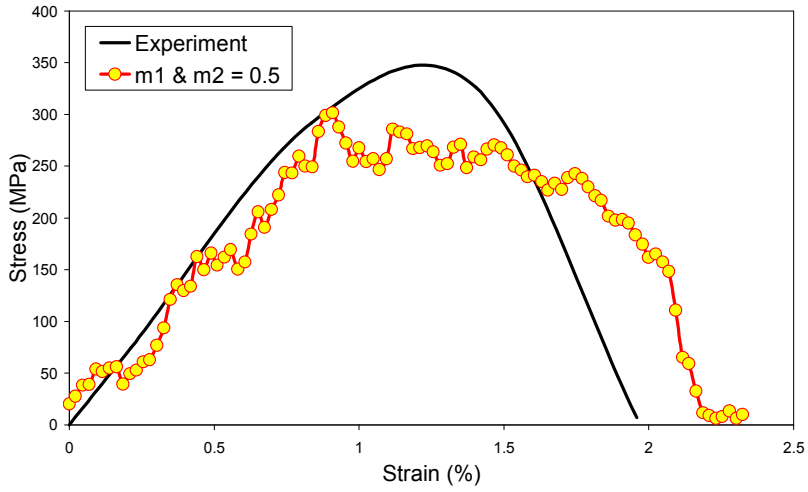

(c)

Figure 4-22. Calibration of damage parameters m1 and m2 by comparing the predicted and experimental stress-strain curves for the dynamic [090] in-plane compression tests at various strain rates (a) 56 s^{-1} (b) 78 s^{-1} (c) 126 s^{-1}.

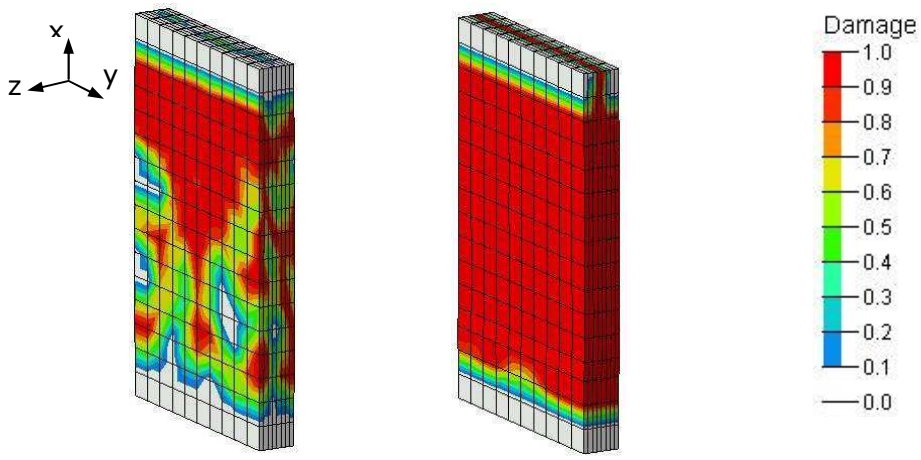

(a) Fibre damage

(b) Failed specimen

Figure 4-23. Comparison of predicted and experimental damage results for the dynamic [090] in-plane compression tests at a strain rate of 126 s^{-1}. (a) predicted fibre damage progression (b) failed specimen.

4.5.6 Mesh Sensitivity

A mesh sensitivity study was performed using the quasi-static in-plane tensile model with three different mesh sizes, shown in Figure 4-24. All the models have a uniform mesh with square elements. The mesh used in the tensile simulations described above is taken as the baseline model which has elements with in-plane dimensions of 2.5 mm x 2.5 mm. A coarse mesh and a fine mesh with element sizes of 5 mm x 5 mm and 1.5 mm x 1.5 mm, respectively, were developed. All the models had one element layer per ply (8 plies).

Figure 4-25 shows comparison of the experimental stress-strain results with the simulation results for all three mesh densities. The different mesh densities have no effect on the predicted elastic response and peak stress. Figure 4-25 shows that the fine and baseline mesh appear to be converging and exhibit an elastic-brittle like response that correlates with the test results. In contrast, the coarse mesh response was more ductile. It is reasonable to conclude that as mesh density increased the damage softening response became more gradual (ductile).

Figure 4-26 compares the experimental damage with the predicted fibre damage for the various densities. At a strain of 1.96%, slightly more damage is predicted in the coarse mesh in comparison to the baseline and fine mesh. Damage was predicted along the entire length of the specimen at a strain of 2.2% for all mesh densities.

The predicted damage is mesh sensitive; however, there appears to be convergence between the baseline and fine mesh cases.

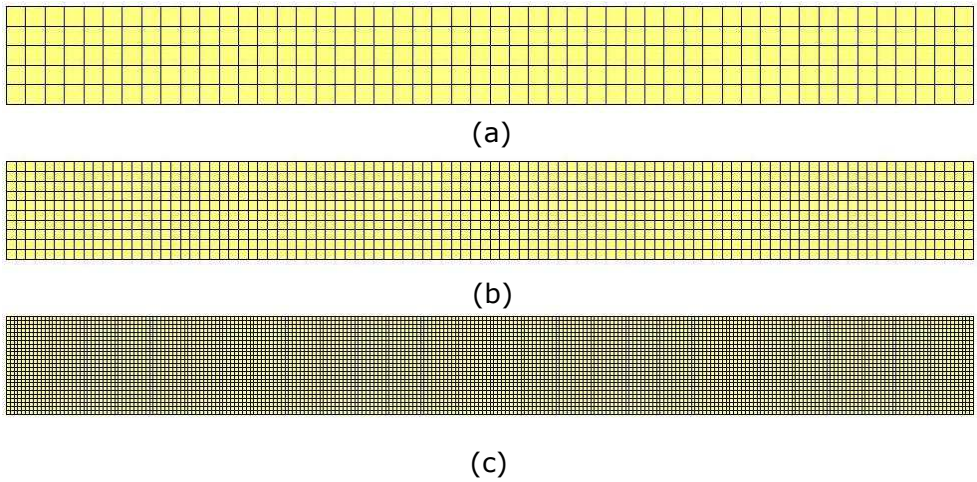

Figure 4-24. (a) Coarse mesh (b) baseline mesh (c) fine mesh.

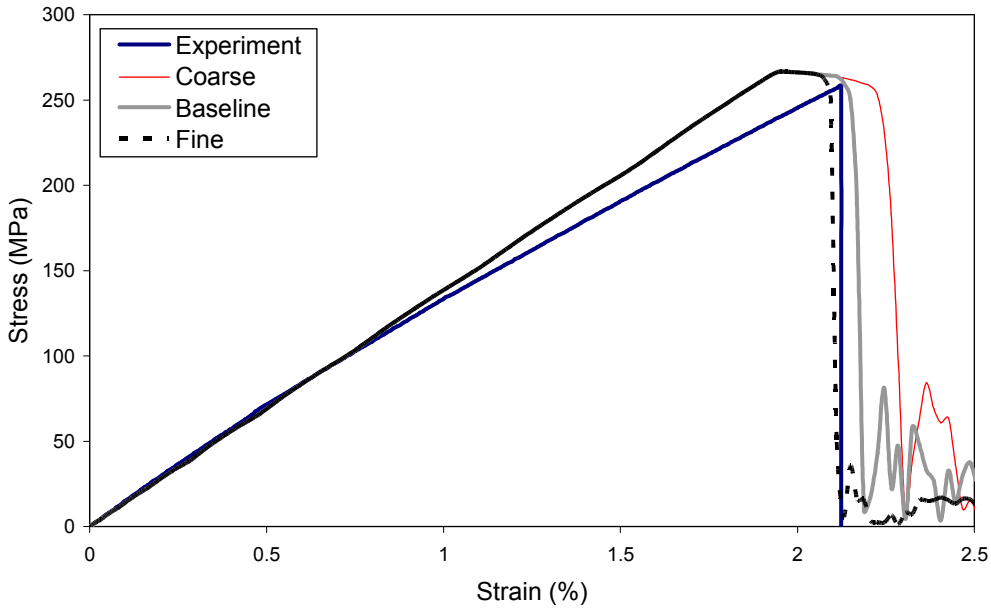

Figure 4-25. Comparison of predicted and experimental stress-strain curves for the quasi-static [090] in-plane tensile test for various mesh densities.

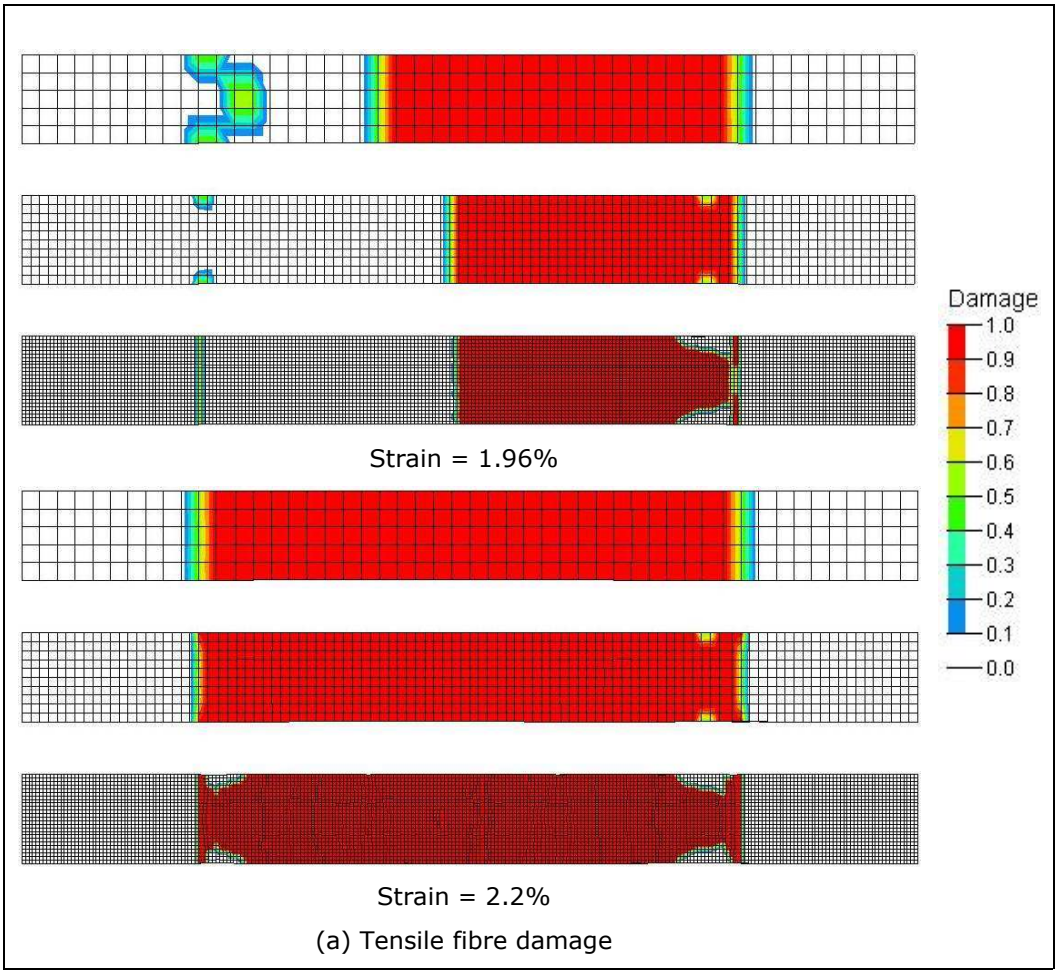

(a) Tensile fibre damage

(b) Failed specimen

Figure 4-26. Comparison of predicted damage and experimental results for the quasi-static [090] tensile test for various mesh densities (a) predicted fibre damage (b) failed specimen.

Table 4-3. Input elastic properties for MAT 162 for modelling Twintex [090] fabric skins.

Parameter	Symbol	Value
Density	ρ	1500 kg/m^3
Longitudinal Young's modulus	E_x	14 GPa
Transverse Young's modulus	E_y	14 GPa
Through-thickness Young's modulus	E_z	5.3 GPa
Poisson's ratio	υ_{yx}	0.12
	υ_{zx}	0.14
	υ_{zy}	0.15
Shear modulus, x-y plane	G_{xy}	1.79 GPa
Shear modulus, y-z plane	G_{yz}	1.66 GPa
Shear modulus, z-x plane	G_{zx}	1.79 GPa
Longitudinal tensile strength	S_{xT}	269 MPa
Longitudinal compressive strength	S_{xC}	178 MPa
Transverse tensile strength	S_{yT}	269 MPa
Transverse compressive strength	S_{yC}	178 MPa
Through-thickness tensile strength	S_{zT}	25 MPa
Crush strength	S_{Fz}	300 MPa
Fibre shear strength	S_{FS}	110 MPa
Shear strength, x-y plane	S_{xy}	23 MPa
Shear strength, y-z plane	S_{yz}	12 MPa
Shear strength, z-x plane	S_{zx}	13.6 MPa

Table 4-4. Calibrated MAT 162 damage parameters for Twintex

Load type	Strain rate (s^{-1})	Damage parameters			
		m1	m2	m3	m4
Shear	Static				-0.15
	33				-4
	70				-4
	91				-4
Tensile	Static	4	4	2	
	36	0.05	0.05	2	
	50	0.05	0.05	2	
	70	0.05	0.05	2	
Compression	Static	4	4	2	
	56	0.5	0.5	2	
	78	0.5	0.5	2	
	126	0.5	0.5	2	

4.6 Material Model Validation

The previous section has outlined a methodology for calibrating the material model damage parameters for quasi-static and dynamic loading cases. This section describes the validation of the material model and the calibrated damage parameters. Quasi-static and dynamic three-point bending tests and a series of low velocity falling weight impact tests are used as a basis for validating the model. These coupon tests were selected because these modes of loading are considered to be representative of the complex nature of loading in structural composite components subjected to crash loads. In the validation process, predicted results are compared with the various experimental results. These comparisons include force and displacement-time histories, damage modes, damage shape and size and damage sequence.

The thermoplastic composite coupon specimens are modelled with MAT 162 using the baseline elastic properties and calibrated damage parameters listed in Table 4-3 and Table 4-4, respectively. For the dynamic analysis, the strain rate parameters listed in Table 4-1 are applied.

4.6.1 Quasi-Static Three - Point Bending Test

4.6.1.1 Experimental setup

Details of the experimental quasi-static three-point bending tests were presented in the previous Chapter. The quasi-static tests were performed on an electro-mechanical test machine at a constant crosshead speed of 5 mm min^{-1}. Twintex coupon beam specimens were simply supported over a span of 80 mm on 5 mm diameter cylindrical rods. A 10 mm diameter cylindrical rod is used to apply a load to the centre of the specimen. All specimens had a stacking a sequence of [090] with a nominal thickness of 4 mm and width of 25 mm. The specimen length is 120 mm.

4.6.1.2 Finite element model

The tests results have shown that a symmetric mode of deformation is expected for this material and geometry; therefore, only half the beam was modelled in order to reduce computational time. The finite element mesh

and boundary conditions for the bending model are shown in Figure 4-27. The beam mesh is refined in the area under the impactor with elements having in-plane dimensions of 1.5 mm x 1.56 mm. The beam mesh was also refined in areas that were in contact with the cylindrical supports. All components are modelled with single point integration quadratic eight node solid elements. Each ply in the beam is represented individually by a layer of solid elements. The cylindrical steel supports and impactor were modelled as rigid bodies. The supports are fully constrained while the impactor is only allowed to translate along the z-axis. The impactor is given a prescribed velocity that is much higher than the actual test in order to reduce the computational time although quasi-static material properties are used. The simulation was terminated when the impactor reached a maximum displacement of 20 mm. Contact between the impactor and the composite plate was modelled using the surface to surface contact algorithm. The same contact type was used to model contact between the composite beam and the supports

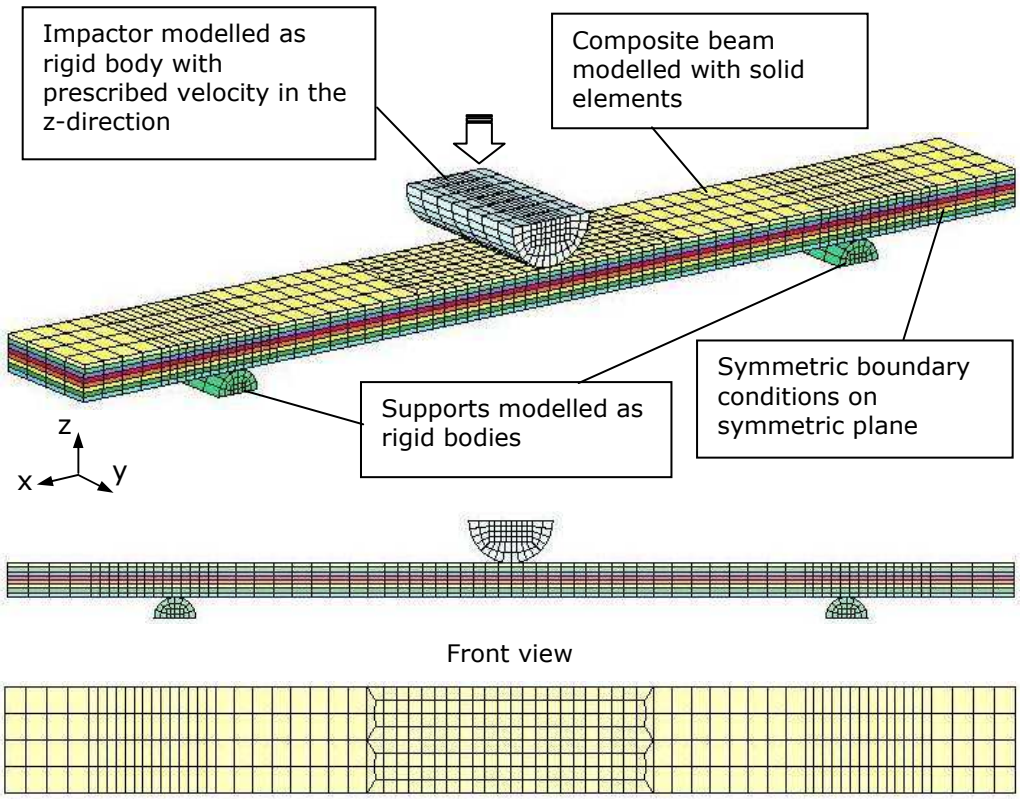

Figure 4-27. Finite element model of quasi-static three-point bending test.

4.6.1.3 Results

Figure 4-28 shows a comparison of the predicted and experimental force-displacement results for the model with the static calibrated parameters. The simulation response is over stiff and the peak load is under estimated by 24 %. In order to ascertain the reason for the discrepancies between the simulations and experimental results, a sensitivity study is conducted.

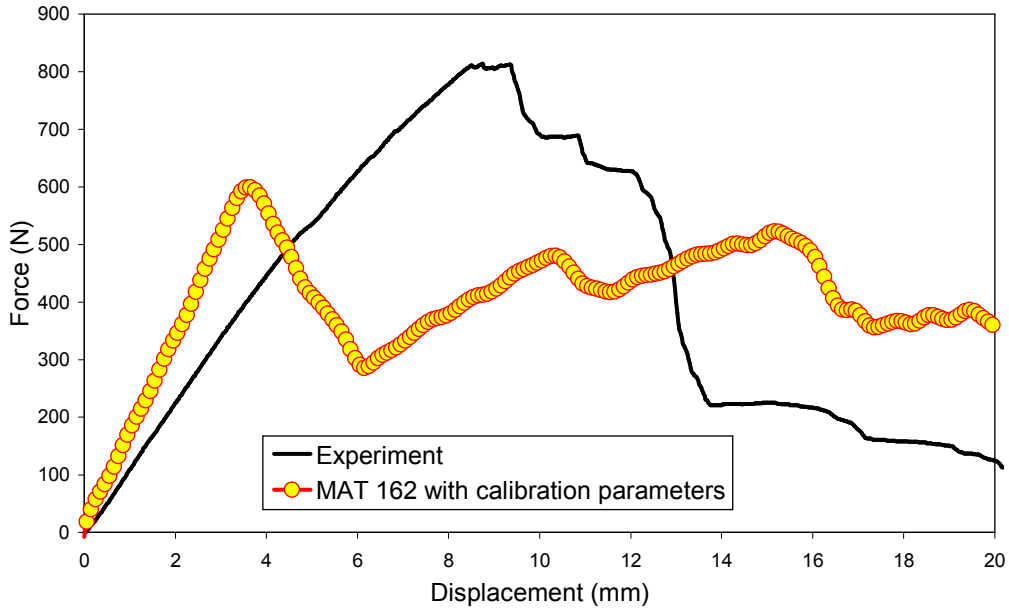

Figure 4-28. Comparison of the predicted and experimental force-displacement response for quasi-static bending model with calibration parameters.

4.6.1.4 Model refinement

The first step in improving the simulation results was to perform a mesh density study. If discrepancies are still observed then the material properties and parameters are refined.

Mesh density

A mesh sensitivity study is conducted using three different mesh densities. The mesh that was used in the initial analysis described above is considered as a baseline model. Two other models were create with different mesh densities, one being a fine mesh under the impactor with elements having in-plane dimensions of 1.5 mm x 0.78 mm and the other a coarse mesh with elements size 2.5 mm x 2.5 mm. All the models have

one solid element layer per ply. Figure 4-29 shows the various mesh densities.

Figure 4-30 shows the force-displacement histories for the various mesh densities. Results obtained for both the coarse and fine mesh are virtually the same as the baseline model, thus exhibiting the same poor correlation between the simulation and experimental results. Therefore, it is reasonable to conclude that the discrepancies between the simulation and experimental results are not related to the mesh density of the beam.

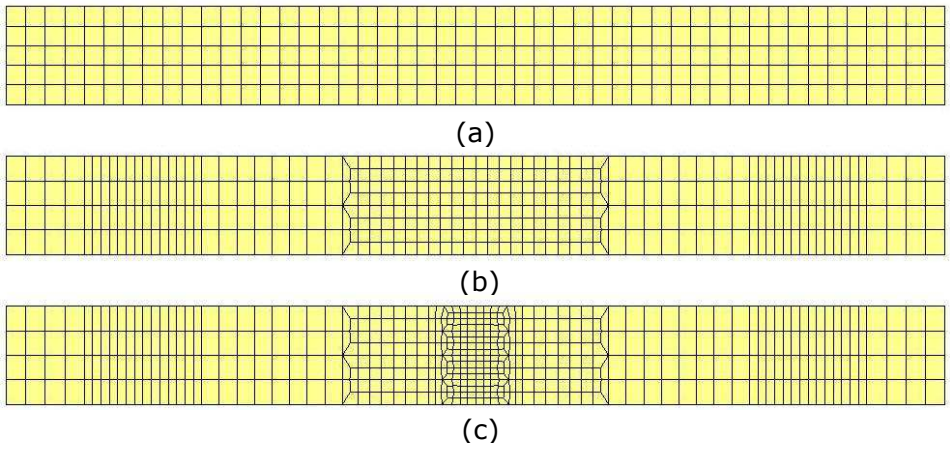

Figure 4-29. Mesh density study (a) Coarse mesh (b) baseline mesh (c) fine mesh.

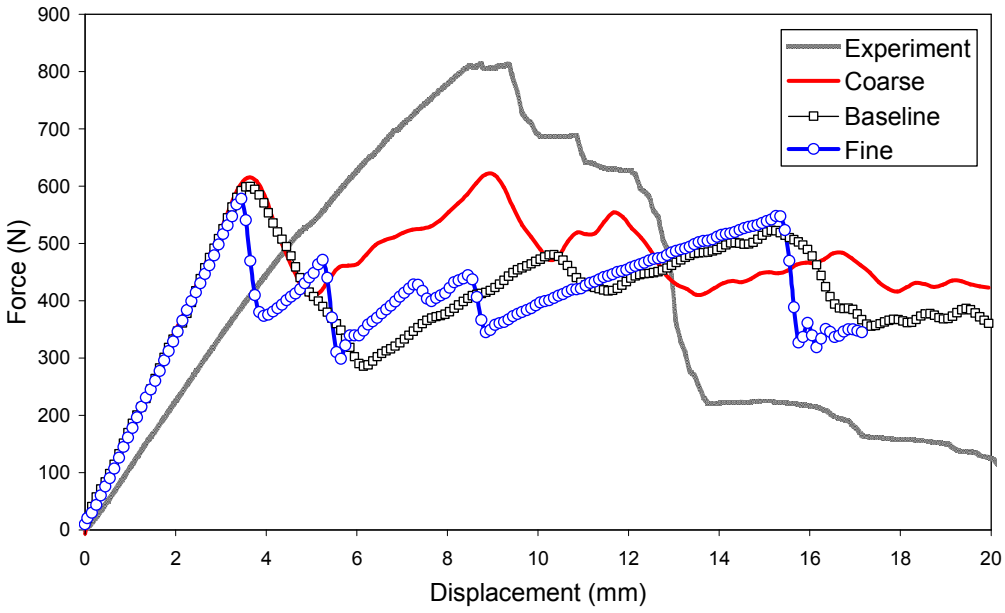

Figure 4-30. Comparison of the predicted and experimental force-displacement response for quasi-static bending model with various mesh densities.

Material properties and damage parameters

In order to improve the predicted results and better understand the reasons for the discrepancies which we have shown to be not mesh related, the material properties and calibrated damage parameters are analysed and refined. In particular the elastic modulus and fibre damage parameters m1 and m2 were investigated using the baseline mesh.

Firstly, the in-plane elastic modulus is refined. It was observed that the average static flexural modulus for Twintex is 8.93 GPa which is 36% less than the in-plane tensile and compression elastic modulus (14 GPa). Therefore, the effect of reducing the elastic modulus to a value similar to the material flexural modulus was investigated using a model with $E_x = E_y = 10$ GPa. Figure 4-31 shows that the simulation with E = 10 GPa gave a good correlation between the predicted and experimental slope of the force-displacement response. However, the peak load is still significantly under estimated.

As a further step, the stress-time response of two elements in the centre of the beam is compared with the force-time results. One element is located at the top surface and the other is at the bottom surface. As expected, Figure 4-32 shows that the element in the top surface is in compression while the bottom element is in tension. Failure first occurs in the compression element which corresponds with the overall failure point for the beam. The observed brittle response of the compression element reflects the high calibration values used for the fibre damage parameters m1 = m2 = 4 which appears to be the cause of the significant under estimation of the overall peak force. Therefore, iterations of simulations were performed with low values for the fibre damage parameters while the elastic modulus was kept at a constant value of 10 GPa. Figure 4-33 shows that m1 = m2 =0.5 provides a good agreement between the simulation and experimental force-displacement results. This simulation is now referred to as the "refined model." The results of the "refined model" indicate that the tensile and compression response of the quasi-static three-point bending test are more elastic-plastic than elastic-brittle.

Figure 4-34 shows the good agreement between the experimental and predicted deformation for the "refined model". The macroscopic damage

modes and sequence show reasonable agreement with the experimental observations where damage occurs in a localised region directly under the impactor. The simulation shows that the initial damage is by matrix and compression fibre failure occurring due to compression and shear stresses in the top surface of the beam. Then matrix and tensile fibre damage develop in the bottom surface due to tensile and shear stresses. Interlaminar stresses also cause the development of delamination at the mid-plane.

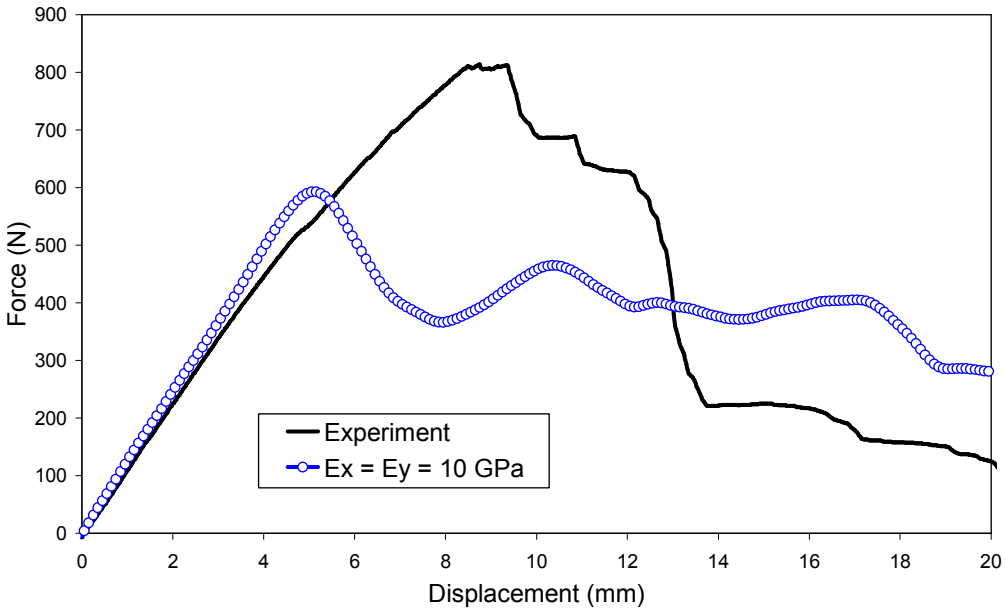

Figure 4-31. Comparison of the predicted and experimental force-displacement response for quasi-static three-point bending model with $E_x = E_y = 10$ GPa.

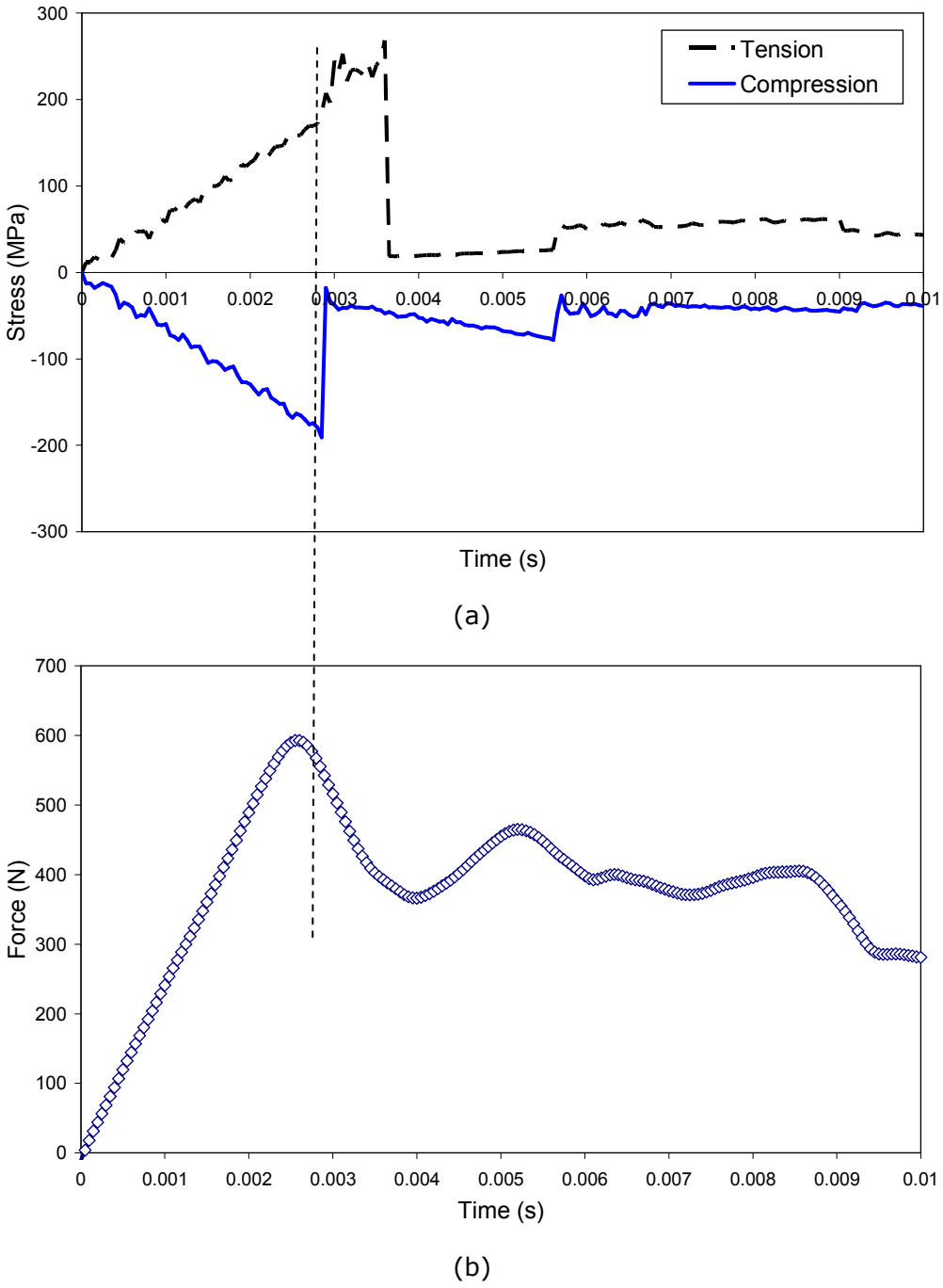

Figure 4-32. (a) The stress-time histories for elements in the centre of the top and bottom surface of the three-point bending model (b) predicted overall force-time history for the quasi-static bending model for m1 = m2 = 4.

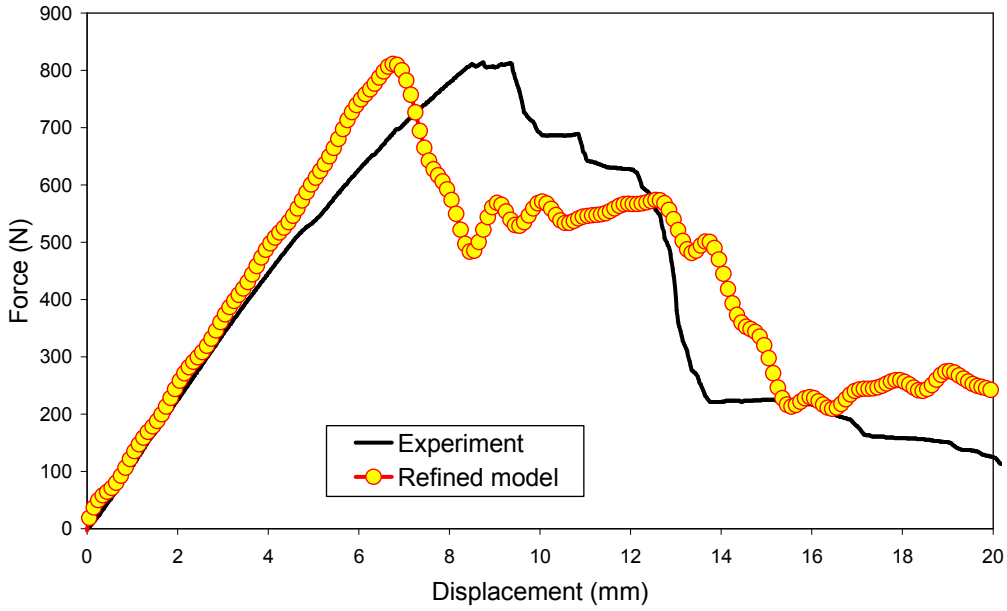

Figure 4-33. Comparison of the predicted and experimental force-displacement response for the refined quasi-static three-point bending model

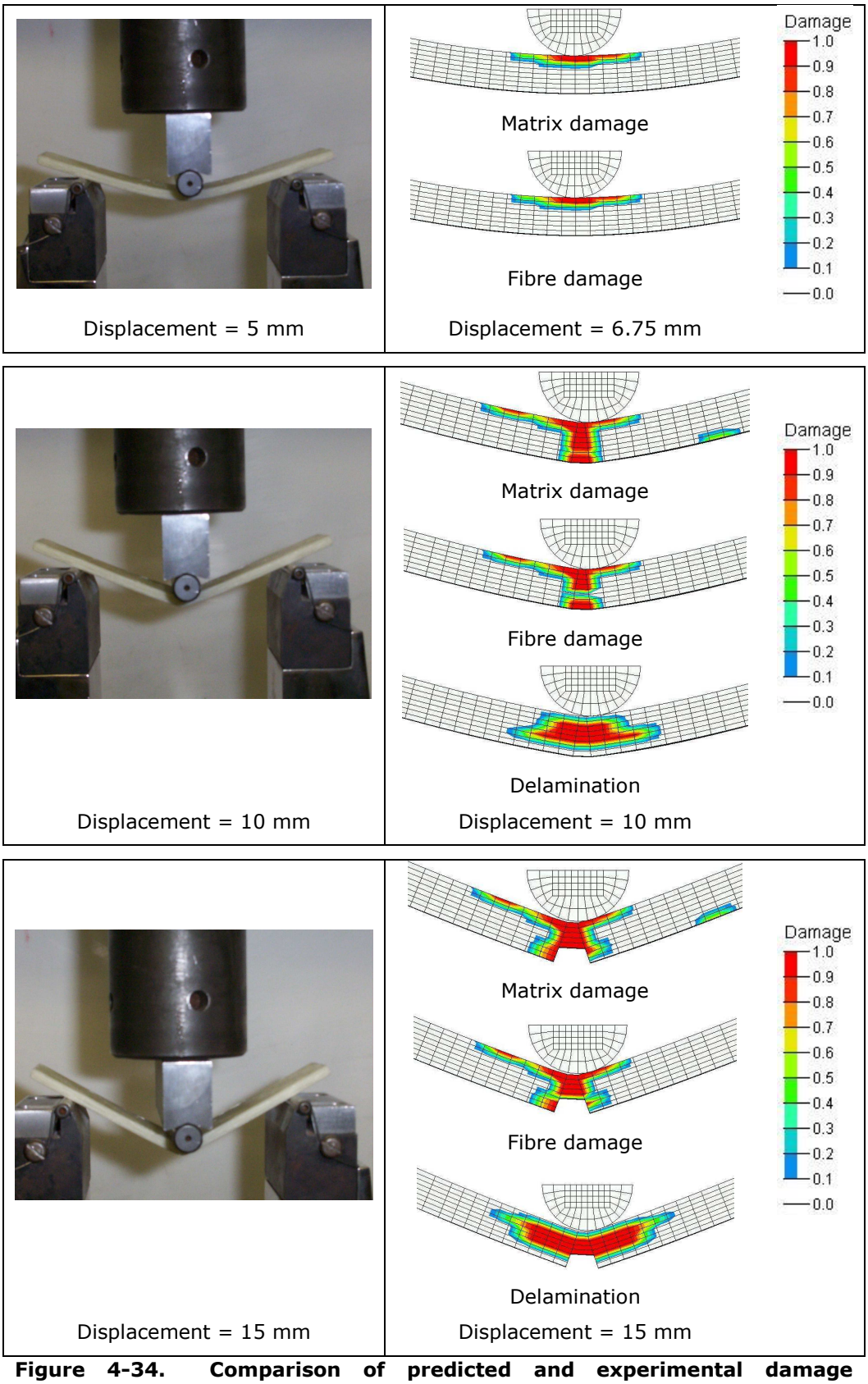

Figure 4-34. Comparison of predicted and experimental damage progression for the quasi-static three-point bending test using the "refined model."

4.6.2 Dynamic Impact Three-Point Bending Test

4.6.2.1 Experimental setup

Details of the dynamic impact bending tests are given in the previous chapter. The dynamic impact bending tests were conducted in a falling weight drop tower. The specimen details are similar to the quasi-static test. The specimen is placed on knife edge type supports with flat tips. The beam was impacted with a cylindrical striker at three loading rates, 3, 5 and 7 ms^{-1}. The striker has a mass of 13 kg. This corresponds to incident energy levels of 58.5, 162.5 and 318.5 J.

4.6.2.2 Finite element model

Figure 4-35 shows the finite model for the dynamic impact bending test. Due to symmetry only half the beam is modelled. All components are modelled with single point integration quadratic eight node solid elements. The mesh, boundary conditions and contact interfaces are similar to the quasi-static model. The impactor is given an initial velocity and an additional nodal lump mass (13 kg) such that the experimental incident energy levels are simulated.

4.6.2.3 Results

The dynamic calibration process produced two different sets of values for the fibre damage parameters for tension and compression. Likewise, there are two different sets of values for the strain rate parameters, C, for tension and compression. However, the MAT 162 model is limited to the input of only one set of values for the strain rate and fibre damage parameters. A comparison of the experimental force-displacement results and the simulation results for two sets of MAT 162 calibrated parameters are presented in Figure 4-36 (a) – (b). One set of simulations referred to as "tensile parameters" in the graph legend, uses the calibrated dynamic tensile values for the fibre damage parameter (m1 = m2 = 0.05) along with the tensile strain rate parameters. The other set of simulations referred to as "compression parameters", uses the calibrated dynamic compression values for the fibre damage parameter (m1 = m2 = 0.5) along with the compression strain rate parameters. For both simulations

the elastic modulus was reduced to E = 10 GPa based on the quasi-static "refined model" (see Section 4.6.1.4).

For the "tensile parameters", simulations show general agreement with the experimental force-displacement results. However, peak force and initial stiffness are slightly over estimated. In addition, the post-peak load response deviates from the experimental curve as the predicted response is too ductile due to the low values used for the fibre damage parameters, i.e. m1 = m2 = 0.05. With the "compression parameters" simulation, the correlation with the experimental results improved. However, the stiffness is still over estimated. There is close correlation between the predicted and experimental peak load for the 3 ms^{-1} impact case. However for the 5 and 7 ms^{-1} cases, the simulation slightly under estimates the peak load. The overall general shape of the prediction results show good agreement with the experiment, especially at higher impact speeds of 5 and 7 ms^{-1}.

Figure 4-37 shows a comparison of the predicted damage progression and the experimental results for the "compression parameters" model at the highest impact velocity of 7 ms^{-1}.

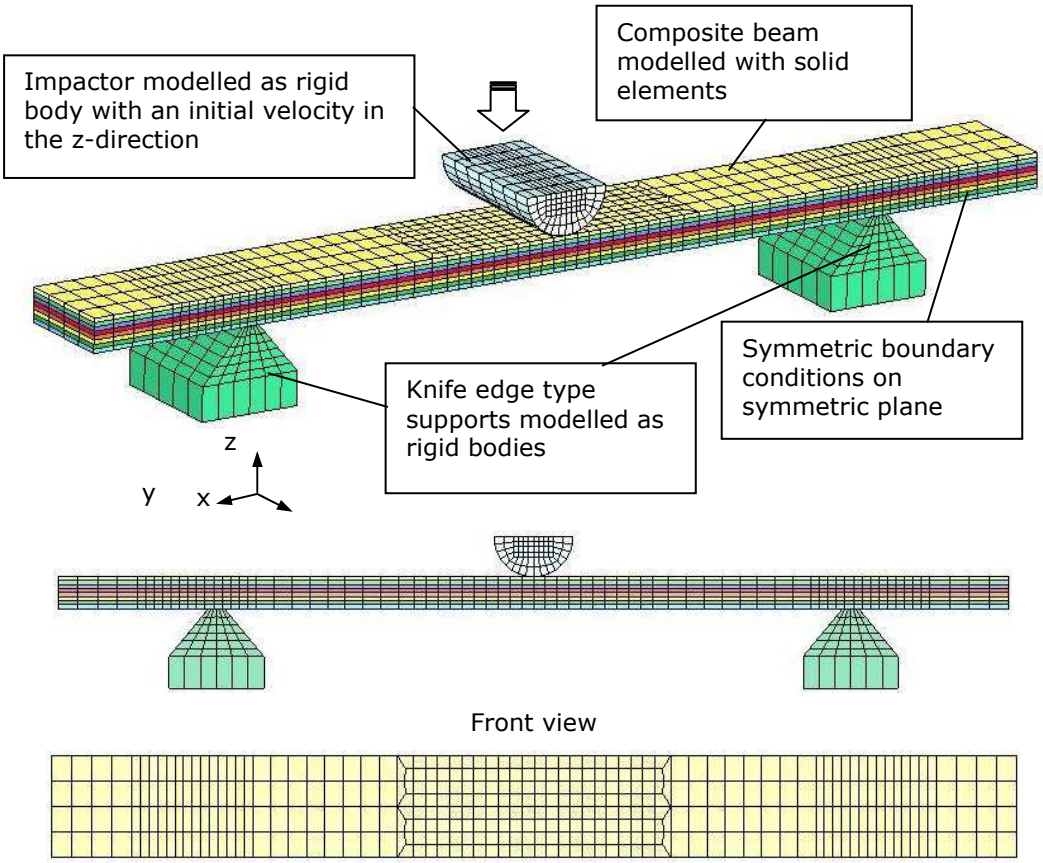

Figure 4-35. Finite element model for dynamic bending test.

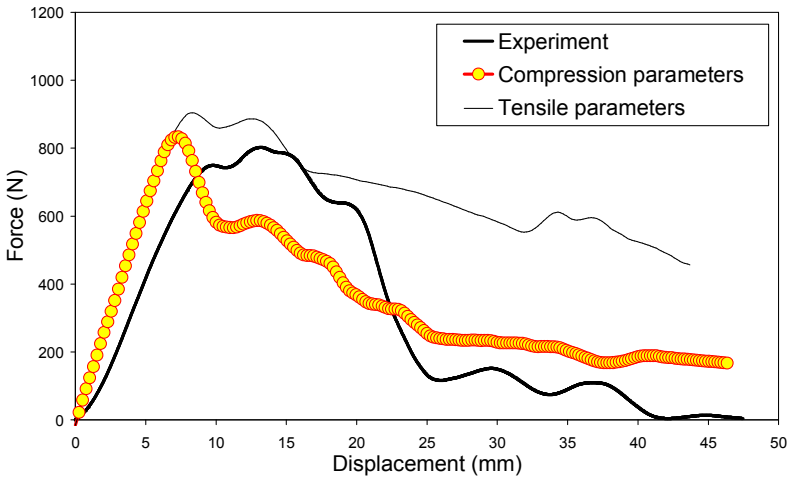

(a)

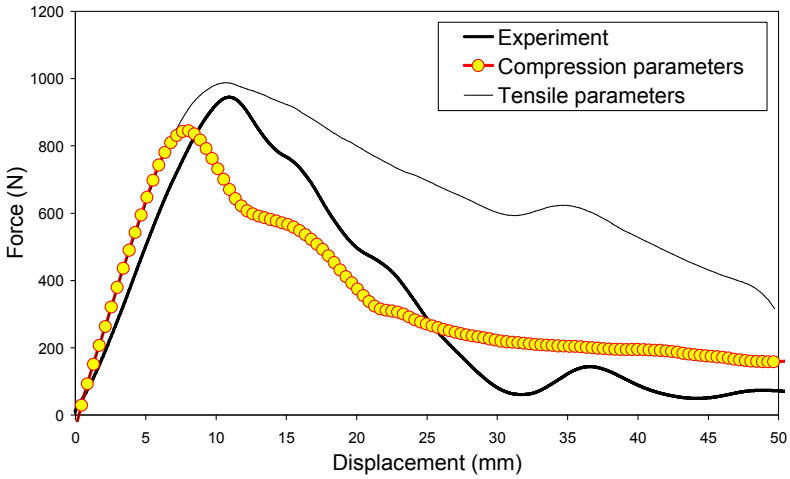

(b)

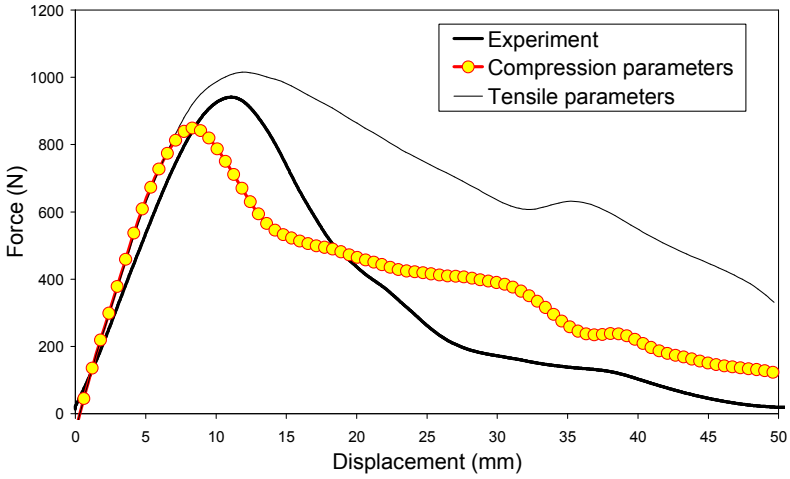

(c)

Figure 4-36. Comparison of the predicted and experimental force-displacement response for the dynamic bending test for the "compression parameters" and "tensile parameters" models at various incident energies (a) 58.5 J, v = 3 ms^{-1} (b) 162.5 J, v = 5 ms^{-1} (c) 318.5 J, v = 7 ms^{-1}.

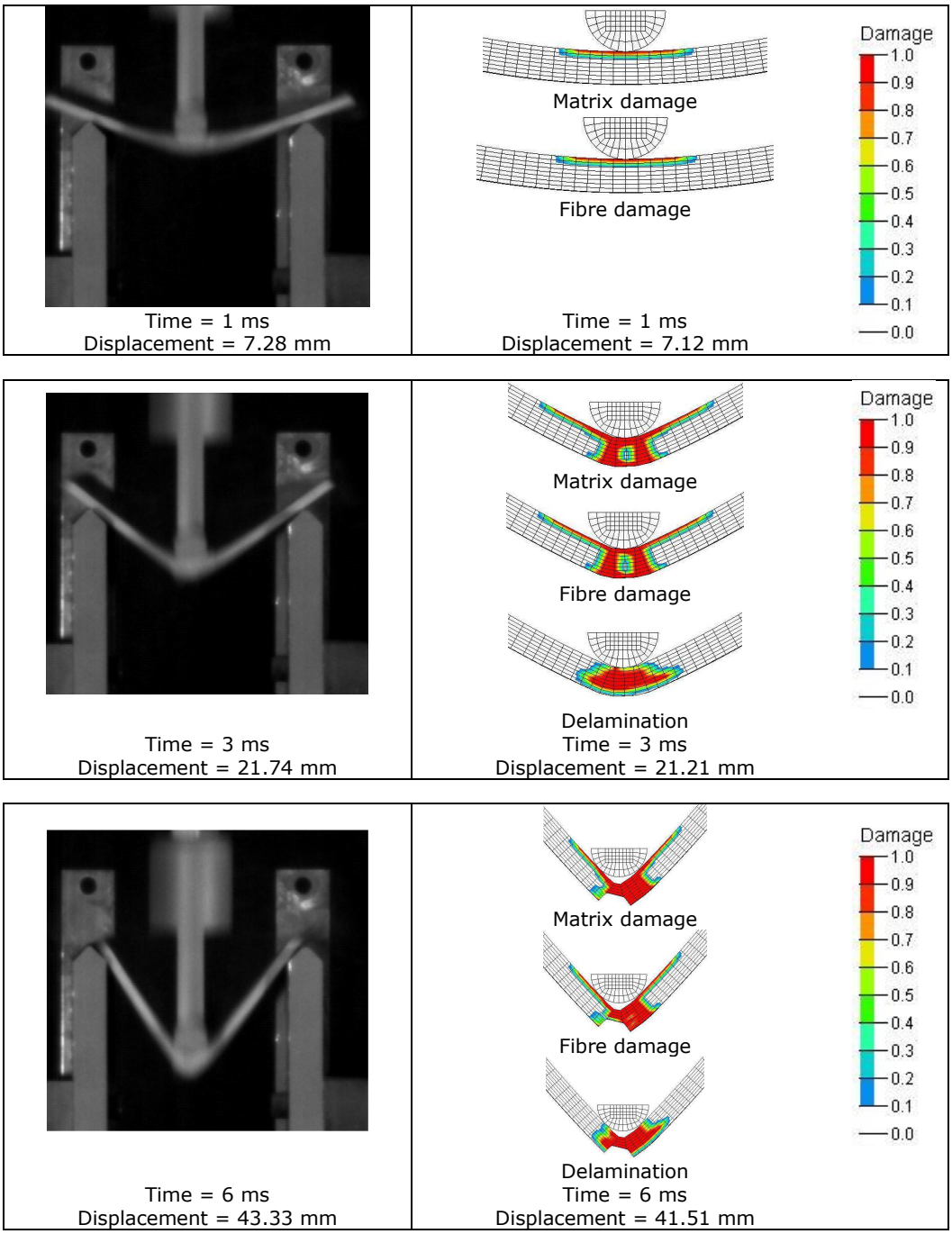

Figure 4-37. Comparison of predicted and experimental damage progression for the dynamic bending test for the "compression parameters" model at the highest impact velocity of 7 ms^{-1}.

4.6.3 Dynamic Impact on a Plate Test

4.6.3.1 Experimental setup

An extensive experimental investigation of the impact response of Twintex thermoplastic composite coupon plates was conducted in a previous research project at various incident energy levels [286]. Of particular interest in this study are the falling weight impact tests that were performed at incident energies of 30, 35 and 40 J. The Twintex coupon plates were 80 mm square with a nominal thickness of 4 mm having a [090] stacking sequence. The test setup is shown in Figure 4-38 (a) and consists of the specimen being clamped under a circular anvil with an internal diameter of 40 mm. An impact load is imparted at the centre of the specimen by a 25.65 kg striker with a 12.7 mm diameter hemispherical tip.

In addition to obtaining the force-time histories, post-test damage was also characterised by using a thermography camera (Agema Thermovision 900).

4.6.3.2 Finite element model

The finite element model for the falling weight impact tests is shown in Figure 4-38 (b). One-half of the plate was modelled due to geometric and material symmetry so as to reduce the computational time. Single point eight node quadrilateral solid elements are used to model the composite plate and impactor. Each ply is represented by a layer of solid elements. Only the impact area of the specimen is modelled and given clamped edge boundary conditions applied at the periphery. The supporting features of the test fixture, such as the clamps are not directly modelled. The impactor is modelled as a rigid body and is only allowed to translate in the z-direction. The impactor is given an initial velocity similar to the test. Contact between the impactor and the composite plate was modelled using the eroding single surface contact algorithm.

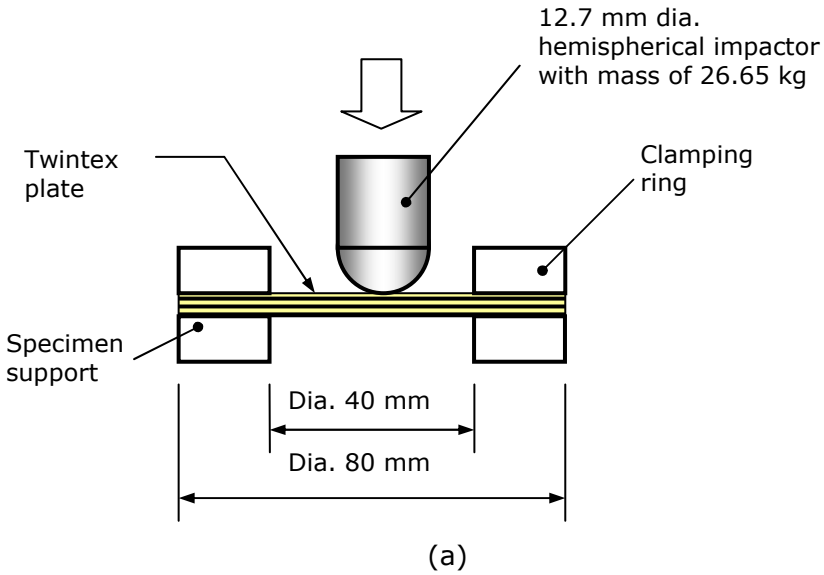

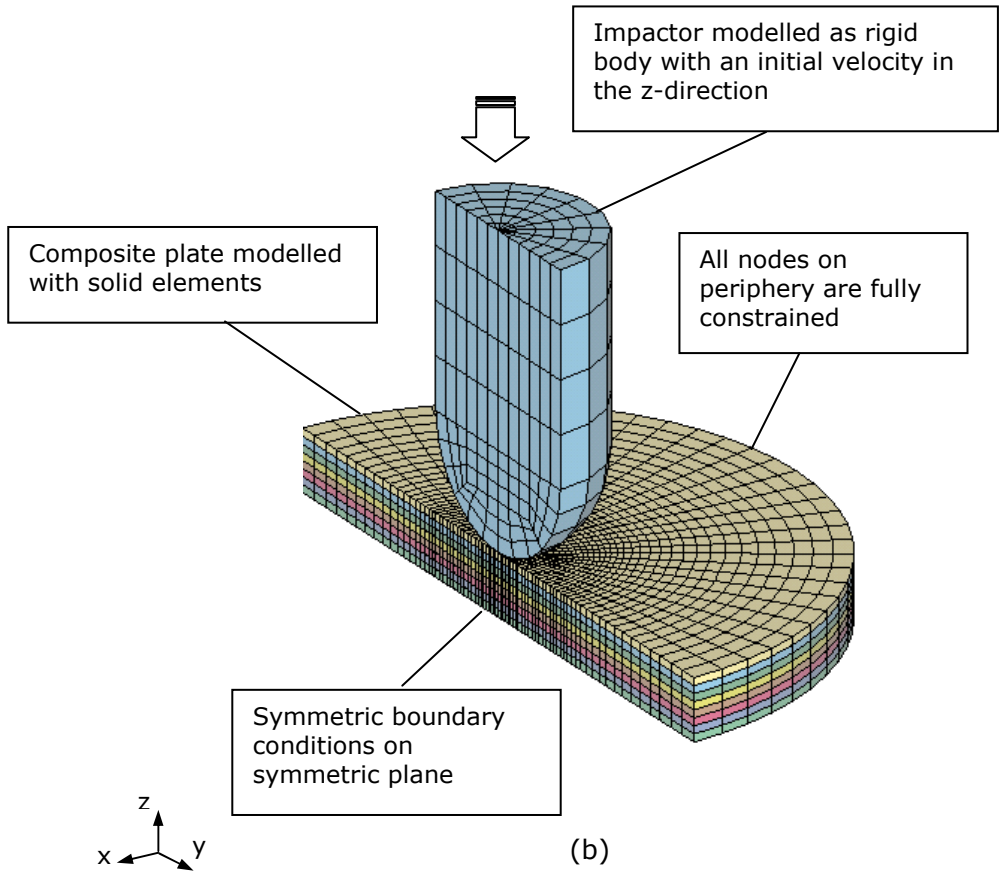

Figure 4-38. Dynamic impact on a plate test (a) schematic of test setup (b) finite element half symmetry model.

4.6.3.3 Results

Similar to the dynamic bending test simulation, the falling weight simulations were also conducted with two sets of MAT 162 calibrated parameters for comparative analysis, i.e. "tensile parameters" and "compression parameters."

Figure 4-39 (a) – (c) clearly shows that the "tensile parameters" simulations yield reasonable good correlation with the experimental force-time histories. However, the "tensile parameters" model does slightly over-predict the peak loads. Despite the "compression parameters" simulation results showing general good agreement with the shape of the experimental curve, the peak load is significantly under estimated in all cases. This is probably due to the high values used for the fibre damage parameters, i.e. m1 = m2 = 0.5 which results in an over estimation of damage in the composite plate. Subsequently, the "compression parameters" model exhibited excessive element erosion resulting in significant load drops.

Figure 4-40 compares the predicted matrix and delamination damage on the mid-ply to experimental thermograph images for the impact events. Both predicted and thermograph images are to the same scale. The qualitative comparison of the size and shape of the predicted damage and the thermograph show good agreement.

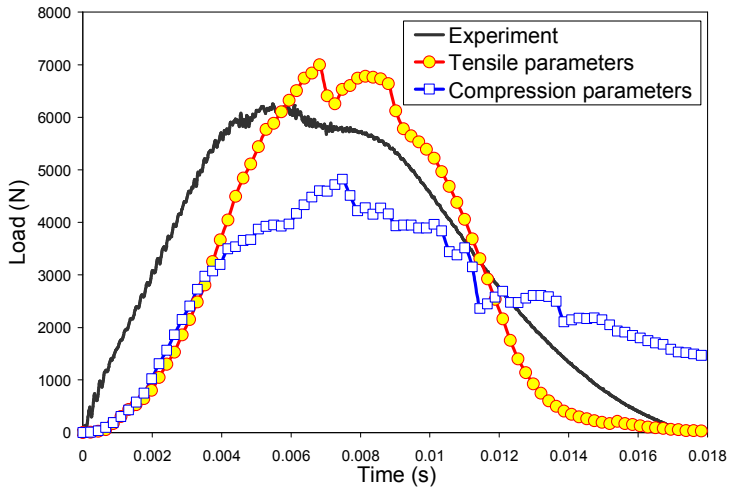

(a)

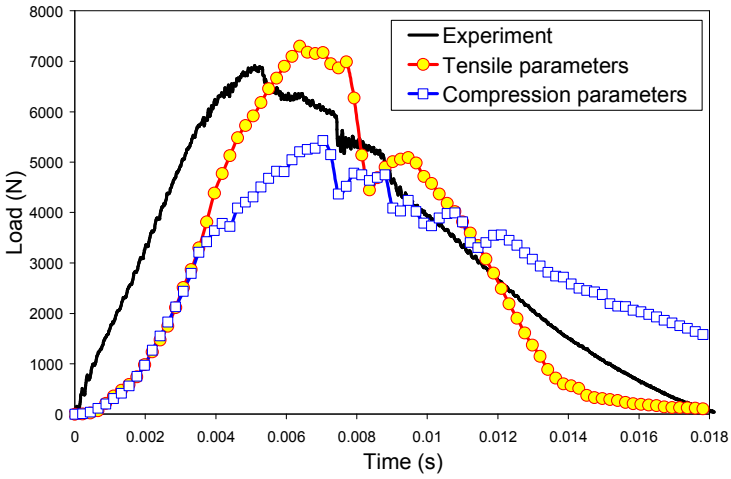

(b)

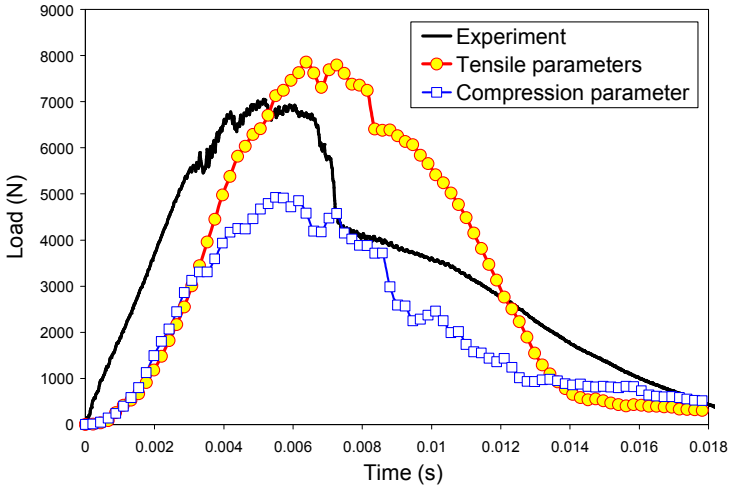

(c)

Figure 4-39. Comparison of the predicted and experimental force-time histories for various incident energy levels (a) 30 J (b) 35 J (c) 40 J.

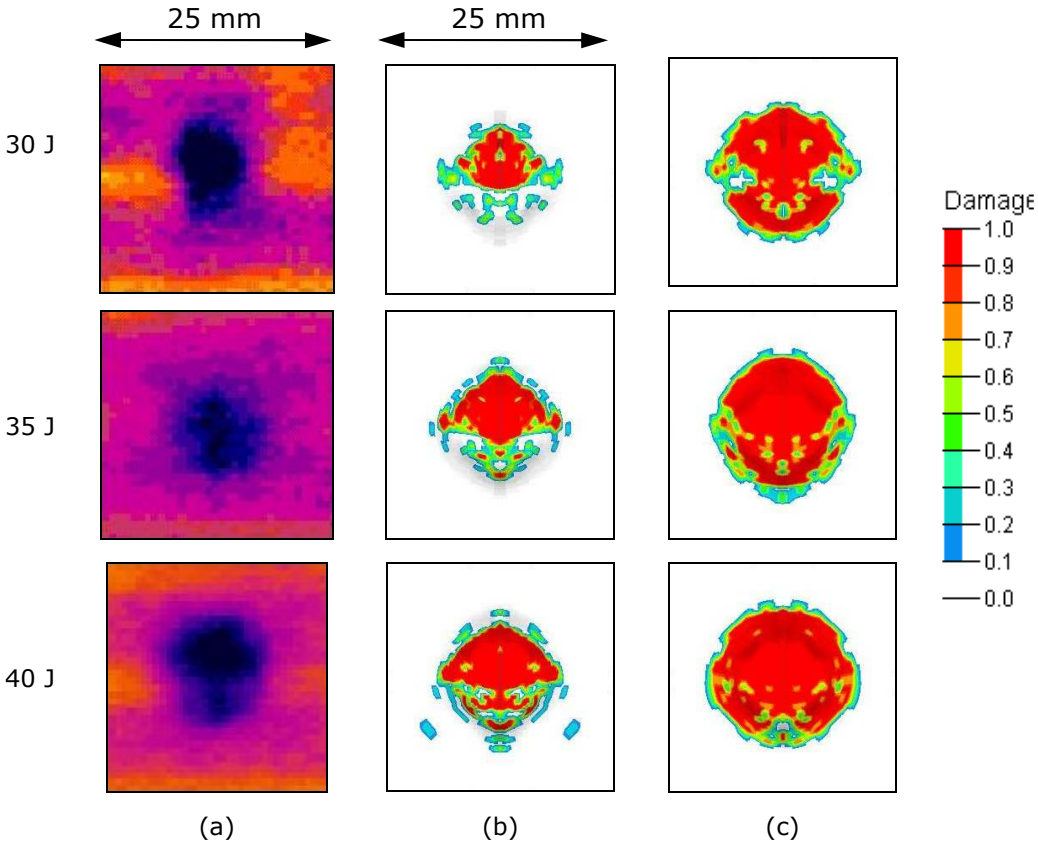

Figure 4-40. Comparison of (a) experimental damage thermograph (b) predicted matrix damage and (c) predicted delamination damage for various impact energies for [090] Twintex plates.

4.7 Structural Validation

In this section the calibrated and validated composite material model was applied to the predictive analysis of a large scale complex shaped automotive demonstrator component. The component is a small passenger vehicle thermoplastic composite side-impact beam.

4.7.1 Thermoplastic Composite Side Impact Beam

The thermoplastic composite side-impact beam that was developed during a previous project named CRACTAC (Crashworthy Automotive Structures Using Thermoplastic Composites). This project was a DTI/EPSRC/Industrial Foresight Vehicle research project [28]. The side impact beam, shown in Figure 4-41, was designed with a tapered "top-hat" section and is constructed from 12 layers of preconsolidated Twintex with a 0/90 stacking sequence [292]. A non-isothermal compression process was used to manufacture the beam [293].

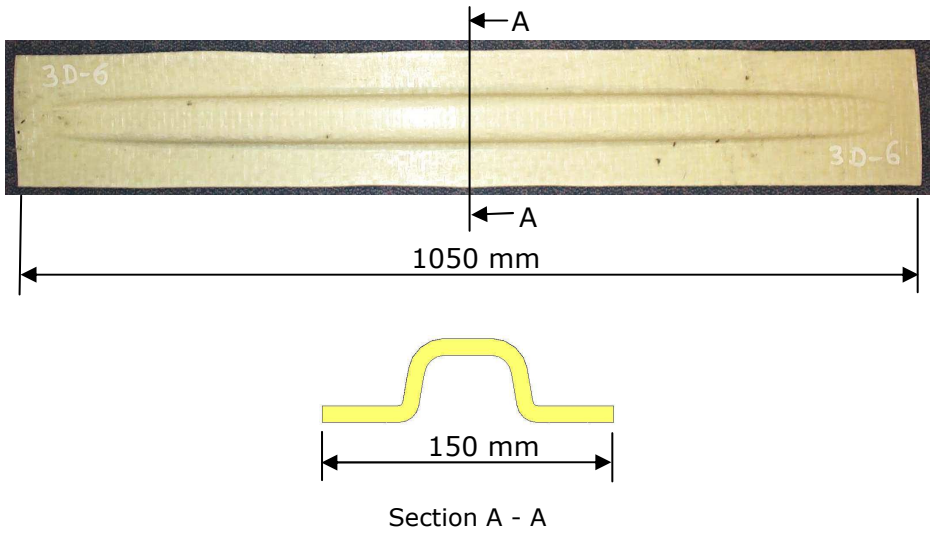

Figure 4-41. Demonstrator thermoplastic composite side impact beam.

4.7.2 Quasi-Static Investigation

4.7.2.1 Experimental setup

The side impact beam was initially tested by MIRA, one of the CRACTAC partners, outside the vehicle using a large scale three-point bending tests with a specially designed rig that was based on the static FMVSS 214 regulation [28, 294]. For this test, the beam is rigidly mounted at one end with a compliant steel bracket and restraining chains (to allow axial translation) at the other end (see Figure 4-42 (a)). A 305 mm diameter half cylinder, located at the beam centre, was used to impart a load at a quasi-static rate of 2 mm min^{-1}.

Load data was captured using a load cell located behind the impactor and displacement was captured using a wire pull displacement transducer attached to the impactor [7].

4.7.2.2 Finite element model

The finite element model for the quasi-static bending test is shown in Figure 4-42 (b). All components are modelled with single point integration quadratic eight node elements. The boundary conditions applied to the model are similar to the actual test. One end is fully constrained while the other end is only allowed translation in the x-direction (see Figure 4-42 (b)). The impactor is given a prescribed velocity that is much higher than the test speed in order to reduce the solution time. Contact between the impactor and beam was modelled using the surface to surface contact algorithm.

The beam is modelled with MAT 162 material model using two sets of calibrated model parameters. The simulation is conducted with the quasi-static calibration results and is referred to as the "calibration parameters" model while the other simulation is conducted with the damage parameters obtained from the static validation three-point bending test simulation ("refined model") and is referred to as the "refined parameters" model.

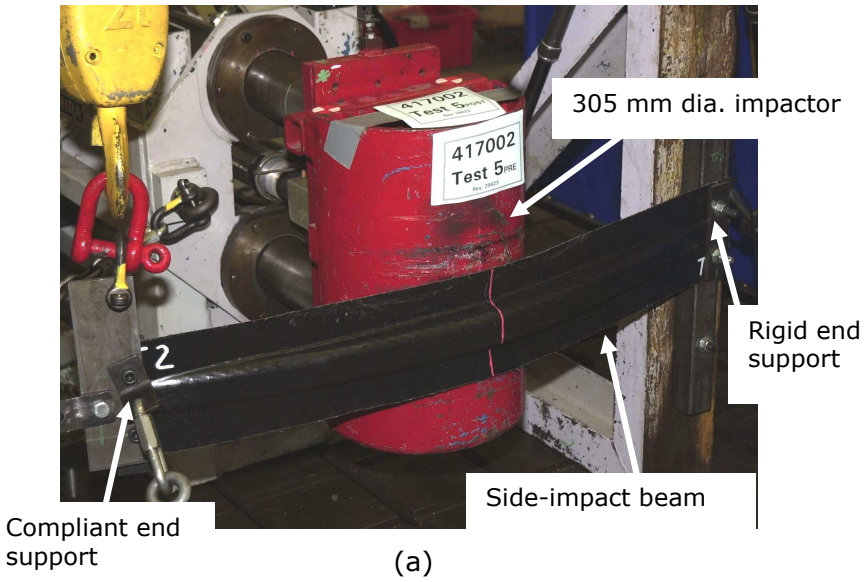

(a)

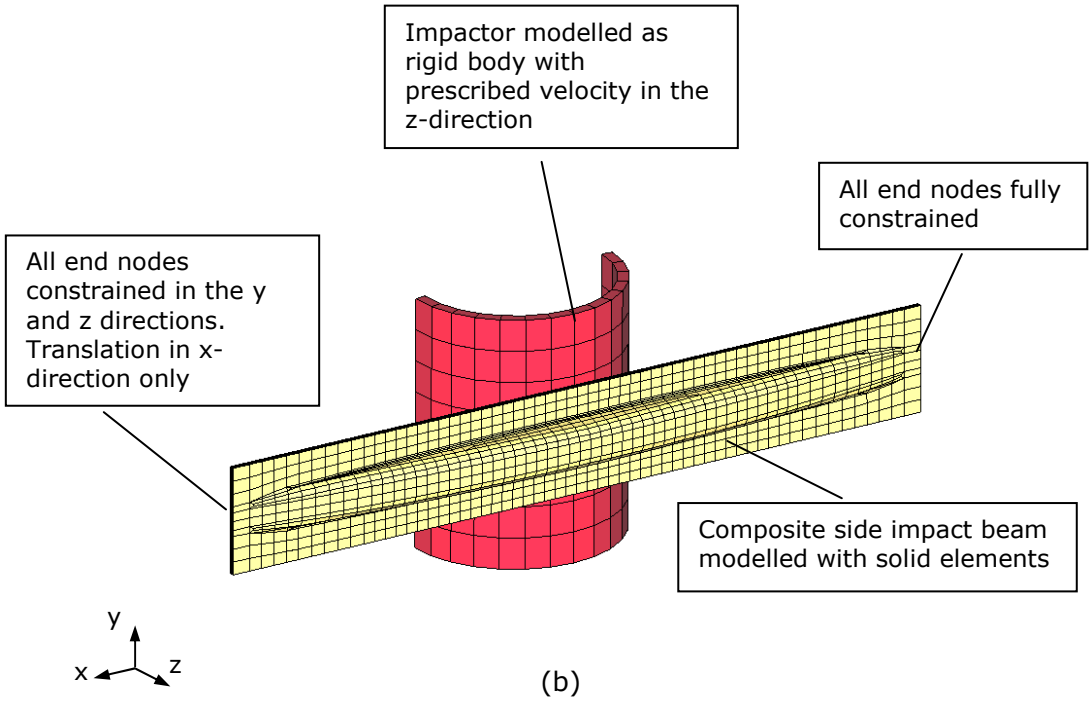

(b)

Figure 4-42. (a) Quasi-static side impact beam test setup (b) finite element model.

4.7.2.3 Results

Figure 4-43 shows a comparison of the experimental and predicted force-displacement response for the quasi-static beam test. The results for two sets of MAT 162 model parameters are presented. The curve referred to as "calibration parameters" used the quasi-static calibration results presented in Table 4-4. While, the "refined parameters" curve uses the parameters from the validation static three-point bending test simulation ("refined model"). The predicted curves show good agreement with the overall shape of the experimental results. The predicted initial elastic response and peak load show good agreement with the experimental results. However, the "refined parameters" model over-predicts the displacement at which the initial peak load occurs. This may be due to an under prediction of the damage levels caused by the low values given to the fibre damage parameters in this model. There are noticeable differences between the two experimental curves, especially in the displacement to initial peak response which may be due to inconsistencies in the material properties and consolidation levels during processing. Therefore, future analysis should investigate material property variability.

Figure 4-44 shows pictures of the experimental deformation of the side impact beam at different displacements. The predicted damage progression for both the "calibrated parameters" and the "refined parameters" models are presented in Figure 4-45. The predicted deformation and damage states show good qualitative agreement with the experimental observations. The damage patterns for the "calibrated parameters" and the "refined parameters" models are very similar except that the damage levels in the "calibrated parameters" model are slightly higher. This is due to the much higher values that were used for m1 and m2 in the "calibrated parameters" model (m1 = m2 = 4) in contrast to the low values in the "refined parameters" model (m1 = m2 = 0.5). In general, the simulations show that the initial damage mode is delamination along the fillets in the "top hat" section which may be due to high stress concentrations. This is followed by matrix and fibre damage due to combined tensile, compression and shear stresses.

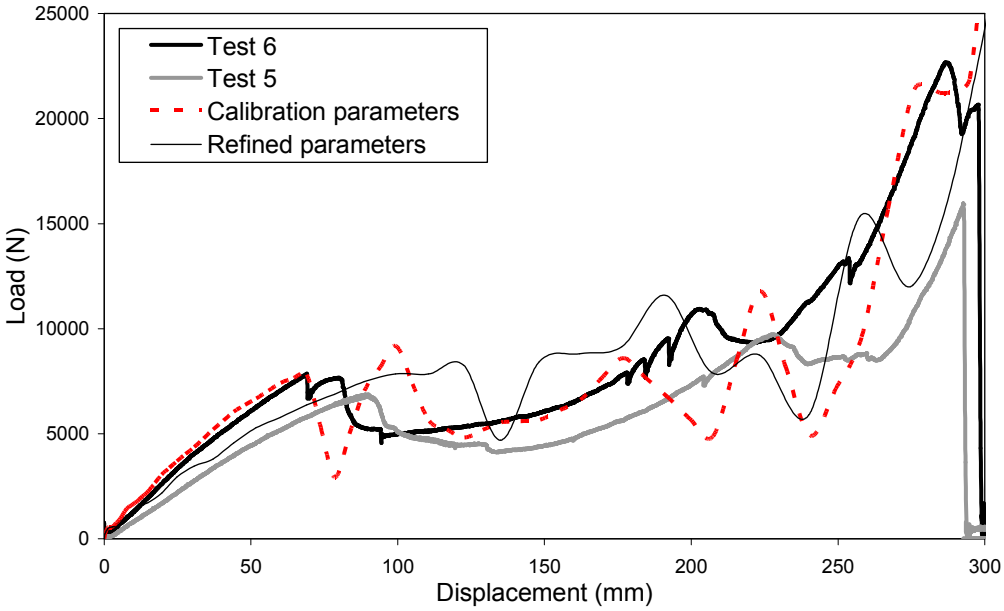

Figure 4-43. Comparison of the predicted and experimental force-displacement response for the side impact beam under quasi-static loading.

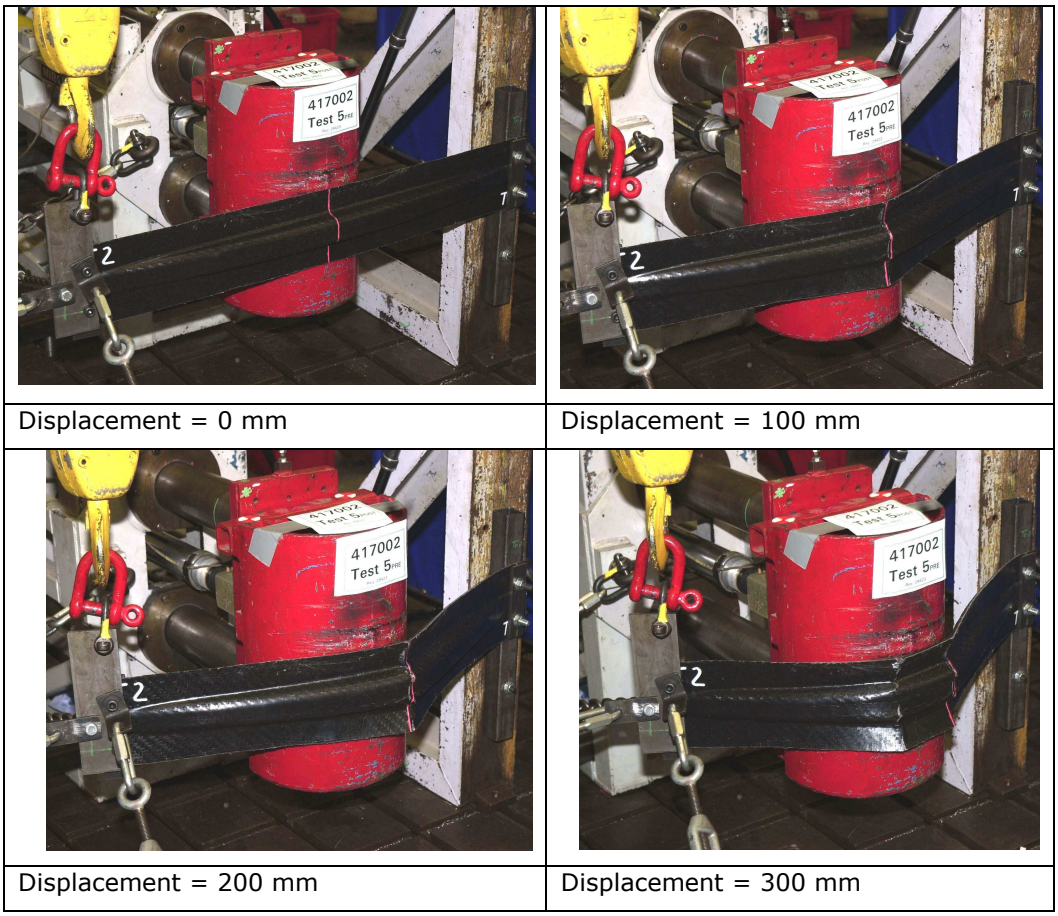

Displacement = 0 mm | Displacement = 100 mm

Displacement = 200 mm | Displacement = 300 mm

Figure 4-44. Experimental deformation and damage in the side impact beam under quasi-static loading.

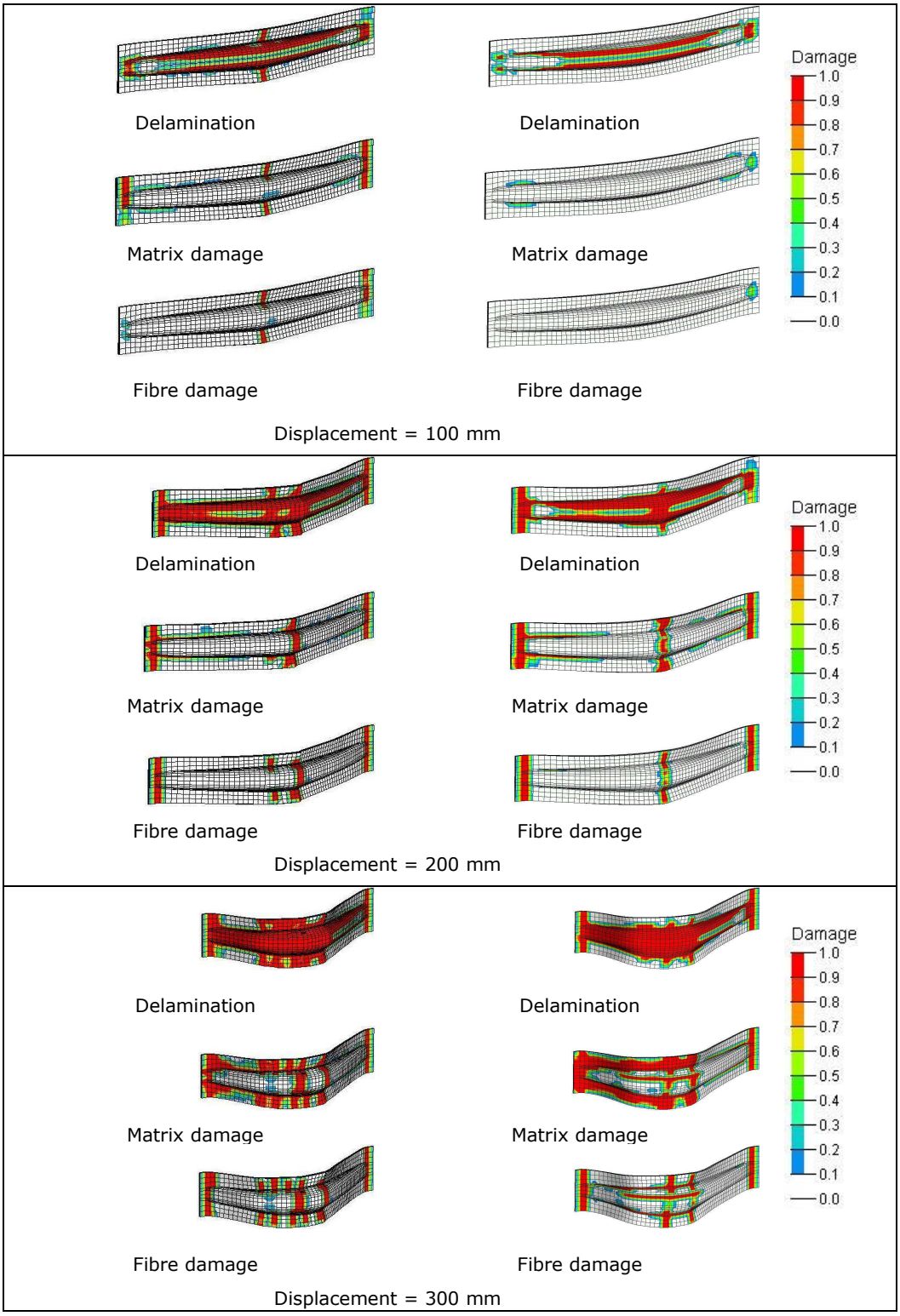

Figure 4-45. Comparison of predicted damage using (a) "calibration parameters" model (b) "refined parameters" model for side impact beam under quasi-static loading.

4.7.3 Dynamic Investigation

4.7.3.1 Experimental setup

Dynamic testing of the side impact beam under three point bending was conducted in a falling weight drop tower during the CRACTAC project [292]. The beam was simply supported over a span of 750 mm (see Figure 4-46 (a)). A load is imparted at the centre of the beam with a half cylinder which has a mass of 19.9 kg and an initial velocity of 8 ms^{-1} corresponding to a high impact energy of 637 J.

Post-test damage was characterised by using a thermography camera (Agema Thermovision 900).

4.7.3.2 Finite element model

Figure 4-46 (b) shows the finite element model for the dynamic impact test for the side impact beam. All components are modelled with single point integration quadratic eight node solid elements. The steel supports and impactor were modelled as rigid bodies. The supports are fully constrained while the impactor is only allowed to translate along the z-axis. The impactor mass and initial velocity are similar to the test. Mass scaling is used to achieve reasonable solution times.

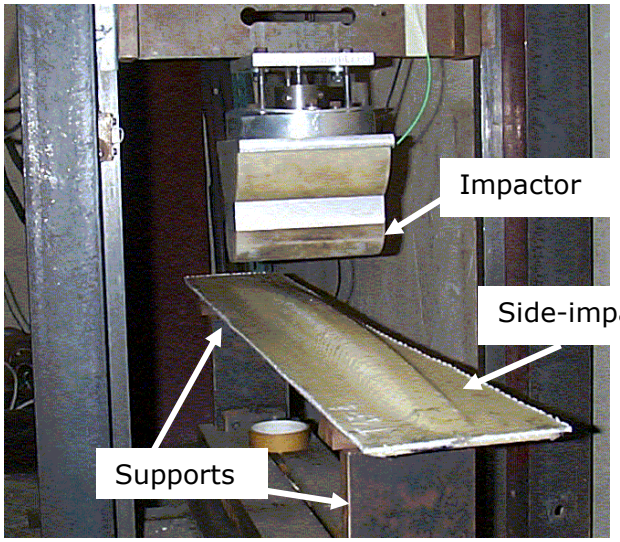

(a)

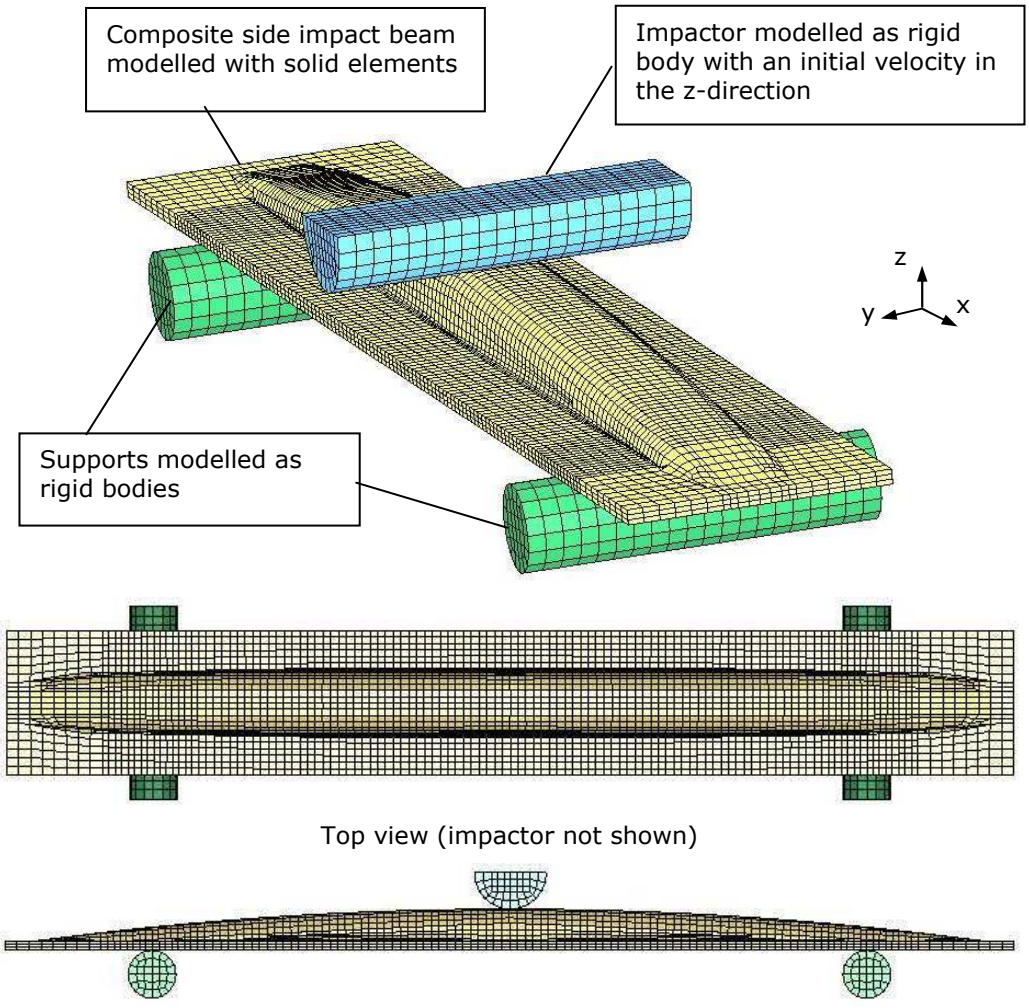

Top view (impactor not shown)

Front view

(b)

Figure 4-46. Dynamic side impact beam test (a) experimental setup (b) finite element model.

4.7.3.3 Results

The MAT 162 input parameters for the dynamic impact test model for the side impact beam were taken from the "compression parameters" validation three-point bending model as these damage parameters gave the best correlation for the dynamic bending simulations (see Section 4.6.2).

Figure 4-47 (a) shows good agreement between the predicted force-time histories and experimental results. The initial elastic response is well predicted. However, the peak load is slightly over estimated. Figure 4-47 (b) shows the excellent agreement between predicted and experimental displacement – time histories. The simulation predicts a rebound at 142 mm which compares very well with the test value of 144 mm. Figure 4-47 (c) also shows the good agreement between the predicted and experimental force-displacement histories.

Figure 4-48 shows a picture of the failed beam and damage thermograph. Figure 4-49 shows predicted damage progression. The qualitative comparison of the size and shape of the predicted damage and the experimental damage thermograph show good agreement. The simulations show that matrix cracks, fibre fracture and delamination all initiate and propagate in a localised region under the impactor in the "top hat" section of the beam. Matrix cracking is the only damage mode that is observed in the flanges of the beam.

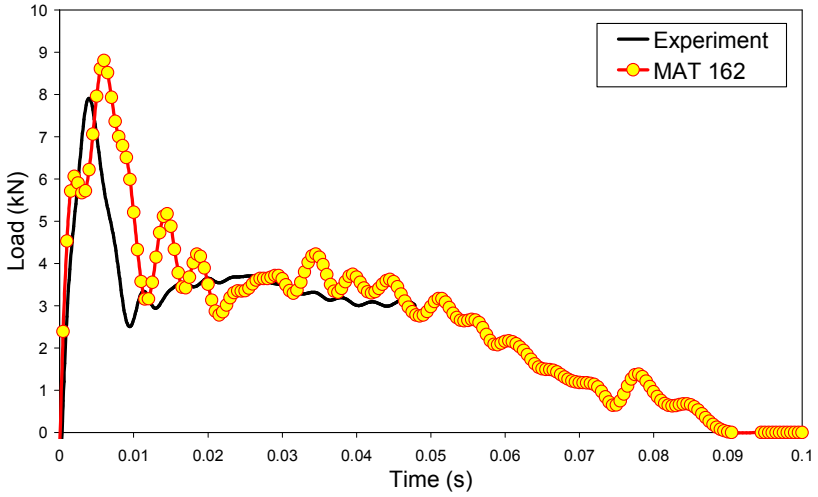

(a)

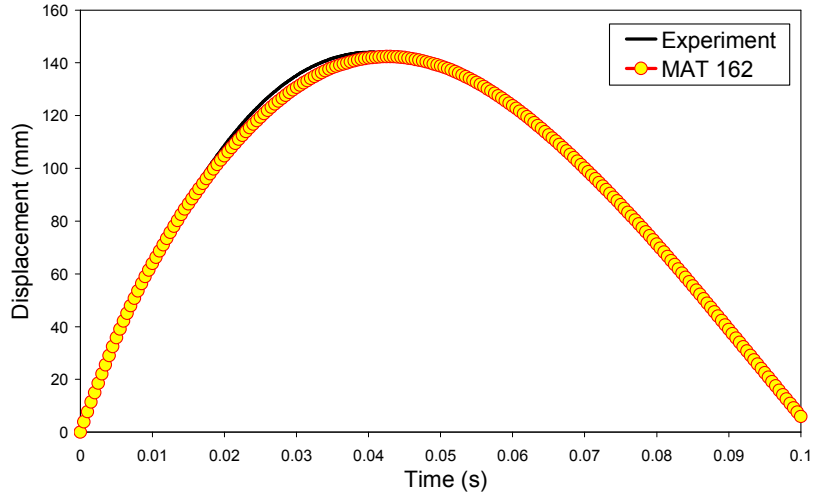

(b)

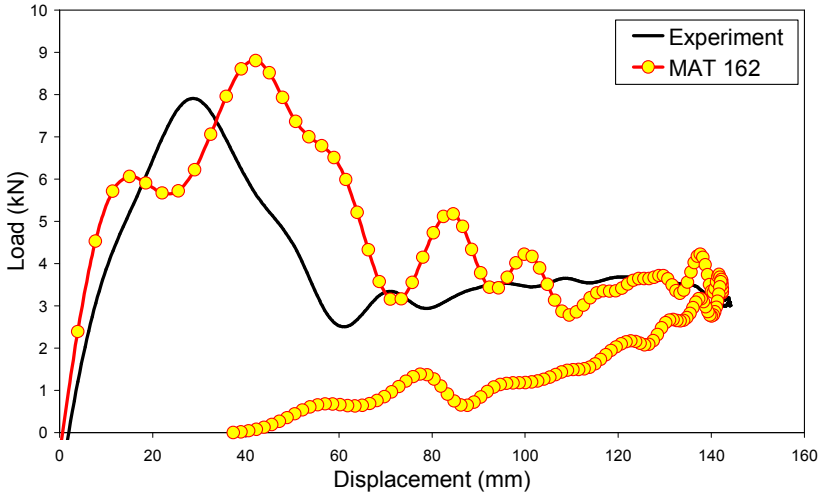

(c)

Figure 4-47. Comparison of predicted and experimental results for the dynamic impact test (a) force-time curves (b) displacement-time curves (c) force-displacement curves

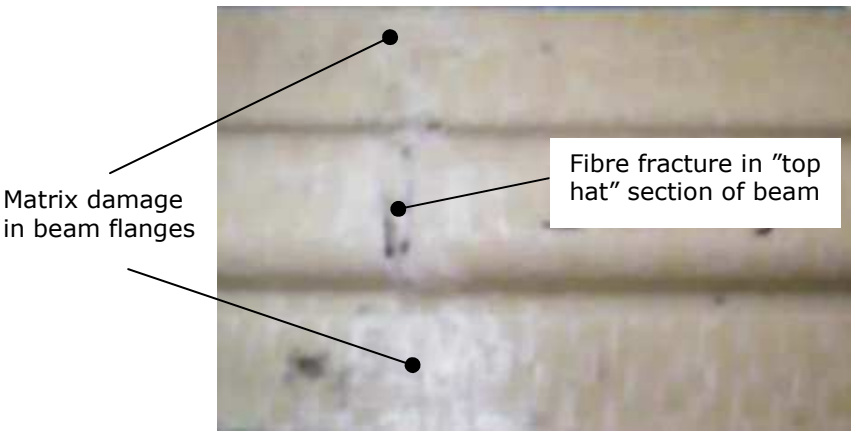

(a)

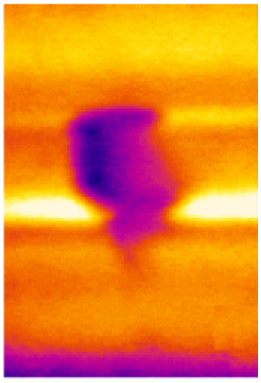

(b)

Figure 4-48. Experimental damage for dynamic impact test on side impact beam (a) picture of failed beam centre (b) thermography showing damage in the centre of the beam

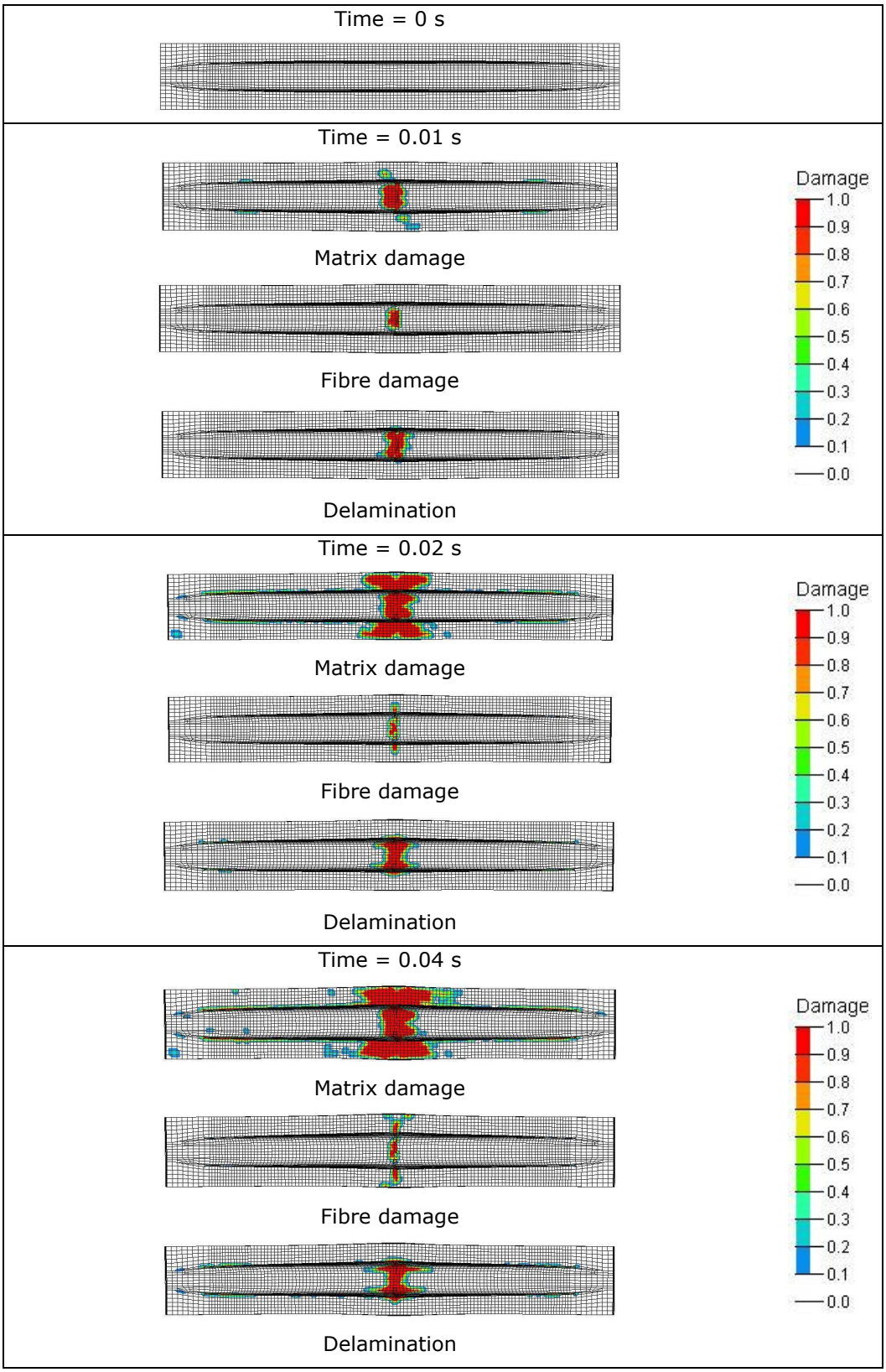

Figure 4-49. Predicted damage progression for simulation of dynamic impact test on thermoplastic composite side impact beam.

4.8 Discussion and Conclusions

Although the MAT 162 model has been successfully validated for simulating impact damage in thermoset composites structures [295, 296], this present research represents the first known attempt to calibrate and validate the MAT 162 model for simulating impact damage in thermoplastic composite structures.

The results of this work have shown that MAT 162 provides a versatile tool for predicting and simulating damage progression in thermoplastic laminate structures under static and dynamic impact loading. However, the study has highlighted a few issues that need further consideration. These are discussed below.

4.8.1 Material Characterisation

A potential limitation of the model is the large number of input parameters that are required. The calibration procedure has to be supported by an extensive material experimental characterisation program that covers a wide range of static and dynamic tests. The need to determine a large number of input values is common to most damage mechanics models. Most of these parameters can be obtained from standard quasi-static tests. However, there are few standard high strain rate test procedures for obtaining dynamic parameters. In this study, the dynamic through thickness properties of the material were not available so static values were used in all cases. Nonetheless, reasonably good correlation between the dynamic impact simulations and experimental results were obtained because in must cases, membrane stresses were the dominant cause of failure. Future investigations should include dynamic tests to obtain through thickness properties and fibre shear punch strength. These properties are important especially if the model is to be applied to ballistic impact scenarios.

4.8.2 Calibration of Damage parameter m

The MAT 162 model has four damage parameters that are used to define the post-elastic response of the material under various loading conditions. As discussed by other researchers, there are no clearly defined methods for calibrating the post-elastic stress strain (softening or hardening) behaviour of composite materials. Consequently, the selection of damage parameters for each failure mode is still considered an unresolved issue. In the open literature, the only reported attempt to calibrate the MAT 162 damage parameters was presented recently by Xiao et al [295]. They presented a method for calibrating the damage parameters for the modelling of S-2 glass/SC-15 epoxy thick section plain weave laminates under quasi-static punch-shear loading. The damage parameters were determined by correlating the experimental load-displacement histories and damage sequence with simulation results. The calibrated parameters were validated by simulating the same test with laminates of different thicknesses which resulted in reasonable predictions of the load-displacement histories. However, a major limitation of this procedure is that the calibrated damage parameters are only valid for this specific quasi-static test on this particular thermoset composite material with the same laminate configuration. Furthermore, Xiao et al did not validate his calibration procedure for large scale composite structures.

In this research, an inverse calibration method has been successfully applied to the identification of the damage parameters. In this method the parameters are obtained iteratively through correlation of simulations with standard static and dynamic coupon tests. The parameters are then validated and fine tuned (if necessary) before application in the predictive modelling of large scale composite structures. Figure 4-50 shows a schematic of the inverse modelling calibration validation procedure. The method allows for a more general application of the calibrated and validated MAT 162 model parameters in predicting the crash response of complex shaped large scale thermoplastic composites structures without having to retune the parameter values. However, due to the mesh sensitivity of the damage parameters it is recommended that the same relative mesh size is used for the calibration, validation and component level analyses so as to avoid incompatible results.

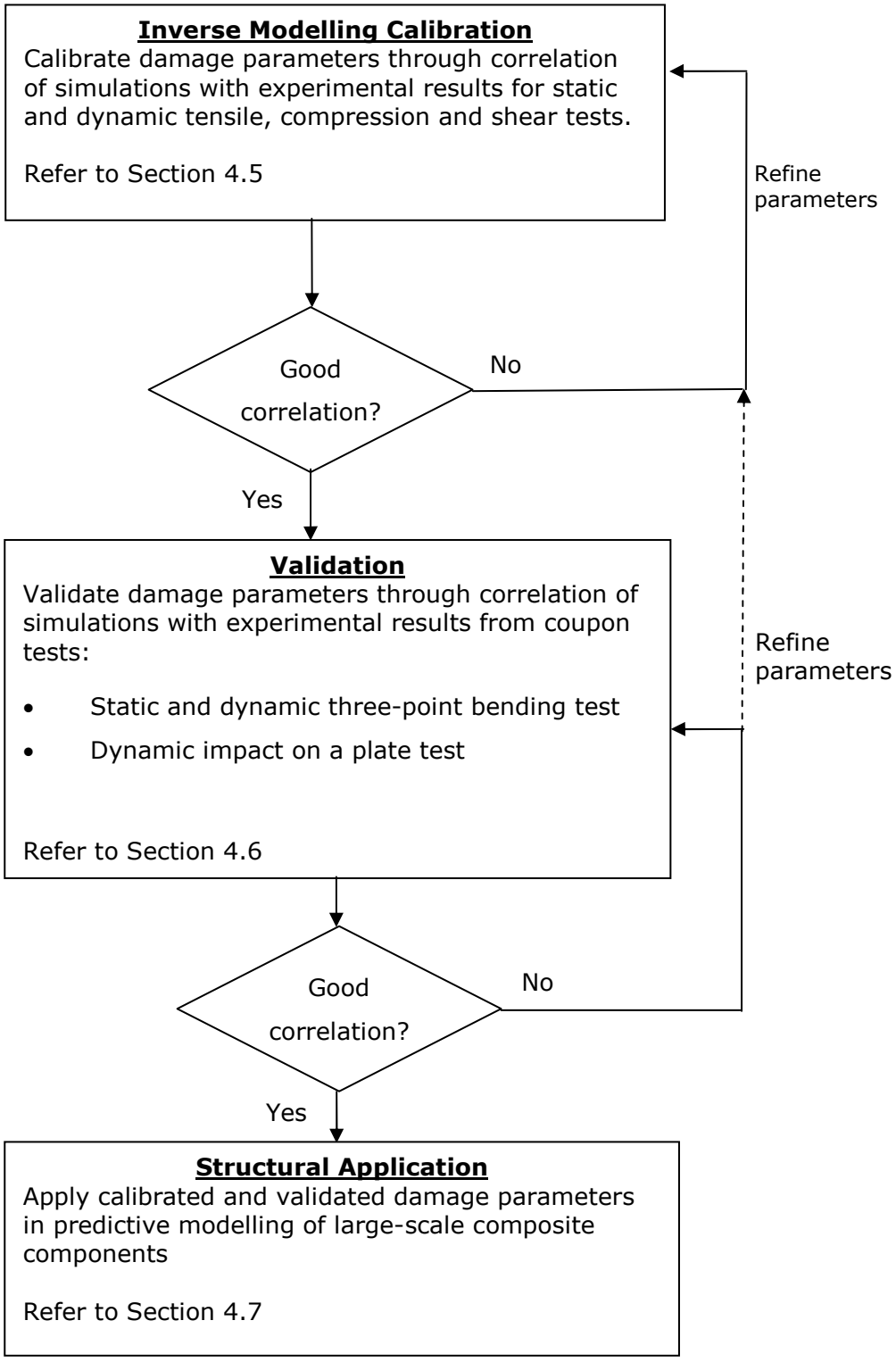

Figure 4-50. Diagram showing proposed inverse modelling calibration and validation procedure for MAT 162 damage parameters.

4.8.3 Asymmetric Tensile and Compression Behaviour

MAT 162 does not allow for different damage parameters for tensile and compression to be used simultaneously. For many composites this assumption is unrealistic [297] as is the case in this study. For dynamic loading the in-plane tensile and compressive response were different which meant that asymmetric values of the fibre damage parameters were selected. For dynamic tensile loading m1 = m2 = 0.05 was selected, while m1 = m2 = 0.5 was used for dynamic compression loading.

Both validation tests involved mixed mode failures that incorporate both tensile and compression effects. Therefore the validation simulations had to be repeated with both sets of damage parameters with the must representative data set being selected for use in the component level analysis. The results show that compression damage parameters provide the best correlation for the dynamic bending simulation while the tensile damage parameters provided good agreement between prediction and experimental falling weight impact results. This suggests that the failure in the dynamic bending specimens resulted in a more abrupt post-elastic response than in the plate impact case where failure was more ductile. This is further illustrated by the fact that the duration of the plate impact tests are almost 3 times longer than the dynamic bending tests. For future investigations, it is recommended that MAT 162 should be modified to allow the input of different damage parameters for both tensile and compression damage behaviour simultaneously. This should result in a more comprehensive characterisation of the material behaviour.

4.8.4 Plastic Deformation

MAT 162 is an elastic-damage model which does not explicitly consider irreversible plastic behaviour. Figure 4-51 shows the stress-strain curve for a single element under tensile cyclic loading. The element is loaded until damage occurs and then unloaded and reloaded. Note that the element unloads and reloads linearly at a reduced elastic modulus along a line that intersects the stress-strain curve at the origin. Therefore, the model may be unable to accurately predict irreversible plastic deformation in a partially damaged composite material. However this will only be an

issue if unloading of the composite contributes to the overall response of the structure. Most impact events exhibit increasing monotonic deformation such that unloading does not affect the overall response of the model [297].

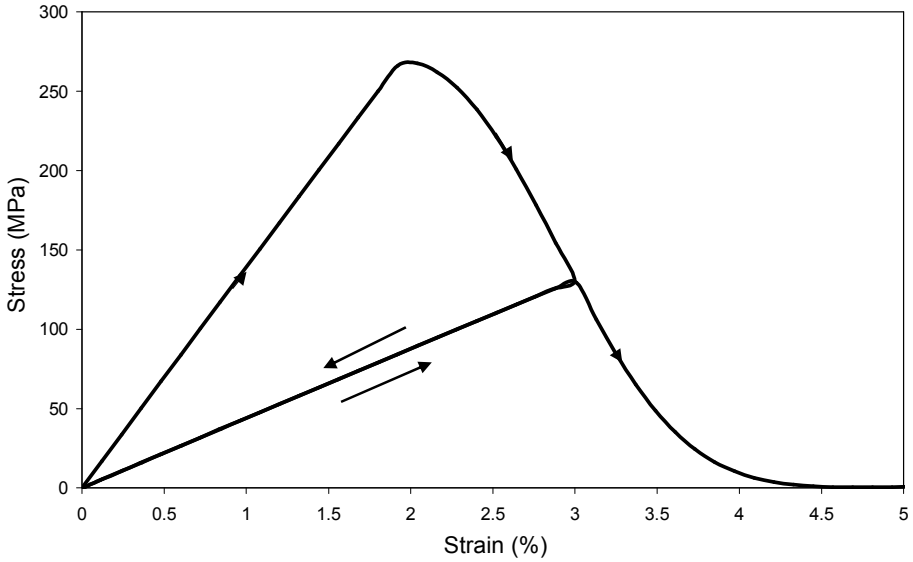

Figure 4-51. Stress-strain response for a single element under tensile cyclic loading for MAT 162.

4.8.5 Localisation and Mesh Sensitivity

Localisation of damage is a well documented problem with most models that are based on the continuum damage mechanics approach [117, 297, 298]. Localisation of damage results in significant mesh dependency in the numerical solution without convergence to a unique solution [117]. Localisation occurs during post-elastic strain softening as narrow and highly strained zones occur when some elements are deformed while others are unloaded [117]. This means that damage can be confined to a very local region in the model. This can be a real problem for complex shaped structures that have a non-uniform mesh size in various regions.

A small level of localisation and mesh sensitivity was observed in this study. However, attempts were made to avoid localisation by using a uniform mesh size in all models, especially in the area of anticipated damage propagation. More sophisticated methods for reducing the effects of localisation have been reviewed by Donadon and Iannucci [298]. These include:

- Inclusion of rate dependence in the constitutive model

- Make stresses dependent on strain gradients
- Smeared crack formulation
- Non-local damage distribution function

Mauricio and Iannucci [298] note that the second suggested solution from the list above is very difficult to implement in the finite element method because the strain gradients are generally not computed or stored. They developed a smear crack formulation where the fracture energy is distributed over the entire volume of the element. For this approach a length parameter relative to the dimension of the elements is introduced into the constitutive law. This length parameter is referred to as the characteristic length and is defined as L = V/A, where V is the element volume and A is the fractured area. However, deriving the fracture area in an element is not a trivial matter.

A non-local function has been implemented in LS-DYNA as MAT_NONLOCAL [118]. This approach can be used to distribute material damage over a representative volume of material specified by the user. However, MAT_NONLOCAL may require additional memory usage and is computationally expensive

It is recommended that in the future, the implementation of the smear crack approach and/or non-local damage distribution with the MAT 162 model be investigated for reducing localisation and mesh dependency.

4.8.6 Element Type

MAT 162 is based on a three-dimensional stress field and has been implemented in LS-DYNA for use with single point integration eight node solid elements only. Solid elements allow for a detailed analysis of the three-dimensional stress state, especially the through thickness response of composite materials under impact loading. However, solid elements are computational expensive. Shell elements are considered to be more computational efficient especially when modelling large scale crash structures.

Several shell element composite damage models are available in LS-DYNA [117, 118] and other commercial finite element codes [179, 283]. In

general, shell element theory is based on the assumption of linear distribution of strain in the in-plane direction. The stresses in the through thickness direction are assumed to be zero [117]. These elements are appropriate for simulating the failure response for composite structures loaded under in-plane loading. However, shell element models cannot accurately predict interlaminar shear stresses and through thickness stresses which determine delamination failure [299]. The capability to model delamination is important because this is a primary mode of failure in composites under dynamic impact and crash loading [117, 299]. Researchers have used interface models or tiebreak contact algorithms for simulating delamination in composite shell models [299]. However, these interface models have been shown to be computationally expensive [299].

MAT 162 offers the advantage of a more computationally efficient approach by being able to predict delamination without the need to define a physical interface between the solid element layers that represent each ply. In addition with increasing low cost computing power that is now becoming available, the use of MAT 162 with solid elements for the crash analysis of larger scale composite vehicle structures will be a standard realistic approach in the near future.

4.8.7 Strain Rate Effects

MAT 162 requires the input of four strain rate parameters. This study has shown that these strain rate parameters are different for dynamic tensile and compression loading. However, MAT 162 does not allow for the different strain rate parameters for tensile and compression to be used simultaneously. Furthermore, the strain rate parameter for shear, C3 is used for both in-plane and through thickness shear rate effects. These features in the model are an oversimplification of the dynamic response of the material. For future work, the MAT 162 model should allow for different strain rate parameters for tensile and compression loading.

4.8.8 Conclusions

Despite the limitations of the model that have been discussed above, MAT 162 presents an advanced damage model that has considerable potential for application to modelling large deformation and damage progression in thermoplastic composite structures under a wide range of impact loads.

A major contribution of this study is the development of a methodology to calibrate and validate the MAT 162 model for simulation and prediction of the progression of damage in thermoplastic composite structures under dynamic impact and crash loads. In this methodology, the model damage parameters were calibrated using an inverse modelling technique. In addition, a novel procedure was successfully established for calibrating the matrix damage parameter m4 for the non-linear hardening shear stress-strain response observed in the experimental quasi-static and dynamic shear tests.

This investigation has verified that the newly implemented MAT 162 material model can be used for the design and optimisation of thermoplastic composite structures that are subjected to crash loads.

Chapter 5

Modelling the Response and Failure of Thermoplastic Composite Sandwich Structures

5.1 Introduction

Foam core thermoplastic composite sandwich structures are being considered for application in vehicle bumpers and frontal structures for pedestrian safety countermeasures [8, 300]. Sandwich structures offer several advantages including high energy absorption capability, good stiffness to weight ratio and recycling potential. Furthermore, the use of an all thermoplastic sandwich with the same polymer used in the skin and core, allows for medium volume one step manufacturing of these structures [8]. However, the literature review in Chapter 2 reveals that very limited research has been conducted on the impact behaviour of thermoplastic composite sandwiches

This chapter presents an experimental and numerical investigation into the quasi-static and dynamic impact behaviour of foam cored thermoplastic sandwich structures. The sandwiches in this study consisted of commingled woven fabric glass fibre reinforced polypropylene composite skins and anisotropic crushable polypropylene foam cores. The sandwich beams are manufactured using an optimised vacuum moulding process. Numerical models of the sandwich structures are developed using the LS-DYNA explicit finite element code. The skins are modelled with the advanced composite damage progression model (MAT 162) for which an inverse calibration technique was developed in the previous chapter. The foam core material is modelled with a transversely anisotropic elasto-plastic material model (MAT 142). A suitable method for simulating the foam core shear fracture is investigated. A comparison of the experimental and finite element response of the sandwich beams under quasi-static and dynamic indentation and bending loads shows that both deformation and failure can be successfully modelled.

5.2 Sandwich Materials

5.2.1 Thermoplastic Composite Skin Material

Sandwich skin laminates were manufactured from Twintex, which is a commingled E-glass/polypropylene, balanced twill weave woven fabric composite, with a 60% fibre weight fraction. Twintex was supplied by Saint Gobain Vetrotex as 0.5 mm thick preconsolidated sheets. See Chapter 3 for further details on Twintex.

5.2.2 Core Material

For the core material, a polypropylene anisotropic crushable foam of density 64 kgm^{-3} is used. The foam material is supplied by Dow Chemical Company under the tradename Strandfoam. The foam is manufactured by extruding polypropylene and a blowing agent through a multi orifice die plate. The foam comes out of the die as individual strands that fuse together to create a honeycomb structure forming a rectangular plank that can be cut to required dimensions. The honeycomb structure and the orientation of the foam strands results in a highly anisotropic material. A more detailed description of Strandfoam is given in Chapter 2. Figure 5-1 shows a schematic of the material configuration for the sandwich beam used in this study.

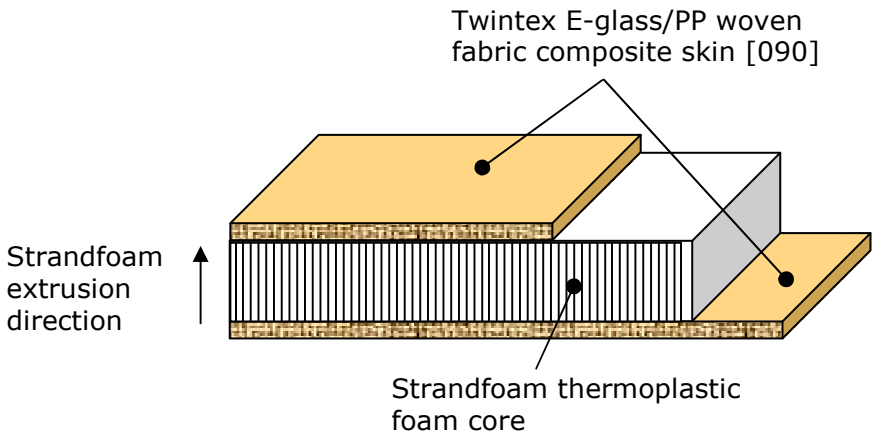

Figure 5-1. Schematic of the material configuration for the thermoplastic composite sandwich beam.

5.3 Vacuum Moulding Process

The sandwich beams were manufactured using a one step vacuum moulding process. Vacuum moulding is a low pressure moulding technique that offers the advantage of low capital investment and ease of installation and operation. Furthermore, it is suitable for the processing of low density foam cored sandwich beams since the low pressure minimises the core crush during the manufacturing of the beam. An investigation into the optimisation of process parameters for the vacuum moulding of thermoplastic sandwich beams has been conducted by Kulandaivel et al [8, 17]. Various moulding parameters such as skin preheat and mould temperature, mould time and pressure have been optimised for maximising the performance and quality of the sandwich beams. The optimised processing parameters from that study were used in this current work and are listed in Table 5-1.

A schematic of the vacuum moulding process is shown in Figure 5-2. The moulding process involved stacking 0.5 mm thick preconsolidated layers of Twintex on two thin Aluminium transfer plates and preheating them in a hot air oven above the melt temperature of the polypropylene matrix. The number of layers of Twintex varied between 2 and 6 layers according to the required skin laminate thickness. The temperature of the skin stacks was monitored using thermocouples inserted into the middle of the stacks. On reaching the preheat temperature, the first skin stack is transferred along with the plate to the vacuum table shown in Figure 5-3. The cold foam is then placed on this hot stack, followed by transfer of the second skin stack which is placed on top of the foam core to form the upper skin. The vacuum silicone membrane is clamped over the sandwich beam and air evacuated from under the membrane to apply a moulding pressure of 0.9 bar for consolidating the skins and bonding to the core. Finally, the beam is removed from the mould and allowed to cool.

Typically, sandwich panels of dimensions 800 mm x 70 mm were manufactured. Sandwich beam specimens were cut from the panels using a band saw. Beams were manufactured with two types of core thickness: 50 mm for indentation tests and 25 mm for bending tests. Beams with skin thicknesses of 1, 2 and 3 mm, were manufactured from 2, 4 and 6 layers of preconsolidated Twintex, respectively.

Step 1. Preheat Twintex stacks on transfer plates in hot air oven

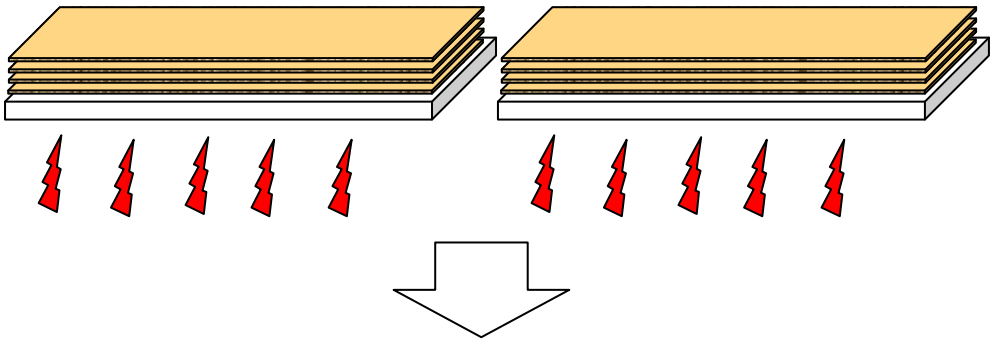

Step 2. Place foam core between Twintex stacks and rapidly transfer to vacuum table

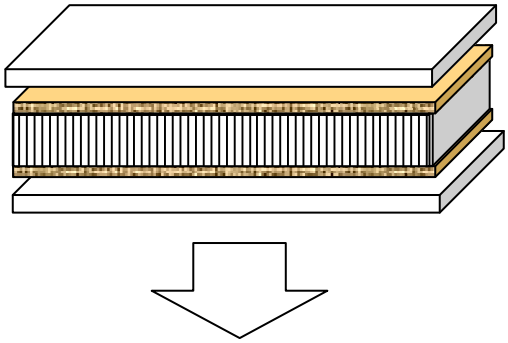

Step 3. Place assembled sandwich in vacuum table and apply 0.9 bar pressure

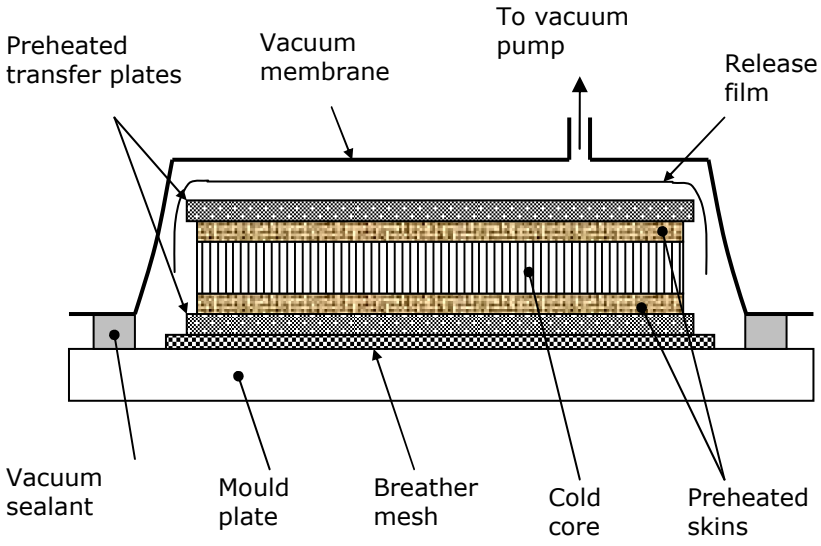

Figure 5-2. Schematic of vacuum moulding process.

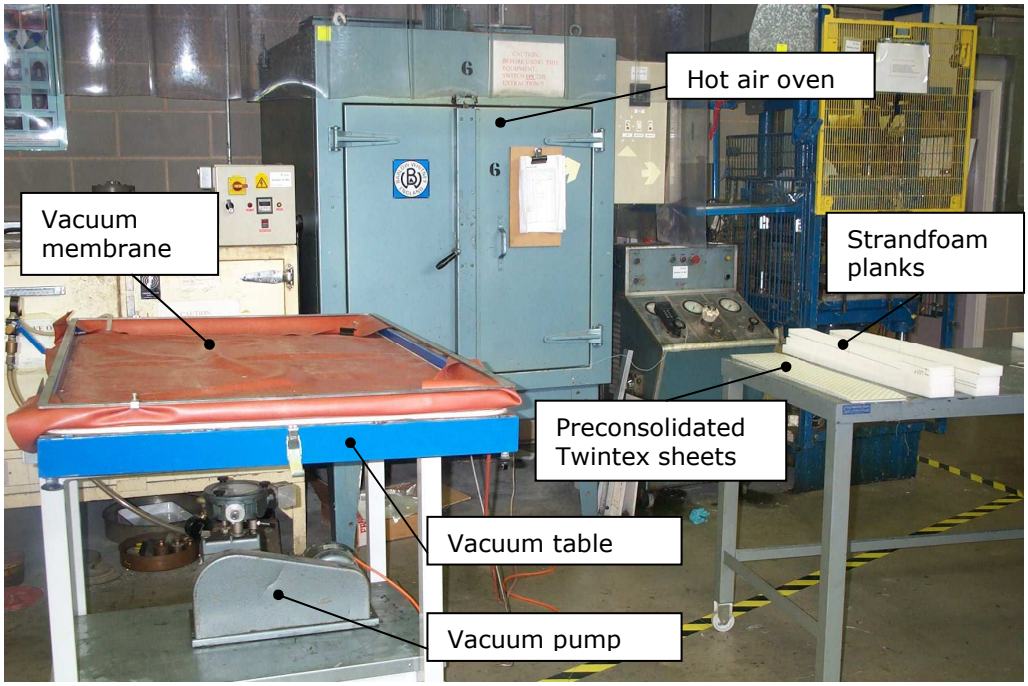

Figure 5-3. Picture of vacuum moulding process.

Table 5-1. Optimised vacuum moulding parameters for sandwich beams.

Moulding Parameter	Optimised Value
Skin preheat temperature	180 - 200 °C
Vacuum table temperature	30 °C
Transfer time	25 – 35 seconds
Mould time	5 – 10 minutes
Mould pressure	0.9 bar

5.4 Characterisation of the Foam Core Material

The quasi-static and dynamic mechanical properties of the Twintex skin material have been obtained through a comprehensive experimental program that was described in Chapter 3. This section describes the experimental program undertaken to characterise the mechanical behaviour of the foam core and thus obtain material properties required for input in the finite element foam material model. The tests were conducted at both quasi-static and dynamic strain rates.

Due to the way in which the foam is manufactured, it is anisotropic. Figure 5-4 shows a schematic of a typical foam plank and the material coordinate system used in this study. The extrusion direction is aligned with the x-axis while the z-axis corresponds to the short transverse. The y-axis is aligned with the longer transverse direction.

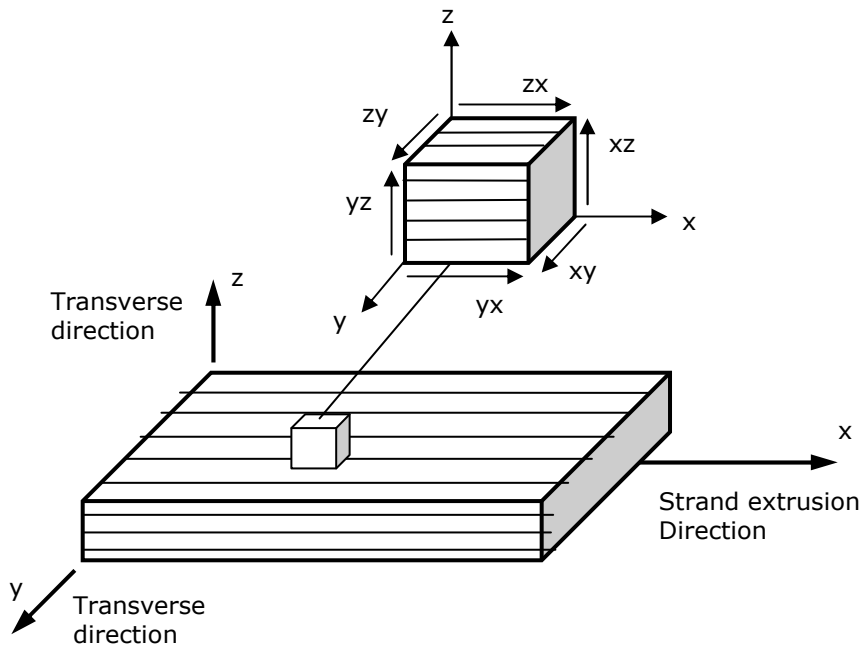

Figure 5-4. Schematic of typical Strandfoam plank and the co-ordinate axes assigned to test specimens.

5.4.1 Compression Tests

5.4.1.1 Test setup

Quasi-static compression tests were conducted on an Instron electromechanical test machine at a crosshead speed of 5 mm min^{-1}. The specimens were supported on a rigid flat plate while another flat plate, attached to the machine crosshead applies a compressive load (see Figure 5-5).

Dynamic compression tests were conducted in an instrumented drop tower using an impactor mass of 8.2 kg at speeds of 3, 5 and 7 ms^{-1} which corresponds to nominal strain rates of 120, 200 and 280 s^{-1}, respectively. As in the quasi-static test, the specimen is supported on a rigid flat plate; however, to impart a compressive dynamic load, the other flat plate impactor is attached to a free falling, weighted crosshead which is guided by two long steel rods.

In all cases, the load was measured using the load cell in the test machine while compressive strain was deduced from the relative displacement of the compression platen.

All compression specimens were cut from Strandfoam planks to dimensions of 50 mm x 50 mm x 25 mm. The tests were conducted in the foam extrusion direction (x-axis) and transverse direction. It was assumed that the normal strength and stiffness properties in the long and short transverse directions were equal. Subsequently, the compression tests were conducted only along the short transverse direction (z–axis).

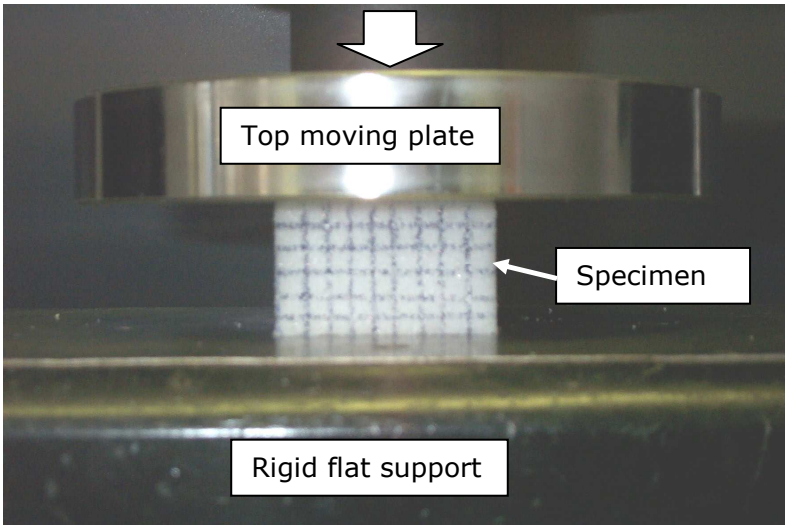

Figure 5-5. Foam compression test setup.

5.4.1.2 Results

A minimum of three repeats per test was undertaken with the results in most cases exhibiting high levels of reproducibility. Therefore only the typical, average stress-strain histories are presented.

Figure 5-6 shows the typical stress-strain response for Strandfoam under compression loading in the extrusion direction at different strain rates. In all cases, the curves show three distinct regions of deformation which is a typical feature of most cellular solids. The initial region exhibits a very steep linear elastic response up a yield point. This first elastic response corresponds with microbuckling of the cells at the strand interfaces [75]. In the second region, the response is approximately perfectly plastic, as the stress level remains almost constant over a long strain range (up to 70 % strain). This is commonly referred to as the plateau region and is the primary energy absorbing stage. In this region, the high level of plasticity is due to macro buckling, inter-strand shear and debonding [75]. The plateau stress at high strain rates (120 – 280 s^{-1}) is oscillatory due to dynamic effects and vibrations in contrast to the smooth response in the quasi-static case. For dynamic strain rates ranging from 120 to 280 s^{-1}, the noisy stress response in the plateau region appears to be rate insensitive, especially at macroscopic strains greater than 20%. Finally, in

the third region, a steep stress rise (densification) occurs as the material compacts and buckled and debonded strands are crushed [75].

Figure 5-7 shows the typical stress-strain response for Strandfoam under compression loading in the transverse direction at different strain rates. Again, there are three distinct regions of deformation. The initial response is linear elastic up to a yield point. In the plateau region there is an approximately linear increase in stress with strain as the foam exhibits some level of strain hardening up to a strain of 60%, after which densification occurs. Like the axial compression response at high strain rates, the plateau stress for transverse compression is also oscillatory and is seen to be rate insensitive for dynamic strain rates between 120 and 280 s^{-1}.

Figure 5-8 and Figure 5-9 show the effect of strain rate on the compressive modulus and yield stress in the extrusion direction (x-axis), respectively. In this study the yield stress in the extrusion direction is taken at the initial upper yield point. It is shown that both yield stress and modulus increased by almost 50% between the quasi-static and the highest strain rate of 280 s^{-1}.

The effect of strain rate on the compressive modulus and yield stress in the transverse direction is shown in Figure 5-10 and Figure 5-11, respectively. In this study, the yield stress in the transverse direction is taken at the yield point at 0.2% offset strain. This was done because of the lack of a clear yield point due to the extensive non-linear hardening response of the foam in the transverse direction. At the highest strain rate (280 s^{-1}) the increase in the modulus is 32% above the quasi-static value, while the yield strength exhibited a dramatic 57% increase.

The quasi-static compressive modulus and yield strength in the extrusion direction are 49% and 61% higher than that of the transverse direction, respectively. There is a similar trend at high strain rates. At the highest strain rate applied in this study (280 s^{-1}), the compressive modulus and yield strength in the extrusion direction are 62% and 64% higher than that of the transverse direction, respectively.

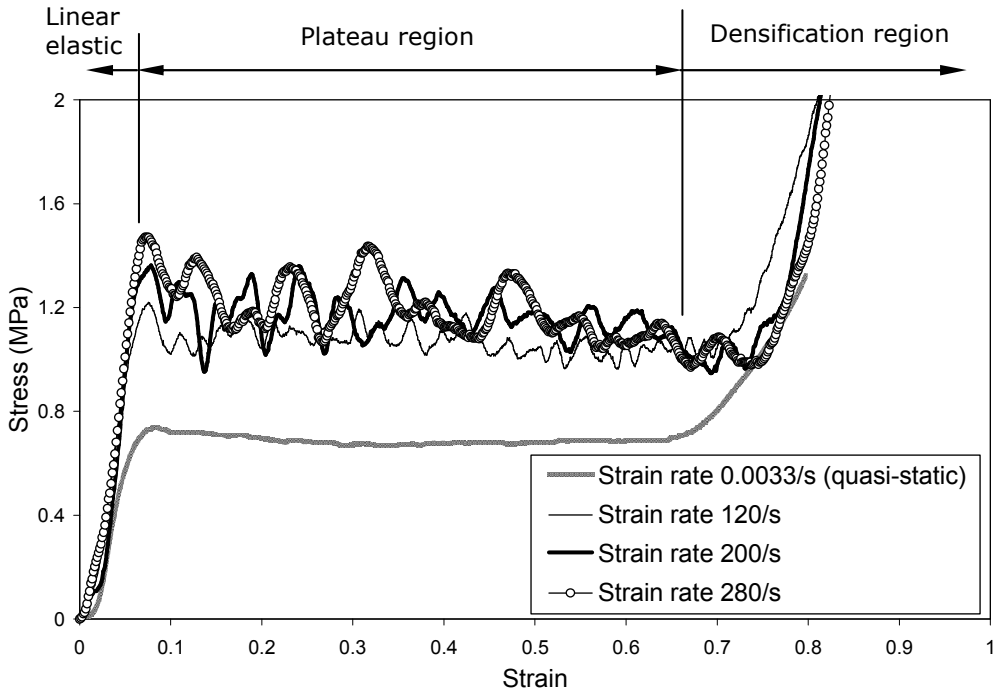

Figure 5-6. Typical compression stress-strain response for Strandfoam at quasi-static and high strain rates (120 – 280 s^{-1}) in the extrusion direction.

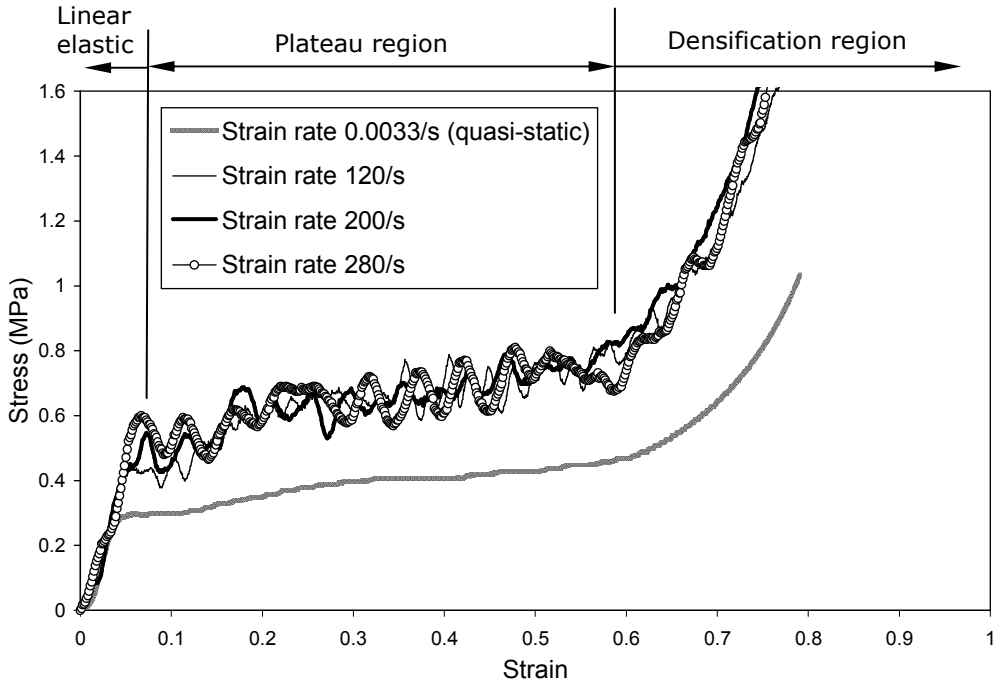

Figure 5-7. Typical compression stress-strain response for Strandfoam at quasi-static and high strain rates (120 – 280 s^{-1}) in the transverse direction.

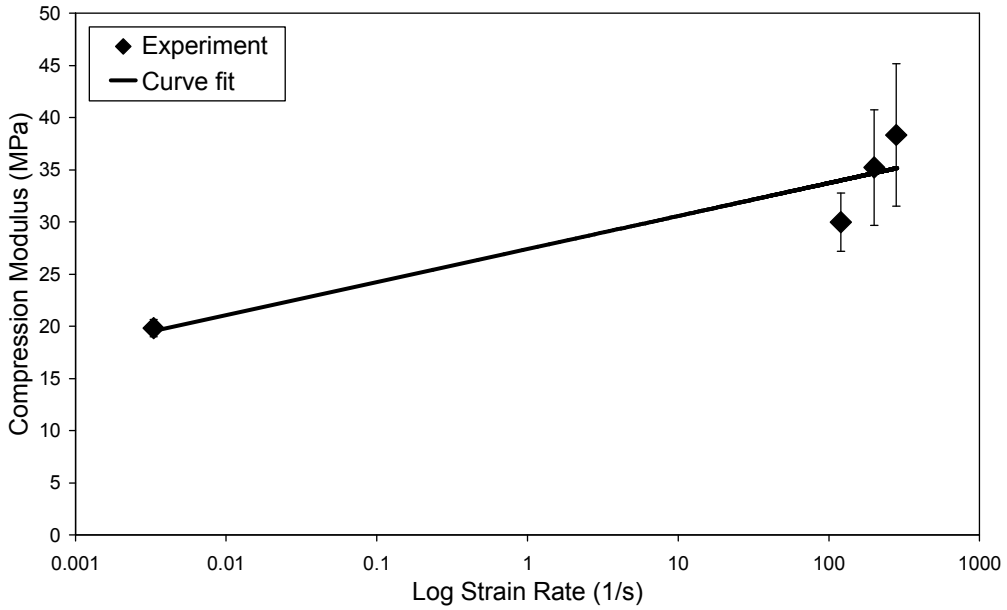

Figure 5-8. The strain rate effect on the compression modulus of Strandfoam in the extrusion direction.

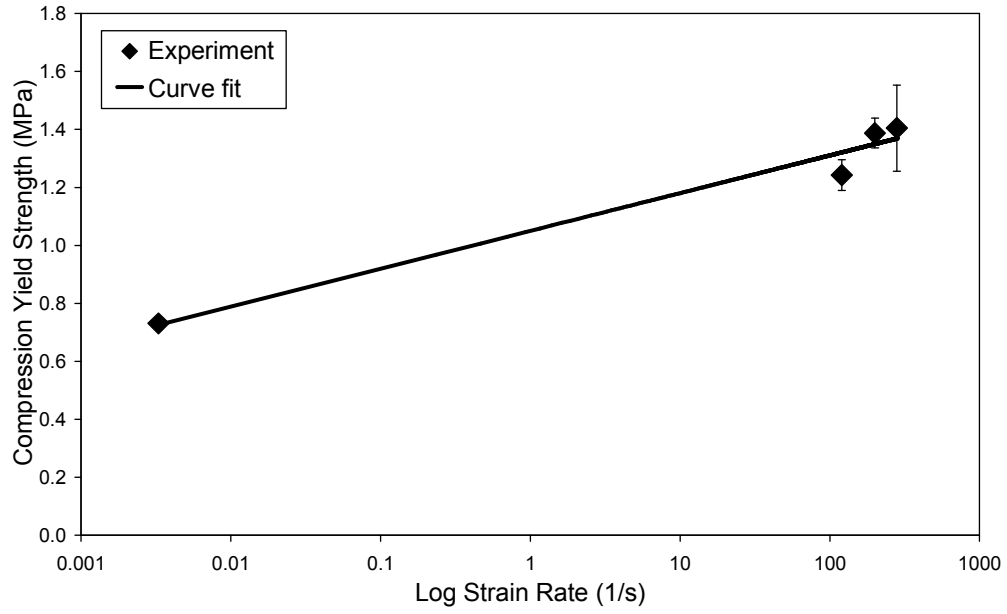

Figure 5-9. The strain rate effect on the compression yield strength of Strandfoam in the extrusion direction.

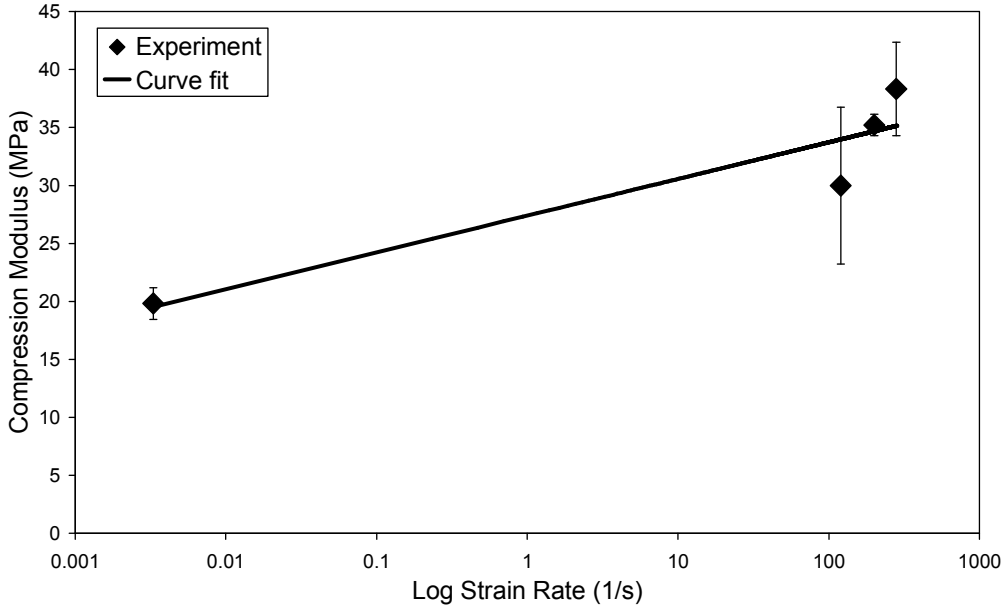

Figure 5-10. The strain rate effect on the compression modulus of Strandfoam in the transverse direction.

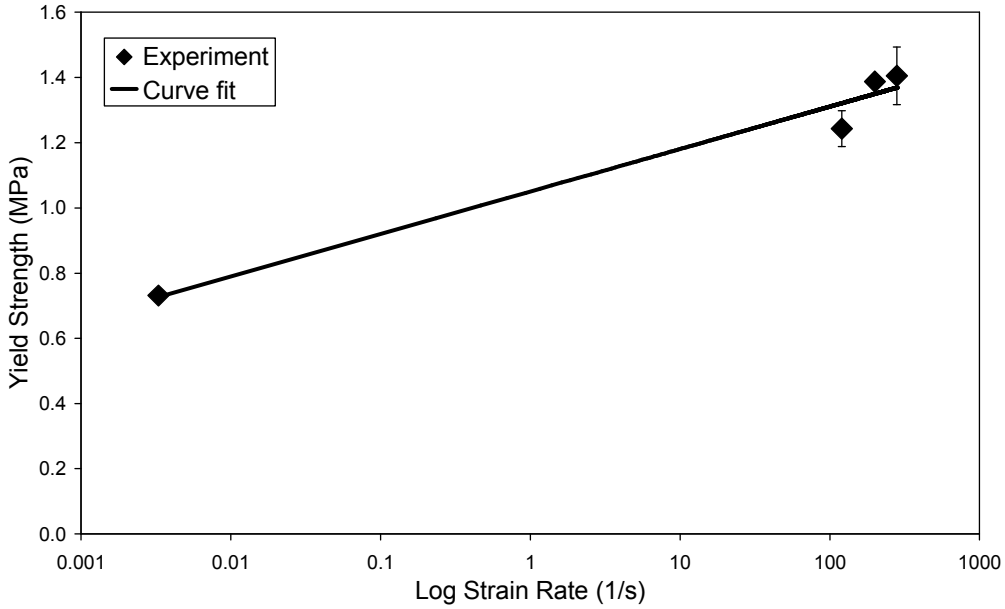

Figure 5-11. The strain rate effect on the compression yield strength of Strandfoam in the transverse direction.

5.4.2 Shear Tests

5.4.2.1 Test setup

An oblique shear impact test as described by Mills and Gilchrist [68] was used to characterise the dynamic shear properties of Strandfoam. For consistency and comparative analysis, the same oblique shear test was also used to obtain the quasi-static shear properties. The test fixture and test setup is shown in Figure 5-12. The fixture consists of a steel V block with upper surfaces at an angle of 45° to the horizontal. A pair of specimens is used in each shear test and each specimen is bonded on V shaped thin intermediate plates. The intermediate plates were then bonded to the V block using double sided adhesive tape. The intermediate plate allowed for easy removal of the failed specimens after each test. A load is applied to the specimens with a V shaped striker. The surface of the striker is covered with 120 medium grade emery cloth to reduce slip.

For the quasi-static shear test, the fixture described above was installed in an Instron electromechanical test machine as shown in Figure 5-12 (a). The test was conducted at a crosshead speed of 5 mm min^{-1} using displacement control.

High strain rate shear tests were conducted in a drop tower using a crosshead mass of 8.2 kg at speeds of 3, 5 and 7 ms^{-1} which correspond to strain rates of 120, 200 and 280 s^{-1}, respectively.

In all cases, the load was measured using the load cell in the test machine while compressive strain was deduced from the relative displacement of the V shaped impactor. The vertical displacement of the impactor was resolved into compressive and shear deflection components which were used to calculate the shear strain. Likewise, the vertical load was resolved into compressive and shear load components which were used to calculate the shear stress. It was assumed, in calculating the shear strain, that there is no slip at the upper surface of the foam.

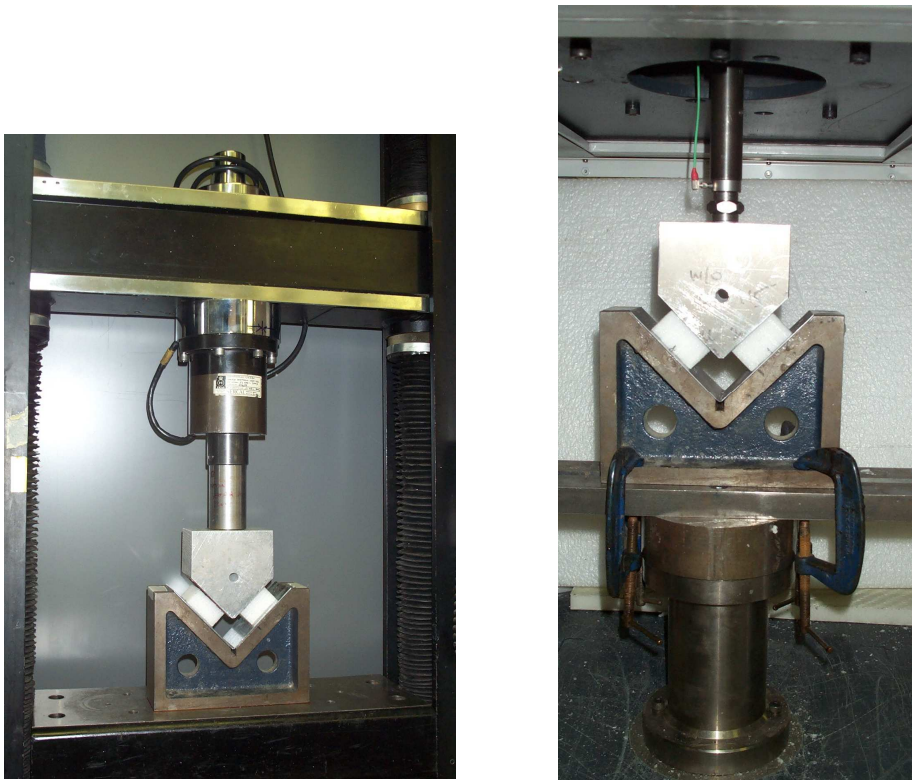

(a) (b)

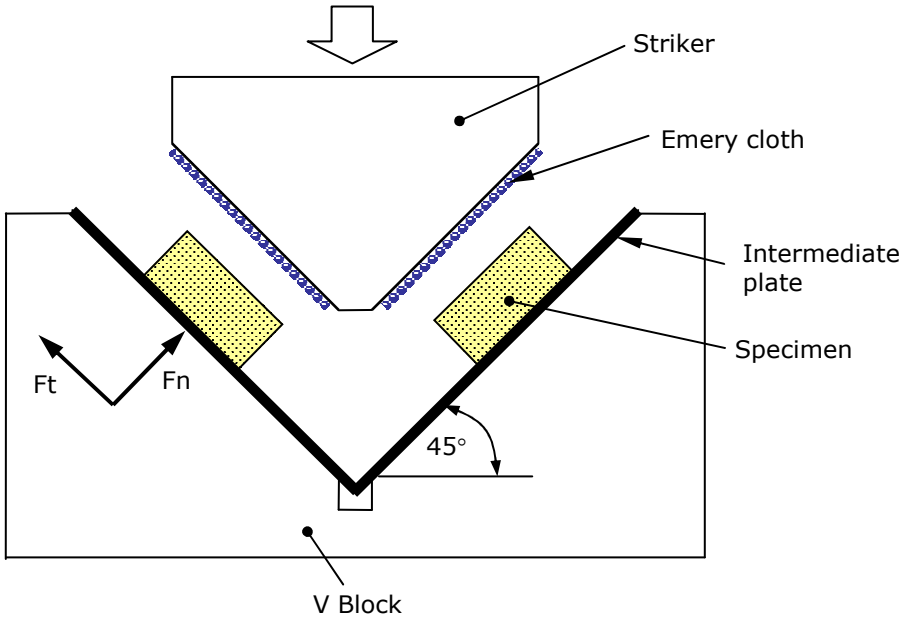

(c)

Figure 5-12. Foam shear test (a) picture of quasi-static shear test setup (b) picture of dynamic shear test setup (c) schematic of shear test.

5.4.2.2 Results

Figure 5-13 shows the typical quasi-static and dynamic shear stress-strain curves for shear loading along the x-y plane as defined in Figure 5-4. At both quasi-static and dynamic strain rates, the x-y shear stress-strain response is qualitatively similar. In all cases the initial response is linear elastic up to the initial yield point, followed by a gradual decrease in the shear stress, after which densification occurs and the shear stress increases sharply. A noticeable difference between the dynamic and static x-y shear stress strain behaviour is that at high strain rates the response is oscillatory in contrast to the smooth static curve. In this study, the x-y shear strength σ_{xy} is defined as the stress at the initial upper yield point

Figure 5-14 shows the typical quasi-static and dynamic shear stress-strain curves for shear loading along the y-z plane as defined in Figure 5-4. The y-z shear stress-strain response is almost elastic-plastic with the plateau region showing a near constant stress of 0.2 MPa up to a strain of 50%. This is followed by densification as the foam is compacted. Again, the y-z shear stress response is seen to be insensitive to strain rate effects. Oscillations can be seen in the dynamic y-z shear stress-strain curves while the static curve is smooth. For all strain rates, the y-z shear stress is about 50% less than the x-y shear stress. In this study the shear stress in the y-z plane is taken at 0.2% offset shear strain.

Figure 5-15 shows the typical quasi-static and dynamic shear stress-strain curves for shear loading along the z-x plane as defined in Figure 5-4. The results are very similar to the y-z shear stress response; however, the plateau region exhibits strain hardening prior to densification. Here too, the z-x shear stress is about 50% less than the x-y shear stress at all strain rates applied in this study.

Figure 5-16, Figure 5-17 and Figure 5-18 show the effect of strain rate on shear properties of Strandfoam. In general, both the shear modulus and shear strength along all shear planes (x-y, y-z and z-x) are seen to exhibit very little strain rate sensitivity within the scatter band of the results.

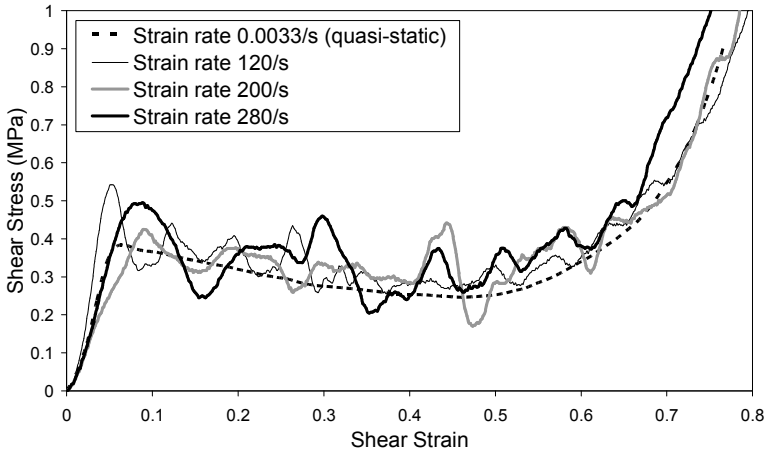

Figure 5-13. Typical shear stress-strain response for Strandfoam at various strain rates in the x-y plane.

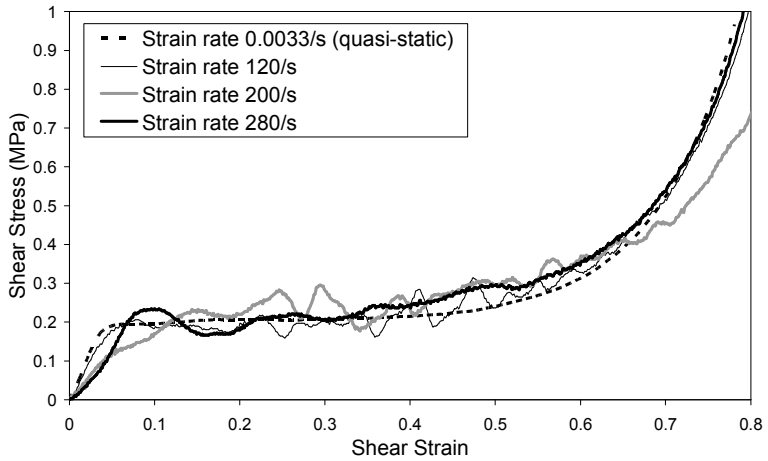

Figure 5-14. Typical shear stress-strain response for Strandfoam at various strain rates in the y-z plane.

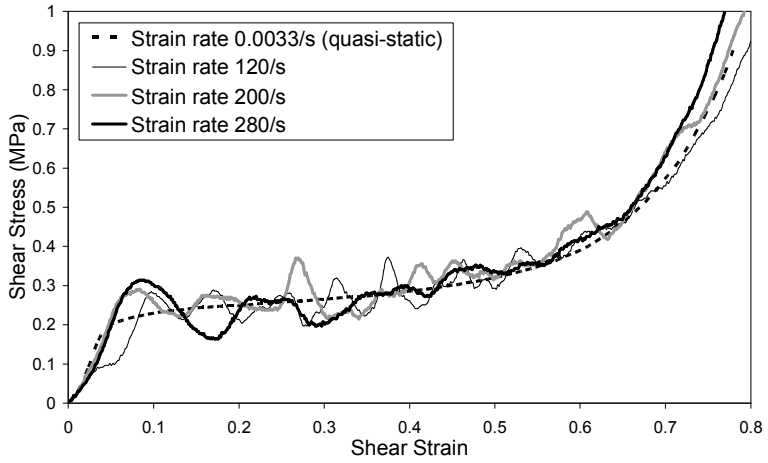

Figure 5-15. Typical shear stress-strain response for Strandfoam at various strain rates in the z-x plane.

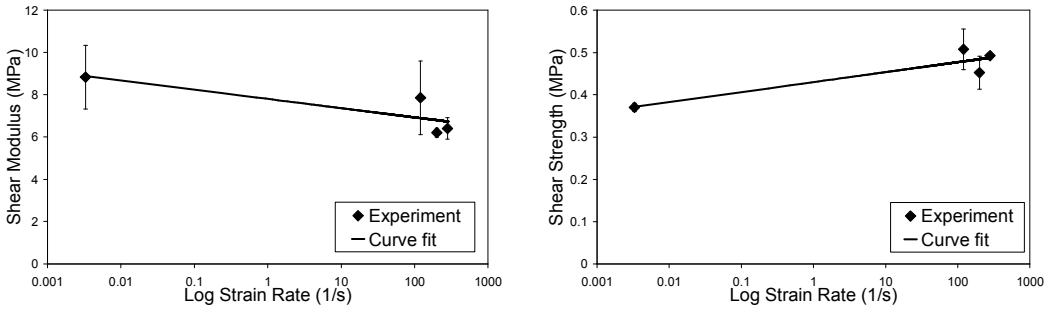

(a) (b)

Figure 5-16. The strain rate effect on the (a) shear modulus and (b) shear strength in the x-y plane for Strandfoam.

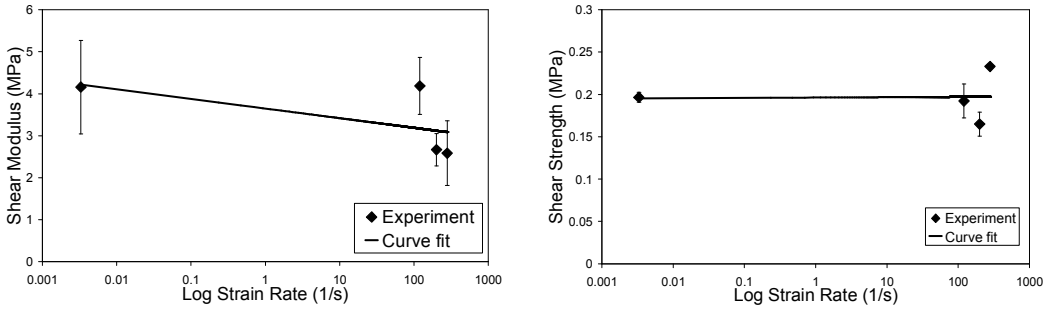

(a) (b)

Figure 5-17. The strain rate effect on the (a) shear modulus and (b) shear strength in the y-z plane for Strandfoam.

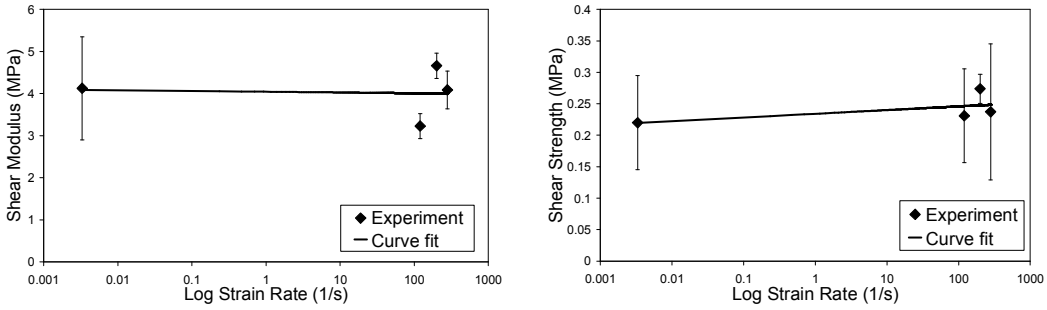

(a) (b)

Figure 5-18. The strain rate effect on the (a) shear modulus and (b) shear strength in the z-x plane for Strandfoam.

5.4.3 Tensile Tests

5.4.3.1 Test setup

Quasi-static tensile tests were conducted in a Tinius Olsen electromechanical test machine fitted with a 5 kN load cell. The test was conducted at room temperature in displacement control at a crosshead speed of 5 mm min^{-1}. Displacement was measured using the machine crosshead while load was measured with the load cell in the machine.

The specimens were 100 mm in length with square ends, 50 mm x 50 mm. The specimen was bonded between two steel "T" profiles and mounted in the test machine as shown in Figure 5-19. The bonding adhesive applied was a two part epoxy (Permabond E515) supplied by Glueline Ltd. The horizontal section of the "T" profile, glued to the foam, was first degreased using acetone, then the surface was roughened using medium grit emery paper and degreased again. The foam was clamped between the "T" sections and the glue was left to cure at room temperature for a minimum of 24 hours prior to testing.

Dynamic tensile tests were not conducted because time constraints in this project did not allow for the design and development a special rig that would be required to carry out such tests. This should be undertaken in the future.

5.4.3.2 Results

Figure 5-20 shows the typical quasi-static tensile stress-strain response for Strandfoam in the extrusion and transverse directions. In the extrusion direction the stress-strain response is linear elastic up to a strain of about 1%, after which there is non-linear yielding up to the maximum stress (0.75 MPa) followed immediately by an abrupt load drop at a strain of 1.9% as the specimen fails. For tensile loading in the transverse direction, the stress-strain response is almost linear elastic up to a maximum stress (0.25 MPa), followed by an abrupt load drop at a strain of 2.2%. The tensile modulus and strength in the extrusion direction are 76% and 68% higher than in the transverse direction, respectively.

Photographs of the failed tensile specimens are shown in Figure 5-21. In all cases, macroscopic failure occurs by a crack across the width of the specimen nearer the end, close to the steel T profiles. The non-linear stress-strain response described above suggests that the deformation mechanism is dominated by progressive plastic stretching of the cell walls prior to ultimate failure. The failure crack in the specimens loaded in the transverse direction occurs along the strand interfaces which suggest that interstrand separation is the primary mode of failure.

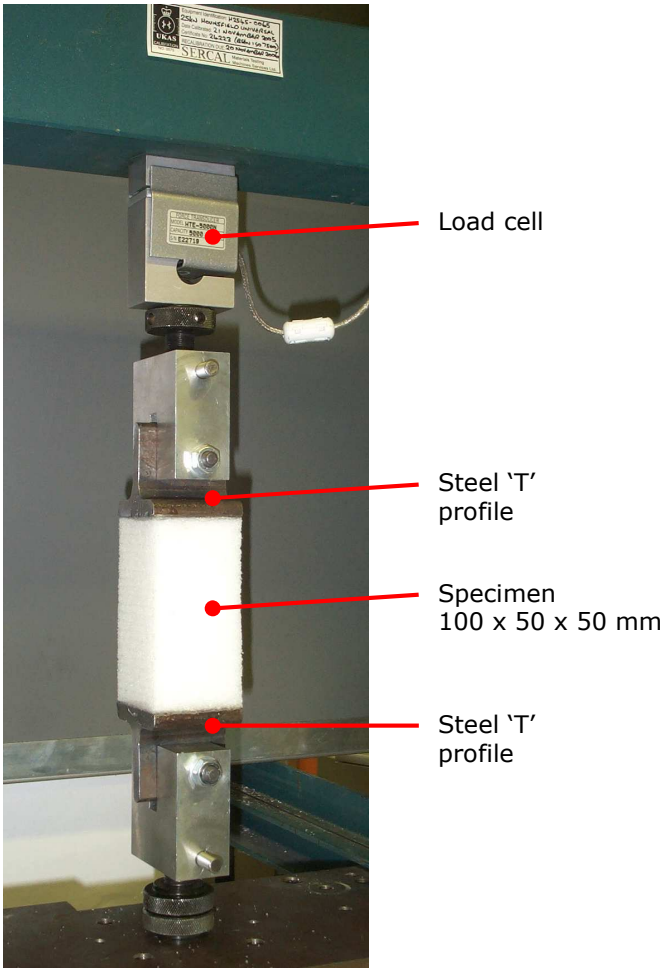

Figure 5-19. Quasi-static tensile test setup for Strandfoam in Tinius Olsen test machine.

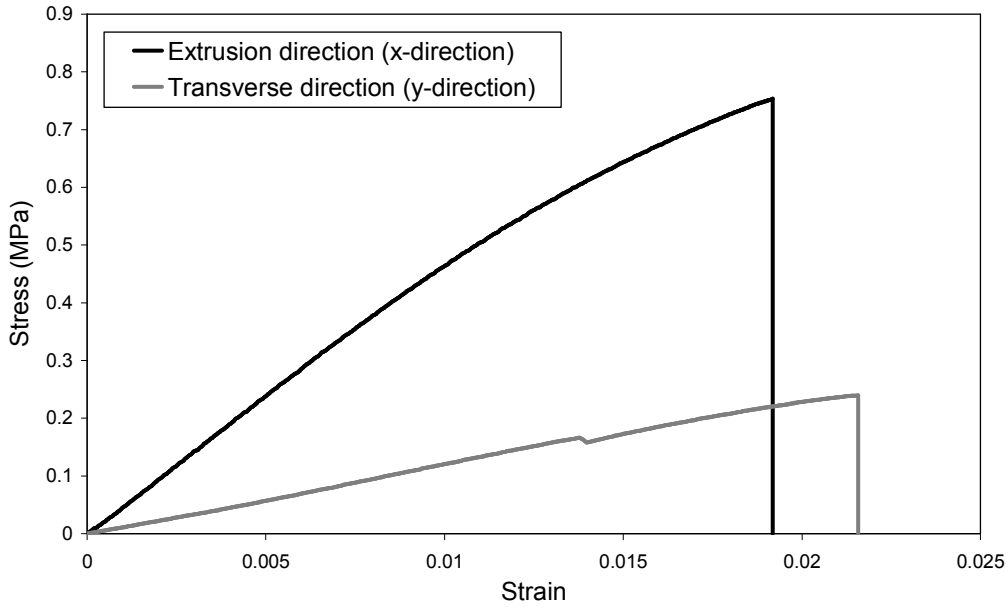

Figure 5-20. Typical quasi-static tensile stress-strain response for Strandfoam in the extrusion and transverse direction.

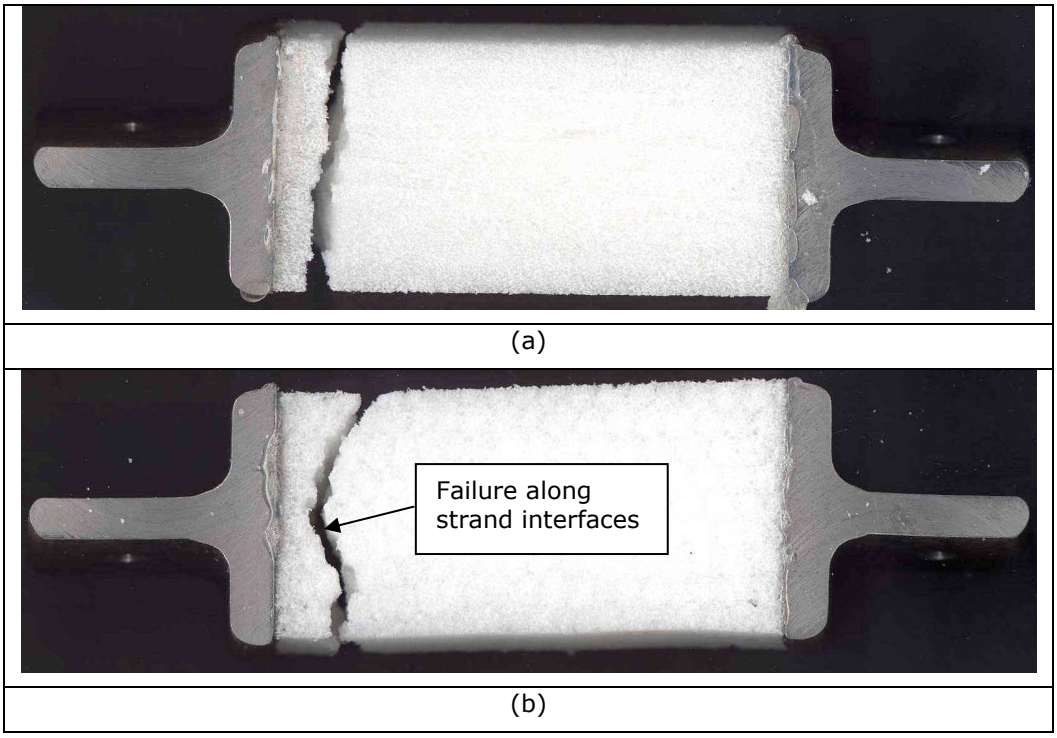

Figure 5-21. Photographs of failure in the tensile foam specimens (a) extrusion direction (b) transverse direction.

5.5 Indentation Behaviour of Sandwich Beams

This section presents an experimental and numerical investigation on the behaviour of thermoplastic sandwich beams under localised indentation loading. The development of a finite element modelling methodology for predicting the indentation response of the sandwich beam is described. Finally, the results of the finite element predictions were compared to the experiments.

5.5.1 Experimental Investigation

5.5.1.1 Quasi-static indentation tests

Quasi-static indentation tests were performed on a Tinius Olsen electromechanical test machine at a crosshead speed of 5 mm min^{-1}. The beams were indented with a 25 mm cylinder across the whole width of the beam cross-section. During the test the beam is supported on a rigid steel base plate. The tests were conducted under displacement control up to a maximum indentation of 45 mm. The quasi-static test setup is shown in Figure 5-22 (a). The specimens were 250 mm long with a width of 30 mm and nominal core thickness of 50 mm. Sandwich beams with three different skin thicknesses were investigated, 1, 2 and 3 mm, respectively. All sandwich beam skins had a [090] fibre orientation aligned along the beam longitudinal axis. The foam was assembled between the skins such that the Strandfoam extrusion direction was aligned with the impact direction, i.e. vertical.

5.5.1.2 Dynamic indentation tests

For this study, particular focus was given to analysing one of the primary indentation failure modes, i.e. core crush. Therefore, for simplicity and to suppress other modes of failure, consideration was given to low velocity impacts at an incident energy level of 15 J. Dynamic impact tests were performed in an instrumented drop tower with an impact mass of 8.2 kg and impact velocity of 2 ms^{-1} which corresponds with an incident energy of 15 J. The dynamic indentation test setup is shown in Figure 5-22 (b). The specimen dimensions are the same as in the quasi-static tests.

Digital images extracted from high speed camera footage were used to investigate the deformation and failure.

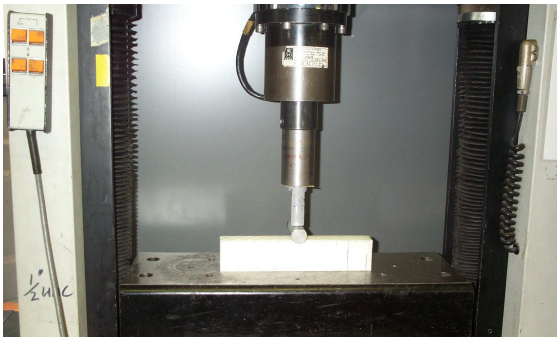

(a)

(b)

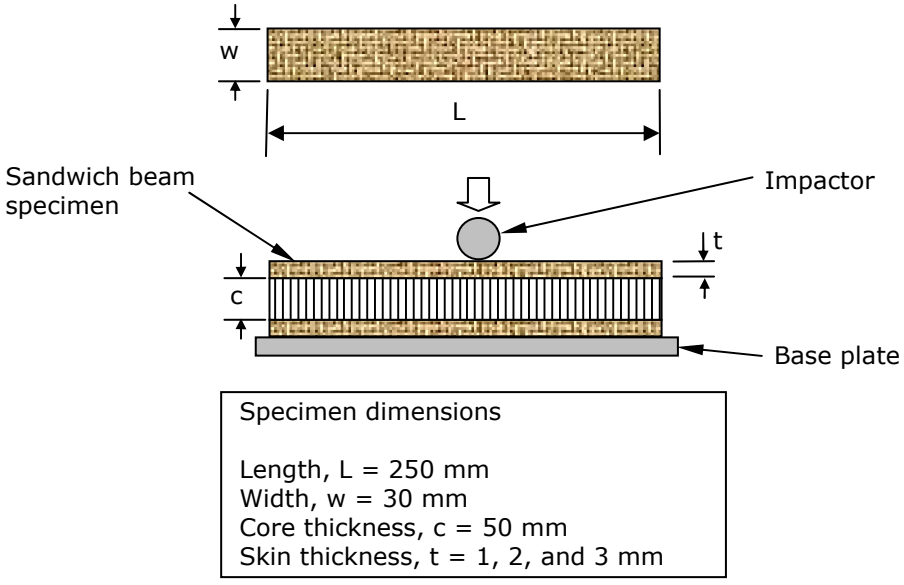

(c)

Figure 5-22. Indentation test (a) picture of quasi-static test setup in the Instron test machine (b) picture of dynamic test setup in the drop tower (c) schematic of indentation test and specimen dimensions.

5.5.2 Finite Element Modelling of the Indentation Behaviour of Sandwich Beams

The indentation behaviour of the sandwich beams is modelled in the LS-DYNA explicit finite element code. Figure 5-23 shows the sandwich beam finite element model. In order to reduce solution time and taking account of geometric and material symmetry, only one half of the sandwich beam was modelled. All the components were modelled with single integration point eight node solid elements. A stiffness based hourglass control was applied so as to prevent the occurrence of hourglassing. Each ply in the skin laminates was represented individually by a layer of solid elements. The cylindrical impactor and supports were modelled as rigid bodies. The supports were fully constrained while the impactor was only allowed to translate along the global Z axis. For the quasi-static analysis, the impactor was given a prescribed velocity which was much higher than that in the actual test so as to reduce the computational run time. For the dynamic model, the impactor was given an initial velocity equivalent to the actual test.

Contact between the impactor and the top composite skin was modelled using the automatic surface to surface contact algorithm within LS-DYNA. The same contact type was used to model contact between the bottom composite skins and the bottom plate.

A local coordinate system was used to define the material coordinates of the foam core. The local x-direction was aligned with the foam extrusion axis and the local y-direction is normal to this axis along the beam as shown in Figure 5-23. The material axes for the skins and all other components are orientated along the global axes.

5.5.2.1 Material Modelling: Composite Skin

The Twintex thermoplastic composite skin material was modelled with the LS-DYNA MAT 162 material model. This material model was described in Chapter 4. The calibration and validation of MAT 162 was also presented in Chapter 4. Table 5-2 summarises the calibrated and validated input

material properties and damage parameters that are used in the sandwich model.

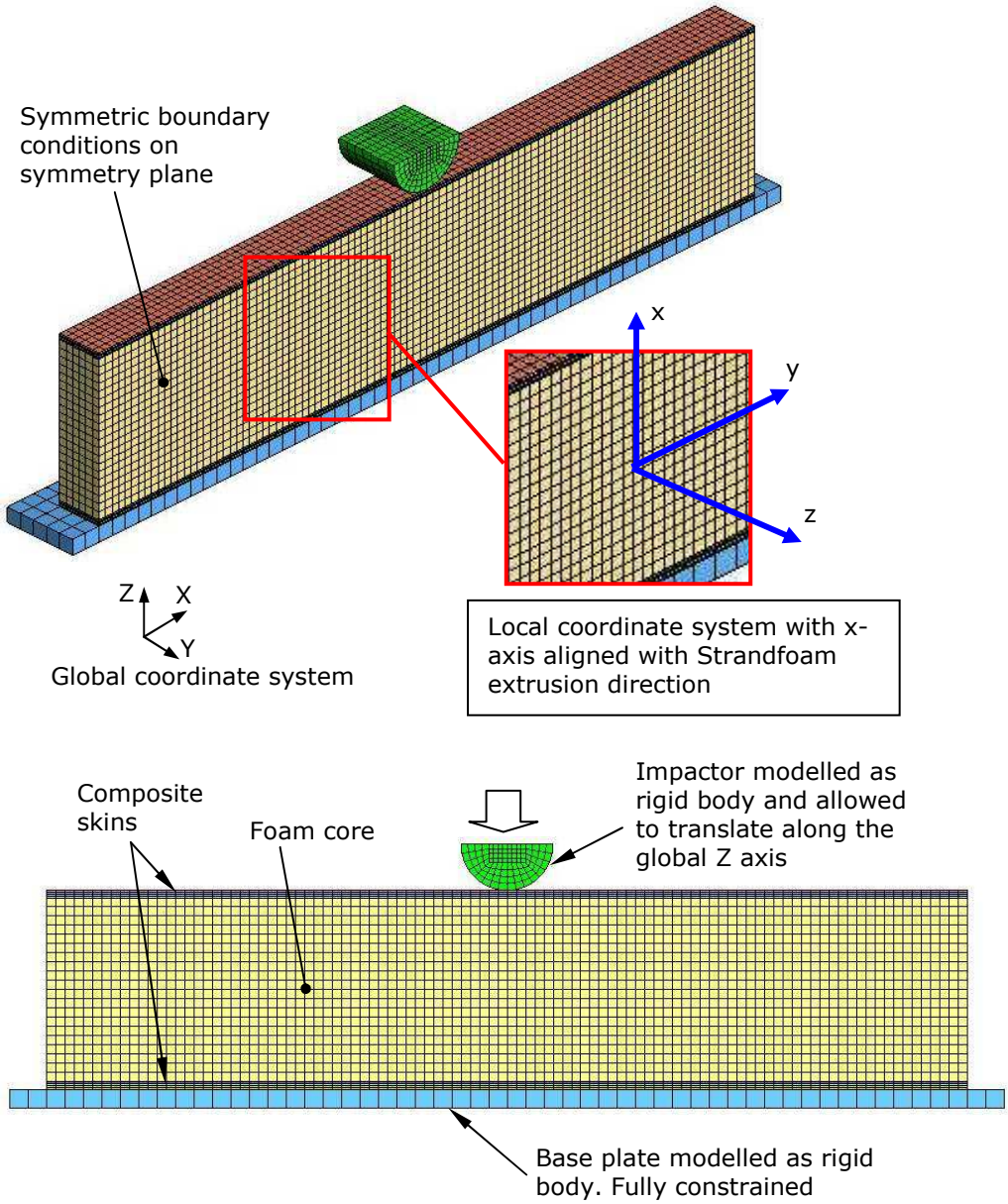

Figure 5-23. Finite element model and boundary conditions for sandwich beam indentation test simulations.

Table 5-2. Input data used for MAT 162 for modelling Twintex [090] fabric skins.

Parameter	Symbol	Value
Density	ρ	1500 kg/m^3
Longitudinal Young's modulus*	E_x	10 GPa
Transverse Young's modulus*	E_y	10 GPa
Through-thickness Young's modulus	E_z	5.3 GPa
	υ_{yx}	0.12
Poisson's ratio	υ_{zx}	0.14
	υ_{zy}	0.15
Shear modulus, x-y plane	G_{xy}	1.79 GPa
Shear modulus, y-z plane	G_{yz}	1.66 GPa
Shear modulus, z-x plane	G_{zx}	1.79 GPa
Longitudinal tensile strength	S_{xT}	269 MPa
Longitudinal compressive strength	S_{xC}	178 MPa
Transverse tensile strength	S_{yT}	269 MPa
Transverse compressive strength	S_{yC}	178 MPa
Through-thickness tensile strength	S_{zT}	25 MPa
Crush strength	S_{Fz}	300 MPa
Fibre shear strength	S_{FS}	110 MPa
Shear strength, x-y plane	S_{xy}	23 MPa
Shear strength, y-z plane	S_{yz}	12 MPa
Shear strength, z-x plane	S_{zx}	13.6 MPa
Columb friction angle	φ	20°
Tensile volume strain limit	EEXPN	2
Strength strain rate coefficient	C1	0.181
Fibre damage parameter (longitudinal)	m1	0.5
Fibre damage parameter (transverse)	m2	0.5
Fibre crush and punch shear damage	m3	2
Matrix damage parameter	m4	-0.15

* Young's modulus was reduced from the experimental value of 14 GPa to 10 GPa so as to improve the correlation between the simulation and bending impact test results (see Chapter 4)

5.5.2.2 Material Modelling: Foam Core

The anisotropic crushable thermoplastic foam core material was modelled with the MAT 142 constitutive model which was recently implemented in LS-DYNA. MAT 142 is a transversely anisotropic elasto-plastic material model.

This material model uses a modified Tsai-Wu yield surface that is defined as:

$$\begin{aligned} &F_{11}\sigma_{xx}^2 + F_{22}\sigma_{yy}^2 + F_{22}\sigma_{zz}^2 + \\ &F_{44}\sigma_{xy}^2 + F_{55}\sigma_{yz}^2 + F_{44}\sigma_{zx}^2 + \\ &2F_{12}\sigma_{xx}\sigma_{yy} + 2F_{12}\sigma_{zz}\sigma_{yy} + F_{12}\sigma_{xx}\sigma_{zz} \le 1 \end{aligned} \qquad \textbf{(5-1)}$$

where, x, y, and z denote the material in-plane and out-of-plane directions; F_{ij} are coefficients of the yield surface; σ_x, σ_y and σ_z are the stresses in the x, y and z directions, respectively; σ_{xy} , σ_{yz} , and σ_{zx} are the shear stresses in the x-y, y-z and z-x planes, respectively.

In this model the modified Tsai-Wu yield surface hardens or softens as a function of volumetric strain. The growth of the yield surface is directional and follows the growth of the material yield stress along the material axes. Furthermore, the yield surface is symmetric which facilitates the application of a single yield value for tension and compression which is determined by the current value of the volumetric strain as described by equation 1-2:

$$\varepsilon_v = 1 - \frac{V}{V_0} \Rightarrow \sigma_{yc} = \sigma_{yt} = \sigma_y(\varepsilon_v) \qquad \textbf{(5-2)}$$

where V_0 is the initial volume; V is the current volume, σ_{yc} is the compressive yield stress; σ_{yt} tensile yield stress and σ_y symmetric yield stress.

5.5.2.3 Determination of Foam Material Model Input Data

The results from the aforementioned experimental foam characterisation test program (Section 5.4) were complied to provide material property input data for the finite element MAT 142 model. More specifically, the density, elastic modulus, and shear modulus, were required. Additionally, the MAT 142 model requires the direct input of the compressive and shear stress-strain curves in a tabulated format. For high strain rate analysis, an approximate averaged compression stress-strain curve is used as shown in Figure 5-24. This was considered appropriate as the dynamic compressive plateau stress only showed marginal strain rate sensitivity over the strain rates applied in this work. The quasi-static shear stress-strain input data was used in the dynamic models because of the relative strain rate insensitivity of the shear stress-strain response. Table 5-3 summaries the foam material input data for the MAT 142 material model.

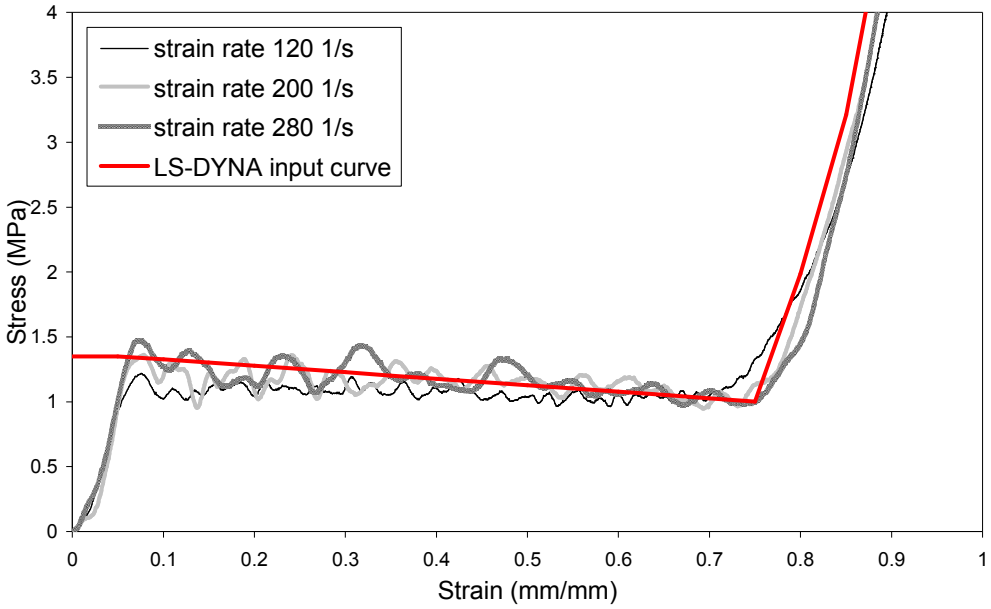

Figure 5-24. Showing dynamic compressive stress-strain input curve for LS-DYNA MAT 142 material model.

Table 5-3. Input data used for MAT 142 for modelling Strandfoam.

Parameter		Static Value	Dynamic Value
Density	ρ	64 kg/m^3	64 kg/m^3
Axial Young's modulus	E_x	19.8 MPa	35 MPa
Transverse Young's modulus	E_y	10.4 MPa	14.8 MPa
Shear modulus in axial plane	G_{xy}	8.83 MPa	8.83 MPa
Shear modulus in transverse plane	G_{yz}	4.2 MPa	4.2 MPa

5.5.3 Quasi-Static Indentation Test Results

5.5.3.1 Sandwich beam with 1 mm skins

Figure 5-25 (a) shows comparison of the typical experimental and simulation force-displacement curves for the sandwich beam with 1 mm thick skins under quasi-static indentation loading. In general, the response of the beam is somewhat similar to the foam compression response that was present in Section 5.4.1. There are three distinct regions of deformation. Initially the force-displacement is linear elastic, until about 500 N. After this, the force-displacement response is non-linear. This non-linear behaviour is induced by progressive localised core crush under the cylindrical impactor along with membrane stretching of the top skin. As the impactor moves down into the specimen, the ends of the sandwich are also pulled up (see Figure 5-25 (b)). At a displacement of about 37 mm, there is a sharp load increase as foam densification occurs. The predicted force-displacement response shows excellent correlation with the experimental results. The significant localised indentation and general deformation of the sandwich beam has been well predicted as shown in Figure 5-25 (c).

Figure 5-26 shows a comparison of the experimental and predicted damage in the 1 mm top skin laminate. Visual inspection of the top skin after the test showed matrix damage and minor fibre fracture which was caused by high local contact stress. The predicted macro-scale damage that included fibre fracture, matrix cracking and delamination shows good qualitative agreement with the experimental observations. However, the fibre damage is slightly overestimated. The simulation shows that delamination is inhibited directly under the impactor due to the high compressive stresses that exist in this area.

As expected, there was no visible damage observed in the bottom skin laminates.

5.5.3.2 Sandwich beam with 2 mm skins

Figure 5-27 (a) shows comparison of the typical experimental and simulation force-displacement curves for the sandwich beam with 2 mm thick skins under quasi-static indentation loading. In general, the force displacement response of the 2 mm skin beam is somewhat similar to the 1 mm skin beam. The initial response is linear elastic up to 700 N, followed by non-linear plastic deformation, after which there is densification of the core which results in a sharp load increase. However, in contrast, the yield load of the 2 mm skin is almost twice that of the 1 mm skin. In this study the yield load is defined as the load at a displacement of 5 mm. Figure 5-27 (b) – (c) show good agreement between the experimental and predicted deformation.

Figure 5-28 shows a comparison of the experimental and predicted damage in the 2 mm top skin laminate. The predicted macro-scale damage which included minor fibre fracture, matrix cracking and delamination shows good qualitative agreement with the experimental observations. However, the fibre damage and delamination are slightly overestimated.

5.5.3.3 Sandwich beam with 3 mm skins

Figure 5-29 (a) shows comparison of the typical experimental and simulation force-displacement curves for the sandwich beam with 3 mm thick skins under quasi-static indentation loading. The beam response is initially linear elastic up to about 1500 N. This is followed by an approximately perfectly plastic deformation with an almost constant load of about 2100 N up to a displacement of 35 mm, at which point densification occurs. The yield load of 1740 N is almost 4 times higher than that of the 1 mm skin sandwich beam. The predicted force-displacement response shows good agreement with the experimental results. Figure 5-29 (b)-(c) show good agreement between the experimental and predicted deformation.

Figure 5-30 shows a comparison of the experimental and predicted damage in the 3 mm top skin laminate. The predicted macro-scale damage which includes minor fibre fracture across the width of the specimen, matrix cracking and delamination shows good qualitative agreement with the

experimental observations. However, the fibre damage and delamination are slightly overestimated.

5.5.4 Dynamic Indentation Test Results

5.5.4.1 Sandwich beam with 1 mm skins

Figure 5-31 (a) shows a comparison of the typical experimental and simulation force-displacement curves for the sandwich beam with 1 mm thick skins under dynamic indentation loading. In general, in its early stages, the dynamic indentation force-displacement response for an incident energy of 15 J is similar to the quasi-static response. Initially, the load-displacement response is linear elastic followed by non-linear deformation up to a maximum load of 1198 N at a displacement of about 16 mm, before unloading as the impactor rebounds. This is a similar magnitude of load at 16 mm as the quasi-static test. Again, the non-linear response is primarily due to localised core crush and membrane stretching in the top skins.

Figure 5-31 shows good agreement between the experimental and simulation results. The peak load is marginally over estimated by 7 %. Additionally, the simulation appears to unload at a faster rate than in the test. This may be due to the prediction of no damage in the top skin which meant that the top skin was able to return to its original position at a faster rate in contrast to the test specimen which may have experience some level of barely visible permanent damage.

5.5.4.2 Sandwich beam with 2 mm skins

Figure 5-32 shows a comparison of the typical experimental and simulation force-displacement curves for the sandwich beam with 2 mm thick skins under dynamic indentation loading. Initially, the load-displacement response is linear elastic followed by non-linear deformation at a maximum load of about 1300 N up to a displacement of about 14 mm, before unloading as the impactor rebounds. The maximum load for the 2 mm skin is higher than for the 1 mm skin sandwich beam but the displacement is lower for the 2 mm skin. Figure 5-32 shows good agreement between the experimental and simulation results.

5.5.4.3 Sandwich beam with 3 mm skins

Figure 5-33 shows a comparison of the typical experimental and simulation force-displacement curves for the sandwich beam with 3 mm thick skins under dynamic indentation loading. In general, the dynamic indentation force-displacement for an incident energy of 15 J is again similar to the quasi-static response. Initially, the load-displacement response is linear elastic followed by non-linear deformation up to a maximum load of about 2000 N at a displacement of about 10 mm, before unloading as the impactor rebounds. The maximum load in this case is higher and the displacements lower than the 2 mm and 1 mm skin sandwich beams. Figure 5-33 shows good agreement between the experimental and simulation results.

In general, the dynamic response over the range of loading and displacement tested is similar to the quasi-static response over the same range regardless of the skin thickness. This indicates limited strain rate response at the rates of testing studied.

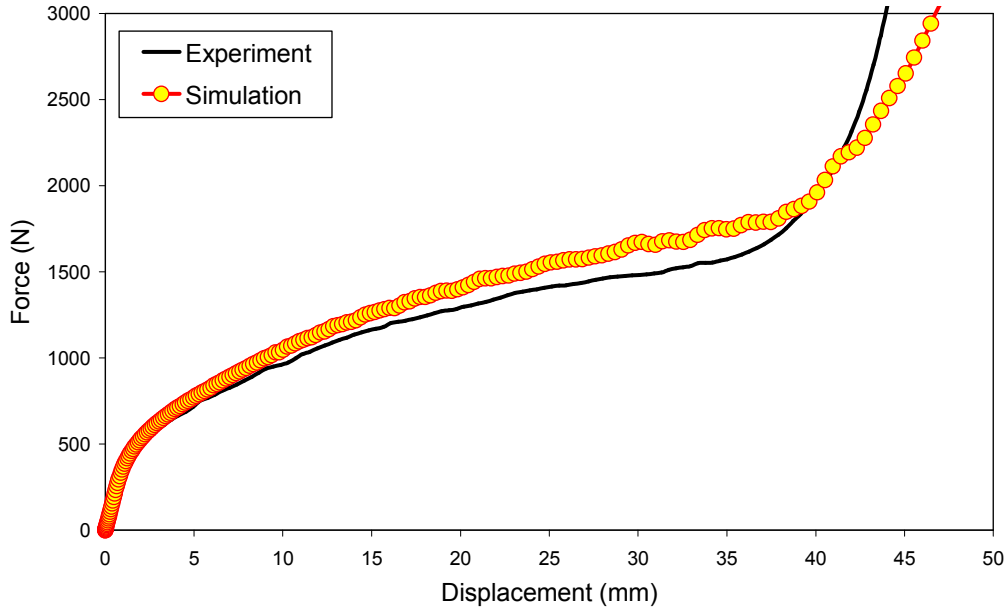

(a)

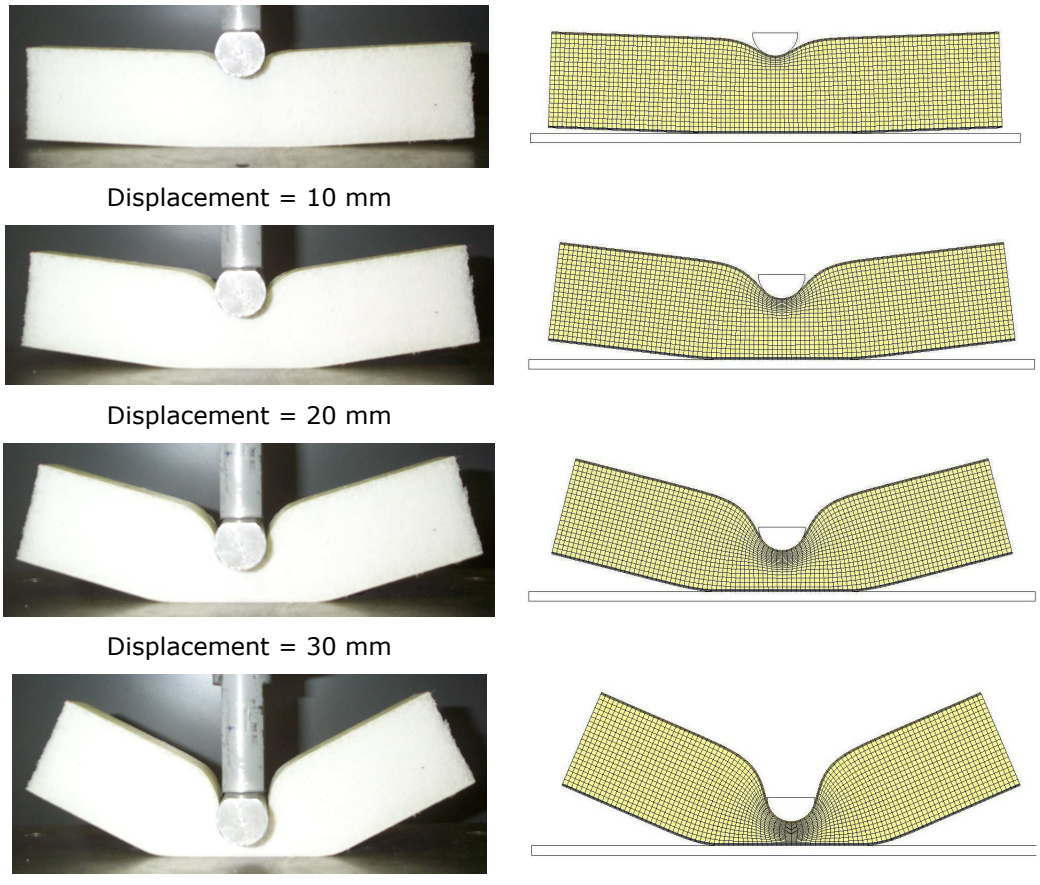

Displacement = 10 mm

Displacement = 20 mm

Displacement = 30 mm

Displacement = 40 mm

(b) (c)

Figure 5-25. Quasi-static indentation test on 1 mm skin sandwich beam (a) comparison of experimental and simulation force-displacement curves (b) experimental deformation and failure modes (c) simulation deformation and failure modes.

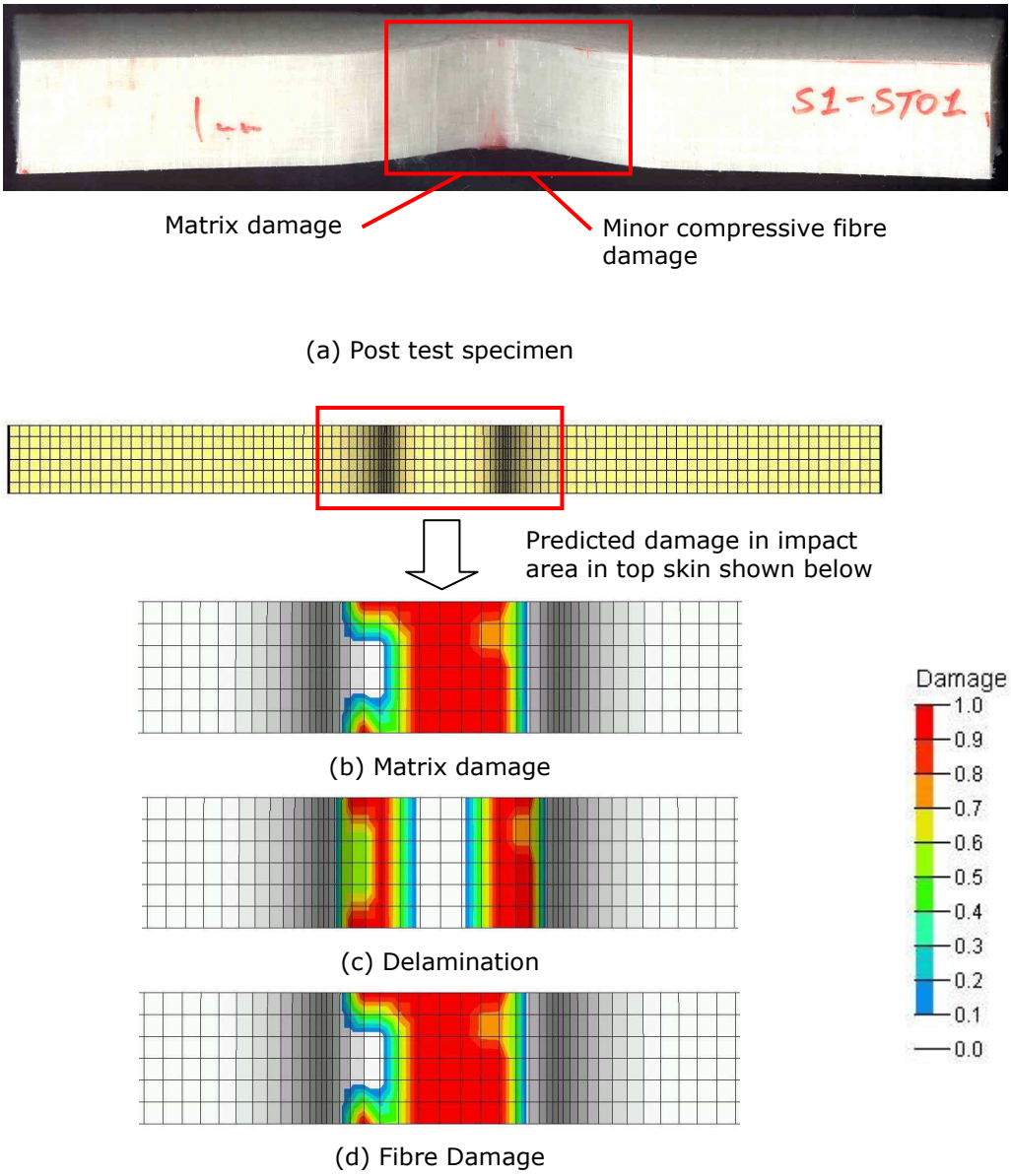

Figure 5-26. Damage in 1 mm top skin (a) experiment and simulation: (b) matrix damage (c) delamination (d) fibre damage for quasi-static indentation test.

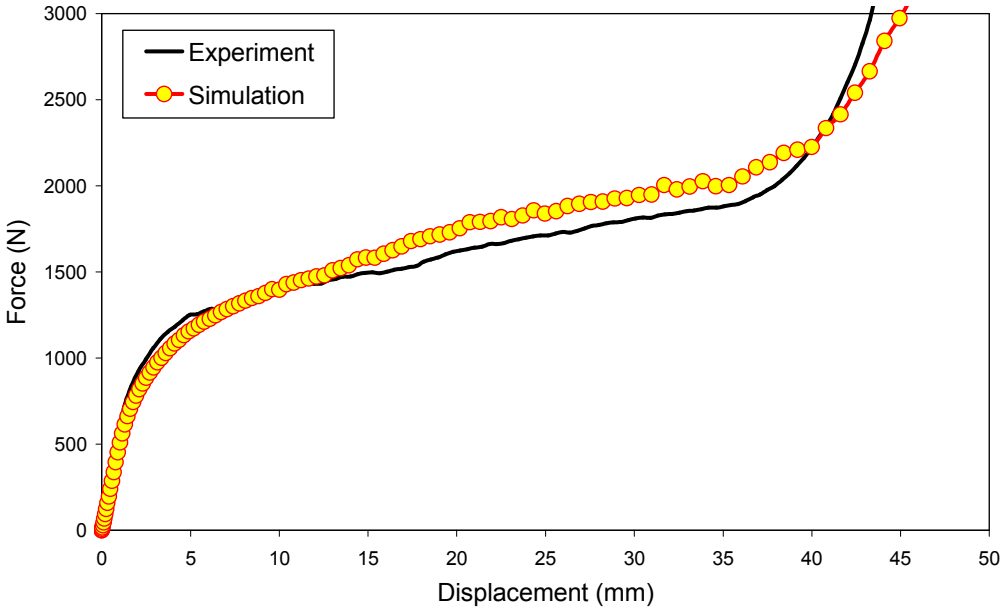

(a)

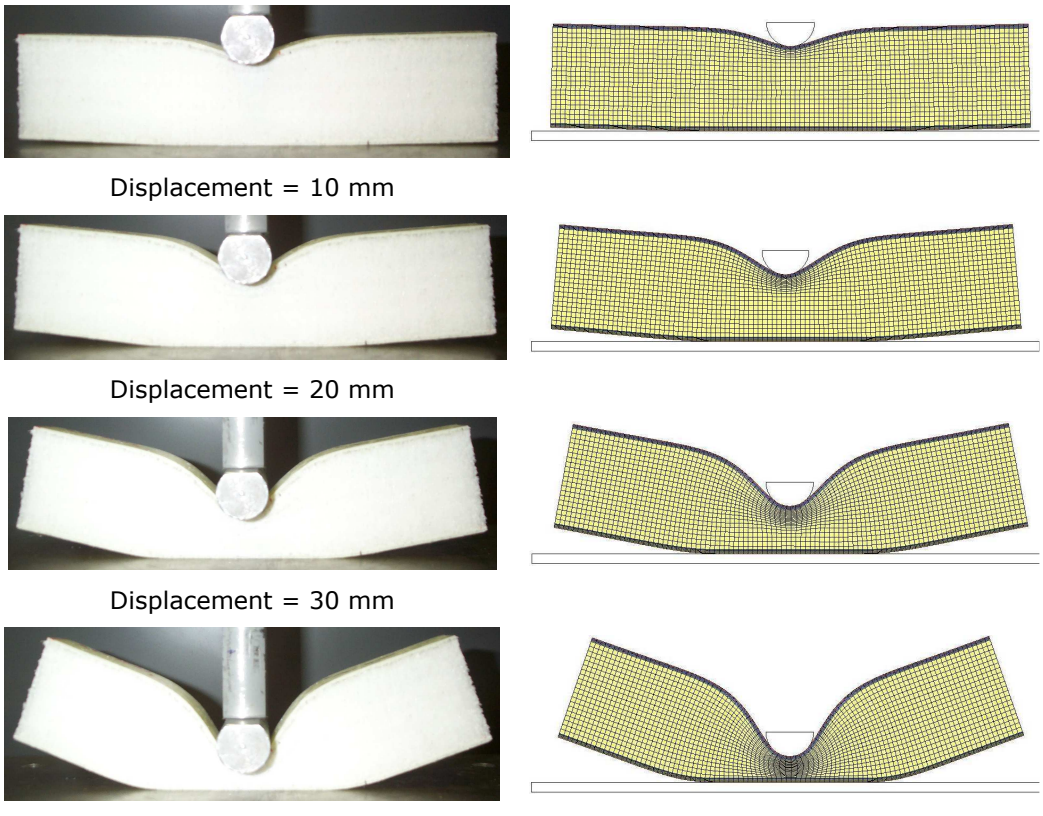

(b) (c)

Figure 5-27. Quasi-static indentation test on 2 mm skin sandwich beam (a) comparison of experimental and simulation force-displacement curves (b) experimental deformation and failure modes (c) simulation deformation and failure modes.

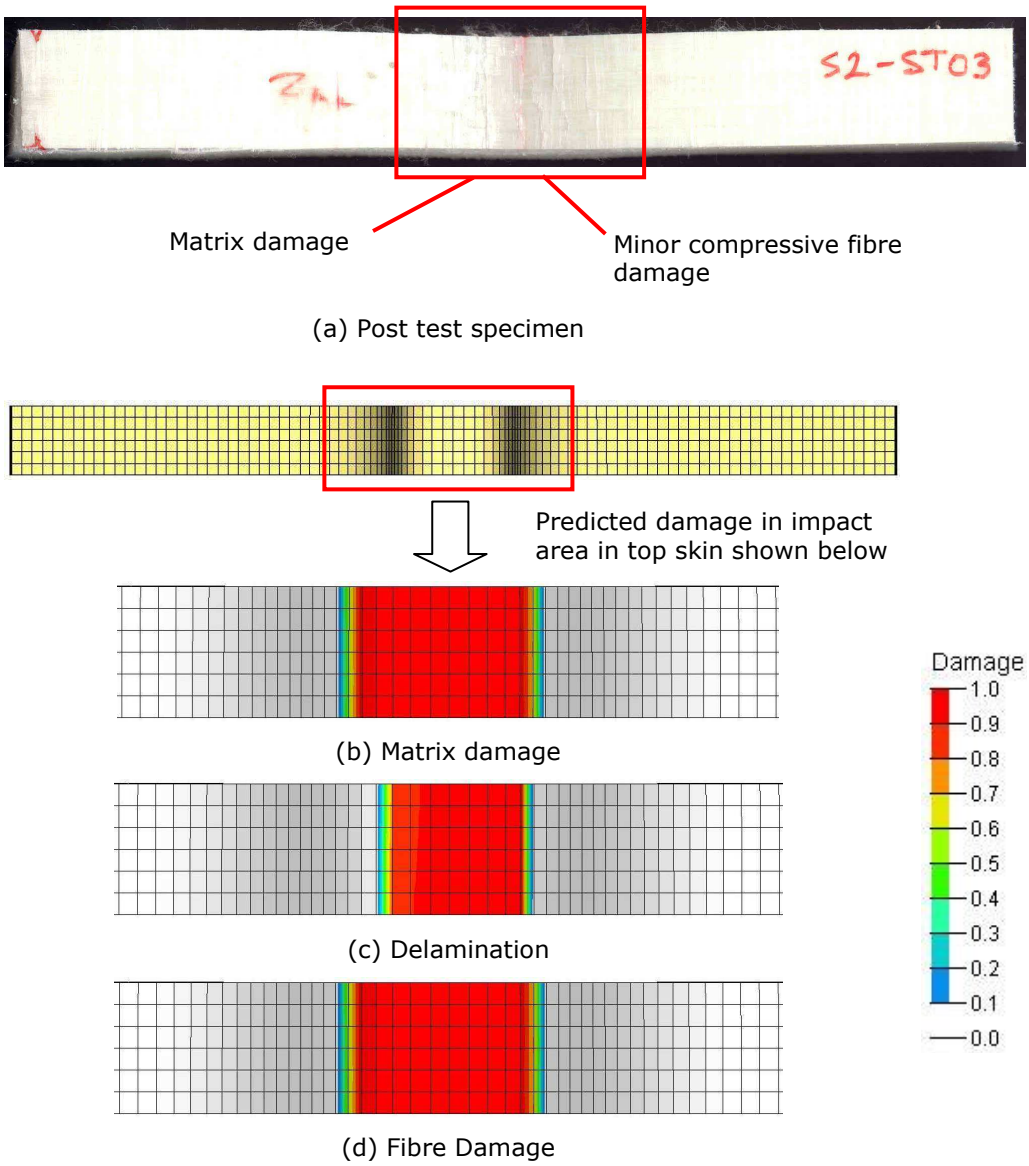

Figure 5-28. Damage in 2 mm top skin (a) experiment and simulation: (b) matrix damage (c) delamination (d) fibre damage for quasi-static indentation test.

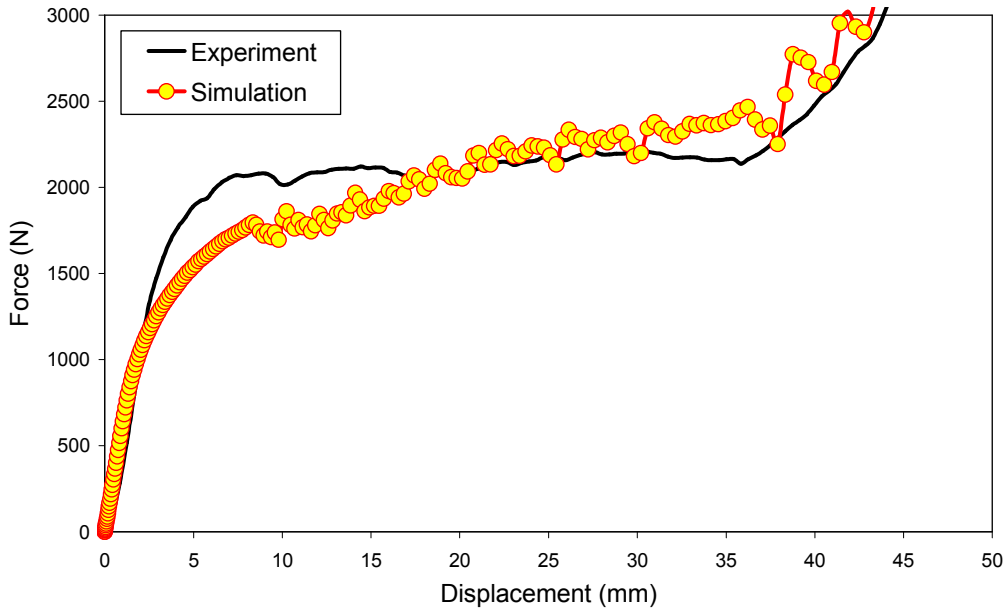

(a)

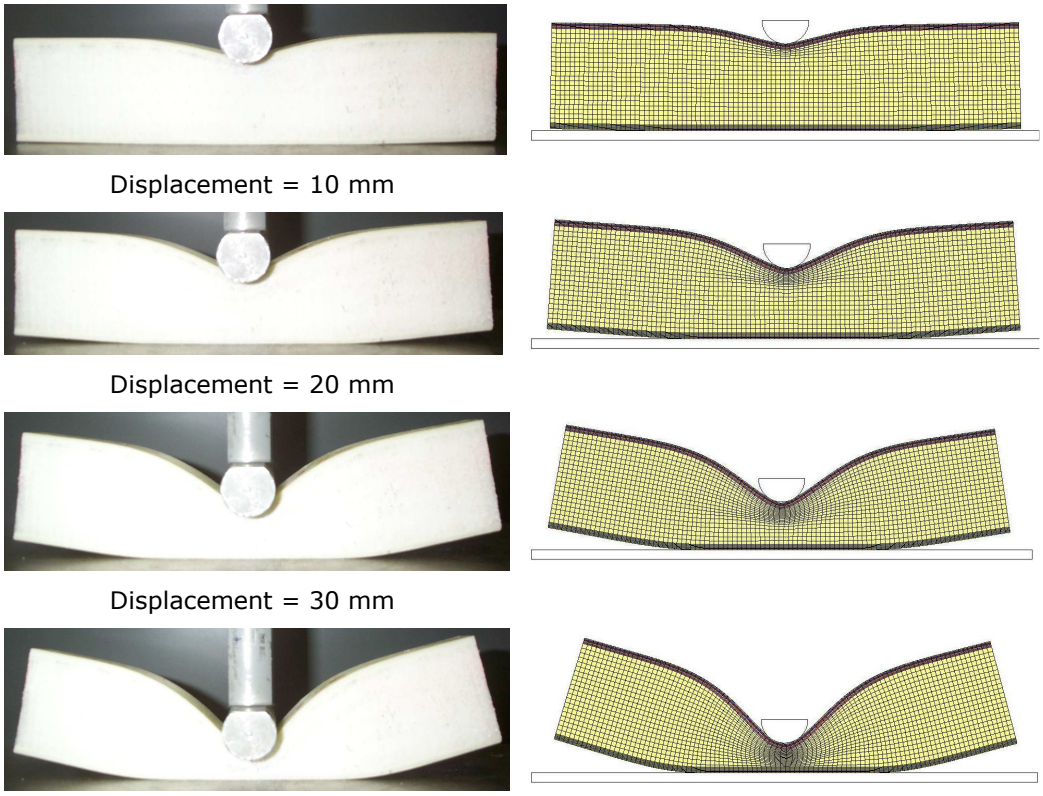

(b) (c)

Figure 5-29. Quasi-static indentation test on 3 mm skin sandwich beam (a) comparison of experimental and simulation force-displacement curves (b) experimental deformation and failure modes (c) simulation deformation and failure modes.

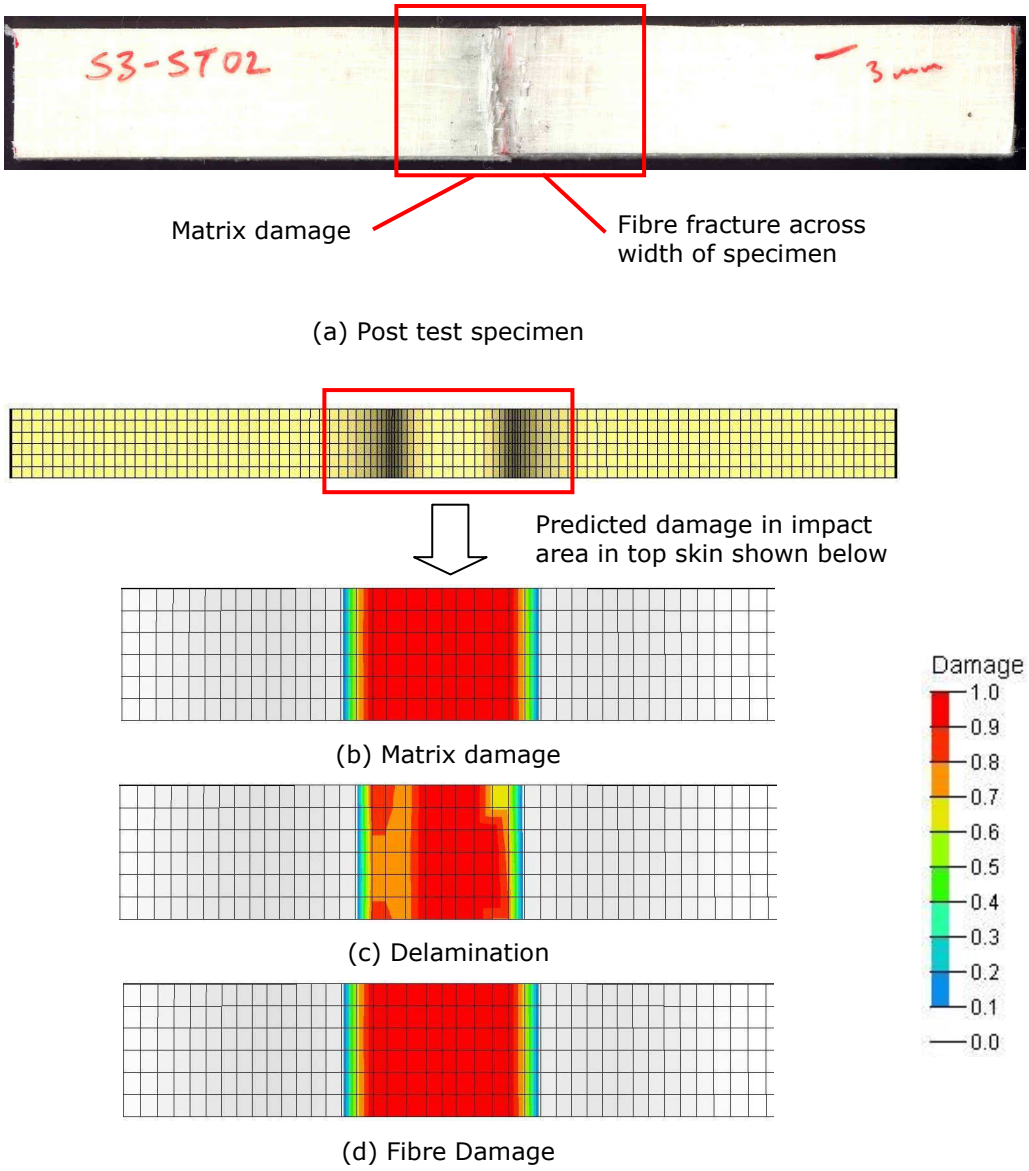

Figure 5-30. Damage in 3 mm top skin (a) experiment and simulation: (b) matrix damage (c) delamination (d) fibre damage for quasi-static indentation test.

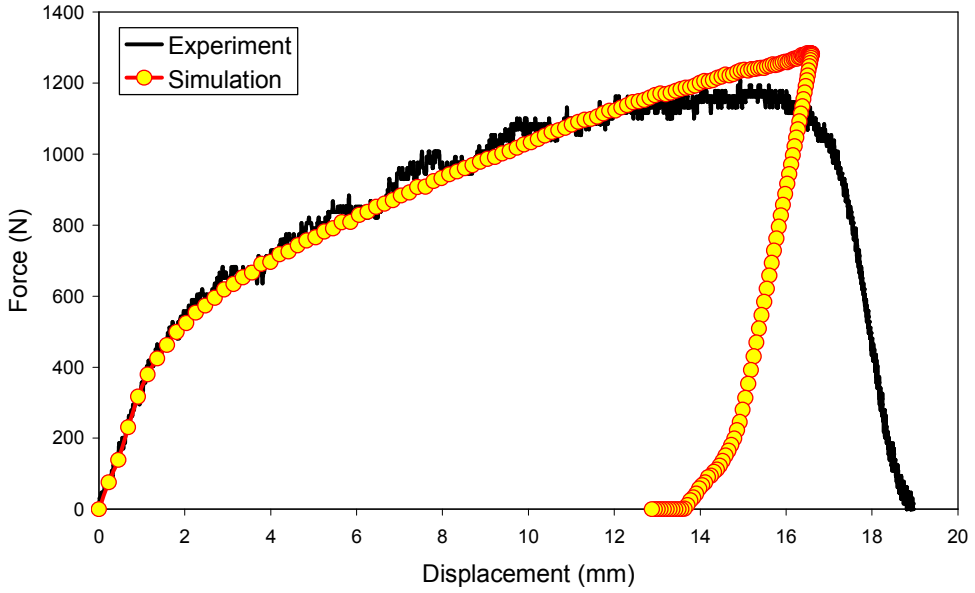

(a)

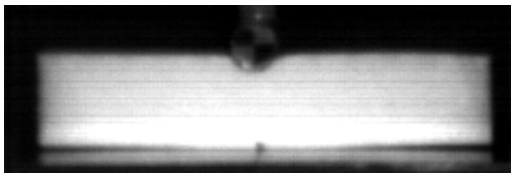

Time = 0.004 s
Displacement = 7.15 mm

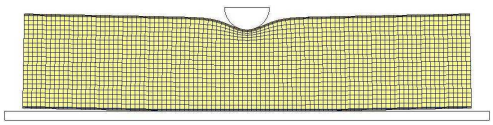

Time = 0.004 s
Displacement = 7.04 mm

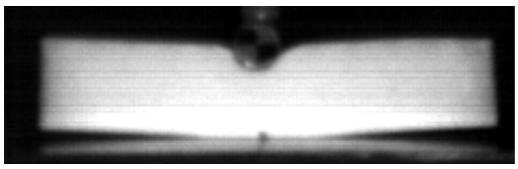

Time = 0.008 s
Displacement = 12.72 mm

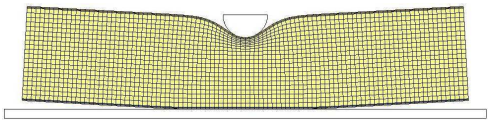

Time = 0.008 s
Displacement = 12.44 mm

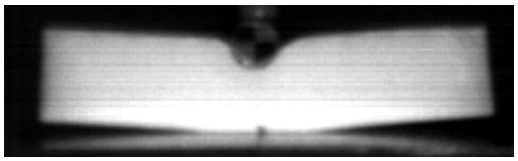

Time = 0.012 s
Displacement = 16.27 mm

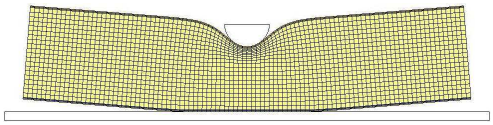

Time = 0.012 s
Displacement = 15.75 mm

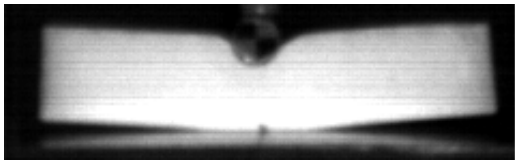

Time = 0.016 s
Displacement = 17.87 mm

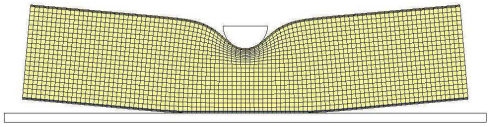

Time = 0.016 s
Displacement = 16.57 mm

(b) (c)

Figure 5-31. Dynamic 15 J indentation test on 1 mm skin sandwich beam (a) comparison of experimental and simulation force-displacement curves (b) experimental deformation and failure modes (c) simulation deformation and failure modes.

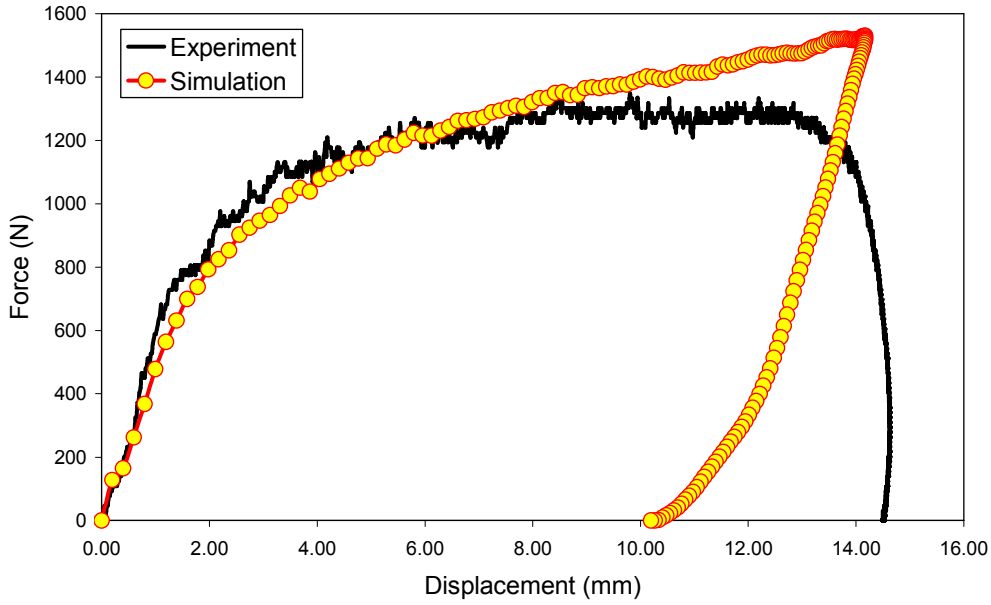

(a)

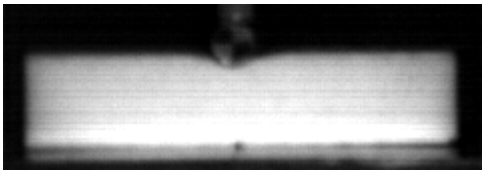

Time = 0.002 s
Displacement = 3.69 mm

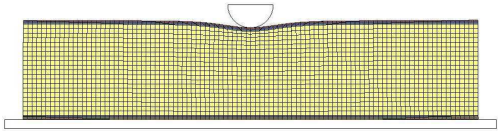

Time = 0.002 s
Displacement = 3.87 mm

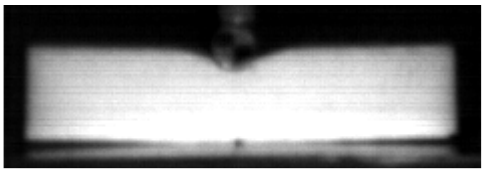

Time = 0.008 s
Displacement = 6.91 mm

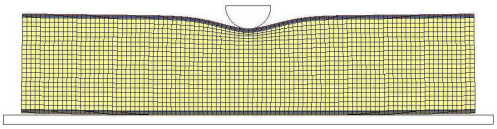

Time = 0.008 s
Displacement = 7.24 mm

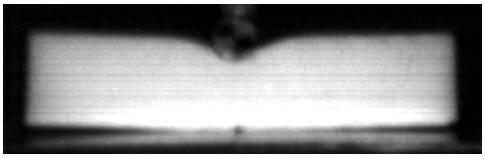

Time = 0.012 s
Displacement = 11.63 mm

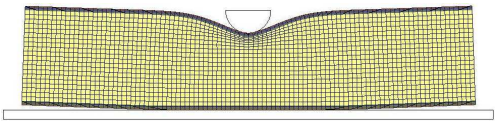

Time = 0.012 s
Displacement = 12.08 mm

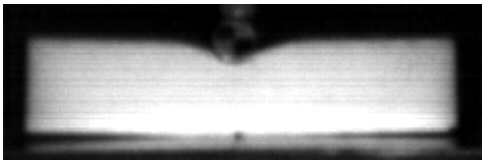

Time = 0.016 s
Displacement = 14.03 mm

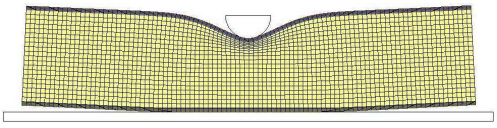

Time = 0.016 s
Displacement = 14.11 mm

(b) (c)

Figure 5-32. Dynamic 15 J indentation test on 2 mm skin sandwich beam (a) comparison of experimental and simulation force-displacement curves (b) experimental deformation and failure modes (c) simulation deformation and failure modes.

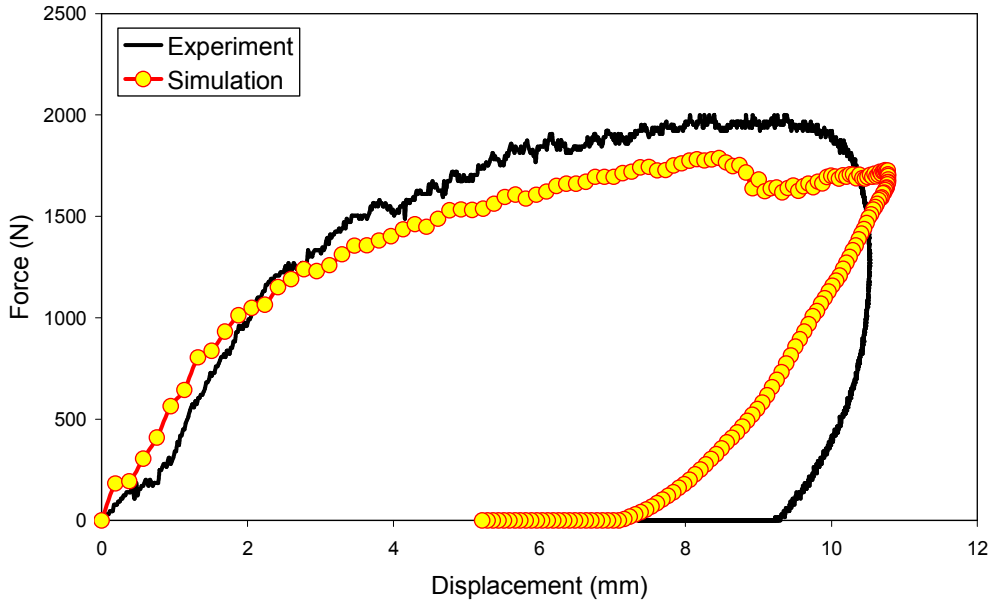

(a)

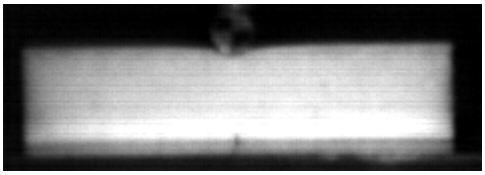

Time = 0.002 s
Displacement = 3.67 mm

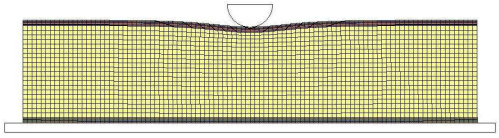

Time = 0.002 s
Displacement = 3.63 mm

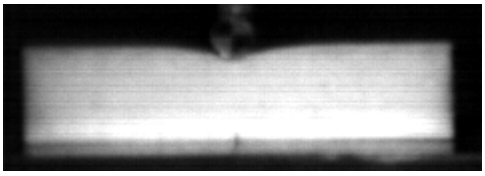

Time = 0.004 s
Displacement = 6.70 mm

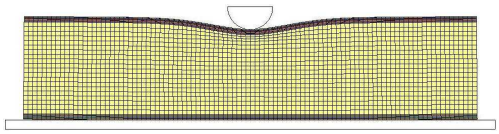

Time = 0.004 s
Displacement = 6.63 mm

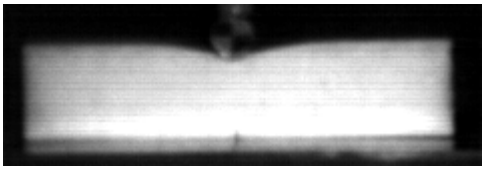

Time = 0.008 s
Displacement = 10.12 mm

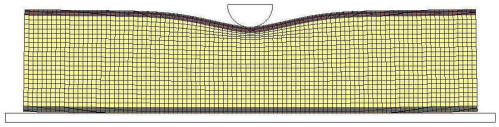

Time = 0.008 s
Displacement = 10.21 mm

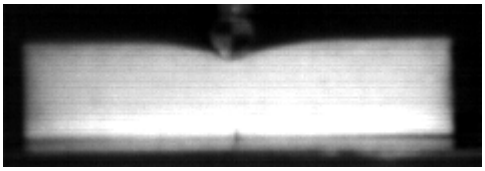

Time = 0.012 s
Displacement = 10.31 mm

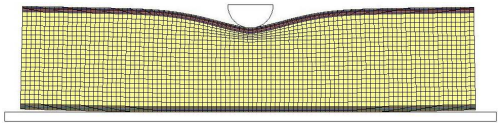

Time = 0.012 s
Displacement = 10.51 mm

(b) (c)

Figure 5-33. Dynamic 15 J indentation test on 3 mm skin sandwich beam (a) comparison of experimental and simulation force-displacement curves (b) experimental deformation and failure modes (c) simulation deformation and failure modes.

5.6 Three-Point Bending Behaviour of Sandwich Beams

This section presents an experimental and numerical investigation into the behaviour of thermoplastic composite sandwich beams under three-point bending loads.

5.6.1 Experimental Investigation

5.6.1.1 Quasi-static three-point bending tests

Quasi-static three-point bending tests were conducted on the TPC sandwich beam specimens according to test standard BS EN 2746. The tests were performed on a Tinius Olsen electromechanical test machine at a crosshead speed of 10 mm min^{-1}. The test setup and specimen dimensions are shown in Figure 5-34. A 25 mm diameter cylindrical impactor is used to apply a load to the centre of the beam. The specimens were simply supported over a span of 200 mm on 10 mm diameter cylindrical steel supports.

All sandwich specimens were 250 mm long with a width of 30 mm and nominal core thickness of 25 mm. Sandwich beams with three different skin thicknesses were investigated, respectively 1, 2 and 3 mm. All sandwich skins had a [090] fibre orientation aligned along the beam longitudinal axis.

5.6.1.2 Dynamic three-point bending tests

Dynamic impact tests on the sandwich beams were performed in an instrumented falling weight drop tower. The tests were conducted with an impact mass and velocity of 8.2 kg and 4.9 ms^{-1}, respectively, which corresponds to an incident energy of 100 J.

The test setup and sandwich beam dimensions are the same as in the quasi-static test (see Figure 5-34 (c)). The displacements and failure response of the beams were recorded with a high speed camera at 1000 frames per second.

(a)

(b)

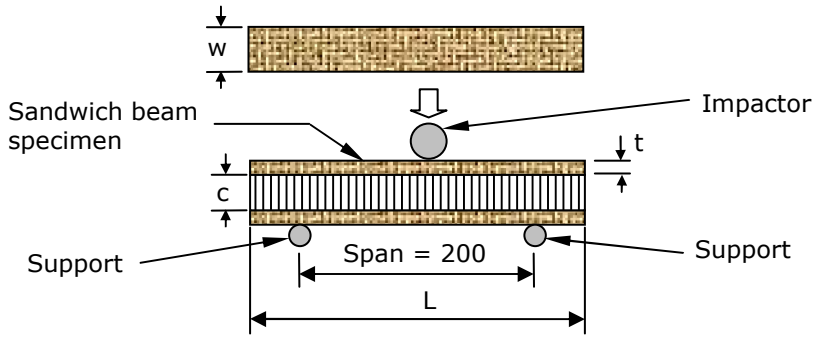

(c)

Figure 5-34. Three-point bending test (a) picture of quasi-static test setup in Tinius Olsen test machine (b) picture of dynamic test setup in drop tower (c) schematic of three-point bending test and specimen dimensions.

5.6.2 Finite Element Modelling of the Three-Point Bending Behaviour of Sandwich Beams

Figure 5-35 shows the sandwich beam finite element model. In order to reduce solution time and taking account of geometric and material symmetry, only one half of the sandwich beam was modelled. All the components were modelled with single integration point eight node solid elements. A stiffness based hourglass control was applied so as to prevent the occurrence of hourglassing. Each ply in the skin laminates was represented individually by a layer of solid elements. The cylindrical impactor and supports were modelled as rigid bodies. The supports were fully constrained while the impactor was only allowed to translate along the global Z axis. For the quasi-static analysis, the impactor was given a prescribed velocity which was much higher than that in the actual test so as to reduce the computational run time. For the dynamic model, the impactor was given an initial velocity equivalent to the actual test.

Contact between the impactor and the top composite skin was modelled using the automatic surface to surface contact algorithm within LS-DYNA. The same contact type was used to model contact between the bottom composite skins and the supports. An eroding single surface contact type was used to model contact between failure surfaces created by element erosion in the foam core (see Section 5.6.2.2).

5.6.2.1 Material Modelling

Similar to the indentation model, the composite skin is modelled with MAT 162 and the foam core is modelled with MAT 142 (see Section 5.5.2.2). Both these models are implemented in the LS-DYNA explicit finite element code. Material input data, as for the indentation FE model, in Table 5-2 and Table 5-3 are used for the skin and core models, respectively

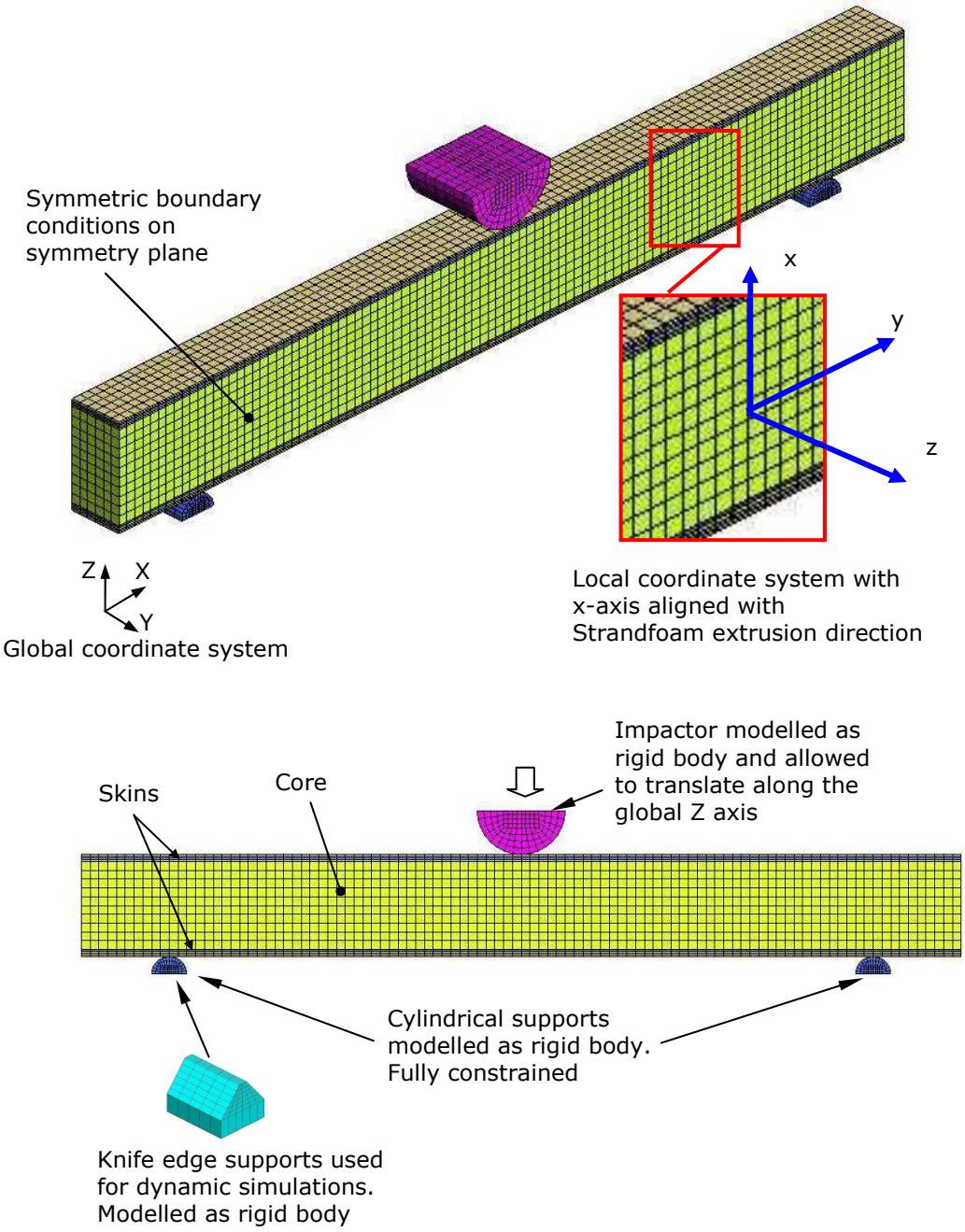

Figure 5-35. Finite element model and boundary conditions for sandwich beam three-point bending test simulations.

5.6.2.2 Modelling fracture

Anisotropic crushable foams, such as Strandfoam, can exhibit brittle core shear fracture under bending loads [14, 17]. Therefore, it is important to be able to model such failure modes; however, modelling fracture in polymeric foams has received only limited attention [14]. The MAT 142 material model used in this study does not include fracture. Mines [14] and Reyes et al [301] have modelled fracture in polymeric and aluminium foam materials, respectively, by deleting elements when a fracture criterion is satisfied. A similar approach has been adopted in this study. Fracture has been modelled by implementing a maximum principal strain fracture criterion to remove elements when the maximum principal strain reaches a specified value:

$\varepsilon_1 \geq \varepsilon_p \rightarrow$ element erosion

where ε_1 is the maximum principal strain and ε_p is the maximum principal strain at failure.

The maximum principal strain, ε_p, was numerically calibrated using an iterative procedure where values for ε_p were determined by correlation of simulations with experimental force-displacement and failure mode results.

This fracture criterion was also used to model failure at the sandwich beam skin-core interface.

5.6.3 Quasi-Static Three-Point Bending Test Results

5.6.3.1 Sandwich beam with 1 mm skin

Figure 5-36 shows a comparison of the typical experiment and simulation force-displacement curves for the sandwich beams 1 mm skins under quasi-static bending loads. There is an initial linear elastic behaviour followed by non-linear yielding up to a maximum load of 376 N and a deflection of about 5.6 mm. This is followed by a gradual decrease in load. The simulation force-displacement curve shows good correlation with the overall shape of the experimental curve. However, at large displacements the simulation underestimates the degree of load reduction after yielding

and consequently over estimates the peak load by about 7 %. This may be due to the simulation underestimating the level of damage in the top skin. The primary failure modes were localised core crush and top face compressive buckling adjacent to the impactor. Figure 5-36 shows that the predicted failure modes exhibit good agreement with the experimental observations.

Figure 5-37 shows a comparison of the experimental and predicted damage in the 1 mm top skin laminate. The predicted macro-scale damage that included minor fibre fracture, matrix cracking and delamination shows good qualitative agreement with the experimental observations. However, the delamination is overestimated.

5.6.3.2 Sandwich beam with 2 mm skin

Figure 5-38 shows a comparison of the typical experiment and simulation force-displacement curves for the sandwich beams with 2 mm skins under quasi-static bending loads. Initial linear elastic behaviour is followed by a non-linear plastic deformation up to a peak load of 1348 N. Further loading leads to core shear fracture which is represented on the load-displacement curve by an abrupt load drop of 93% of the maximum value to a load of about 100 N at 11 mm before slowly rising to an apparent residual plateau load. Core shear fracture is then followed by skin-core debonding in the bottom skin-core interface which is characterised by the core separating and shear slipping over the bottom skin.

Simulations of the test were conducted with and without the implementation of element eroding maximum principal strain fracture criterion (see Section 5.6.2.2). For the simulation without the fracture criterion, the initial load-displacement response is well predicted by the simulation. However, as expected, core shear fracture and the corresponding load drop are not represented.

For the simulations with fracture, Figure 5-38 shows the force-displacement curves for various values of the maximum principal strain ε_p. In all cases, core shear fracture has been predicted which corresponded to an abrupt load drop. However, unlike in the test, first failure is skin-core debonding as element erosion occurs along the top skin-core interface

before propagating in the core. Skin-core debonding and shear slipping in the bottom skin-core interface is also predicted. In all the simulations with fracture, the post-failure response is oscillatory in contrast to the smooth residual response in the test. The oscillations are primarily due to the element erosion. Additionally, the contact algorithm may be associated with these oscillations as the core and skin contact each other after element erosion caused by skin-core debonding. Despite these discrepancies core shear fracture is fairly well predicted and it is proposed that a value of ε_p of 0.13 gives the closest agreement with the experimental results.

After the test, although the core failed, the beam returned to its original pre-test shape with no damage observed in the top and bottom skins. Likewise, the simulations did not predict any damage in the skins.

5.6.3.3 Sandwich beam with 3 mm skin

Figure 5-39 shows a comparison of the typical experiment and simulation force-displacement curves for the sandwich beams with 3 mm skins under quasi-static bending loads. The load-displacement response is similar to the 1 mm skin beam with an initial linear elastic behaviour, then non-linear yielding up to a maximum load followed by gradual reduction in load. However, the peak load is 43 % higher than in the case of the 1 mm skin. The 3 mm beam simulation gave an asymmetric deformation mode similar to the experimental results. In the experiments, the beam failed by minor core shear fracture and skin-core debonding at one end of the beam. The fracture criterion was not implemented in this analysis because the level of core shear fracture was considered to be too low to be appropriately described by the element erosion approach.

Figure 5-40 shows a comparison of the experimental and predicted damage in the 3 mm top skin laminate. The predicted macro-scale damage that included minor fibre fracture, matrix cracking and delamination shows good qualitative agreement with the experimental observations. However, the fibre damage is overestimated.

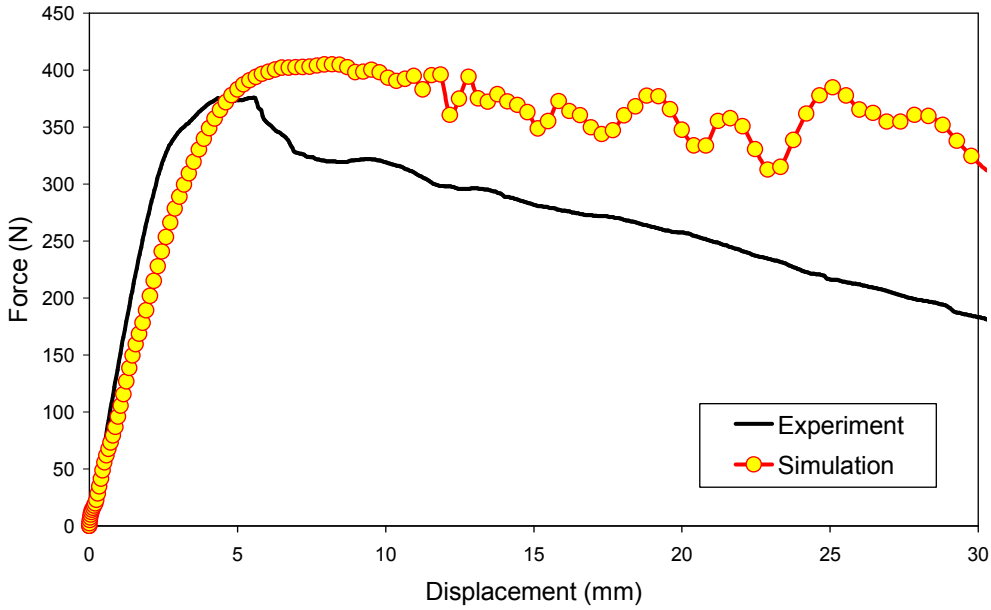

(a)

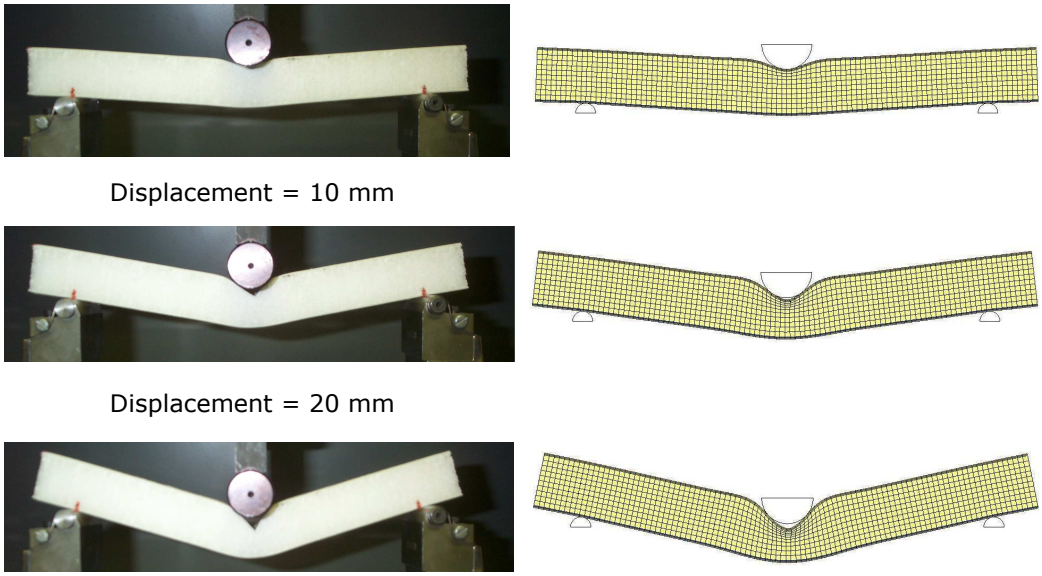

Displacement = 10 mm

Displacement = 20 mm

Displacement = 30 mm

(b) (c)

Figure 5-36. Quasi-static bending test on 1 mm skin sandwich beam (a) comparison of experimental and simulation force-displacement curves (b) experimental deformation and failure modes (c) simulation deformation and failure modes.

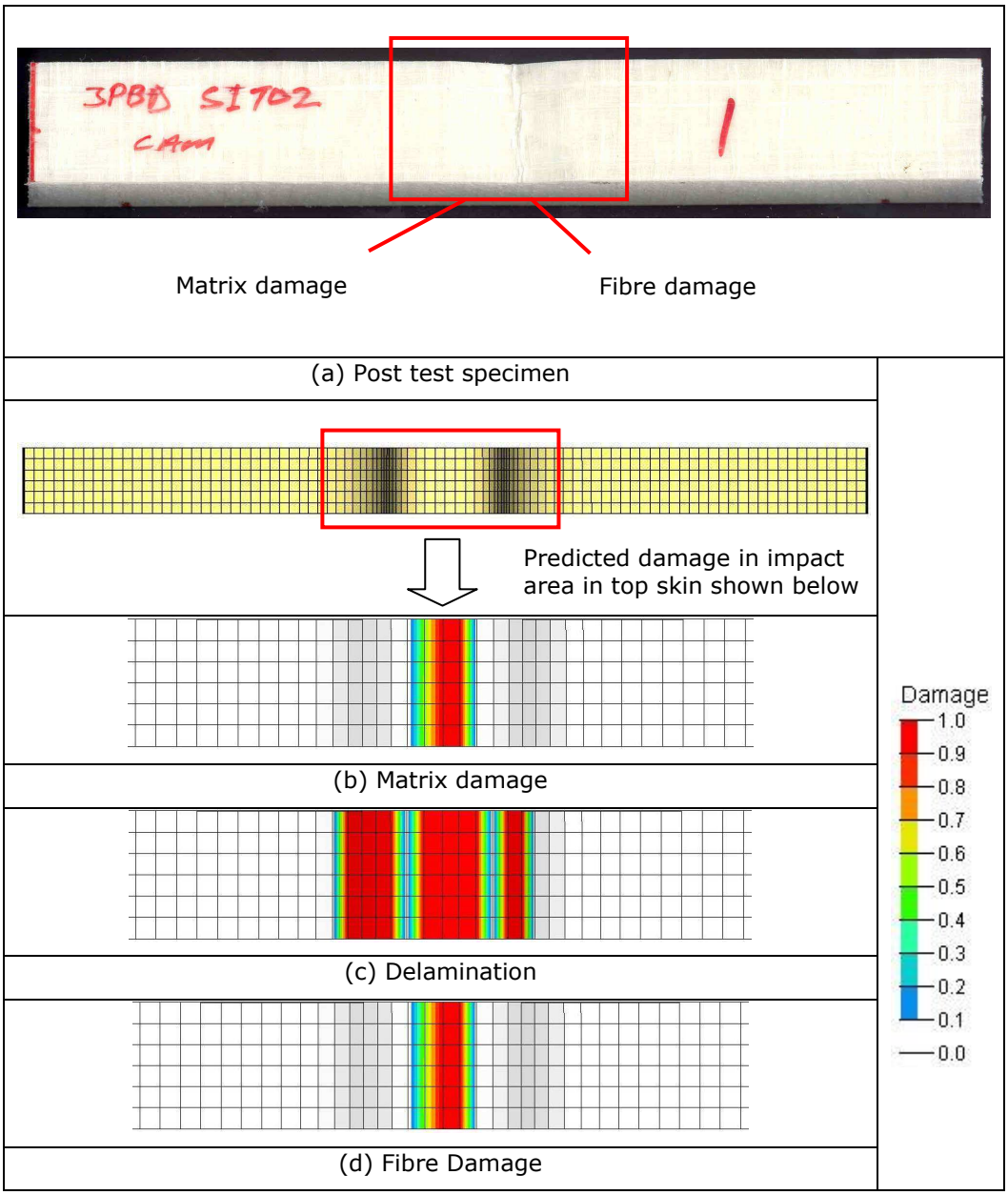

Figure 5-37. Damage in 1 mm top skin (a) experiment and simulation: (b) matrix damage (c) delamination (d) fibre damage for sandwich beam under quasi-static bending load.

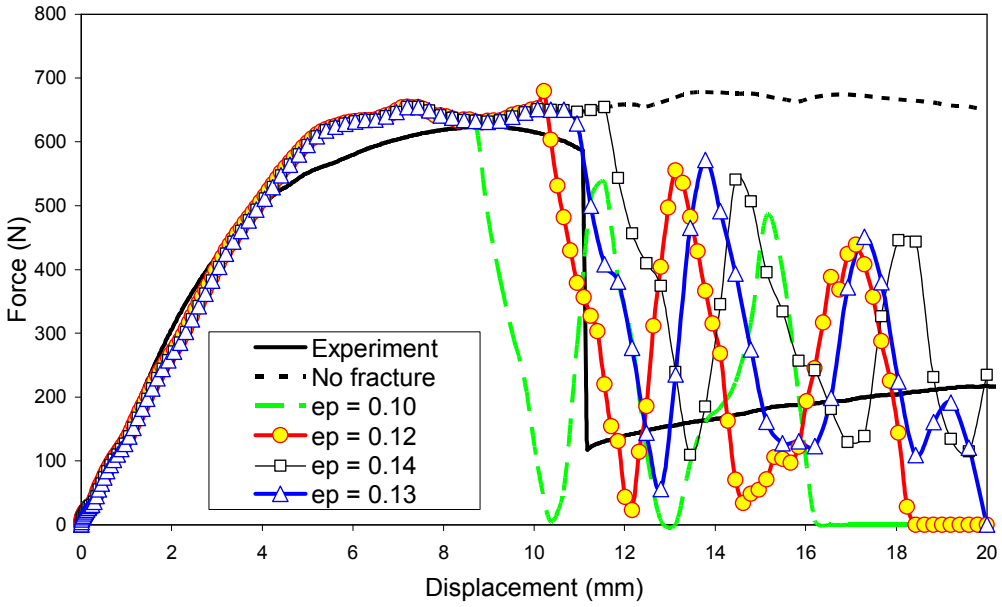

(a)

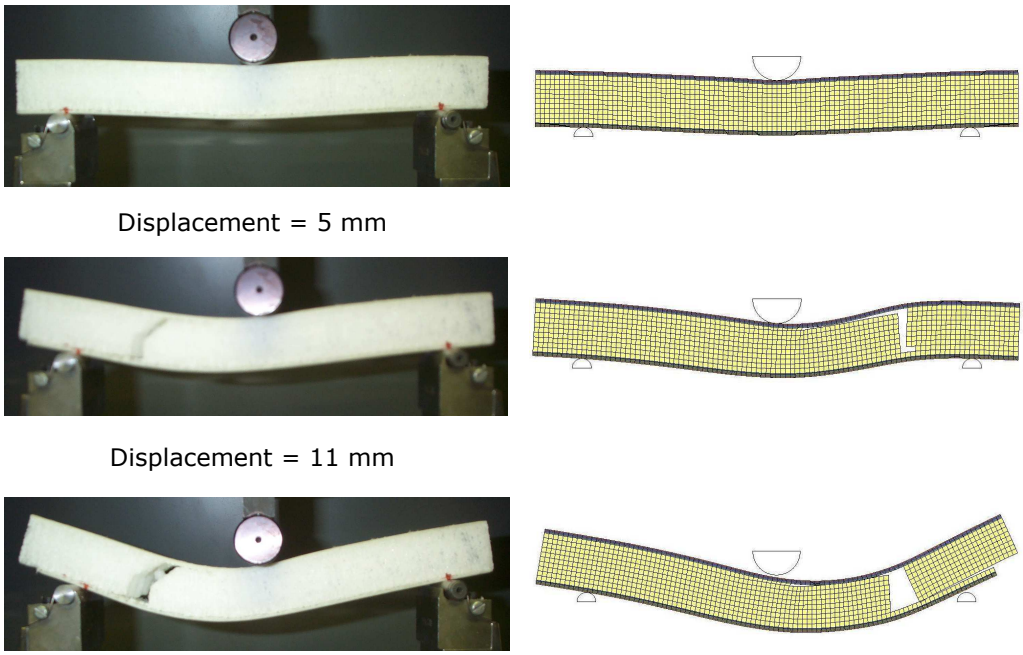

Displacement = 5 mm

Displacement = 11 mm

Displacement = 20 mm

(b) (c)

Figure 5-38. Quasi-static bending test on 2 mm skin sandwich beam (a) comparison of experimental and simulation force-displacement curves (b) experimental deformation and failure modes (c) simulation deformation and failure modes.

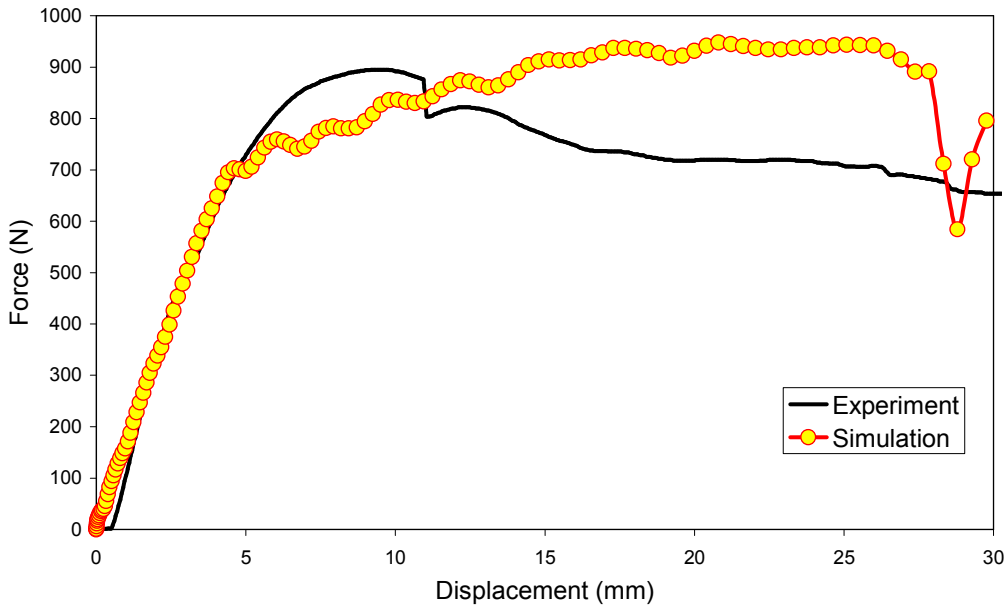

(a)

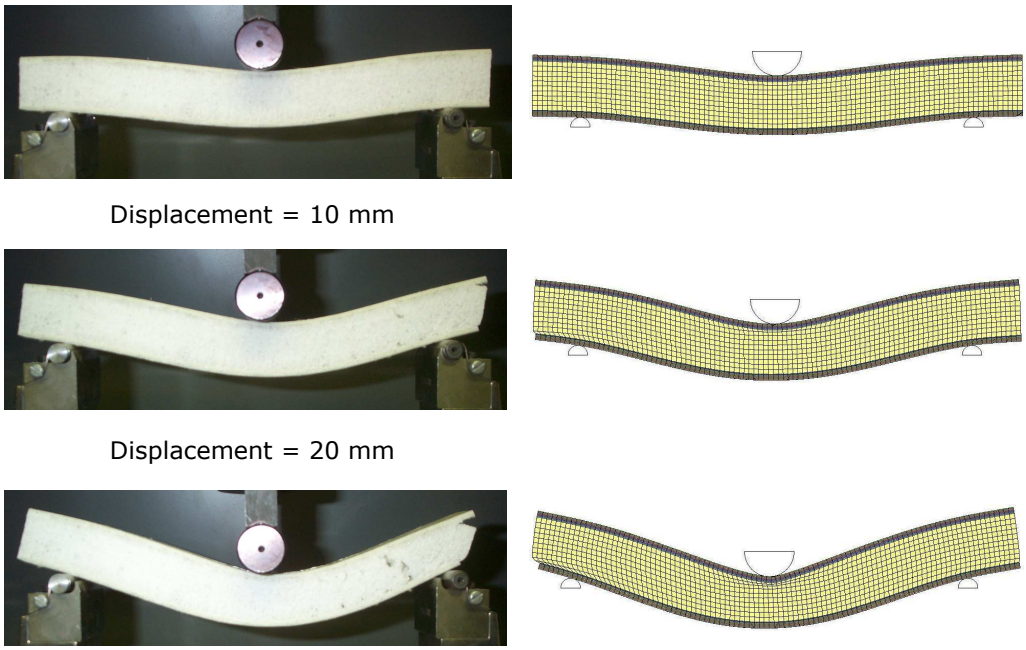

Displacement = 10 mm

Displacement = 20 mm

Displacement = 30 mm

(b) (c)

Figure 5-39 Quasi-static bending test on 3 mm skin sandwich beam (a) comparison of experimental and simulation force-displacement curves (b) experimental deformation and failure modes (c) simulation deformation and failure modes.

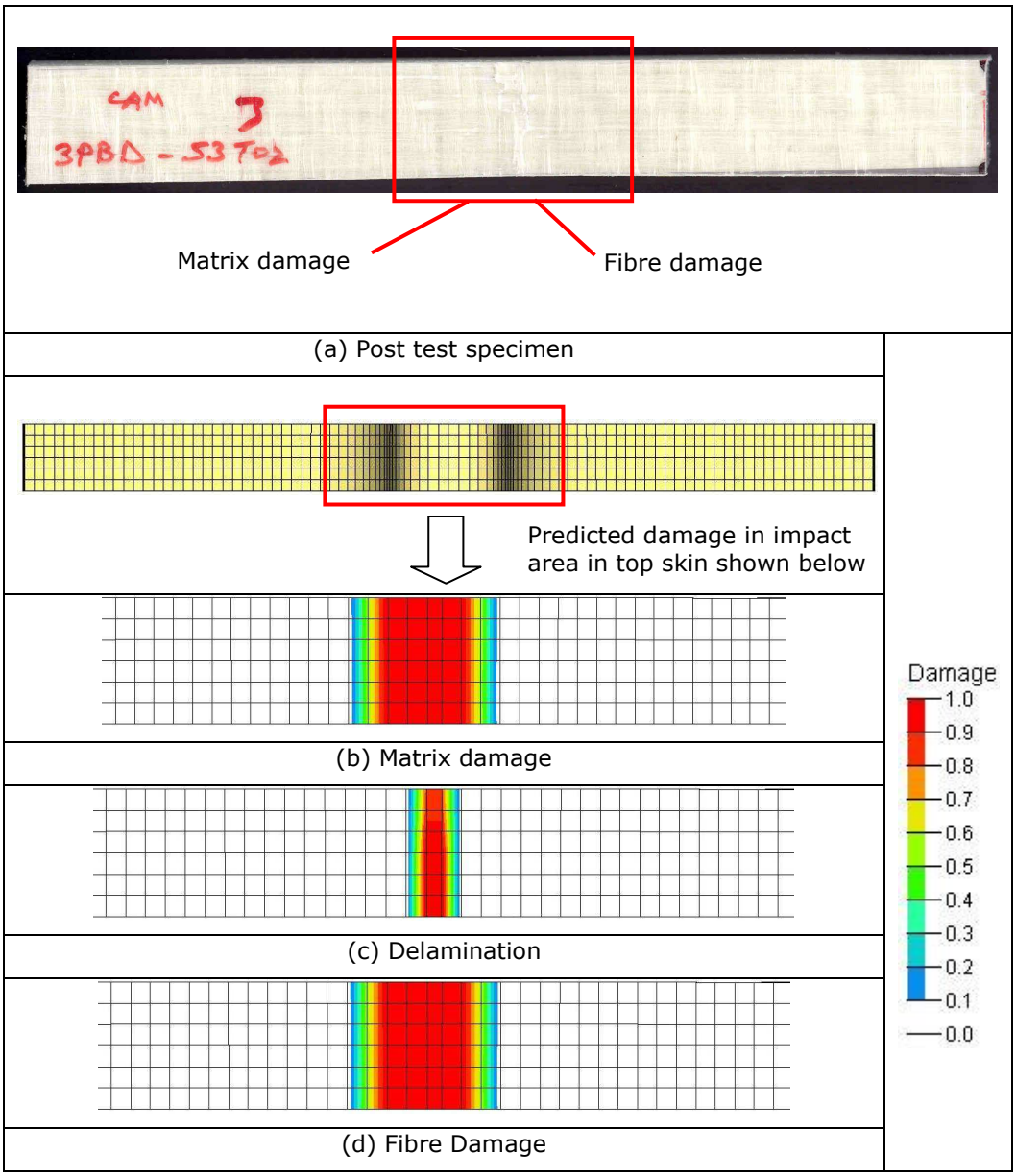

Figure 5-40. Damage in 3 mm top skin (a) experiment and simulation: (b) matrix damage (c) delamination (d) fibre damage for sandwich beam under quasi-static bending load.

5.6.4 Dynamic Three-Point Bending Test Results

5.6.4.1 Sandwich beam with 1 mm skin

Figure 5-41 shows a comparison of the simulation and experimental results for the 1 mm skin sandwich beam under dynamic loading. By contrast with quasi-static loading, in this case, core shear fracture does occur. The experimental force-time history is fairly oscillatory which is due in part to inertial effects and vibration of the beam. The initial response is very stiff and is linear elastic up to the initial peak load of about 320 N, after which there is a gradual load drop as localised core crush is induced. This is followed by an increase in load again to the second peak load followed by a noisy plateau which ends with an abrupt load drop as the specimen fails by core shear fracture at about 2.2 ms followed by skin-core debonding. Simulations were conducted with various values of ε_p and it is proposed that a value of ε_p of 0.06 gives the closest agreement with the experimental results. The simulation captures the general description of the force-displacement response. However, the initial peak load is under estimated by 26% while the second peak load is over estimated by 24%. In addition, the second peak load occurs much later in the simulation than in the actual test.

As shown in Figure 5-41, the near symmetric failure through core shear fracture and skin-core debonding observed in the test has been predicted by the model. However, in the test, core shear fracture occurs adjacent to the impactor, while in contrast, the predicted shear fracture occurs nearer the supports. Furthermore, the skin-core debonding occurs along the bottom skin-core interface while in the simulation this mode of failure propagates along the top skin-core interface.

5.6.4.2 Sandwich beam with 2 mm skin

Figure 5-42 shows a comparison of the simulation and experimental results for the 2 mm skin sandwich beam under dynamic loading. The force-history response is similar to the 1 mm skin beam results with an initial linear elastic response up to an initial peak load of 500 N followed by a gradual load drop. This followed by an increase in load again to the second peak load before an abrupt load reduction due to core shear failure at

about 1 ms. Simulations were conducted with various values of ε_p and it is proposed that a value of ε_p of 0.04 gives the closest agreement with the experimental results. The predicted force-time history shows good agreement with the general shape of the experimental response. The predicted initial peak load (483 N) shows excellent agreement with the experimental results. However, the predicted second peak load occurs at a later time than in the experiment and is overestimated by 20%.

As shown in Figure 5-42, the beam fails primarily by symmetric core shear fracture followed by skin-core debonding which has been predicted by the simulation. However the failure sequence is not well captured. In the test, core shear fracture initiates at about 1 ms followed by skin-core debonding. However, the simulation predicts the occurrence of skin-core debonding occurring first between 1 and 2 ms which is then followed by core shear fracture. It was observed, that there is less core crush and much more global bending than in the 1 mm skin sandwich beam case.

5.6.4.3 Sandwich beam with 3 mm skin

Figure 5-43 shows a comparison of the simulation and experimental results for the 3 mm skin sandwich beam under dynamic loading. Again, the force-time history shows a similar response to the 1 and 2 mm results. However, for the 3 mm beam, core shear failure that results in a sudden load drop after the second peak load occurs earlier than in the 1 and 2 mm test, just below 1 ms. The Simulations were conducted with various values of ε_p and it is proposed that a value of ε_p of 0.06 gives the closest agreement with the experimental results. Again the predicted force-time history shows good agreement with the general shape of the experimental curve. The predicted initial peak load shows excellent correlation with that observed experimentally. However, the second and third load peaks are significantly under and over-predicted, respectively. The noticeably high peak loads after core shear failure (between 1.2 to 2.5 ms) is likely to be associated with the contact algorithm as the element erosion at the skin-core interface causes the core to shear slip over the bottom skin resulting in spurious contact forces.

Figure 5-43 shows that the predicted core shear fracture and skin-core debonding correlates reasonably well with the experimental observations, although exact fracture locations are difficult to predict.

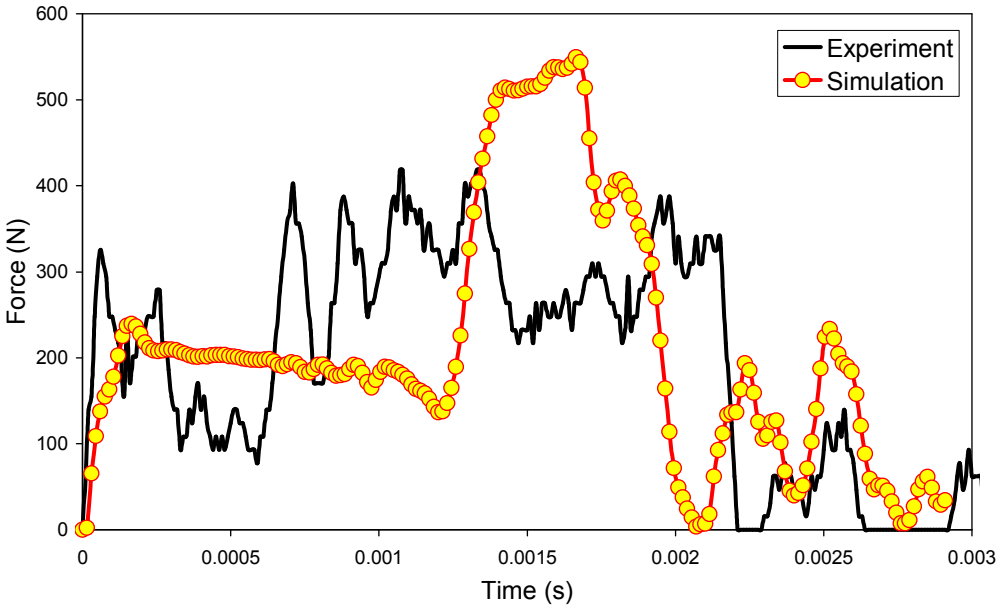

(a)

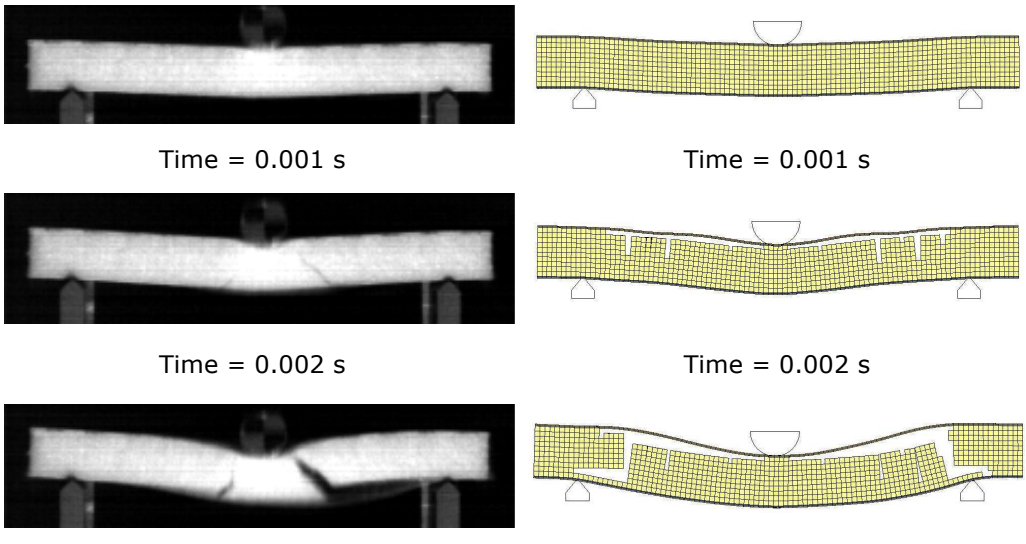

(b) (c)

Figure 5-41. Dynamic bending test on 1 mm skin sandwich beam (a) comparison of experimental and simulation force-displacement curves (b) experimental deformation and failure modes (c) simulation deformation and failure modes.

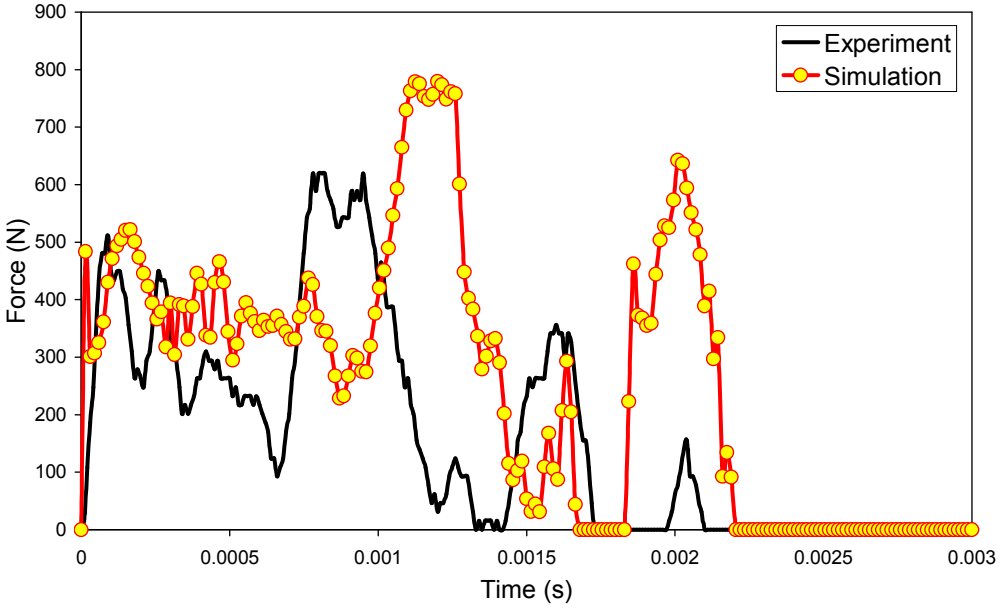

(a)

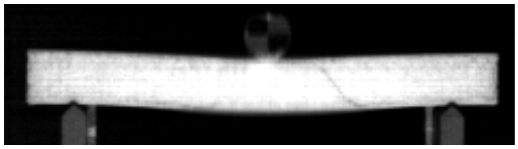

Time = 0.001 s

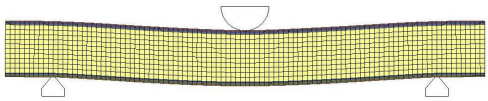

Time = 0.001 s

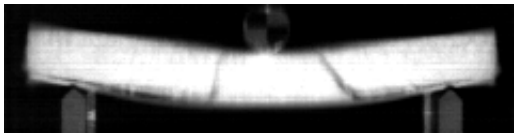

Time = 0.002 s

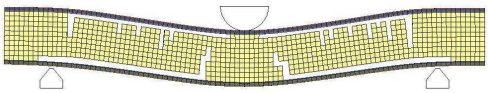

Time = 0.002 s

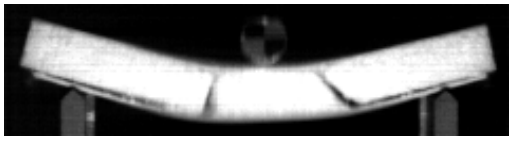

Time = 0.003 s

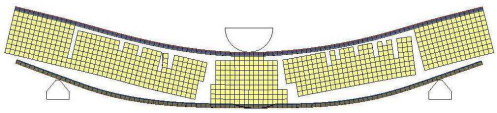

Time = 0.003 s

(b) (c)

Figure 5-42. Dynamic bending test on 2 mm skin sandwich beam (a) comparison of experimental and simulation force-displacement curves (b) experimental deformation and failure modes (c) simulation deformation and failure modes.

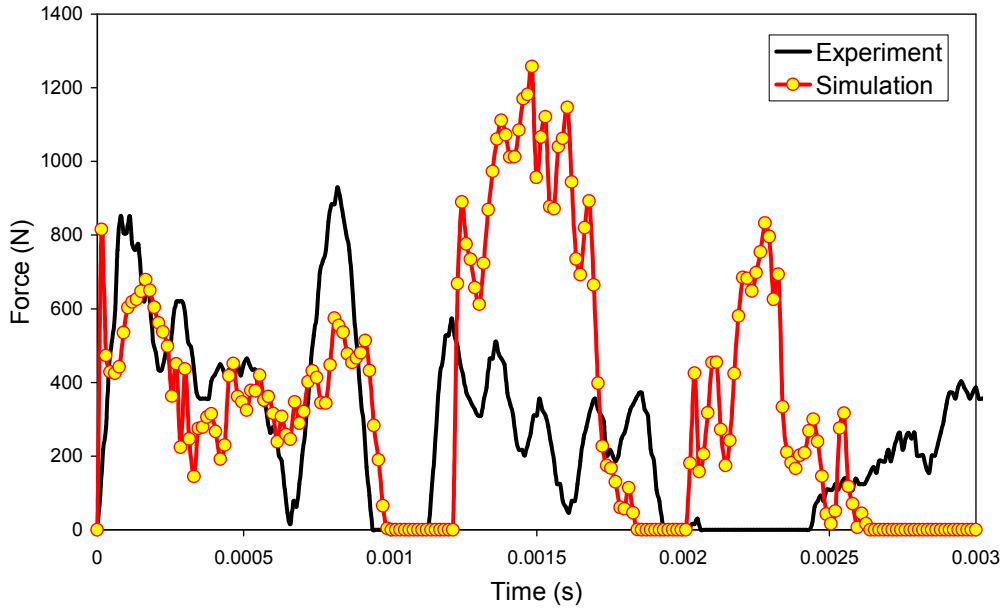

(a)

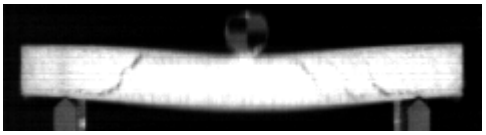

Time = 0.001 s

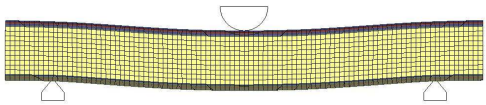

Time = 0.001 s

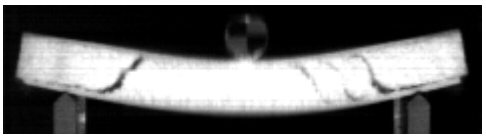

Time = 0.002 s

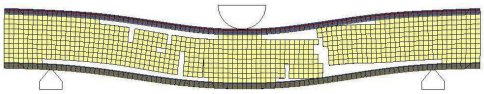

Time = 0.002 s

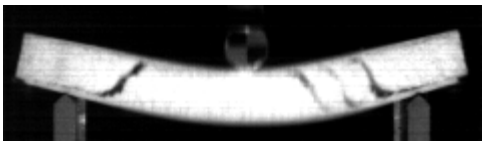

Time = 0.003 s

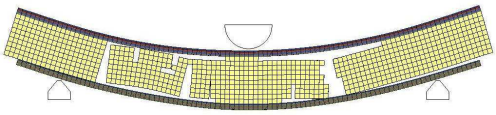

Time = 0.003 s

(b) (c)

Figure 5-43. Dynamic bending test on 3 mm skin sandwich beam (a) comparison of experimental and simulation force-displacement curves (b) experimental deformation and failure modes (c) simulation deformation and failure modes.

5.7 Discussion

This chapter has presented an experimental and numerical investigation into the behaviour of foam cored thermoplastic composite sandwich structures. One of the primary objectives of this work was to develop and validate a predictive modelling methodology for thermoplastic composite sandwich structures under static and dynamic impact loading. The sandwich beams were analysed under both localised indentation and bending loads

This section provides a discussion of the results in this chapter

5.7.1 Foam Characterisation

The mechanical behaviour of Strandfoam has been characterised using shear, compression and tensile tests under quasi-static and high strain rate loading. Under compression loading the foam response in both the extrusion and transverse directions was initially linear elastic up to a yield point which was followed by a long stress plateau and finally, densification. However, the foam response in the extrusion direction is much more enhanced than in the transverse direction. This is due to the hexagonal strands coupled with the inter-strand bond strength [75] which results in a much higher stiffness as well as yield strength in the extrusion direction. In the plateau region, the ductile, almost perfectly plastic response was due to macro strand buckling and interstrand shear and debonding. At high strain rates, there is an almost 50% increase in the compression stiffness and yield strength in the extrusion direction. This significant increase is likely to be due to viscoelastic effects; strain rate effects in the polypropylene material as well as air in the foam cells. In contrast, Strandfoam showed very little strain rate sensitivity under shear loading.

Strandfoam exhibited a much lower performance under tensile loading due to the quasi-brittle nature of the cellular material failure. This resulted in far less energy being absorbed in tension in contrast to the high energy absorbing efficiency observed in compression.

5.7.2 Modelling Localised Indentation and Bending loads

5.7.2.1 Indentation loading

This work has shown that the force-displacement response of the sandwich beam is highly non-linear under indentation loading. This non-linearity is induced by localised core crush under the impactor as the foam strands buckle and inter-strand shear occurs. High membrane stresses develop in the top skins which results in the ends of the beam being lifted off the supporting rigid plate as the impactor moved down into the specimen. The top skin was also seen to exhibit multiple failure modes such as matrix damage, fibre fracture and delamination under or near the impactor. These failure modes were induced by the high membrane and contact stresses in the impact area. For the three different skin thicknesses assessed in this study, it was shown that the amount of localised core crush under the impactor decreases with increasing skin thickness as the top skin exhibits more global bending. This suggests that thicker skins were better able to distribute the load along the beam. Furthermore, the yield load increased with increasing skin thickness. The results deduced from the finite element model for the indentation tests show good agreement with the experimental results. However, damage in the top skin was only assessed using visual observation and a more detailed qualitative and quantitative damage assessment procedure is suggested for future work to better compare simulation and test results. This was not done in this study due to time constraints.

5.7.2.2 Bending loads

Under static and dynamic bending loads the sandwich beam exhibited a more complex array of failure modes. It was shown that the primary failure modes of the sandwich beam under static bending loads were local core crush, top face compression buckling and core shear fracture. For the 1 mm thin skins, local core crush and top face buckling were more prevalent as plastic hinges developed in the top skin under the impactor due in part to the lower stiffness of the thinner skin. As skin thickness increased to 2 mm, there was less core crush and ultimate failure was now by core shear fracture followed by skin-core debonding. For the 3 mm skin the beams exhibits global bending with minor core shear.

Unlike the static case, under dynamic bending core shear is the primary failure mode for all the beams. Additionally, the location of core shear fracture varied with skin thickness. For thin skin sandwich beams the core shear cracks occurred adjacent to the impactor but as skin thickness increases, the crack location progressively moved towards the supports. This is caused by the variation in stress distribution along the length of the beam as skin thickness increases with thicker skins providing better load distribution.

In this present study simulation results for the static bending test force-displacement response showed reasonably good correlation. However, for dynamic bending loads, the more complex, oscillatory post-initial failure response involving beam vibration and multiple load peaks was more difficult to simulate. For the 1 and 2 mm skin dynamic bending tests, the simulation force-time histories were noticeably slower than that of the test. This difference in the time scale between the simulation and experiment has also been reported by Morgenthaler et al [266] and Fritzsche et al [265] who used the LS-DYNA explicit finite element code to simulate dynamic bending impact on sandwich panels (290 mm long, 70 mm wide) consisting of glass/epoxy woven fabric skins and crosslinked PVC and Airex (linear PVC) foam cores. Morgenthaler et al [266] attributed the slower simulation results to the influence of air in the foam core which was not taken into account in the foam material model. In their work, the foam core was modelled with the orthotropic foam material model, MAT 126 [87, 118]. The shortfalls of the MAT 126 material model have been well documented by Hirth et al [77]. In this present study the foam core is modelled with the MAT 142 model that is implemented within LS-DYNA. It is proposed that the discrepancy between the simulation and experiment may be due to strain rate effects in the foam core that were not explicitly taken into account in the MAT 142 material model. In this study, the dynamic compressive stress-strain input for the model was an average data set over the high strain rates applied. However, this dynamic compressive stress-strain data is only valid for a particular strain rate (about $200s^{-1}$). This may also explain the over estimation of the dynamic secondary peak loads or in some cases under estimation of the same.

Shaw and Sata [302] have suggested that the failure of foam is governed by the maximum principal stress, independent of the minor principal stress.

That conclusion has been supported by Li et al [303] and Mines [14]. In this study a maximum principal strain fracture criteria coupled with element erosion was used to model core shear fracture and skin-core debonding. This approach is similar to that adopted by Mines [14] who also used a maximum tensile principal strain fracture criteria along with element erosion to simulate core failure in Rohacell PMI foam core, glass/epoxy skin sandwiches under static and dynamic bending loads. The foam core was modelled with the LS-DYNA MAT 83 material model which is originally based on theory presented by Fu Chang et al [304]. Mines [14] calibrated the MAT 83 foam model using a combined shear and compression test from which a maximum principal strain value of 0.0168 was derived. Above this value the foam was deemed to have failed and the element was deleted.

In this present study, experimental data from a combined shear-compression test similar to that used by Li et al [303] and Mines [14] was not available for Strandfoam. Subsequently, the value for the maximum principal strain was numerically calibrated by comparing simulation results with experiments. The selected values of "best fit" for the maximum principal strain in both the static and dynamic cases were higher than the experimental tensile strain for the Strandfoam. This discrepancy may be due to the presence of shear strains in the core. Mines and Jones [305] has shown that the core material underneath the impact loading area is subject to multiaxial stress where the response and failure of the foam material depends on its interactive behaviour under compressive and shear stresses. Furthermore, Li et al [303] also notes that the tensile strength is influenced by both the compression and shear stresses in the core.

In the future, further testing of Strandfoam under combined loading conditions is required for a more precise understanding of the failure behaviour. This will also allow for the development of a more fundamental method of calibrating the maximum principal strain fracture criteria. In particular, the following tests should be performed: hydrostatic and combined shear and compression tests.

Mines [14] has noted that a drawback of the maximum principal strain criteria is that inconsistencies occur in the failure surface because this criteria does not take into account hydrostatic effects and the effects of

strains in other principal directions. He concluded that a more sophisticated failure criteria for modelling foam fracture is required. In addition, the application of element erosion may also result in a mesh sensitive solution [14]. However, this may be resolved by using a non-local approach that has been implemented in LS-DYNA to regularise the solution. The non local approach was not applied in this study.

Research in developing accurate failure criteria for foams is growing. In the open literature the following criteria have been applied with varying success: maximum principal stress criteria (Jung and Shyu [254]), Rankine criteria (Corgliano et al [306]), volumetric strain and an energy based criteria both coupled with element erosion (Reyes et al [301]) and continuum damage mechanics (Horrigan et al [307]). In the future, these failure models should be investigated with respect to their suitability for modelling core fracture in an anisotropic crushable foam such as Strandfoam. Given the complexity of foam failure, the approach with the most potential for fundamental development appears to be continuum damage mechanics. This approach has a good theoretical background and is currently an active research area for composites. However, very little work has been done on the application of damage mechanics for modelling foam failure [307].

5.7.3 Conclusions

This study has presented a modelling methodology for simulating the impact response and failure modes of thermoplastic composite sandwich beams under static and dynamic indentation and bending loads. An approach for simulating core shear fracture and skin-core debonding has been presented. The simulation of damage progression in the sandwich beam skins with the MAT 162 model has served to further validate the capabilities of this model.

Further refinement of the foam model is required so as to better account for the complex failure modes of the foam material under impact loading. A more fundamental approach to accounting for strain rate effects in the foam model is required. While the current maximum principal strain fracture criterion provides useful predictions of core shear, further work is required in developing a more accurate fracture criterion for skin-core

debonding. Other methods such as fracture mechanics, stress based fracture criteria, interface elements, damage mechanics and tied contact algorithms are worth investigating in the future.

Chapter 6

Conclusions and Recommendations

6.1 Introduction

In this chapter the main contributions and conclusions drawn from the findings of this doctoral investigation are presented. Finally, recommendations for future work are outlined.

6.2 Thesis Contribution to Knowledge

The primary contributions of this doctoral study can be summarised as follows:

6.2.1 Contributions to the Characterisation of Thermoplastic Composite Material Properties

- The mechanical properties of the Twintex, E-glass/polypropylene commingled woven fabric thermoplastic composite have been characterised at both quasi-static and high strain rates using tensile, compression, shear and bending experimental techniques.
- The in-plane tensile properties of Twintex were presented for quasi-static and high strain rate loading (up to 70 s^{-1}). The investigation showed that the in-plane tensile modulus and strength dramatically increased with increasing strain rate. It was shown that under tensile high strain rate loading the tensile stress-strain response is almost elastic-perfectly plastic in contrast, to the abrupt failure exhibited under static tensile loads. It was also shown that the primary failure mode in tension was by matrix cracks in the 90° fibre bundles (tow) that propagate in the through-thickness direction followed by tow interfacial debonding and interply delamination. Final failure was by fibre through-thickness shear.
- The in-plane compression properties of Twintex were presented for quasi-static and high strain rates (up to 126 s^{-1}). The investigation showed that the in-plane compression modulus and strength

dramatically increased with increasing strain rate. The results show that under compressive loading, failure is initiated by fibre micro buckling and fibre kinking which is followed by fibre through-thickness shear along a distinct shear band fracture plane.

- The shear properties of Twintex were presented for quasi-static and high strain rates (up to 91 s^{-1}). The tests showed that the in-plane shear modulus and strength decreased with increasing strain rate. It was shown that failure was by trans-ply through-thickness cracks, inter-ply delamination, and fibre pull-out along the ±45° direction of the fibre layout which gives a V shaped in-plane failure surface.
- A novel shear punch test method was used to obtain the static through thickness shear strength and failure morphology of the Twintex thermoplastic composite. The main benefits of this technique are its simplicity and reliability in contrast to the more complex Iosipescu shear test. It was shown that the through-thickness shear strength is 4 times the value of the in-plane shear strength. This suggests that the through-thickness shear failure is fibre dominated in contrast to the in-plane shear response which tends to be governed by matrix damage.
- The static and dynamic flexural response of Twintex was investigated. It was shown that the flexural modulus was relatively strain rate insensitive wile the flexural strength increased with increasing strain rate. It was shown that under bending loads, a mixed mode failure occurs with compression failure in the top layers and tension failure in the bottom layer. Delamination in the mid-plane of the specimens was observed at high strain rates due to high interlaminar shear stresses. The onset of failure led to a gradual reduction in flexural strength.

6.2.2 Predictive Modelling of Damage Progression in Thermoplastic Composite Material

- This work has developed a modelling methodology for predicting damage progression and large deformation in thermoplastic composites using the advanced MAT 162 constitutive material model within the LS-DYNA explicit finite element code.

- This investigation presented an inverse modelling technique for calibrating and validating the LS-DYNA MAT 162 advanced material model for simulating damage progression in thermoplastic composites. In this methodology, the damage parameters were systematically obtained by correlating simulations with standard coupon tests (tensile, compression and shear). A novel strategy for calibrating the non-linear shear response of Twintex was presented.
- The calibrated parameters are validated by simulating a series coupon level three-point bending test and low velocity impact tests.
- The predictive modelling methodology has been successfully validated for simulating damage progression and large deformation in large scale complex shaped thermoplastic composite components.

6.2.3 Characterisation of Anisotropic Crushable Thermoplastic Foam Properties

- This work has presented the characterisation of the static and dynamic mechanical properties of the anisotropic crushable polypropylene foam supplied by Dow Chemical Company under the trade name Strandfoam.
- The investigation showed that there was almost a 50% increase in the compression modulus and strength in the extrusion direction as strain rate increased.
- The static and dynamic shear properties were investigated using an oblique shear test fixture with a surface angle of 45°. It has been shown that the shear properties show very little strain rate sensitivity.
- The static tensile properties have been investigated. It has been shown that the tensile modulus and strength in the extrusion direction are 76% and 68% higher than in the transverse direction, respectively. Failure in the foam under tensile loading in the extrusion direction is dominated by plastic stretching in the cell walls prior to ultimate failure while strand interface separation is the primary mode of failure for transverse tensile loading.

6.2.4 Modelling the Failure Modes of Thermoplastic Composite Sandwich Structures

- An extensive experimental study of the response of foam cored thermoplastic composite sandwich structures with Twintex skins and Strandfoam cores under static and dynamic localised indentation and bending loads has been presented.
- The experimental indentation investigation has shown that the primary failure modes for the thermoplastic sandwich beam under static and dynamic (up to 15 J) indentation loading are: localised core crush, top face compression and plastic deformation including damage. The top skin exhibited visible matrix damage and compressive fibre fracture. The amount of localised core crush reduced with increasing skin thickness.
- It has been shown that the dominant failure modes in the sandwich beam under quasi-static bending loads are face compression (buckling), core shear fracture, skin-core debonding and local core crush.
- For dynamic bending loading, the sandwich beams fail primarily by core shear fracture and skin-core debonding. Furthermore, the location of the core shear fracture along the beam moved further away from the impactor as skin thickness increased. This is due to the thick skins providing better load distribution along the length of the beam
- A finite element modelling methodology for simulating the failure modes and large deformation of thermoplastic sandwich structures has been evaluated and presented.
- The application of the LS-DYNA MAT 162 damage model to skin behaviour in combination with a novel approach to modelling core shear fracture and skin-core debonding using a principal strain failure criterion along with element erosion has resulted in good correlation between the experimental and simulation results.
- For quasi-static loading of the beams, reasonable agreement for both load-displacement and failure has been achieved between simulations and experimental results. For dynamic loading, elastic response, initial peak loads and the occurrence of core shear fracture and skin-

core debonding have also been simulated well. However, under the dynamic loading rates, the more complex post initial failure response involving beam vibration and multiple load peaks were more difficult to simulate.

- Further refinement of the foam material model, in particular, is needed for better qualitative and quantitative correlations.

6.3 Recommendations for Future Work

The present research highlights a number of issues which require further investigation. The following recommendations are therefore made:

6.3.1 Thermoplastic Composite Material Characterisation

- There is a need to establish standard experimental techniques for characterising composite materials at high strain rates. This would allow for better comparative analysis of dynamic data between different materials for tests conducted at various test houses.
- In this study the mechanical properties of Twintex were characterised at intermediate strain rates. It is recommended that the mechanical properties of Twintex be evaluated at higher strain rates using techniques such as the split Hopkinson bar. This will be necessary for calibrating finite element material models for high velocity impact applications such as in crash, ballistics and blast analysis.
- The shear punch fixture presented in this study was designed to be used for both static and dynamic analysis of the through-thickness shear properties of Twintex. However, the dynamic tests were not conducted due to time constraints in the project. It is recommended that in the future dynamic shear punch tests are conducted using the fixture developed in this study. This will be of particularly importance for ballistic and blast analysis.
- Biaxial testing should be conducted so as to obtain the biaxial response of Twintex which would aid in identifying suitable failure criteria for this material.
- The through-thickness compression and tensile strength were estimated in this study. These properties should be experimentally evaluated in the future.

6.3.2 Composite Material Model Improvements

This research has identified a number of limitations with the MAT 162 composite material model. Further modifications to the model should include:

- MAT 162 does not allow for different values of the damage parameters for tensile and compression loading to be used simultaneously. This can lead to inaccurate representation of mixed mode failure that is encountered in, for example, beam bending where there is tensile loading in the bottom layers and compression loading in the top layers. For future investigations MAT 162 should be modified to allow for the simultaneous input of different damage parameters for various load cases.
- A small level of localisation and mesh sensitivity was observed in this study. Localisation was reduced by using a uniform mesh size in all modes, especially where damage was anticipated. In future, it is recommended that a smear crack approach and/or non-local damage distribution method be applied with the MAT 162 model so as to reduce localisation and mesh dependency.
- Currently the MAT 162 model has been implemented for solid elements only. Solid elements allow for a more detailed analysis of the three-dimensional stress state within the composite material under impact loading. However, they are computationally expensive. It is recommended that a shell element version of MAT 162 be developed especially for use in simulating large scale composite structures under crash loads.
- MAT 162 requires the input of four strain rate constants. This study has shown that these strain rate constants are different for dynamic tensile and compression loading. However, MAT 162 does not allow for the different strain rate constants for tension and compression to be used simultaneously. Furthermore, the strain rate constant for shear, C3, is used for both in-plane and through thickness shear rate effects. These features in the model are an oversimplification of the dynamic response of the material. For future work, the MAT 162 model should allow the input of different strain rate constants for tensile and compression loading.

6.3.3 Foam and Sandwich Model Improvements

- Further refinement of the foam model is required so as to better account for the complex failure modes of the foam material under impact loading. The current maximum principal strain fracture criterion provides useful predictions of core shear and skin-core debonding; however, further work is required in developing a more accurate simulation of foam fracture. Other methods such as fracture mechanics, stress based fracture criteria, interface elements, damage mechanics and tied contact algorithms are worth investigating in the future.
- More detailed experimental analysis of skin-core debonding is required using techniques such as the cracked sandwich beam (CSB), double cantilever beam (DCB), end notch flexural (ENF) and mixed mode bending (MMB) tests.
- The compressive properties of Strandfoam were shown to be significantly strain rate sensitive. Therefore, a more fundamental approach to accounting for strain rate effects in the foam model is required.

6.3.4 Extended Loading Investigations

In this study, the finite element model has been validated for composite structures that were primarily subjected to static and dynamic out-of-plane impact bending loads. Further validation is now required for composite structures subjected to a variety of other loading conditions, such as in-plane deformation and crush, for example, axial tube crush and edgewise loading of sandwich structures. Furthermore, the model needs to be validated for applications beyond low velocity impact scenarios. Further work is required to validate the model for simulating thermoplastic composite structures under ballistic and blast impacts. Other loading modes that are of interest include torsion and multiaxial loading.

References

1. *Rigid Shell-Lightweight Core*, in *Polymotive*. 2007. p. 15-17.
2. Jacob, A., K. Simpson, G. Marsh, and R. Stewart, *Reinforced Plastics Automotive Supplement*. 2003: Elsevier Science.
3. Jacob, A., *Car makers increase their use of composites.* Reinforced Plastics, 2004. **48**(2): p. 26-32.
4. Tornqvist, R. and B. Baser, *Structural Modules with Improved Crash Performance Using Thermoplastic Composites.* SAE, 2002(2002-01-1038): p. 603-613.
5. Zenkert, D., *The Handbook of Sandwich Construction*. 1997, London: Engineering Material Advisory Services (EMAS).
6. Griffiths, B., *Glass-Reinforced Thermoplastic Succeeds in Car Crash Structure*, in *Composite Technology*. October 2006. p. 52-54.
7. Wilson, M., *Finite Element Analysis of Glass Fibre Reinforced Thermoplastic Composites for Structural Automotive Components*, in *PhD Thesis*. 2003, The University of Nottingham: Nottingham.
8. Kulandaivel, P., R. Brooks, M. Dunmore, C.D. Rudd, and D. McNally. *Processing and Performance of Thermoplastic Composite Sandwich Beams for Automotive Applications*. in *Proceedings of the 37th ISTC-SAMPE Conference*. 2005. Seattle, WA.
9. Plantema, F.J., *Sandwich Construction*. Airplane, Missile, and Spacecraft Structures, ed. N.J. Hoff. Vol. 3. 1966, New York: John Wiley and Sons.
10. Skawinski, O., C. Binetruy, P. Krawczak, J. Grando, E. Bonneau, J.-M. Scanzi, and B. Hilaire. *Modelling of Bending Behaviour of Glass/PP - PP Foam Core Sandwich Panels Manufactured by Isothermal Compression*. in *ECCM-10*. 2002. Brugge, Belgium.
11. Passaro, A., P. Corvaglia, O. Manni, L. Barone, and A. Maffezzoli, *Processing-properties relationship of sandwich panels with polypropylene-core and polypropylene-matrix composite skins.* Polymer Composites, 2004. **25**(3): p. 307-318.
12. Allen, H.G., *Analysis and Design of Structural Sandwich Panels*. 1969, London: Pergamon Press.
13. Mines, R.A.W. and A. Alias, *Numerical Simulation of the Progressive Collapse of Polymer Composite Sandwich Beams Under Static Loading.* Composites Part A: Applied Science and Manufacturing, 2002. **33**: p. 11-26.
14. Mines, R.A.W., *On the Numerical Simulation of the Progressive Collapse of Polymer Composite Sandwich Beams Under Impact Loading*, in *Advances in Dynamics and Impact Mechanics*, C.A. Brebbia and G.N. Nurick, Editors. 2003, WIT Press: Boston.
15. Vinson, J.R., *The Behavior of Sandwich Structures of Isotropic and Composite Materials*. 1999, Lancaster: Technomic.
16. *Thermoformable Composite Panels*. [cited 10/01/2007]; Available from: http://www.flexformtech.com/pdf/2006/Composites%20World%20%20'%20Thermoformable%20Composite%20Panels'.pdf.
17. Kulandaivel, P., *Manufacturing and Performance of Thermoplastic Composite Sandwich Structures*, in *PhD Thesis*. 2006, The University of Nottingham: Nottingham.

18. *Twintex Demonstrator*. [cited 10/01/2007]; Available from: http://www.saint-gobainvetrotex.com/pdf/twintex_demonstrator.pdf.
19. Brooks, R. and M. Pharaoh. *Crashworthy Automotive Structures Using thermoplastic Composites (CRACTAC)*. in *Automotive Composites Seminar*. 2003. Coventry, UK: IMechE.
20. Reinhart, T. and L.L. Clements, *Introduction to Composites*, in *Engineered Materials Handbook Volume 1 Composites*. 1987, ASTM International. p. 27-37.
21. Dhakal, H.N., Z.Y. Zhang, M.O.W. Richardson, and O.A.Z. Errajhi, *The low velocity impact response of non-woven hemp fibre reinforced unsaturated polyester composites.* Composite Structures, 2007. **81**(4): p. 559.
22. Vaidya, U.K. *Advanced Composites and Plastics Education Module*. 2005 [cited 10/01/2007]; Available from: http://www.eng.uab.edu/epcl/mod.htm.
23. Wakeman, M.D. and C.D. Rudd, *Compression Molding of Thermoplastic Composites*, in *Comprehensive Composite Materials*, A. Kelly and C. Zweben, Editors. 2000, Pergamon Press: Oxon. p. 915-963.
24. Ning, H., G.M. Janowski, U.K. Vaidya, and G. Husman, *Thermoplastic sandwich structure design and manufacturing for the body panel of mass transit vehicle.* Composite Structures, 2007. **80**(1): p. 82.
25. Wakeman, M., *Non-isothermal Compression Moulding of Glass Fibre Reinforced Polypropylene*, in *PhD Thesis*. 1997, The University of Nottingham: Nottingham.
26. Engineered Materials Handbook Volume 1 Composites, ed. C.A. Dostal, M.S. Woods, and A.W. Ronke. 1987: ASTM International.
27. *Saint Gobain Vetrotex*. [cited 10/10/2003]; Available from: http://www.twintex.com/.
28. Rudd, C.D., R. Brooks, A.C. Long, N.A. Warrior, M.J. Wilson, and C. Santulli. *Development of a Crashworthy Composite Side Intrusion Beam Using Long Glass Fibre Reinforced Polypropylene for the Foresight Vehicle Programme*. in *Proceedings of the SAE Future Car Congress (Technical Paper 02P-354)*. 2002. Washington, Virginia, USA.
29. Warrior, N.A., M.J. Wilson, R. Brooks, and C.D. Rudd, *Modelling of Glass Thermoplastic Composite Side-Impact Structures.* International Journal for Crashworthiness, 2001. **6**(4): p. 553-559.
30. Nicholas, T., *Material Behaviour at High Strain Rates*, in *Impact Dynamics*, J.A. Zukas, et al., Editors. 1982, John Wiley & Sons: New York. p. 277-332.
31. Sierakowski, R.L., *Strain rate effects in composites.* Applied Mechanics Reviews, 1997. **50**(12 pt 1): p. 741-761.
32. Adams, D.F., *Composites in automotive applications: Design*, in *Comprehensive Composite Materials*, A. Kelly and C. Zweben, Editors. 2000, Pergamon Press: Oxon. p. 113-148.
33. Adams, D.F., *Test Methods for Mechanical Properties*, in *Comprehensive Composite Materials Vol 5*, A. Kelly and C. Zweben, Editors. 2000, Pergamon Press: Oxon. p. 113-148.
34. Sims, G.D., *Standards will cut composites industry costs.* Reinforced Plastics, 1998. **42**(8): p. 54-55.
35. *Twintex Technical Data Sheet*. [cited 10/01/2007]; Available from: http://www.twintex.com/pdf/sgvx_twintex_PPP.pdf.

36. *Physical Properties for FEA Modelling of Twintex*. 2005 [cited 10/10/2005]; Available from: www.twintex.com/pdf/FEA%20Modeling%20Report.pdf.
37. Hamouda, A.M.S. and M.S.J. Hashmi, *Testing of composite materials at high rates of strain: Advances and challenges.* Journal of Materials Processing Technology, 1998. **77**(1-3): p. 327-336.
38. Barre, S., T. Chotard, and M.L. Benzeggagh, *Comparative study of strain rate effects on mechanical properties of glass fibre-reinforced thermoset matrix composites.* Composites - Part A: Applied Science and Manufacturing, 1996. **27**(12): p. 1169-1181.
39. Groves, S.E., R.J. Sanchez, R.E. Lyon, and A.E. Brown. *High strain rate effects for composite materials*. in *Proceedings of the 11th Symposium on Composite Materials, May 4-5 1992*. 1993. Pittsburgh, PA, USA: Publ by ASTM, Philadelphia, PA, USA.
40. Todo, M., K. Takahashi, P. Beguelin, and H.H. Kausch, *Strain-rate dependence of the tensile fracture behaviour of woven-cloth reinforced polyamide composites.* Composites Science and Technology, 2000. **60**(5): p. 763-771.
41. Thiruppukuzhi, S.V. and C.T. Sun, *Models for the strain-rate-dependent behavior of polymer composites.* Composites Science and Technology, 2001. **61**(1): p. 1-12.
42. Fernie, R., *Loading Rate Effects on the Energy Absorption of Lightweight Tubular Crash Structures*, in *PhD Thesis*. 2002, The University of Nottingham: Nottingham.
43. Hsiao, H.M. and I.M. Daniel, *Strain rate behavior of composite materials.* Composites Part B:Engineering, 1998. **29**(5): p. 521-533.
44. Lifshitz, J.M., *Impact Strength of Angle Ply Fiber Reinforced Materials.* Journal of Composite Materials, 1976. **10**: p. 92-101.
45. Montiel, D.M. and C.J. Williams. *Method for evaluating the high strain rate compressive properties of composite materials*. in *10th Conference on Composite Materials: Testing and Design, Apr 24-25 1990*. 1992. San Francisco, CA, USA: Publ by ASTM, Philadelphia, PA, USA.
46. Kolsky, H., *An Investigation of the Mechanical Properties of Materials at Very High Rates of Loading.* Proceeding of the Physical Society (London), 1949. **62-B**: p. 676-700.
47. Hauser, F., *Techniques for Measuring Stress-Strain Relations at High Strain Rates.* Experimental Mechanics, 1966: p. 395-402.
48. Lindholm, U.S., *Some Experiments with the Split Hopkinson Pressure Bar.* Journal of the Mechanics and Physics of Solids, 1964. **12**: p. 317-335.
49. Mulliken, A.D., *Low to High Rate Deformation of Armorphous Polymers: Experiments and Modelling*, in *Masters Thesis*. 2002, Massachusetts Institute of Technology: Massachusetts.
50. Weeks, C.A. and C.T. Sun, *Modeling Non-linear Rate-dependent Behavior in Fiber-reinforced Composites.* Composites Science and Technology, 1998. **58**(3-4): p. 603-611.
51. Armenàkas, A.E. and C.A. Sciammarella, *Response of Glass-fibre-reinforced Epoxy Specimens of High Strain Rates of Tensile Loading.* Experimental Mechanics, 1973. **13**: p. 433-440.
52. Daniel, I.M., R.H. LaBedz, and T. Liber, *New Methods for Testing Composites at Very High Strain Rates.* Experimental Mechanics, 1981. **21**: p. 71-77.
53. Chamis, C.C. and G.T. Smith, *Environmental and High Strain Rates Effects on Composites for Engine Applications.* AIAA Journals, 1984. **22**(1): p. 128-134.

54. Harding, J. and L.M. Welsh, *A Tensile Testing Technique for Fibre-Reinforced Composites at Impact Rates of Strain.* Journal of Materials Science, 1983. **18**(6): p. 1810-1826.
55. Gibson, L.J. and M.F. Ashby, *Cellular Solids Structure and Properties*. 2 ed. Cambridge Solid State Science Series, ed. D.R. Clarke, S. Suresh, and I.M. Ward. 1997, Cambridge: Cambridge University Press.
56. Berthelot, J.-M. and É. Lolive, *Non-linear Behaviour of Foam Cores and Sandwich Materials, Part 1: Materials and Modelling.* Journal of Sandwich Structures and Materials, 2002. **4**: p. 219-247.
57. Borsellino, C., L. Calabrese, and A. Valenza, *Experimental and numerical evaluation of sandwich composite structures.* Composites Science and Technology, 2004. **64**(10-11): p. 1709-1715.
58. Corigliano, A., E. Rizzi, and E. Papa, *Experimental characterization and numerical simulations of a syntactic-foam/glass-fibre composite sandwich.* Composites Science and Technology, 2000. **60**(11): p. 2169.
59. Zhang, J., N. Kikuchi, V. Li, A. Yee, and G. Nusholtz, *Constitutive modeling of polymeric foam material subjected to dynamic crash loading.* International Journal of Impact Engineering, 1998. **21**(5): p. 369-386.
60. Belingardi, G., M.P. Cavatorta, and R. Duella, *Material characterization of a composite-foam sandwich for the front structure of a high speed train.* Composite Structures, 2003. **61**(1-2): p. 13.
61. Stender, C., H. Nahme, and P. Du Bois. *Numerical Simulation of Foams for Automotive Crashworthiness Analysis*. in *EuroPAM*. 2003. Mainz, Germany.
62. Subhash, G., Q. Liu, and X.-L. Gao, *Quasistatic and high strain rate uniaxial compressive response of polymeric structural foams.* International Journal of Impact Engineering, 2006. **32**(7): p. 1113.
63. Tagarielli, V.L., V.S. Deshpande, and N.A. Fleck, *The high strain rate response of PVC foams and end-grain balsa wood.* Composites Part B: Engineering. **In Press, Corrected Proof**: p. 2457.
64. Tagarielli, V.L., V.S. Deshpande, and N.A. Fleck, *The dynamic response of composite sandwich beams to transverse impact.* International Journal of Solids and Structures, 2007. **44**(7-8): p. 2442.
65. Rizzi, E., E. Papa, and A. Corigliano, *Mechanical behavior of a syntactic foam: experiments and modeling.* International Journal of Solids and Structures, 2000. **37**(40): p. 5773.
66. Bilkhu, S.S., M. Founas, and G.S. Nusholtz, *Determination of cellular foam material properties for use in finite elements analysis.* Experimental Techniques, 1994. **18**(1): p. 23-25.
67. Loup, D.C., R.C. Matteson, and A.W.J. Gielen. *Material Characterisation of PVC Foam Under Static and Dynamic Laoding*. in *7th International Conference on Sandwich Structures*. 2005. Aalborg, Denmark: Springer.
68. Mills, N.J. and A. Gilchrist, *Shear and Compressive Impact of Polypropylene Bead Foam.* Cellular Polymers, 1999. **18**(3): p. 157-174.
69. Kanny, K., H. Mahfaz, T. Thomas, and S. Jeelani, *Static and Dynamic Characterization of Polymer Foams Under Shear Loads.* Journal of Composite Materials, 2004. **38**(8): p. 629-639.
70. Yoon, K.J., C.K. Kim, and H. Park, *Nonlinear Flexural Deflection of Thermoplastic Foam Core Sandwich Beam.* Journal of Composite Materials, 2002. **36**(13): p. 1529-1539.

71. Daniel, I.M., G.K.-A. Wang, and J.L. Abot, *Failure Modes of Sandwich Beams.* International Journal of Damage Mechanics, 2002. **11**: p. 309-334.
72. K. W. Suh, C.P.P., M. J. Maurer, M. H. Tusim, R. De Genova, R. Broos, D. P. Sophiea, *Lightweight Cellular Plastics.* Advanced Materials, 2000. **12**(23): p. 1779-1789.
73. Maurer, M.J. *High Efficiency Energy Absorbing (EA) Foam for Automotive Vehicle Crashworthiness Applications*. in *Detriot Auto Interiors Show Conference*. 2001. Detriot.
74. Gandhe, G.V. and M.H. Tusim, *High Efficiency Energy Absorption Olefinic Foam.* SAE, 1999(1999-01-0296): p. 196-199.
75. Burr, S.T. and G.D. Vogel, *Material Model Development for Impact Analysis of Oriented Polypropylene Foam Structures.* SAE Paper No. 2001-01-0310, 2001.
76. Park, C.P. and G.A. Garcia, *Development of Polypropylene Plank Foam Products.* Journal of Cellular Plastics, 2002. **38**: p. 219-228.
77. Hirth, A., P. Du Bois, and K. Weimar. *A Material Model for Transversely Anistropic Crushable Foam in LS-DYNA*. in *7th International LS-DYNA Users Conference*. 2002. Dearborn, Michigan.
78. Ochoa, O.O. and J.N. Reddy, *Finite Element Analysis of Composite Laminates*. 1 ed. Solid Mechanics and its Applications, ed. G.M.L. Gladwell. Vol. 7. 1992, Dordrecht: Kluwer.
79. Jacob and Goulding, *An Explicit Finite Element Primer*. 2002: NAFEMS.
80. Pickett, A.K., E. Haug, and J. Ruckert, *A fracture damaging law suitable for anisotropic short fibre/matrix materials in an explicit finite element code.* Composites, 1990. **21**(4): p. 297-304.
81. Haug, E. and A. De Rouvray, *Crash Response of Composite Structures*, in *Structural Crashworthiness and Failure*, N. Jones and T. Wierzbicki, Editors. 1993, Elsevier: Essex. p. 237-294.
82. Du Bois, P., *Crashworthiness Engineering Course Notes*. 2004, California: Livermore Software Technology Corporation.
83. McCallum, S.C. and C. Constantinou. *The Influence of Bird Shape in Bird Strike Analysis*. in *Proceedings of the 5th European LS-DYNA Users' Conference*. 2005. Birmingham, UK.
84. Staples, J.F., M. Pitzer, and P. Du Bois. *Developement of Shipping Package Drop Analysis Capability at Westinghouse*. in *8th International LS-DYNA Users' Conference*. 2004. Dearborn, Michigan, USA.
85. Wilson, M. and B. Ricketts. *Validation Simulation of New Railway Rolling Stock Using the Finite Element Method*. in *Proceedings of the 4th European LS-DYNA Users' Conference*. 2003. Ulm, Germany.
86. *PAM-CRASH/PAM-SAFE Solver Notes Manual*. 2000, ESI Group: France.
87. Hallquist, J.O., *LS-DYNA Theory Manual*. 1998, Livermore: Livermore Software Technology Corporation.
88. *Altair Engineering*. [cited 10/01/2006]; Available from: www.altair.com/.
89. *Papers and Documents for LS-DYNA*. [cited 10/01/2005]; Available from: http://www.dynalook.com/index.html.
90. Becker, A.A., *An introductory guide to finite element analysis*. 2004, Bury St Edmunds: Professional Engineering.
91. Spyrakos, C.C. and J. Raftoyiannis, *Linear and Nonlinear Finite Element Analysis in Engineering Practice*. 1997, Pittsbugh: Algor.
92. Zienkiewicz, O.C. and R.L. Taylor, *The finite element method*. 5 ed. Vol. 1. 2000, Oxford: Butterworth-Heinemann.

93. Cheung, Y.K. and M.F. Yeo, *A practical introduction to finite element analysis*. 1979, London: Pitman.
94. Liu, G.-R., *The finite element method: a practical course*. 2003, Oxford: Butterworth-Heinemann.
95. Reddy, J.N., *Introduction to the Finite Element Method*. 2003: McGraw-Hill Education.
96. Noor, A.K., *Bibliography of Books and Monographs on Finite Element Technology.* Applied Mechanics Review, 1991. **44**(6): p. 307-317.
97. Matthews, F.L., G.A.O. Davies, D. Hitchings, and C. Scoutis, *Finite Element Modelling of Composite Materials and Structures*. 2000, Cambridge: Woodhead.
98. Barbero, E.J., G.F. Abdelal, and A. Caceres, *A micromechanics approach for damage modeling of polymer matrix composites.* Composite Structures, 2005. **67**(4): p. 427.
99. Bahei-El-Din, Y.A., G.J. Dvorak, and S. Utku, *Finite element analysis of elastic-plastic fibrous composite structures.* Computers & Structures, 1981. **13**(1-3): p. 321-330.
100. Cooper, E. and N.A. Warrior, *Elastic-Plastic Material Model for Finite Element Analysis of Crashworthy Composites.* Plastics, Rubber and Composites, 2002. **31**(6): p. 262-269.
101. Ozcan, R., *Elastic-plastic stress analysis in thermoplastic composite laminated plates under in-plane loading.* Composite Structures, 2000. **49**(2): p. 201-208.
102. Nanda, A. and T. Kuppusamy, *Three-dimensional elastic-plastic analysis of laminated composite plates.* Composite Structures, 1991. **17**(3): p. 213-225.
103. Kwon, Y.W. and K.Y. Byun, *Development of a new finite element formulation for the elasto-plastic analysis of fiber-reinforced composites.* Computers & Structures, 1990. **35**(5): p. 563-570.
104. Agarwal, B.D., J.M. Lifshitz, and L.J. Broutman, *Elastic-plastic finite element analysis of short fibre composites.* Fibre Science and Technology, 1974. **7**(1): p. 45-62.
105. Swanson, S.R., *Elastic Impact Stress Analysis of Composite Plates and Cylinders*, in *Impact Behaviour of Fibre-Reinforced Composite Materials and Structures*, S.R. Reid and G. Zhou, Editors. 2000, Woodhead: Cambridge. p. 186-211.
106. Cooper, E., *An Elastic-Palstic Finite Element Model for Composite Crash Structures*, in *PhD Thesis*. 2002, The University of Nottingham: Nottingham.
107. Vaziri, R., M.D. Olson, and D.L. Anderson, *Finite element analysis of fibrous composite structures: A plasticity approach.* Computers & Structures, 1992. **44**(1-2): p. 103-116.
108. Warrior, N.A., *Anisotropic Materials*, in *Material Models and Modes of Failure*. 2002, The University of Nottingham: Lecture Notes.
109. Reddy, J.N. and A. Miravete, *Practical Analysis of Composite Laminates*. 1995, Florida: CRC Press.
110. Bayandor, J., R.S. Thomsen, M.L. Scott, and M.Q. Nguyen, *Investigation of Impact and Damage Tolerance in Advanced Aerospace Composite Structures.* International Journal for Crashworthiness, 2003. **8**(3): p. 297-306.
111. Chang, F.-K. and K.-Y. Chang, *A Progressive Damage Model for Laminated Composites Containing Stress Concentrations.* Journal of Composite Materials, 1987. **21**: p. 835-855.
112. Hallett, S.R. and D.D. Symons. *Testing and Modelling of Impact Failure Mechanisms in Carbon Fibre*. in *Proceedings of NAFEMS World Congress '97 on Design, Simulaiton, Optimisation, Reliability*

and Applicability of Computaitonal Methods. 1997. Stuttgart, Germany.
113. Hou, J.P., N. Petrinic, C. Ruiz, and S.R. Hallett, *Prediction of impact damage in composite plates.* Composites Science and Technology, 2000. **60**(2): p. 273-281.
114. Hou, J.P., N. Petrinic, and C. Ruiz, *A delamination criterion for laminated composites under low-velocity impact.* Composites Science and Technology, 2001. **61**(14): p. 2069-2074.
115. Davies, G.A.O., X. Zhang, G. Zhou, and S. Watson, *Numerical Modelling of Impact Damage.* Composites, 1994. **25**(5): p. 342-350.
116. Okoli, O.I. and A. Abdul-Latif, *Failure in composite laminates: overview of an attempt at prediction.* Composites Part A: Applied Science and Manufacturing, 2002. **33**(3): p. 315-321.
117. Schweizerhof, K., K. Weimar, T. Münz, and T. Rotterner. *Crashworthiness Analysis with Enhanced Composite Materials Models in LS-DYNA-Merits and Limits*. in *5th International LS-DYNA Users' Conference*. 1998. Southfield, Michigan.
118. Hallquist, J.O., *LS-DYNA Keyword User's Manual Version 970*. 2003, Livermore: Livermore Software Technology Corporation.
119. Mamalis, A.G., D.E. Manolakos, M.B. Ioannidis, and D.P. Papapostolou. *The static and dynamic axial collapse of CFRP square tubes: Finite element modelling*. Composite Structures 2005 2004/0 [cited 25 October 2005]; 347-360]. Available from: http://www.sciencedirect.com.
120. Hörmann, M. and M. Wacker. *Simulation of the Crash Performance of Crash Boxes Based on Advanced Thermoplastic Composite*. in *5th European LS-DYNA Users Conference*. 2005. Birmingham, UK.
121. Carlsson, L.A., J.W. Gillespie, and B.R. Pipes, *On the Analysis and Design of the End Notched Flexure (ENF) Specimen for Mode II Testing.* Journal of Composite Materials, 1986. **20**: p. 594-604.
122. Daniewicz, D. and G. Frantziskonis, *Edge delamination in laminated composites.* Composite Structures, 1992. **21**(3): p. 141-153.
123. Hashemi, S., J. Kinloch, and J.G. Williams, *The Effects of Geometry, Rate and Temperature on the Mode I, Mode II and Mixed-Mode I/II Interlaminar Fracture of Carbon-Fibre/Poly(ether-ether ketone) Composites.* Journal of Composite Materials, 1990. **24**: p. 918-956.
124. Hwang, S.-F. and C.-L. Hu, *Tearing Mode Interlaminar Fracture toughness of Composite Materials.* Polymer Composites, 2001. **22**(1): p. 57-64.
125. Lammerant, L. and I. Verpoest, *Modelling of the interaction between matrix cracks and delaminations during impact of composite plates.* Composites Science and Technology, 1996. **56**(10): p. 1171-1178.
126. Lammerant, L. and I. Verpoest, *The interaction between matrix cracks and delaminations during quasi-static impact of composites.* Composites Science and Technology, 1994. **51**(4): p. 505-516.
127. Rinderknecht, S. and B. Kroplin, *Delamination Growth Simulation with Moving Mesh Technique*, in *Advances in Non-Linear Finite Element Methods*, B.H.V. Topping and M. Padadrakis, Editors. 1994, CIVIL-COMP: Edinburgh. p. 187-197.
128. Abrate, S., *Impact on Laminated Composites: Recent Advances.* Applied Mechanics Review, 1994. **47**(11): p. 517-544.
129. Armanios, E.A., L.W. Rehfield, and F. Weinstein, *Understanding and Predicting Sublaminate Damage Mechanisms in Composite Structures*, in *Composite Materials: Testing and Design*, S.P. Garbo, Editor. 1990, ASTM STP 1059, American Society for Testing and Materials: Philadelphia. p. 231-249.

130. Borg, R., L. Nilsson, and K. Simonsson, *Simulation of delamination in fiber composites with a discrete cohesive failure model.* Composites Science and Technology, 2001. **61**(5): p. 667-677.
131. Corigliano, A., *Formulation, identification and use of interface models in the numerical analysis of composite delamination.* International Journal of Solids and Structures, 1993. **30**(20): p. 2779-2811.
132. Crisfield, M.A., Y. Mi, G.A.O. Davies, and H.B. Hellweg. *Finite Element Methods and the Progressive Failure-Modelling of Composites Structures*. in *Computational Plasticity: Fundamental Applications*. 1997. Barcelona: CIMNE.
133. Davidson, B.D., *Three Dimensional Analysis and Resulting Design Recommendations for Unidirectional and Multidirectional End-Notched Flexure Tests.* Journal of Composite Materials, 1995. **29**(16): p. 2108-2133.
134. Konig, M., R. Krugger, and H. Parisch. *A Finite Element Approach for Predicting Delamination Growth*. in *Proceedings of NAFEMS World Congress '97 on Design, Simulaiton, Optimisation, Reliability and Applicability of Computaitonal Methods*. 1997. Stuttgart, Germany.
135. Lourenco, N.F., *Predictive Finite Element Method for Axial Crush of Composite Tubes*, in *PhD Thesis*. 2002, The University of Nottingham: Nottingham.
136. Miravete, A. and M.A. Jiménez, *Application of the Finite Element Method to Prediction of the Onset of Delamination.* Applied Mechanics Review, 2002. **55**(2): p. 89.
137. Wisheart, M. and M.O.W. Richardson, *The finite element analysis of impact induced delamination in composite materials using a novel interface element.* Composites Part A: Applied Science and Manufacturing, 1998. **29**(3): p. 301-313.
138. Yan, A.-M., E. Marechal, and H. Nguyen-Dang, *A finite-element model of mixed-mode delamination in laminated composites with an R-curve effect.* Composites Science and Technology, 2001. **61**(10): p. 1413-1427.
139. Zheng, S. and C.T. Sun, *A double-plate finite-element model for the impact-induced delamination problem.* Composites Science and Technology, 1995. **53**(1): p. 111-118.
140. Tay, T.E., *Characterisation and Analysis of Delamination Fracture in Composites: An Overview of Developments from 1990 to 2001.* Applied Mechanics Review, 2003. **56**(1): p. 1-32.
141. Geubelle, P.H. and J.S. Baylor, *Impact-induced delamination of composites: a 2D simulation.* Composites Part B: Engineering, 1998. **29**(5): p. 589-602.
142. Allix, O. and P. Ladeveze, *Interlaminar interface modelling for the prediction of delamination.* Composite Structures, 1992. **22**(4): p. 235-242.
143. Allix, O., P. Ladeveze, and A. Corigliano, *Damage analysis of interlaminar fracture specimens.* Composite Structures, 1995. **31**(1): p. 61-74.
144. Corigliano, A. and O. Allix, *Some aspects of interlaminar degradation in composites.* Computer Methods in Applied Mechanics and Engineering, 2000. **185**(2-4): p. 203-224.
145. Kachanov, L.M., *On Creep Fracture Time.* Izv. Akad. Nauk SSR Otd. Tekhn. Nauk, 1958(8): p. 26-31 (In Russian).
146. Talreja, R., *Damage Characterization by Internal Variables*, in *Damage Mechanics of Composite Materials*, R. Talreja, Editor. 1994, Elsevier: Amsterdam. p. 53-78.

147. Murakami, S., *Mechanical Modelling of Material Damage.* Journal of Applied Mechanics, 1988. **55**: p. 280-286.
148. Joshi, S.P. and G. Frantziskonis, *Damage evolution in laminated advanced composites.* Composite Structures, 1991. **17**(2): p. 127-139.
149. Frantziskonis, G. and S.P. Joshi, *Damage evolution and constitutive behavior of advanced composites.* Composite Structures, 1990. **16**(4): p. 341-357.
150. Frantziskonis, G., *Distributed damage in composites, theory and verification.* Composite Structures, 1988. **10**(2): p. 165-184.
151. Talreja, R., *Continuum modelling of damage in ceramic matrix composites.* Mechanics of Materials, 1991. **12**(2): p. 165-180.
152. Talreja, R., *Transverse Cracking and Stiffness Reduction in Composites Laminates.* Journal of Composite Materials, 1985. **19**: p. 355-375.
153. Allen, D.H., *Damage Evolution in Laminates*, in *Damage Mechanics of Composite Materials*, R. Talreja, Editor. 1994, Elsevier: Amsterdam. p. 79-114.
154. Allen, D.H., C.E. Harris, and S.E. Groves, *A thermomechanical constitutive theory for elastic composites with distributed damage--I. Theoretical development.* International Journal of Solids and Structures, 1987. **23**(9): p. 1301-1318.
155. Allen, D.H., C.E. Harris, and S.E. Groves, *A thermomechanical constitutive theory for elastic composites with distributed damage--II. Application to matrix cracking in laminated composites.* International Journal of Solids and Structures, 1987. **23**(9): p. 1319-1338.
156. Allen, D.H., *Homogenization principles and their application to continuum damage mechanics.* Composites Science and Technology, 2001. **61**(15): p. 2223-2230.
157. Phillips, M.L., C. Yoon, and D.H. Allen, *A computational model for predicting damage evolution in laminated composite plates.* Transactions of the ASME. Journal of Engineering Materials and Technology, 1999. **121**(4): p. 436-444.
158. Ladeveze, P. and E. LeDantec, *Damage modelling of the elementary ply for laminated composites.* Composites Science and Technology, 1992. **43**(3): p. 257-267.
159. Ladeveze, P., *A damage computational method for composite structures.* Computers & Structures, 1992. **44**(1-2): p. 79-87.
160. Ladeveze, P., L. Guitard, L. Champaney, and X. Aubard, *Debond modeling for multidirectional composites.* Computer Methods in Applied Mechanics and Engineering, 2000. **185**(2-4): p. 109-122.
161. Ladeveze, P., O. Allix, J.-F. Deu, and D. Leveque, *A mesomodel for localisation and damage computation in laminates.* Computer Methods in Applied Mechanics and Engineering, 2000. **183**(1-2): p. 105-122.
162. Ladeveze, P. and G. Lubineau, *On a damage mesomodel for laminates: micro-meso relationships, possibilities and limits.* Composites Science and Technology, 2001. **61**(15): p. 2149-2158.
163. Ladeveze, P. and G. Lubineau, *An enhanced mesomodel for laminates based on micromechanics.* Composites Science and Technology, 2002. **62**(4): p. 533-541.
164. Ladeveze, P. and G. Lubineau, *Pont entre les {{ micro }} et {{ meso }} mecaniques des composites stratifies: Relationships between 'micro' and 'meso' mechanics of laminated composites.* Comptes Rendus Mecanique, 2003. **331**(8): p. 537-544.

165. Ladeveze, P. and G. Lubineau, *On a damage mesomodel for laminates: micromechanics basis and improvement.* Mechanics of Materials, 2003. **35**(8): p. 763-775.
166. Daudeville, L. and P. Ladeveze, *A damage mechanics tool for laminate delamination.* Composite Structures, 1993. **25**(1-4): p. 547-555.
167. Allix, O. and J.F. Deü, *Delayed -Damage Modelling for Fracture Prediction of Laminated Composites Under Dynamic Loading.* Engineering Transactions, 1997. **45**(1): p. 29-46.
168. Barbero, E.J. and L. Paolo, *An Inelastic Damage Model for Fibre Reinforced Laminates.* Journal of Composite Materials, 2002. **36**(8): p. 941-962.
169. Pickett, A.K., J. Ruckert, D. Ulrich, and E. Haug. *Material Damage Law Suitable for Crashworthiness Investigation of Random and Directional Fibre Composite Materials*. in *XVIII Internaitonal Finite Element Congress*. 1989. Baden-Baden.
170. Haug, E., O. Fort, A. Tramecon, M. Watanabe, and I. Nakada, *Numerical Crashworthiness Simulation of Automotive Structures and Components Made of Continuous Fiber Reinforced Composite and Sandwich Assemblies.* SAE Paper 910152, 1991: p. 245-258.
171. Nakada, I. and E. Haug, *Numerical Simulation of Crash Behaviour of Composite Structures for Automotive Applications.* Matériaux & Techniques, 1994(1-2): p. 33-38.
172. McCarthy, M.A. and J.F.M. Wiggenraad, *Numerical investigation of a crash test of a composite helicopter subfloor structure.* Composite Structures, 2001. **51**(4): p. 345-359.
173. *Crashworthy Automotive Structures Using Thermoplastic Composites (CRACTAC) Report*. 2001, The University of Nottingham/The University of Warwick.
174. Rudd, C.D., R. Brooks, A.C. Long, N. Warrior, M.J. Wilson, and C. Santulli. *Development of a Crashworthy Composite side Intrusion Beam Using Long Glass Fibre Reinforce Polypropylene for the Foresight Vehicle Programme*. in *Future Car Congress*. 2002. Washington: SAE.
175. Curtis, C.D., *Energy Absorption and Crush Behaviour of Composite Tubes*, in *PhD Thesis*. 2000, The University of Nottingham: Nottingham.
176. Morozov, E.V. and V.A. Thomson, *Simulating the progressive crushing of fabric reinforced composite structures.* Composite Structures, 2006. **76**(1-2): p. 130.
177. Mikkor, K.M., R.S. Thomson, I. Herszberg, T. Weller, and A.P. Mouritz, *Finite element modelling of impact on preloaded composite panels.* Composite Structures, 2006. **75**(1-4): p. 501.
178. Johnson, A.F. and J. Simon. *Modelling Fabric Reinforced Composites Under Impact Load*. in *EUROMECH 400: Impact and damage Tolerance Modelling of Composite Materials and Structures*. 1999. Imperial College of Science Technology & Medicine, London.
179. Johnson, A.F., *Modelling fabric reinforced composites under impact loads.* Composites Part A: Applied Science and Manufacturing, 2001. **32**(9): p. 1197-1206.
180. Johnson, A.F. and M. Holzapfel, *Modelling soft body impact on composite structures.* Composite Structures, 2003. **61**(1-2): p. 103-113.
181. Johnson, A.F., A.K. Pickett, and P. Rozycki, *Computational methods for predicting impact damage in composite structures.* Composites Science and Technology, 2001. **61**(15): p. 2183-2192.

182. Greve, L. and A.K. Pickett, *Modelling damage and failure in carbon/epoxy non-crimp fabric composites including effects of fabric pre-shear.* Composites Part A: Applied Science and Manufacturing, 2006. **37**(11): p. 1983.
183. Greve, L. and A.K. Pickett, *Delamination testing and modelling for composite crash simulation.* Composites Science and Technology, 2006. **66**(6): p. 816.
184. Pickett, A.K. and M.R.C. Fouinneteau, *Material characterisation and calibration of a meso-mechanical damage model for braid reinforced composites.* Composites Part A: Applied Science and Manufacturing, 2006. **37**(2): p. 368.
185. Lamb, A.J., *Experimental Investigation and Numerical Modelling of Composite-Honeycomb Materials Used in Formula 1 Crash Structures*, in *PhD Thesis*. 2007, Cranfield University.
186. Matzenmiller, A., J. Lubliner, and R.L. Taylor, *A constitutive model for anisotropic damage in fiber-composites.* Mechanics of Materials, 1995. **20**(2): p. 125-152.
187. Williams, K.V. and R. Vaziri, *Application of a damage mechanics model for predicting the impact response of composite materials.* Computers & Structures, 2001. **79**(10): p. 997-1011.
188. Iannucci, L. *Composite Design Using a Damage Mechanics Methodology*. in *Designing Cost-Effective Composites*. 1998. London: IMECHE Conference Transactions.
189. Iannucci, L., R. Dechaene, M. Willows, and J. Degrieck, *A failure model for the analysis of thin woven glass composite structures under impact loadings.* Computers & Structures, 2001. **79**(8): p. 785-799.
190. Iannucci, L., *Progressive failure modelling of woven carbon composite under impact.* International Journal of Impact Engineering, 2006. **32**(6): p. 1013.
191. Iannucci, L. and M.L. Willows, *An energy based damage mechanics approach to modelling impact onto woven composite materials: Part II. Experimental and numerical results.* Composites Part A: Applied Science and Manufacturing, 2007. **38**(2): p. 540.
192. Iannucci, L. and M.L. Willows, *An energy based damage mechanics approach to modelling impact onto woven composite materials--Part I: Numerical models.* Composites Part A: Applied Science and Manufacturing, 2006. **37**(11): p. 2041.
193. Williams, K.V., R. Vaziri, and A. Poursartip, *A physically based continuum damage mechanics model for thin laminated composite structures.* International Journal of Solids and Structures, 2003. **40**(9): p. 2267-2300.
194. McGregor, C.J., R. Vaziri, A. Poursartip, and X. Xiao, *Simulation of progressive damage development in braided composite tubes under axial compression.* Composites Part A: Applied Science and Manufacturing. **In Press, Corrected Proof**: p. 173.
195. Xiao, X., *Evaluation of a composite damage constitutive model for PP composites.* Composite Structures, 2007. **79**(2): p. 163.
196. Yen, C.-F. *Ballistic Impact Modelling of Composite Materials*. in *7th International LS-DYNA Users Conference*. 2002. Dearborn, Michigan.
197. Chan, S., Z. Fawaz, K. Behdinan, and R. Amid, *Ballistic limit prediction using a numerical model with progressive damage capability.* Composite Structures, 2007. **77**(4): p. 466.
198. Deka, L.J., S.D. Bartus, and U.K. Vaidya. *Damage Evolution and Energy Absorption of FRP Plates Subjected to Ballistic Impact Using a Numerical Model*. in *9th International LS-DYNA Users' Conference*. 2005. Dearborn, Michigan, USA.

199. Xiao, J.R., B.A. Gama, and J.J.W. Gillespie, *Progressive damage and delamination in plain weave S-2 glass/SC-15 composites under quasi-static punch-shear loading.* Composite Structures, 2007. **78**(2): p. 182.
200. Tasdemirci, A. and I.W. Hall, *Numerical and experimental studies of damage generation in a polymer composite material at high strain rates.* Polymer Testing, 2006. **25**(6): p. 797.
201. Kwon, Y.W. and A. Altekin, *Multilevel, Micro/Macro-Approach for Analysis of Woven-Fabric Composite Plates.* Journal of Composite Materials, 2002. **36**(8): p. 1005-1022.
202. Jiang, D. and D. Shu, *Stress distribution in damaged composite laminates under transverse impact.* Composite Structures. **In Press, Corrected Proof**.
203. Li, C.F., N. Hu, Y.J. Yin, H. Sekine, and H. Fukunaga, *Low-velocity impact-induced damage of continuous fiber-reinforced composite laminates. Part I. An FEM numerical model.* Composites Part A: Applied Science and Manufacturing, 2002. **33**(8): p. 1055-1062.
204. Li, C.F., N. Hu, J.G. Cheng, H. Fukunaga, and H. Sekine, *Low-velocity impact-induced damage of continuous fiber-reinforced composite laminates. Part II. Verification and numerical investigation.* Composites Part A: Applied Science and Manufacturing, 2002. **33**(8): p. 1063-1072.
205. Yazdchi, M., S. Valliappan, and W.C. Zhang, *A Continuum Model for Dynamic Damage Evolution of Anistropic Brittle Materials.* International Journal for Numerical Methods in Engineering, 1996. **39**: p. 1555-1583.
206. Simo, J.C. and J.W. Ju, *Strain and Stress Based Continuum Damage Models - I. Formulation.* International Journal for Numerical Methods in Engineering, 1987. **23**(7): p. 821-840.
207. Simo, J.C. and J.W. Ju, *Strain and Stress Based Continuum Damage Models - II. Computational Aspects.* International Journal for Numerical Methods in Engineering, 1987. **23**(7): p. 841-869.
208. Park, C.P., *Polyolefin Foam*, in *Handbook of Polymeric Foams and Foam Technology*, D. Klempner and K.C. Frisch, Editors. 1991, Hanser: Munich.
209. Reddy, J.N. and D.H. Robbins Jr., *Theories and Computational Models for Composite Laminates.* Applied Mechanics Review, 1994. **47**(6): p. 147-169.
210. Ha, K.H., *Finite Element Analysis of Sandwich Plates an Overview.* Computers & Structures, 1990. **37**(4): p. 397-403.
211. Noor, A.K., S.W. Burton, and C.W. Bert, *Computational Models for Sandwich Panels and Shells.* Applied Mechanics Review, 1996. **49**(3): p. 155-199.
212. Nayak, A.K., S.S.J. Moy, and R.A. Shenoi, *Quadrilateral Finite Elements for Multilayer Sandwich Plates.* Journal of Strain Analysis, 2003. **38**(5): p. 377-394.
213. Birman, V., *On the Choice of Shear Correction Factor in Sandwich Structures.* Journal of Sandwich Strutures and Materials, 2002. **4**: p. 83-95.
214. Cho, Y.B. and R.C. Averill, *First-order zig-zag sublaminate plate theory and finite element model for laminated composite and sandwich panels.* Composite Structures, 2000. **50**(1): p. 1-15.
215. Vlachoutsis, S., *Shear Correction Factors for Plates and Shells.* International Journal for Numerical Methods in Engineering, 1992. **33**: p. 1537-1552.

216. Yang, H.T.Y., S. Saigal, A. Masud, and R.K. Kapania, *A Survey of Recent Shell Finite Elements.* International Journal for Numerical Methods in Engineering, 2000. **47**: p. 101-127.
217. Malkus, D.S. and T.J.R. Hughes, *Mixed finite element methods -- Reduced and selective integration techniques: A unification of concepts.* Computer Methods in Applied Mechanics and Engineering, 1978. **15**(1): p. 63-81.
218. Manet, V., W.-S. Han, and A. Vautrin, *Hybrid Finite Elements for the Comutation of Sandwich Plates.* International Journal for Numerical Methods in Engineering, 2001. **50**: p. 467-486.
219. Spilker, R.L., *A hybrid-stress finite-element formulation for thick multilayer laminates.* Computers & Structures, 1980. **11**(6): p. 507-514.
220. Spilker, R.L. and B.E. Engelmann, *Hybrid-stress isoparametric elements for moderately thick and thin multilayer plates.* Computer Methods in Applied Mechanics and Engineering, 1986. **56**(3): p. 339-361.
221. Spilker, R.L. and N.I. Munir, *Comparison of hybrid-stress element through-thickness distributions corresponding to a high-order plate theory.* Computers & Structures, 1980. **11**(6): p. 579-586.
222. Spilker, R.L. and T.H.H. Pian, *A study of axisymmetric solid of revolution elements based on the assumed-stress hybrid model*1.* Computers & Structures, 1978. **9**(3): p. 273-279.
223. Tong, P., S.T. Mau, and T.H.H. Pian, *Derivation of geometric stiffness and mass matrices for finite element hybrid models*1.* International Journal of Solids and Structures, 1974. **10**(8): p. 919-932.
224. Wang, S.S. and F.G. Yuan, *A singular hybrid finite element analysis of boundary-layer stresses in composite laminates.* International Journal of Solids and Structures, 1983. **19**(9): p. 825-837.
225. Hinton, E. and H.C. Huang, *A family of quadrilateral Mindlin plate elements with substitute shear strain fields.* Computers & Structures, 1986. **23**(3): p. 409-431.
226. Pai, P.F. and A.N. Palazotto, *A higher-order sandwich plate theory accounting for 3-D stresses.* International Journal of Solids and Structures, 2001. **38**(30-31): p. 5045-5062.
227. Reddy, J.N., *A Simple Higher-Order Theory for Laminated Composite Plates.* Journal of Applied Mechanics, 1984. **51**: p. 745-752.
228. Rohwer, K., *Application of higher order theories to the bending analysis of layered composite plates.* International Journal of Solids and Structures, 1992. **29**(1): p. 105-119.
229. Thomsen, O.T. and J.R. Vinson, *Modelling of Tapered Sandwich Panels Using a Higher-Order Sandwich Theory Formulation.* AIAA Journal, 2002. **40**(9): p. 1867-1875.
230. Cho, Y.-B. and R.C. Averill, *An improved theory and finite-element model for laminated composite and sandwich beams using first-order zig-zag sublaminate approximations.* Composite Structures, 1997. **37**(3-4): p. 281-298.
231. Di Sciuva, M., *An Improved Shear-Deformation Theory for Moderately Thick Multilayered Anisotropic Shells and Plates.* Journal of Applied Mechanics, 1987. **54**: p. 589-596.
232. Di Sciuva, M., *Development of an anisotropic, multilayered, shear-deformable rectangular plate element.* Computers & Structures, 1985. **21**(4): p. 789-796.

233. Carrera, E., *A refined multilayered finite-element model applied to linear and non-linear analysis of sandwich plates.* Composites Science and Technology, 1998. **58**(10): p. 1553-1569.
234. Carrera, E. and H. Parisch, *An evaluation of geometrical nonlinear effects of thin and moderately thick multilayered composite shells.* Composite Structures, 1997. **40**(1): p. 11-24.
235. Di Sciuva, M., M. Gherlone, and D. Lomario, *Multiconstrained optimization of laminated and sandwich plates using evolutionary algorithms and higher-order plate theories.* Composite Structures, 2003. **59**(1): p. 149-154.
236. Di Sciuva, M. and U. Icardi, *Numerical assessment of the core deformability effect on the behavior of sandwich beams.* Composite Structures, 2001. **52**(1): p. 41-53.
237. Icardi, U., *A three-dimensional zig-zag theory for analysis of thick laminated beams.* Composite Structures, 2001. **52**(1): p. 123-135.
238. Icardi, U., *Higher-order zig-zag model for analysis of thick composite beams with inclusion of transverse normal stress and sublaminates approximations.* Composites Part B: Engineering, 2001. **32**(4): p. 343-354.
239. Owen, D.R.J. and Z.H. Li, *A Refined Analysis of Laminated Plates by Finite Element Displacement Methods - I. Fundamentals and Static Analysis.* Computers & Structures, 1987. **26**(6): p. 907-914.
240. Pin Tong and T.H.H. Pian, *A variational principle and the convergence of a finite-element method based on assumed stress distribution*1.* International Journal of Solids and Structures, 1969. **5**(5): p. 463-472.
241. Manet, V., *On the computation of interface stresses by finite elements for sandwich materials.* Composite Structures, 1999. **44**(4): p. 289-295.
242. Manet, V., W.-S. Han, and A. Vautrin. *Static Analysis of Sandwich Plates by Finite Elements*. in *Mechanics of Sandwich Structures Proceedings of the EUROMECH 360 Colloquium*. 1997. Saint-Etienne, France: Kluwer Academic Publishers.
243. Carrera, E., *Development, Ideas, and Evaluations Based Upon Reissner's Mixed Variational Theorem in the Modelling of Multilayered Plates and Shells.* Applied Mechanics Review, 2001. **54**(4): p. 301-329.
244. Rao, K.M. and H.-R. Meyer-Piening, *Analysis of thick laminated anisotropic composite plates by the finite element method.* Composite Structures, 1990. **15**(3): p. 185-213.
245. Toledano, A. and H. Murakami, *A high-order laminated plate theory with improved in-plane responses*1.* International Journal of Solids and Structures, 1987. **23**(1): p. 111-131.
246. Carrera, E., *CZ[deg] requirements--models for the two dimensional analysis of multilayered structures.* Composite Structures, 1997. **37**(3-4): p. 373-383.
247. Carrera, E., *A Study of Transverse Normal Stress Effect on Vibration of Multilayered Plates and Shells.* Journal of Sound and Vibration, 1999. **225**(5): p. 803-829.
248. Carrera, E. and L. Demasi, *Two Benchmarks to Assess Two-Dimensional Theories of Sandwich, Composite Plates.* AIAA Journal, 2003. **41**(7): p. 1356-1362.
249. Carrera, E. and L. Demasi, *Classical and Advanced Multilayered Plate Elements Based Upon PVD and RMVT. Part 1: Derivation of Finite Element Matrices.* International Journal for Numerical Methods in Engineering, 2002. **55**: p. 191-231.

250. Carrera, E. and L. Demasi, *Classical and Advanced Multilayered Plate Elements Based Upon PVD and RMVT. Part 2: Numerical Implementations.* International Journal for Numerical Methods in Engineering, 2002. **55**: p. 253-291.
251. Carrera, E. and F. Niglia. *A Refined Multilayered FEM Model Applied to Sandwich Structures*. in *Mechanics of Sandwich Structures Proceedings of the EUROMECH 360 Colloquium*. 1997. Saint-Etienne, France: Kluwer Academic Publishers.
252. Burton, W.S. and A.K. Noor, *Assessment of computational models for sandwich panels and shells.* Computer Methods in Applied Mechanics and Engineering, 1995. **124**(1-2): p. 125-151.
253. Meraghni, F., F. Desrumaux, and M.L. Benzeggagh, *Mechanical behaviour of cellular core for structural sandwich panels.* Composites Part A: Applied Science and Manufacturing, 1999. **30**(6): p. 767-779.
254. Lee, Y.-J. and Y. Shyu. *Low Velocity Impact Failure Analysis of Sandwich Beam*. in *Proceedings of ICCM 11*. 1997. Gold Coast, Australia.
255. Quaresimin, M. and L. Michelazzo. *Numerical Modelling and Experimental Analysis of Composite Sandwich Structures*. in *Virtual Prototyping Today: Impact and Future Trends*. 2002. Stezzano, Italy.
256. Sharma, S.C., H.N.N. Murthy, and M. Krishna, *Low-velocity impact response of polyurethane foam composite sandwich structures.* Journal of Reinforced Plastics and Composites, 2004. **23**(17): p. 1869-1882.
257. Aktay, L., A.F. Johnson, and M. Holzapfel, *Prediction of impact damage on sandwich composite panels.* Computational Materials Science, 2005. **32**(3-4): p. 252.
258. Lindholm, C.-J. *Impact and Indentation Behaviour of Sandwich Panels*. in *7th International Conference on Sandwich Structures*. 2005. Aalborg, Denmark: Springer.
259. Olsson, R., *Engineering Method for Prediction of Impact Response and Damage in Sandwich Panels.* Journal of Sandwich Structures and Materials, 2002. **4**.
260. Koissin, V., A. Shipsha, and V. Rizov, *The inelastic quasi-static response of sandwich structures to local loading.* Composite Structures, 2004. **64**(2): p. 129.
261. Rizov, V., A. Shipsha, and D. Zenkert, *Indentation study of foam core sandwich composite panels.* Composite Structures, 2005. **69**(1): p. 95.
262. Rizov, V.I., *Non-linear indentation behavior of foam core sandwich composite materials--A 2D approach.* Computational Materials Science, 2006. **35**(2): p. 107.
263. Lim, T.S., C.S. Lee, and D.G. Lee, *Failure Modes of Foam Core Sandwich Beams under Static and Impact Loads.* Journal of Composite Materials, 2004. **38**(18): p. 1639-1662.
264. Berger, L., R. Stadelmann, C. Dransfeld, K. Loiselet, S. Derler, and R. Stampfli. *Damage Initiation During Impact Loading of Sandwich Panels*. in *22nd International SAMPE Europe Conference Proceedings*. 2001. Paris.
265. Fritzsche, P., M. Minder, J. Mueller, I. Wyss, L. Berger, and C. Dransfeld. *Simulation des Sandwichversagens unter Impact*. in *DYNAmore LS-DYNA Forum Proceedings*. 2002. Bad Mergentheim, Germany (in German language).
266. Morgenthaler, M., L. Berger, P. Fritzsche, I. Wyss, J. Mueller, S. Derler, and R. Stampfli. *Optimising the Design of Sandwich Beams*

for Impact Load by Simulations. in *24th International SAMPE Europe Conference Proceedings*. 2003. Paris.
267. Lolive, É. and J.-M. Berthelot, *Non-linear Behaviour of Foam Cores and Sandwich Materials, Part 2: Indentation and Three-Point Bending.* Journal of Sandwich Structures and Materials, 2003. **4**: p. 297-352.
268. Russo, A. and B. Zuccarello, *Experimental and numerical evaluation of the mechanical behaviour of GFRP sandwich panels.* Composite Structures, 2007. **81**(4): p. 575.
269. ASTM-D3039, *Standard Test Method for Tensile Properties of Polymer Matrix Composite Materials.* ASTM International, 1995.
270. ASTM-D3518, *Standard Test Method for In-Plane Shear Response of Polymer Matrix Composite Materials by Tensile Test of a ±45° Laminate.* ASTM International, 1995.
271. Harding, J. *The High -Speed Punching of Woven-Roving Glass-Reinforced Composites*. in *Institute of Physics Conference*. 1979: The Institute of Physics.
272. ASTM-D732-02, *Standard Test Method for Shear Strength of Plastic by Punch Tool*. 2002, ASTM International.
273. BS-EN-ISO-14125:1998, *Fibre-Reinforced Plasrtic Composites - Determination of Flexural Properties.* British Standard.
274. Liu, K. and M.R. Piggott, *Shear Strength of Polymers and Fibre Composites: 1. Thermoplastic and Thermoset Polymers.* Composites, 1995. **26**(12): p. 829-840.
275. ASTM-D732-02, *Standard Test Method for Shear Strength of Plastics by Punch Tool.* ASTM International, 2002.
276. Chiem, C.-Y. and Z.-G. Liu, *The Relationship Between Tensile Strength and Shear Strength in Composite Materials Subjected to High Strain Rates.* Journal of Engineering Materials and Technology, 1988. **110**: p. 191-193.
277. Johnson, A.F. and G.D. Sims, *Short Time Behaviour of Thermolastics.* 1981. **1**(1): p. 63-71.
278. Papadakis, N., N. Reynolds, M. Pharaoh, P. Wood, and S. Gordon. *Strain Rate Effects Characterisation on the Tensile Properties of Thermoplastic Unidirectional Composite Laminates*. in *ECCM-10*. 2002. Brugge, Belgium.
279. Kellas, S., J. Morton, and K. Jackson, *Damage and Failure Mechanisms in Scaled Angled-Ply Laminates*, in *Composite Materials: Fatigue and Fracture, ASTM STP 1156*, W.W. Stinchcomb and N.E. Ashbaugh, Editors. 1993, American Society for Testing and Materials: Philadelphia. p. 257-280.
280. Lariviere, D., P. krawczak, C. Tiberi, and P. Lucas, *Interfacial Properties in Commingled Yarn Thermoplastic Composites.* Polymer Composites, 2004. **25**(6): p. 577-584.
281. Hosur, M.V., J. Alexander, U.K. Vaidya, and S. Jeelani, *High strain rate compression response of carbon/epoxy laminate composites.* Composite Structures, 2001. **52**(3-4): p. 405-417.
282. Harding, J., *Effect of strain rate and specimen geometry on the compressive strength of woven glass-reinforced epoxy laminates.* Composites, 1993. **24**(4): p. 323-332.
283. ESI, *PAM-CRASH/PAM-SAFE Solver Notes Manual*. 2002, France: ESI Group.
284. *LS-DYNA Support*, www.dynasupport.com, downloaded: September 10, 2006.
285. Heyerman, J.B., *On the Crashworthiness of Foam-Filled Ultralight Automotive Structures*, in *Masters Thesis*. 2000, University of Toronto: Toronto.

286. Santulli, C., R. Brooks, A.C. Long, N. Warrior, and C.D. Rudd, *Impact Properties of Compression Moulded Commingled E-glass Polypropylene Composites.* Plastics, Rubber and Composites, 2002. **31**(6): p. 270-277.
287. Hashin, Z., *Failure Criteria for Unidirectional Fiber Composites.* Journal of Applied Mechanics, 1980. **47**: p. 329-334.
288. Dasari, A. and R.D.K. Misra, *On the Strain Rate Sensitivity of High Density Polyethylene and Polypropylenes.* Materials Science and Engineering A, 2003. **358**: p. 356-371.
289. Collings, T.A., *Transverse Compressive Behaviour of Unidirectional Carbon Fibre Reinforced Plastics.* 1974. **5**(3): p. 108-116.
290. Abrate, S., *Impact on Laminated Composite Materials.* Applied Mechanics Review, 1991. **44**(4): p. 155-190.
291. Urban, J., *Crushing and Fracture of Lightweight Structures*, in *PhD Thesis*. 2003, Technical University of Denmark: Lyngby.
292. Santulli, C., *Drop-Weight Impact on the Side Intrusion Beam Trials*, in *CRACTAC Report [CD-ROM]*. 2000, University of Nottingham.
293. Wakeman, M.D., T.A. Cain, C.D. Rudd, R. Brooks, and A.C. Long, *Compression moulding of glass and polypropylene composites for optimised macro- and micro- mechanical properties--1 commingled glass and polypropylene.* Composites Science and Technology, 1998. **58**(12): p. 1879-1898.
294. FMVSS-214, *Federal Motor Vehicle Safety Standard FMVSS 214 - Side Impact Protection.* Federal Motor Vehicle Safety Standard, 2002.
295. Xiao, J.R., B.A. Gama, and J.W. Gillespie Jr., *Progressive Damage and Delamination in Plain Weave S-2 Glass/SC-15 Composites Under Quasi-Static Punch-Shear Loading.* Composite Structures, 2007. **78**(2): p. 182-196.
296. Tasdemirci, A. and I.W. Hall, *Numerical and Experimental Studies of Damage Generation in a Polymer Composite Material at High Strain Rates.* Polymer Testing, 2006. **25**: p. 797-806.
297. Deslauriers, P.F., D.S. Cronin, and A. Duquette. *Numerical Modeling of Woven Carbon Composite Failure*. in *8th International LS-DYNA Users' Conference*. 2004. Dearborn, Michigan, USA.
298. Donadon, M.V. and L. Iannucci. *An Objectivity Algorithm for Strain Softening Material Models*. in *9th International LS-DYNA Users' Conference*. 2005. Dearborn, Michigan, USA.
299. Greve, L. and A.K. Pickett, *Delamination Testing and Modelling for Composite Crash Simulation.* Composites Science and Technology, 2005. **66**(6): p. 816-826.
300. *Directive 2003/102/EC of the European Parliament and Council relating to the protection of pedestrians and other vulnerable road users*. http://europa.eu.int/comm/enterprise/automotive/pagesbackground/pedestrianprotection/index.htm.
301. Reyes, A., O.S. Hopperstad, T. Berstad, A.G. Hanssen, and M. Langseth, *Constitutive modeling of aluminum foam including fracture and statistical variation of density.* European Journal of Mechanics - A/Solids, 2003. **22**(6): p. 815-835.
302. Shaw, M.C. and T. Sata, *The Plastic Behaviour of Cellular Materials.* International Journal of Mechanical Science, 1966. **8**: p. 469-478.
303. Li, Q.M., R.A.W. Mines, and R.S. Birch, *The crush behaviour of Rohacell-51WF structural foam.* International Journal of Solids and Structures, 2000. **37**(43): p. 6321-6341.
304. Chang, F., J.O. Hallquist, D.X. Lu, B.K. Shahidi, C.M. Kudelko, and J.P. Tekelly, *Finite Element Analysis of Low Density High-Hysteresis*

Foam Materials and the Application in the Automotive Industry. SAE, 1994(940908).
305. Mines, R.A.W. and N. Jones, *Approximate elastic-plastic analysis of the static and impact behaviour of polymer composite sandwich beams.* Composites, 1995. **26**(12): p. 803-814.
306. Corigliano, A., E. Rizzi, and E. Papa, *Experimental characterization and numerical simulations of a syntactic-foam/glass-fibre composite sandwich.* Composites Science and Technology, 2000. **60**(11): p. 2169-2180.
307. Horrigan, D.P.W. and R.R. Aitken. *Modelling and Analysis of Impact Damaged Honeycomb Sandwich*. in *Second International Symposium on Impact and Friction of Solids, Structures and Intelligent Machines*. 2000. Montreal, Quebec, Canada.

Appendix A Publications

Brown, K., R. Brooks, and N. Warrior. *Numerical Simulation of Damage in Thermoplastic Composite Materials*. in Proceedings of the 5th European LS-DYNA Users' Conference. 2005. Birmingham, UK.

Brown, K., R. Brooks, and N. Warrior. *The Effect of Strain Rate on the Compression Properties of a Thermoplastic Composite*. in Proceedings of the 4th Materials Research Conference. 2005. London, UK.

Brown, K., R. Brooks, and N. Warrior. *Finite Element Analysis of Impact Damage in Thermoplastic Composite Materials*. in Proceedings of the TCN CAE International Conference. 2005. Lecce, Italy.

Brown, K., R. Brooks, and N. Warrior. Simulation of Impact Damage Progression in Thermoplastic Composite Structures. in Proceedings of the 27th International SAMPE Europe Conference. 2006. Paris, France.

Brown, K., R. Brooks, and N. Warrior. *Modelling the Impact Behaviour of Thermoplastic Composite Sandwich Structures*. in Proceedings of the 16th International Conference on Composite Materials (ICCM). 2007. Kyoto, Japan.

Appendix B Shear Punch Fixture

General assembly drawing for shear punch fixture.